

Engineering protein-based modulators of allergic, temporal, and checkpoint blockade anti-cancer immunity

by

Adrienne Marie Rothschilds

B.S. Bioengineering, B.A. Political Science

University of Washington, 2012

SUBMITTED TO THE DEPARTMENT OF BIOLOGICAL ENGINEERING IN PARTIAL FULFILLMENT OF
THE REQUIREMENTS FOR THE DEGREE OF

DOCTOR OF PHILOSOPHY IN BIOLOGICAL ENGINEERING

AT THE

MASSACHUSETTS INSTITUTE OF TECHNOLOGY

JUNE 2019

© 2019 Massachusetts Institute of Technology. All rights reserved.

Signature redacted

Signature of Author: _____

Department of Biological Engineering

May 21, 2019

Signature redacted

Certified by: _____

K. Dane Wittrup, PhD

Carbon P. Dubbs Professor in Chemical Engineering and Biological Engineering, MIT

Signature redacted

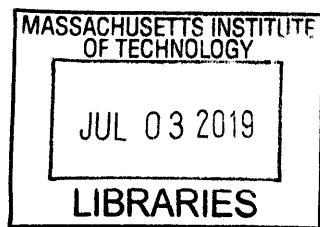
Thesis Supervisor

Accepted by: _____

Forest White, PhD

Professor & Graduate Program Chair

Department of Biological Engineering, MIT



ARCHIVES

THESIS COMMITTEE:

K. Dane Wittrup, PhD

Carbon P. Dubbs Professor in Chemical Engineering and Biological Engineering, MIT
Thesis Supervisor

Darrell J. Irvine, PhD

Professor of Materials Science & Engineering and Biological Engineering, MIT
Thesis Chair

Michael Birnbaum, PhD

Assistant Professor of Biological Engineering, MIT

Engineering protein-based modulators of allergic, temporal, and checkpoint blockade anti-cancer immunity

by

Adrienne Marie Rothschilds

Submitted to the Department of Biological Engineering on May 21, 2019
in Partial Fulfillment of the Requirements for the Degree of
Doctor of Philosophy in Biological Engineering

Abstract

Effective cancer treatment of the future requires incorporating diverse and innovative aspects of immunity to fight against cancer, accounting for pharmacokinetic and temporal barriers of therapeutics, and engineering approaches to understand and improve upon current immunotherapies. This thesis addresses these challenges in three projects utilizing the Wittrup Lab's quantitative, engineering approach to protein-based cancer immunotherapy.

In the first project, I attempted to harness the potency of allergic reactions against cancer by designing IgE class antibodies against two mouse tumor antigens and comparing them with traditional IgG antibodies. These IgE antibodies elicited modest or no tumor control, and limited efficacy could be due to fast pharmacokinetic clearance, absence of human-like allergic effector cells in mice, or tumor-suppressive effects from mast cells responding to IgE.

The second project described in this thesis focused on synchronizing combination immunotherapies with the temporal progression of the anti-cancer immune response. In this work, anti-tumor antibodies were combined with the cytokines interleukin 2 (IL2) and interferon alpha (IFN α). The order of administration of these therapies decoupled strong efficacy from dose-limiting toxicity in two tumor models. Given before IFN α , IL2 activated natural killer cells and heightened their responsiveness to subsequent IFN α , which was ultimately toxic and unnecessary for therapeutic efficacy. This project's proof of concept that efficacy and toxicity could be unlinked in immunotherapy began to establish a framework to use for rational combination therapy treatment schedule design, with the goal of treating with each agent when that piece of the immune system is active.

Finally, the third project used the Wittrup Lab's system of yeast surface display to engineer novel antibodies against the checkpoint blockade target cytotoxic T lymphocyte associated protein 4 (CTLA-4) as tools to improve understanding of the anti-CTLA-4 mechanism of action against cancer. Although the first wave of antibodies made had favorable characteristics against CTLA-4 as a soluble target, they bound a CTLA-4 epitope too close to the cell surface and so could not be used for therapeutic studies. Next generation sequencing on the yeast libraries identified alternative CTLA-4 binding antibody sequences, and these will be tested in future mechanistic and therapeutic studies.

Thesis Supervisor: K. Dane Wittrup, PhD, Carbon P. Dubbs Professor in Chemical Engineering and Biological Engineering, MIT

Table of Contents

Abstract.....	3
Acknowledgments.....	8
List of Figures and Tables.....	10
Chapter 1. Introduction	12
1.1 Re-emergence of immunotherapy for cancer	12
1.2 Immunotherapy comes in many shapes and forms.....	13
1.3 Thinking outside the box to the fight against cancer.....	14
1.4 Temporal framework for the anti-cancer immune response	15
1.5 Preclinical and clinical examples of temporal immunity	16
Preclinical examples	16
Clinical examples	18
1.6 Thesis overview	20
1.7 Glossary	20
1.8 Acknowledgments.....	21
Chapter 2. Elucidating the mechanisms of IgE anti-cancer immunity in an intact mouse immune system	22
Abstract	22
2.1 Introduction.....	22
2.2 Results	25
Constructing anti-tumor IgE and validating effector functions in vitro	25
IgE targeting tumor antigens confers weak tumor control in cytokine and antibody combination therapies	26
Limited IgE on tumor cells and short pharmacokinetic half-life of IgE-TA99 indicate intraperitoneal injection may not effectively reach the tumor	27

IT injection of IgE targeting tumor antigens performed worse or similarly to IP treatment in improving survival	29
B cells were main cellular perturbations in tumor, spleen, and blood after IgE treatment .	30
Improving mast cell or dendritic cell responses to IgE did not increase therapeutic efficacy	32
Biodistribution showed that therapeutic IgE-TA99 honed to basophils in tumor, spleen, and blood.....	33
Supplemental figures.....	35
2.3 Discussion.....	39
2.4 Materials and methods	40
Mice	40
Cell lines and media.....	41
Tumor treatment experiments.....	41
Protein production and purification.....	41
Degranulation assay	42
Pharmacokinetics	42
Biodistribution and flow cytometry	43
Therapeutic mast cell tumor study	43
Statistics.....	43
2.5 Acknowledgments.....	44
Chapter 3. Decoupling toxicity from efficacy in cancer immunotherapy by modulating the order and timing of combination immunotherapy	45
Abstract	45
3.1 Introduction.....	45
3.2 Results	47

The order of eIL2 with respect to IFN α decouples efficacy and toxicity	47
Inflammatory serum cytokines are partially responsible for toxicity of staggered eIL2 and IFN α	49
NK cells contribute to toxicity but not efficacy	51
Staggering eIL2 before IFN α increases NK cell activation and sensitivity to IFN α	53
Minimal treatment course and amount of anti-tumor antibody needed for efficacy in combination with eIL2 and IFN α	55
Extending timing concepts: checkpoint blockade and antigen-independent tumor targeting	57
3.3 Discussion.....	64
3.4 Materials and methods	65
Mice	65
Cell lines and media.....	66
Tumor treatment experiments.....	66
Depletion and neutralization studies	66
Protein production and purification.....	67
Flow cytometry	67
Systemic cytokine and chemokine levels	67
Organ and blood toxicity	68
Statistical analysis.....	68
ICS on KP mice	69
3.5 Supplemental figures	70
3.6 Acknowledgments.....	86

Chapter 4. Engineering CTLA-4 binders to understand and improve upon mechanisms of anti-CTLA-4 cancer immunotherapy 88

 Abstract 88

 4.1 Introduction..... 88

 4.2 Results 90

 Yeast surface display strategy to find B7-noncompetitive CTLA-4 binders nc19 and nc20.. 90

 Characterization of nc19 and nc20 as scFvs in yeast binding assays 94

 Nc19 and nc20 did not bind cell surface CTLA-4 95

 Epitope mapping to characterize why nc19 and nc20 did not bind surface CTLA-4..... 99

 New set of sorts to bias library away from nc19 and nc20 uncovers new clones, but all B7-competitive 102

 Next gen sequencing 105

 4.3 Discussion..... 118

 4.4 Materials and methods 119

 Sequences..... 119

 Protein expression and purification 119

 Yeast surface display 119

 Next generation sequencing Illumina library preparation 120

 Matlab, excel, graphpad files from Illumina sequencing data analysis and framework identification..... 122

 4.5 Acknowledgments..... 125

Chapter 5. Perspective and future directions..... 126

References 128

Acknowledgments

During the 6 years I spent pursuing my PhD at MIT, so many people have influenced my path both personally and professionally. These wonderful humans include the friendly staff of the Koch Institute; the welcoming biological engineering community of students, staff, and professors; the teammates of the innumerable soccer teams on which I played; mentors and friends made during my many extracurricular pursuits; the friends who have become like family in Boston and around the US; and my biological family. Some of these people have moved in and then out of my life, although still leaving a mark on who I am. Others have stayed with me through this whole experience, and it is them who I would like to specifically mention.

Firstly, to Dane, my PhD advisor: My journey from UC Berkeley in California to MIT would never have started without you. You supported me as I wove my way through three different PhD projects, allowing me to be imaginative and create new ideas, but offering grounded and brilliant scientific advice on whether and how to implement such ideas. Your advice on matters relating to cancer immunotherapy, protein engineering, wine, and Boston fine dining is unparalleled. Thanks for putting up with all my sass during my time in your lab, and sometimes throwing the sass right back at me.

To my soccer teammates: Soccer was a huge part of my life during my PhD, but it is actually the people and not the sport who made the experience invaluable. Many players came and went, but from almost the beginning a core group of us stayed together: Kelly, Zeninjor, Brett, Jacob, Ashvin, Varesh, Bo, and Deepak. We had some unforgettably epic experiences together as we captured gold championship cups in recreational silver level soccer leagues! I'm so grateful for all of your friendship over the years.

Many people in organizations around Boston have also influenced and mentored me. To the amazing mentors and friends in Novartis' IO group, the Innovation Institute, and Vida Ventures – thank you so much for giving me a chance to grow and learn outside my PhD lab!

To the many friends made at MIT Biological Engineering, and especially in my cohort: There are too many of you to name. Every time we see each other around campus or grab coffee or beers, I remember how lucky I am to have shared life at MIT with such inspiring, brilliant, and down-to-earth people. Looking forward to staying in touch with all of you.

To the friends outside MIT: spending time with you was an invaluable reminder of life outside my PhD. Whether we bonded during wine-infused cat playdates or shared our career ambitions and lives during long walks along the Charles, thank you for being there for me over the years.

To Wittrup Lab members, past and present: You are an inspiration both personally and scientifically. You made the lab and office a fun and intellectually stimulating environment, and I marvel every day what a privilege it is to be surrounded by such brilliant people. In particular, Alice, Monique, Naveen, Alison, and Noor, you guys became dear friends as well as labmates. In addition to always being there for me with scientific advice, you also have made invaluable contributions to my personal life and shared a lot of tears and laughter with me. Thank you. Also to Grayson, during the 2 years you were my UROP, thank you for being a fantastic scientist and human being.

To my non-biological family members: Naveen, Khoi, Deena, Kelly, and Emily, I seriously love you and won't be able to adequately thank you in words. Naveen, ever since we both joked about how we wouldn't get places in the Wittrup Lab, and no matter how busy you were or how many impressive experiments or professional activities you juggled, you ALWAYS were there for me in and outside the lab to give advice or just share a beer. Khoi, we've shared so many serious chats, laughter, and adventures over the years; I'm so grateful for your constant loyalty and friendship. Deena, there's been so many things in both of our lives over the last 6 years, but the constancy of your support and inspiration from your resilient approach to life has really made me who I am. Kelly, thank you for sharing so much laughter and seriousness with me in labs, spin studios, pug runs, yoga studios, soccer fields, restaurants, beaches, other states, and other countries. Emily, even though we have both grown older and more jaded during the 11 (!?) years we've been friends, I can't wait to keep making each other laugh about the stupid little things in life over the next 100 years and am eternally grateful to have you in my life.

To my biological family, including grandparents, aunts, uncles, cousins, Dad, Mom, Chris, Thomas, and Daniel: I love you so much. You nurtured me from a young age, first inspiring me to love learning and making me who I am today. Dad, it was you who first taught me to play soccer when I joined Chris' team as a 4-year-old, and put me on water skis around the same age. You've continued to gently push me forward to the next brighter thing since, and I wouldn't be here without you. Mom, from when you homeschooled us, your patience with us kids and persistent love and support has never wavered since you first inspired me to learn. I continue to bake the recipes you gave me every day, and feeling your presence has gotten me through many hard grad school times. Chris, you've always been one of my best friends despite our 1 year 11 months and 3 weeks age difference. Seriously though, no matter where we've lived across the country, we've shared a lot of life and laughs together and I look forward to many more. Thomas, we've had some ridiculous hypothetical science and life discussions, but they're unforgettable and I'm grateful for your continued friendship, love and support and look forward to rock climbing together soon! Danny, although we're many years apart in age, your quirky and brilliant humor has always made me laugh and our serious and hilarious conversations make me realize just how much we relate and how grateful I am for your friendship and love.

And with that, my rambling thanks are over. Cheers, friends and lovers!

List of Figures and Tables

Figure 1: Examples of temporally programmed combination immunotherapies ⁴⁹	19
Figure 2: Comparison of immune effector cells describes some differences between IgG-mediated and IgE-mediated activation against a target.....	23
Figure 3: Comparison of characteristics of IgG and IgE antibodies relevant for therapeutic development.....	24
Figure 4: Initial characterization of IgE	25
Figure 5: Mast cell degranulation and implications for optimal IgE concentration	26
Figure 6: IgE antibodies provide weak or no therapeutic efficacy in B16F10 and MC38 tumor models	27
Figure 7: Tumor distribution and pharmacokinetics of IgE-TA99	29
Figure 8: Survival curves for Intratumoral injections of IgE.....	30
Figure 9: Cell populations found in the tumor 24 hours after treatment.....	31
Figure 10: Survival curves from mast cells injected IT	32
Figure 11: Survival curve for treatment of CD11c hFcεR1α transgenic mice.....	33
Figure 12: Biodistribution of IgE-TA99 or TA99 24 hours after IP or IT injection.....	34
Figure 13: Chromatography of IgE antibodies	35
Figure 14: Tumor area curves for the IP IgE tumor studies	36
Figure 15: Tumor area curves for the IT IgE tumor studies	37
Figure 16: Tumor area curves for the mast cell injection tumor studies.....	38
Figure 17: Tumor area curves for the tumor studies in CD11c hFcεR1αTG mice	38
Figure 18: Degranulation assay protocol overview	42
Figure 19: Delaying eIL2 eliminated the weight loss toxicity but did not affect therapeutic efficacy	48
Figure 20: A variety of inflammatory agents were responsible for toxicity of staggered eIL2 before IFNα	51
Figure 21: NK cells were important for toxicity but not for therapeutic efficacy	53
Figure 22: Staggering eIL2 before IFNα increased the NK cell activation prior to exposure to IFNα.....	54
Figure 23: Pilot study leaving off TA99, MSA-IL2, or IFNα in the 2nd dose	55
Figure 24: Testing antibodies as vaccines theory with varied TA99 dosing.....	56
Figure 25: Survival studies with 2.5F-Fc, PD-1, TIGIT, TIM-2, and IFNα combinations	58
Figure 26: Ant-CTLA-4 alone drove strong therapeutic efficacy.....	59
Figure 27: Timing of tumor infiltrating lymphocytes in CTLA-4 combinations	60
Figure 28: Temporal fluctuations in surface CTLA-4 expression.....	61
Figure 29: Using anti-CTLA-4 in 5-agent combination therapy in the KP genetic lung tumor model	63
Figure 30: Tumor and full weight loss curves for eIL2 before and after IFNα	72
Figure 31: Weight loss time courses and tumor curves for 2.5F-Fc studies and BALB/c, C3H mice	73
Figure 32: Bloodwork and organ toxicity.....	76
Figure 33: PLSR analysis on luminex time course data	78
Figure 34: Full time course of each cytokine or chemokine in luminex assay for every treatment condition	80
Figure 35: Weight loss time course and tumor area curves for neutralization and depletion	82
Figure 36: Cellular depletion weight loss, example flow staining, and NK depletion full weight loss and tumor areas.....	84
Figure 37: NK activation representative flow plots	85
Figure 38: NK IFNα signaling protein representative flow plots	86
Figure 39: 6 different antibodies to make using B7-competitive and noncompetitive CTLA-4 binders	90
Figure 40: ELISAs validated CTLA-4-, CD28-, and B7.1- Fc fusion proteins	91
Figure 41: Schematic for yeast surface display for B7-noncompetitive CTLA-4 binders	92
Figure 42: Sort strategy for engineering novel CTLA-4 binders from the clean H3 scFv library	93
Figure 43: CDR regions are listed for nc19, nc20 and a variety of CTLA-4 antibodies	94

Figure 44: Yeast binding assays characterizing nc19 and nc20 as scFvs 95

Figure 45: CTLA-4 surface binding to nc19 and nc20 was not detected with a secondary antibody 96

Figure 46: Detecting binding of fluorophore labeled 9d9 or nc20 to surface CTLA-4 97

Figure 47: nc19 and nc20 as full-length antibodies still bound the soluble antigens used in yeast sorts.... 98

Figure 48: Choosing residues for CTLA-4 epitope mapping for nc19 and nc20..... 100

Figure 49: mCTLA-4-Fc epitope mapping results for nc19 and nc20 scFv yeast binding assay 101

Figure 50: 6 new clones were expressed as antibodies and tested from 2x generation of yeast sorts..... 103

Figure 51: CTLA-4 binding with B7 competition of 6 new clones from 2x generation..... 104

Figure 52: Venn diagram of Illumina results..... 106

Figure 53: Enrichment plot showing scatter of H3 enrichment in 2x and 2 over the parent library 1 107

Figure 54: Selected H3s were extracted from the enrichment 2x versus 2 plot analysis 108

Figure 55: Cluster validation analysis on unique H3s in each library..... 110

Figure 56: Dendrogram plots were made describing libraries 2 and 2x..... 112

Figure 57: Scattered enrichment in each H3 grouped by cluster 114

Figure 58: H3 enrichment scores plotted against read count 115

Figure 59: Summary table of H3s to pursue after next generation Illumina sequencing 117

Figure 60: Illumina library design 121

Chapter 1. Introduction

1.1 Re-emergence of immunotherapy for cancer

In 2013, cancer immunotherapy, also known as immuno-oncology (IO), was named Science magazine's Breakthrough of the Year ¹ because of its demonstrated potential to transform oncology. In the 6 years since 2013, so-called **checkpoint blockade** antibodies targeting **programmed cell death protein 1 (PD-1)** and **cytotoxic T lymphocyte associated protein 4 (CTLA-4)** that take the brakes off the immune system have gained approval from the FDA for indications such as melanoma, lung cancer, renal cancer, and many others ². In 2018 alone, there were nearly 1300 clinical stage IO agents and around 2100 known agents in preclinical research stages ³. Cementing its place in medical history, the 2018 Nobel Prize in Physiology or Medicine was given to two pioneers of the cancer immunotherapy field named James Allison and Tasuku Honjo.

Many pivotal clinical approvals in the IO landscape occurred in the last 5-10 years, but the recent surge of immunotherapies is really a re-emergence of immunological anti-cancer efforts that accumulated over the last century. Although researchers understood little about the immune system at the time, Dr. William Coley observed in the late 19th century that bacteria from infection could mediate cancer rejection ⁴. Over the next century, research on 'Coley's toxins' showed that they somehow induced immune cell attack of cancer ⁵ and a bacteria derived from weakened Tuberculosis called BCG gained clinical approval in 1990 and is still used today to treat bladder cancer. Proteins called cytokines were also being evaluated at that time with known immunological targets, and these help provide a mechanistic link between the immune system and tumor regression. In the late 1980s, the first cancer patients were treated with a protein called **Interleukin 2 (IL2)**, which is a cytokine that targets immune cells rather than cancer cells ⁶. This therapy was revolutionary because it was the first proof of concept that a protein targeting the immune cells could mediate cancer regressions. The efficacy of IL2 as a cancer treatment was cemented by the mid-1990s when it was approved for metastatic renal cancer in 1992 and metastatic melanoma in 1998 ⁷. In parallel with the efforts surrounding IL2, another cytokine called interferon alpha (IFN α), a **type I IFN**, began to show anti-cancer clinical efficacy in 1985 against metastatic renal cell carcinoma ⁸ and with approval in 1986 against hairy-cell leukemia ⁹. Since IFN α has direct anti-proliferative effects on many types of tumor cells, its importance as an immune stimulant was not confirmed until many years later. The field of immunotherapy may have been born with the approvals of IL2 and IFN α , but the toxicity of these agents and lackluster responses in many indications ¹⁰ stalled new immunotherapy approvals during the 2000s. Additionally, despite known connections between IL2, IFN α , and the immune system, mechanisms of direct immune surveillance of cancer were not published until the late 1990s and early 2000s ^{11,12} and clinical research began to focus again on new immunotherapy agents modulating an important immune cell type called T cells.

As researchers and clinicians finally showed unequivocally that therapies like IL2 and IFN α could control cancer by using the immune system, preclinical research into the proteins CTLA-4 and PD-1 had matured. CTLA-4 and PD-1 are proteins that restrain the activity of T cells, a type of immune

lymphocyte critical to long term immunological surveillance and control. Antibodies blocking CTLA-4 and PD-1 from engagement with their natural ligands were shown to take the brakes off T cell activation, leading them to be termed checkpoint blockade antibodies. The first preclinical studies showing efficacy of antibodies blocking CTLA-4¹³ and PD-1 or PD-L1¹⁴⁻¹⁶ against mouse cancer models were completed in the late 1990s and early 2000s. Clinical development was slow because of hesitancy over the concept of nonspecifically activating T cells to fight cancer. However, Medarex and subsequently Bristol-Myers Squibb developed the anti-CTLA-4 antibody Ipilimumab. The first pivotal phase III clinical trial showing efficacy of Ipilimumab (anti-CTLA-4) against unresectable metastatic melanoma was published in 2010¹⁷, and FDA approval of Ipilimumab followed in 2011. Approval of Ipilimumab ushered in the new wave of immunotherapy in the years following. By the time successful clinical trial results began pouring in for the anti-PD-1 antibodies Nivolumab (Bristol-Myers Squibb)¹⁸ and Pembrolizumab (Merck)¹⁹, expedited FDA approval followed in 2014. With that, it was on to the races for the field of cancer immunotherapy.

1.2 Immunotherapy comes in many shapes and forms

So, what is cancer immunotherapy? Well, a cancer immunotherapy is any type of agent or modality that can induce interaction of the immune system with cancer and lead to tumor control. Immunotherapies can be proteins, like the aforementioned cytokine therapies IL2 and IFN α or the checkpoint blockade antibodies targeting PD-1 or CTLA-4. Immunotherapies can also be composed of cells, like T cells, dendritic cells, or natural killer (NK) cells. In fact, in 2017, the FDA approved the first T cell therapies made by Novartis and Kite that were engineered to express chimeric antigen receptors (CAR T cells) that target CD19 on lymphoma and leukemia. Although typically occurring in combination therapy with cells or proteins, chemical agents like chemotherapy, small molecule kinase inhibitors, and even radiation therapy can act as immunotherapies if they induce or work with the immune system to induce anti-cancer effects. As the previous sentence alludes, immunotherapies can occur in combinations. Sometimes, the combinations act in orthogonal ways to recruit disparate immunological mechanisms to both fight against cancer. Many times, combination immunotherapies work synergistically, meaning that the sum of the effects is actually greater than either therapy's individual effects.

One type of immunotherapy upon which the second and fourth chapters of this dissertation focus, is antibodies. Antibodies, in their simplest form, can be thought of as adapter proteins between a target and immune cells. The variable region of antibodies binds strongly to a target called the antigen, and vary widely in sequence in order to accommodate binding to a wide variety of antigens. The constant region of antibodies is called the Fc region, and this region binds to Fc receptors on immune cells to help them recognize the antigen target. There are several different kinds of Fc regions that can either cause immune attack of the target antigen ('activating' isotype) or just innocently stick to immune cell receptors ('silent' isotype). In type of antibody-based immunotherapy discussed previously called checkpoint blockade, the antigen target (like CTLA-4 or PD-1) for the antibody variable region is actually on immune cells. The more general term for antibodies, whose variable region targets immune cells to elicit anti-cancer function, is immunomodulatory antibodies. While this class of antibody includes checkpoint

blockade, it also includes other antibodies like **tumor necrosis factor receptor (TNFR) superfamily** agonists, which bind and stimulate receptors that help activate T cells or other immune cells. The mechanisms of many immunomodulatory antibodies are very complex and not yet fully understood. In addition to expression on a type T cell called CD8 T cells that help fight against cancer, immunomodulatory antibody targets are also expressed on a subset of T cells called **regulatory T cells** (Tregs). When Tregs are activated, they actually have suppressive effects on the immune system and can prevent other types of T cells, like CD8 T cells, from attacking the tumor. Anti-CTLA-4, which is the focus of the fourth chapter of this dissertation, is a great example of this complexity. Blocking CTLA-4 on CD8 T cells helps these T cells to become primed to fight cancer, but it could be a valuable target to use to get rid of Tregs. Currently, it is an open question whether or not anti-CTLA-4 should have an activating Fc (targeting CTLA-4+ cells for attack) or a silent Fc (merely blocking CTLA-4), with different Fcs on two different clinical antibodies Ipilimumab (active human IgG1 isotype) and Tremelimumab (silent human IgG2 isotype).

In contrast to immunomodulatory antibodies, another class of antibodies in cancer immunotherapy are tumor targeting antibodies, on which the second chapter of this dissertation focuses. While the constant regions of immunomodulatory antibodies are sometimes active and sometimes silent, the constant regions of tumor targeting antibodies are almost all active. Since the variable regions of these antibodies are engineered to bind antigens overexpressed (or only expressed) on tumor cells, the Fc region of these antibodies should always activate Fc receptors to attack cancer. A host of antibodies against cancer are already in the clinic, such as Cetuximab (targeting EGFR) for head and neck, colorectal, and non-small cell lung cancer, Rituximab (targeting CD20) for non-Hodgkin's B-cell lymphoma, Trastuzumab (targeting HER2) for breast and ovarian cancer, and Dinutuximab (targeting GD2) for neuroblastoma. Although there are five different classes of antibody including IgA, IgD, IgE, IgG, and IgM, the Fc regions of these clinical anti-cancer antibodies all fall into the class of IgG, the most abundant antibody type in the blood. The Fc regions of these IgG antibodies with activating isotypes bind Fc γ receptors on cells such as NK cells, macrophages, neutrophils, eosinophils, dendritic cells to induce inflammation. IgG-based tumor targeting antibodies can significantly improve survival in some indications, but merely slow tumor growth or even fail to elicit a response at all in other types of cancer.

1.3 Thinking outside the box to the fight against cancer

Considering innovative cancer immunotherapies of the future, it is important to take a step back and try to think outside the box a little bit. As mentioned previously, the bladder cancer immunotherapy BCG actually was conceived when Dr. Coley observed tumors shrinking because of injection. Are there other situations, outside cancer, when the immune system is active from which we can learn important lessons or develop new immunotherapies?

The phenomena of allergy is an interesting part of immunity that affects many people around the world in annoying and sometimes deadly ways. Some people have seasonal allergy symptoms of nasal congestion or itchiness. Others might experience an allergic reaction with localized swelling around a bug bite. Allergy can manifest itself in deadly ways when a person with a food allergy

consumes the wrong food, and enters anaphylactic shock. Investigating how the immune system performs these different functions could inform re-directing the allergic mechanisms and effector cells involved toward cancer, on which this dissertation focuses in chapter 2. When organ rejection occurs after transplantation, how does the immune system mount a sustained response against the organ? When the immune system fights for a longer period of time against cancer, it gets exhausted and sometimes cannot sustain a long-term response. Are there lessons about the duration of immunity in organ rejection that we could use to battle against cancer? Bacteria such as uropathogenic e coli, salmonella, tuberculosis, staphylococcus, and some chlamydia species have evolved ways to invade and survive inside mammalian cells. Could we take advantage of these mechanisms to design therapies that cross the cell membrane, or build designer bacteria that produce valuable therapeutics near the sites of tumors? Could we learn lessons from the HIV virus about how to infect and replicate in CD4 T cells, and use those lessons to target genetic CRISPR-based therapies to those cell types? All of these are open questions, and asking questions like these can help drive the next waves of immunotherapy.

1.4 Temporal framework for the anti-cancer immune response

Since my most impactful thesis work is in chapter 3, the following sections of the introduction will introduce temporal immunity, which my work and others' have shown to be critical in orchestrating an effective, nontoxic anti-cancer immune response.

As previously discussed, cancer immunotherapy includes multiple modalities, including cytokines, antibodies, vaccines, and cell therapies – often used in combination. Recent clinical successes with combinations of immunomodulatory checkpoint blockade antibodies targeting PD-1 and CTLA-4 have validated the importance of immunotherapy by demonstrating the immune system's ability to durably control tumors with cure rates of up to 58% in advanced melanoma ²⁰. Antibodies targeting the PD-1 pathway have been approved for 23 different indications as of April 2019, and have already received 5 new FDA approvals so far in 2019 ². Despite these successes, many patients and tumor types still do not respond to immunotherapy or have to exit treatment due to adverse events. Numerous efforts – including prodrugs that become activated at the tumor and localizing therapy through direct injection into the tumor – are underway to address these issues by restricting the location of immune activation, in order to achieve improved safety and efficacy focused on tumor tissue ²¹⁻²⁴. However, insufficient attention has been paid so far to the critical issue of timing. The immune system is not a static process, and so immunotherapy treatments need to be rationally designed to take into account the temporal stage of the immune system in order to properly initiate immunity and synergize innate and adaptive immunity.

A temporal framework for understanding the progression of innate and adaptive events in the anti-cancer immune response has been proposed ²⁵. Since cancer often suppresses the immune system into an equilibrium phase ^{26,27}, the first step in an immune response against cancer is generation of antigen through initiation of a tumor cell death event ²⁵. Prior to treatment, the system is asynchronous, but commencement of treatment can initiate a timed series of responses where the duration of delays between milestones is reasonably predictable, as the

following examples describe. An initiating wave of cell death can be achieved by a variety of cytotoxic agents including chemotherapy, radiotherapy (RT), and tumor cell targeting antibodies. Next, **antigen presenting cells** (APCs) such as DCs sample the bolus of tumor debris released in the microenvironment and traffic to lymph nodes to present antigen and prime T cells. This process is not instantaneous, and may take hours or days to align with recently characterized circadian fluxes of lymphocytes through the lymph nodes ²⁸ to reach a maximal level of APC/T cell interactions. Immunotherapy can potentiate these processes with administration of stimulator of interferon genes (STING) agonists or cytokines such as type I IFNs to mature APCs, or administering immunomodulatory antibodies such as TNFR superfamily agonists that enhance signaling during T cell priming ²⁹.

Once T cells are primed by APCs in the draining lymph nodes within the first few days after tumor cell death ³⁰, these lymphocytes re-enter circulation until they find and can infiltrate the tumor, which can be enhanced by gradients of local chemokines such as CXCL9 or CXCL10 ³¹. After the wave of infiltration of freshly primed T cells into the tumor on the order of 4-7 days after tumor cell death, cytotoxic T lymphocytes (CTLs) then engage tumor cells through their TCRs. This wave of tumor cell killing by CD8+ CTLs, which can persist when checkpoint blockade antibodies block negative signaling, can then reset the clock of the anti-cancer immune response to begin again and even help spread the response to new tumor antigens ³². Despite awareness of the cyclic nature of the immune response, current immunotherapy treatment schedules are often stuck in a traditional “persistent dose - to maximum tolerated dose” perspective that squanders opportunities to exploit potential golden windows of timing.

1.5 Preclinical and clinical examples of temporal immunity

How can lessons learned about the natural rhythms of the immune system be applied to cancer immunotherapy treatment schedules? Such lessons are especially important for combination therapies (anti-PD-1 and anti-CTLA-4 ³³; anti-PD-1/CTLA-4 and IL2 (NCT02983045)), which are increasingly recognized as critical for preventing tumor **immune escape**. Combination therapy agents are valuable because they activate different steps in the anticancer response, yet these combination agents are most often dosed simultaneously or in treatment schedules dictated by each individual agent’s FDA approval process, instead of aligning with the underlying immune temporal dynamics. Such disruption of the naturally timed interplay of innate and adaptive immunity may harm therapeutic efficacy and lead to toxicity from futile over-stimulation. A handful of preclinical and clinical studies offer vignettes of successful incorporation of timing into both the **duration of treatment** and **sequence of treatments** for combination immunotherapy (Figure 1).

Preclinical examples

Using checkpoint blockade as an example of duration of treatment, reports suggest that anti-PD-1 antibodies might curtail the memory response in some circumstances, as in the case of the therapeutic survival benefit of a **4-1BB** antibody, which were diminished when combined with anti-PD-1 treatment compared to anti-4-1BB alone in the E μ -myc transgenic C57BL/6 murine

spontaneous B-cell lymphoma model³⁴. Although anti-PD-1 is generally dosed clinically every 2-4 weeks until disease progression or intolerable toxicity ensues, the extended duration of anti-PD-1 treatment merits further scrutiny if it has the potential to impair immune memory formation. Of note, a meta-analysis of the combination treatments of ipilimumab (anti-CTLA-4) and nivolumab (anti-PD-1) in the CheckMate 067 (advanced melanoma, NCT01844505) and 069 (unresectable or metastatic melanoma, NCT01927419) clinical trials showed that patients discontinuing treatment due to adverse events did not present different outcomes than patients completing the full treatment³⁵. Consequently, this questions the paradigm that toxicity and efficacy are a priori linked and suggests that a shorter treatment duration might not necessarily compromise efficacy.

Sequencing of immunotherapies, defined here as purposefully choosing an order of administration for individual agents, has shown success in enhancing therapeutic efficacy. Combination therapies incorporating TNFR superfamily agonists have benefitted from such approaches in several recent preclinical studies. Combination treatments of the anti-tumor antibody trastuzumab (targeting HER2) with anti-CD137 agonistic antibodies, in vitro and in the BT474M1 cell line breast cancer xenograft model injected into athymic nude Foxn1^{nu} mice, have shown that efficacy depends on dosing the anti-CD137 antibody after trastuzumab, given that NK cells could upregulate CD137 only after they initiated tumor cell death through trastuzumab³⁶. The importance of delaying anti-CD137 to align with the natural rhythm of NK cell activation was also confirmed with the EGFR antibody cetuximab in PBMCs isolated from human head and neck cancer patients, where increased NK cell expression of CD137 correlated with increased percentages of EGFR-specific CD8⁺ T cells comparing before versus after cetuximab treatment³⁷.

Following these data, since agonist antibodies targeting TNFR superfamily members may exert their effects mostly after tumor antigen generation but before or during CTL-induced tumor cell killing, we posit that using these agents after a tumor targeting antibody, but before checkpoint blockade would make sense. Indeed, in a PD-1 refractory, orthotopic mammary cancer mouse model, anti-PD-1 combination abrogated the efficacy of agonistic OX40 antibody alone³⁸. However, when anti-PD-1 was given after anti-OX40 (but not concurrently or in reverse order), the two synergized for improved survival. In addition, in another study, intraperitoneal administration anti-PD-1 antibody concurrent with anti-OX40 and an HPV16 E7 peptide vaccine was shown to decrease numbers of tumor-infiltrating E7 antigen specific CD8⁺ T cells in a syngeneic mouse TC-1 tumor model relative to anti-OX40 and vaccine³⁹. However, many ongoing clinical trials of OX40 agonist antibodies in combination with checkpoint blockade have not, to our knowledge, incorporated sequencing, which may not bode well for the predicted outcomes.

From another angle, preclinical studies in syngeneic mouse tumor models have demonstrated that staggering IFN α two days after the combination of IL2 and a cytotoxic agent (such as the murine anti-TRP1 antibody TA99 in the B16F10 mouse model in C57BL/6 mice) dramatically improved survival from 0 to 60-100% relative to concurrent administration of all three agents³⁰. The mechanism for the survival advantage of delayed IFN α likely involves DC maturation after (instead of before) exposure to antigens, since administration of IFN α one day before an OVA vaccine lowered the numbers of antigen-specific CD8⁺ T cells in the blood compared to no IFN α , or administering IFN α one day after the vaccine³⁰. Toxicity in the form of 10-20% weight loss associated with this combination therapy independent of the presence of tumors, and in multiple

mouse species, could be eliminated without affecting anti-tumor efficacy (in the B16F10 model in C57BL/6 mice) by IL2 administration with or after (delayed) IFN α in this triple combination⁴⁰. Although IFN α and IL2 were some of the first FDA-approved immunotherapies, combinations of these two therapies with chemotherapy, compared to IFN α and chemotherapy without IL2, have exhibited increased toxicity effects and failed to improve efficacy in a clinical trial of metastatic melanoma(NCT00002669)⁴¹. Collectively, these findings suggest that properly phasing dosing regimens might potentially revive combination strategies that have failed in the past by revisiting different clinical dose scheduling.

Other preclinical studies in the CT26 colon cancer model in BALB/c mice examining combinations of immunotherapy with RT have suggested that agents such as anti-CTLA-4 used to deplete Tregs as well as TGF β inhibitors can help precondition the tumor microenvironment to respond to RT, if they are optimally delivered before RT^{42,43}. For example, delivering anti-CTLA-4 seven days before RT compared with one or seven days after RT in the same CT26 model system improved survival from 50% to 100%⁴³. Tumor cell debris after RT-induced killing may be more likely to be taken up by APCs like dendritic cells, which promote a subsequent T cell response against cancer, if cells like Tregs are first depleted⁴⁴ as can be accomplished by anti-CTLA-4 antibodies⁴⁵. Although we do not yet have the tools to precisely predict responses to temporal sequencing of every immunotherapy combination, these preclinical examples begin to indicate when along the anti-cancer immune response each type of therapy may be most valuable.

Clinical examples

Clinical examples exploring duration or sequencing of combination immunotherapies have often been motivated by attempted avoidance of adverse events. For example, the recently published results of CheckMate 067 trial combining ipilimumab and nivolumab for advanced melanoma documented grades 3 or 4 adverse events in 59% of combination-treated patients, which was double the rate for either individual therapy²⁰. The unmet clinical need to maintain or improve combination checkpoint blockade efficacy while reducing adverse events inspired trials such as CheckMate 064. In this phase 2 trial, administering nivolumab before ipilimumab resulted in a higher proportion of responding patients at week 25 compared with giving these agents in the reverse order (41% compared with 20%), although grades 3 or higher adverse events stayed high at 50% and 43% for the respective groups⁴⁶. Interpretation of the results from CheckMate 064 is complicated because grades 3-5 adverse events were highest during ipilimumab treatment (whether before or after nivolumab)⁴⁶, but this study is still an important step towards bringing timing to the clinic. It is not just combinations of two or more immunotherapies that can benefit from sequenced approaches in the clinic. A phase 2 trial showed that cycles of treatment with the BRAF inhibitor Vemurafenib dosed prior to ipilimumab lowered hepatotoxicity relative to concurrent dosing of these two agents in BRAF mutated advanced or metastatic melanoma (NCT01673854)⁴⁷. Another ongoing phase 2 clinical trial is exploring BRAF mutated metastatic melanoma, and investigating double combinations of targeted therapies (BRAF and MEK inhibitors) sequenced with nivolumab and ipilimumab (NCT02631447)⁴⁸. Lastly, a phase 3 clinical trial in BRAF mutated stage III-IV melanoma is also testing combinations of BRAF inhibitors either before or after nivolumab and ipilimumab (NCT02224781). Although timing studies for immunotherapy are still in their infancy, these ongoing trials will be instructive for future

combinations of cytotoxic agents with checkpoint blockade and may provide further encouragement and validation for sequenced combination therapies in general.

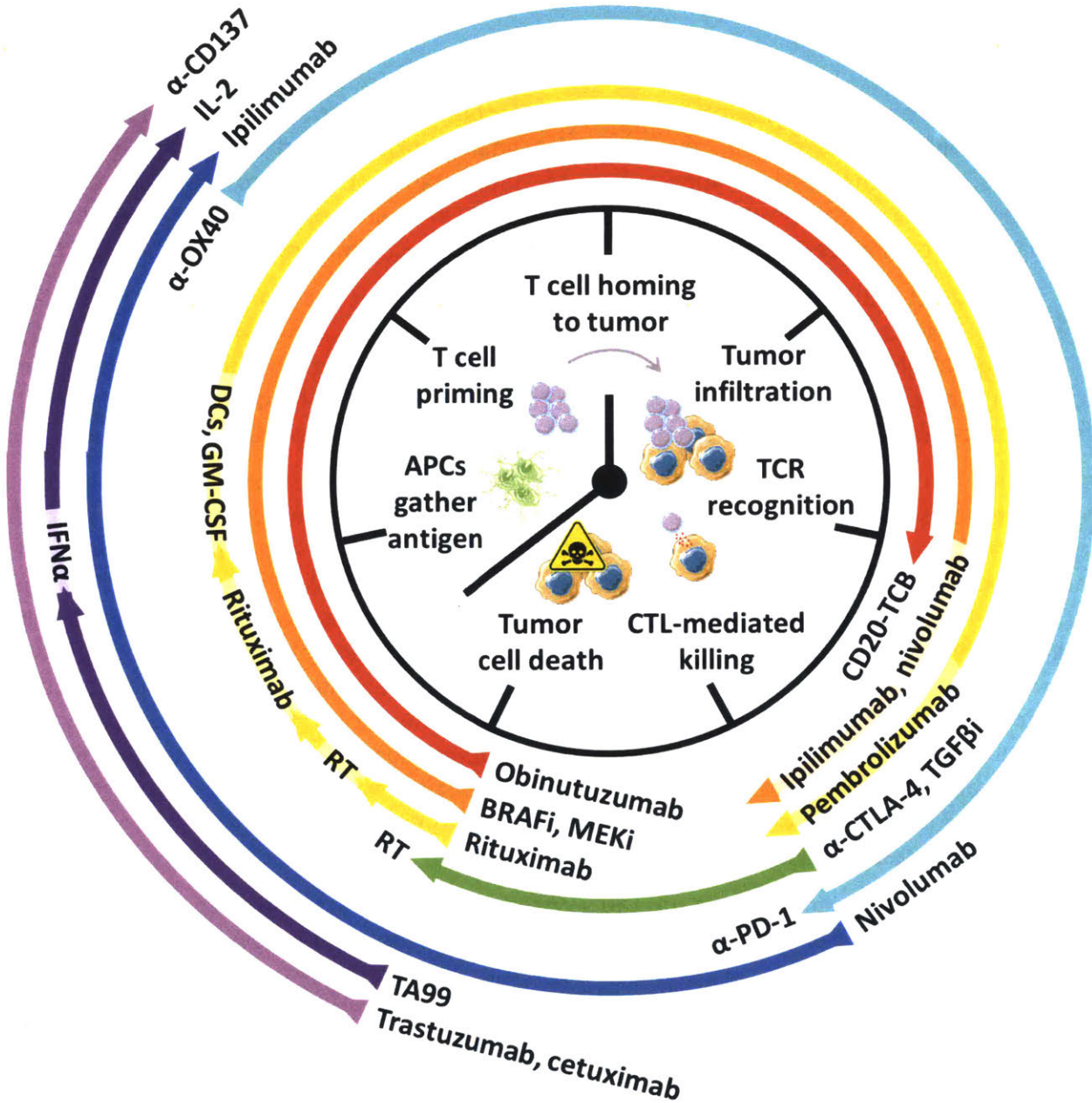


Figure 1: Examples of temporally programmed combination immunotherapies ⁴⁹
 Preclinical and clinical examples of temporally programmed combination cancer immunotherapies are super-imposed along the steps of the anti-cancer immune response. Although many immunotherapies such as anti-CTLA-4 have potential to affect more than one step, they are positioned coincidentally with combination partners (such as anti-PD-1) to reflect the particular treatment schedule used in the reference. TCB, T cell bispecific antibody. The references to these examples are color-coded: Red: Bacac et al., 2018 ⁵⁰; Orange: Amin et al., 2016 ⁴⁷ and Ascierto et al., 2017 ⁴⁸; Yellow: Kolstad et al., 2015 ⁵¹ and NCT02677155; Green: Young et al., 2014, 2016 ^{42,43}; Cyan: Messenheimer et al., 2017 ³⁸ and Shrimali et

1.6 Thesis overview

Effective cancer treatment of the future requires incorporating diverse and innovative aspects of immunity to fight against cancer, accounting for pharmacokinetic and temporal barriers of therapeutics, and engineering approaches to understand and improve upon current immunotherapies. This thesis addresses these challenges in three projects utilizing the Wittrup Lab's quantitative, engineering approach to protein-based cancer immunotherapy therapeutics.

In the first project, I attempted to harness the potency of allergic reactions against cancer by designing IgE class antibodies against two mouse tumor antigens and comparing them with traditional IgG antibodies. These IgE antibodies elicited modest or no tumor control, and lack of efficacy may be due to fast pharmacokinetic clearance, absence of human-like allergic effector cells in mice, or tumor-suppressive effects from mast cells responding to IgE.

The second project described in this thesis focused on synchronizing combination immunotherapies with the temporal progression of the anti-cancer immune response. In this work, anti-tumor antibodies were combined with the cytokines IL2 and IFN α . The order of administration of these therapies decoupled strong efficacy from dose-limiting toxicity. Given before IFN α , IL2 activated NK cells and heightened their responsiveness to subsequent IFN α . This strong NK cell response was not necessary for efficacy since depletion of these cells or giving IL2 at the same time or after IFN α did not affect survival in tumor-bearing mice. This project's proof of concept that efficacy and toxicity are not linked in immunotherapy helps build a framework upon which to time administration of innate and adaptive combination immunotherapies. If immunotherapy treatment schedules could be more rationally designed to treat with each agent when that piece of the immune system is active, we could continue to strengthen the anti-cancer immune response without associated toxicities.

Finally, the third project used the Wittrup Lab's system of yeast surface display to engineer novel antibodies against the checkpoint blockade target CTLA-4 as tools to improve understanding of anti-CTLA-4 mechanism of action against cancer. Although antibodies were made that had favorable characteristics against CTLA-4 as a soluble target, they failed to bind to surface CTLA-4 and so could not be used to address any mechanistic questions surrounding CTLA-4. Next generation sequencing was used to identify rare, alternative CTLA-4 binding sequences, and these were made available for future testing and development. In addition to the new sequences identified, recommendations were made for strategies to improve CTLA-4 binder engineering.

1.7 Glossary

4-1BB (also known as CD137): a costimulatory receptor expressed on the surface of a variety of cell types including T cells, natural killer cells, and dendritic cells.

Antigen presenting cell (APC): cells such as dendritic cells that take up antigens and are subsequently involved in priming and costimulation of T cells.

Bispecific antibodies: antibodies that have two different target specificities because they have a different variable region on each of their two arms.

Checkpoint blockade: a class of immunotherapy involving antagonizing receptors that stop or weaken lymphocyte activity (e.g. PD-1, CTLA-4).

Cytokine release syndrome: a harmful condition where the body produces excess inflammation in response to immunotherapy.

Cytotoxic T lymphocyte associated protein 4 (CTLA-4): a “checkpoint” receptor expressed on regulatory T cells and activated CD8⁺ and CD4⁺ effector T cells that blocks T cell costimulation.

Duration of treatment: the period of time for which a particular treatment is administered.

Immune escape: a process by cancer escapes the immune system through soluble factors that suppress immune cells or cancer cell surface receptors that prevent immune recognition.

Interleukin 2 (IL2): an inflammatory cytokine with many functions including enhancing antibody-mediated cell killing and proliferation of lymphocytes.

Programmed cell death protein 1 (PD-1): “checkpoint” receptor expressed on the surface of T cells that inhibits T cell activation.

Regulatory T cells (Tregs): a type of immune cell that restrains activation of the immune system.

Sequence of treatments: the order in which individual agents in combination therapies are administered.

Tumor necrosis factor receptor (TNFR) superfamily: a group of receptors exerting related costimulatory effects on either APCs or T cells. Members of this family include 4-1BB (also known as CD137), OX40, CD40, and CD30.

Type I interferons (IFNs): inflammatory cytokines such as IFN α with many functions including activation and maturation of APCs.

1.8 Acknowledgments

This chapter references material from: Rothschilds et al, Cell Trends in Immunology, 2019 ⁴⁹.

Chapter 2. Elucidating the mechanisms of IgE anti-cancer immunity in an intact mouse immune system

Abstract

Antibody therapeutics against cancer have long relied on the IgG isotype because it is the most abundant and has a wide range of effector functions. Expanding the antibody repertoire to the IgE isotype could activate a localized, potent, allergic-type immune response against cancer. Previous work using anti-cancer IgE in mice utilized human effector cells or IgE receptor expression, so potential mechanisms of IgE-tumor interactions in the native mouse immune system remain elusive. In this work, we explore possible cellular mechanisms of cancer control using IgE in the full mouse immune system. We cloned, expressed and validated two IgE antibodies targeting the mouse B16F10 melanoma line (IgE-TA99) and the mouse MC38 colon carcinoma line (2.5F-FcE), respectively. Against subcutaneous B16F10 tumors, IgE-TA99 showed modest improvement in survival in combination with an extended half-life version of IL2 compared with untreated mice. Although the fast pharmacokinetic half-life of IgE-TA99 prevented it from reaching the tumor, intratumoral (IT) injection of IgE-TA99 did not improve therapeutic efficacy. Very limited changes in potential effector cell numbers were seen 24 hours after IgE-TA99 injection, however drops in splenic and blood B cells could indicate that these cells were activated and migrated to the tissue. Improving the availability of IgE effector cells by IT injection of mast cells or using a transgenic mouse model with human FcεRI expression on dendritic cells, IgE-TA99 treatment did not improve survival against B16F10 tumors. Tracking biodistribution of IgE-TA99 ultimately showed that it was mainly taken up by basophils, which could potentially initiate the modest anti-tumor efficacy seen by communication with cells like B cells.

2.1 Introduction

Tumor targeting antibodies play a role in the anti-cancer immune response through inflammation initiated through bridging interactions between cancer cells and immune cells (Figure 2). A host of antibodies against cancer are already in the clinic, such as Cetuximab (targeting EGFR) for head and neck cancer, colorectal, non-small cell lung cancer, Rituximab (targeting CD20) for non-Hodgkin's B-cell lymphoma, Trastuzumab (targeting HER2) for breast and ovarian cancer, and Dinutuximab (targeting GD2) for neuroblastoma. Although there are five different classes of antibody including IgA, IgD, IgE, IgG, and IgM, the Fc regions of these clinical anti-cancer antibodies all fall into the class of IgG, the most abundant antibody type in the blood. The Fc regions of IgG antibodies bind Fcγ receptors on cells such as NK cells, macrophages, neutrophils, eosinophils, dendritic cells to induce inflammation. IgG-based tumor targeting antibodies can significantly improve survival in some indications, but merely slow tumor growth or even fail to elicit a response at all in other types of cancer. Exploring a different class of antibody could open the door to a whole new set of immune cells to activate against cancer.

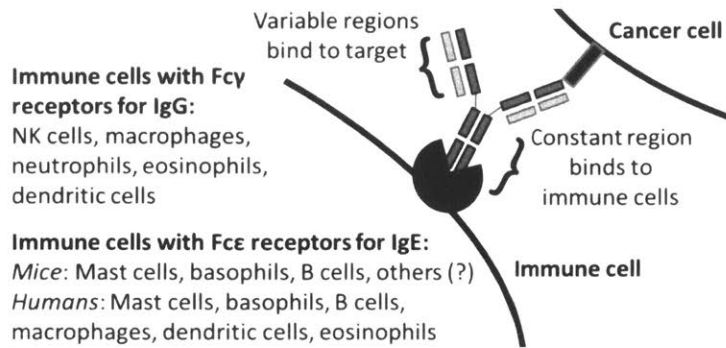


Figure 2: Comparison of immune effector cells describes some differences between IgG-mediated and IgE-mediated activation against a target.

One alternative class of antibodies to IgG that is capable of initiating potent immune activation is IgE. IgE is the antibody class responsible for the strong allergic hypersensitivity response, which can cause life-threatening anaphylaxis when it occurs systemically. Epidemiological studies suggest that levels of circulating IgE are lower in cancer patients, and that incidence of allergy is also lower in patients with cancer⁵². Harnessing the strength of the IgE-mediated allergic immune response in a local manner against cancer could unleash canonical allergic mediators like histamine, interleukins 1, 4, 6, and 13, TNF α , IFN α , chymase, tryptase, prostaglandins, and leukotrienes to fight cancer^{53,54}. Unfortunately, the roles of many of these mediators as pro- or anti-cancer are debated. For example, histamine has been documented to promote melanoma growth⁵⁵, but exogenously dosed histamine can also suppress tumor growth⁵⁶. Mast cells, one of the primary cell types involved in the IgE-mediated allergic response, can also play opposing roles in the tumor microenvironment and are known to promote angiogenesis⁵⁷. Depending on the intestinal tumorigenesis model, mast cell deficient mice could develop more tumors⁵⁸ or could reduce tumor incidence⁵⁹. Although mast cells are the canonical cell type of allergic immunity, other cell types such as basophils, B cells, monocytes, eosinophils, and dendritic cells also play a role in IgE-mediated immunity (Figure 2).

In considering switching from IgG to IgE, a less characterized class of antibody therapeutically, there are a few important differences to note between IgG and IgE. Firstly, in forming bridging interactions between tumor cells and effector cells, the types of possible immune effector cells vary between IgG and IgE (Figure 2). The IgG Fc region can engage with Fc γ receptors on a variety of cells including natural killer (NK) cells, macrophages, neutrophils, eosinophils, and dendritic cells, which can then initiate target attack through processes like antibody-dependent cellular cytotoxicity (ADCC) and antibody-dependent cellular cytotoxicity (ADCP). The wide diversity of potential IgE effector cells, including mast cells, basophils, B cells, macrophages, dendritic cells, and eosinophils, suggest that IgE antibodies targeting cancer could engage in orthogonal mechanisms of activation to IgG and that combinations of IgE and IgG tumor targeting antibodies would not be redundant. One aspect of IgE posing challenges for preclinical therapeutic characterization is that the immune effector cell populations are much more limited in mice than humans. Mice do not have a trimeric form of the Fc ϵ RI receptor that in humans is found on important immune effector cells like dendritic cells⁶⁰. There are also some structural and pharmacokinetic differences between IgG and IgE that have mixed implications for therapeutic development of IgE. IgE has 4 heavy chain constant domains, as opposed to the 3 of IgG. The 100-

fold higher affinity of IgE for its Fc receptors and longer tissues residence may be beneficial for IgE over IgG, but it's shorter serum half-life of hours-to-days instead of the days (or even weeks) half-life typical for IgG could pose challenges for biodistribution of therapeutic IgE into tumors (Figure 3).

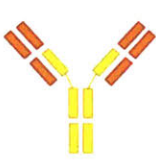

	IgG	IgE
Structure		
Ig Receptor Affinity	Up to 10^{-8} M	10^{-10} M
Serum Half-Life	Days - Weeks	Hours to Days
Tissue Residence	Hours	Days - Weeks

Figure 3: Comparison of characteristics of IgG and IgE antibodies relevant for therapeutic development.

Some previous efforts to target IgE antibodies to tumors in a field called Allergo-Oncology have had success. An antibody called MOv18-IgE with human IgE constant regions targeting the folic acid receptor on the human ovarian cell line IGROV1 had stronger tumor control in SCID mice days 29 and 35 after subcutaneous tumor inoculation than the human IgG1 antibody of same specificity⁶¹. In this case, the efficacy of MOv18-IgE was dependent on injection of 3×10^6 human peripheral blood mononuclear cells (PBMCs). Subsequent work also showed that two injections of MOv18-IgE and human PBMCs days 1 and 16 after intraperitoneal (IP) inoculation of a HUA ovarian carcinoma xenograft increased survival in nude mice compared with treatment of PBMCs and MOv18-IgG1⁶². In other studies without human PBMCs, but in a human FcεRIa transgenic mouse model, treatment days 2 and 4 after IP tumor inoculation with an IgE antibody of human constant regions targeting HER2/*neu* improved survival using the murine mammary carcinoma line D2F2/E2 (engineered to express human HER2/*neu*)⁶³. In the same human transgenic FcεRI mice, an antibody targeting prostate specific antigen (PSA) was injected in complex with PSA as a vaccine that improved survival from subsequent subcutaneous tumor challenge with CT26-PSA cells compared with vaccination with IgG1-PSA complexes⁶⁴. Despite these prior examples of tumor control, the effects of IgE antibodies targeting cancer without exogenously added effector cells or transgenic human FcεRI expression are limited. Basic mechanisms of IgE effector functions with unperturbed distributions of immune cells in mice are lacking. In this manuscript, we will explore the therapeutic opportunities, define challenges, and elucidate potential mechanisms anti-cancer IgE in the native mouse immune system.

2.2 Results

Constructing anti-tumor IgE and validating effector functions in vitro

To construct an IgE antibody specific for a mouse tumor cell line, we chose to use the mouse IgG2c antibody TA99 as a template. TA99 is an antibody specific to the antigen TRP-1, which is overexpressed on melanoma cells including the mouse tumor cell line B16F10. To make IgE-TA99, the heavy chain variable region of TA99 was cloned in-stream with the four heavy chain constant domains of mouse IgE (Figure 4 (a)). This modified TA99 heavy chain was expressed in HEK cells with the mouse TA99 kappa light chain to make IgE-TA99. A PAGE gel showed expected size properties of native and reduced IgE-TA99 compared with IgG-TA99 (TA99) (Figure 13). Using flow cytometry, we verified that IgE-TA99 binds to B16F10 cells expressing TRP-1 on the surface as well as to the mouse mast cell line C1.MC/C57.1 that expresses the mouse high affinity FcεRI receptor (Figure 4 (b)).

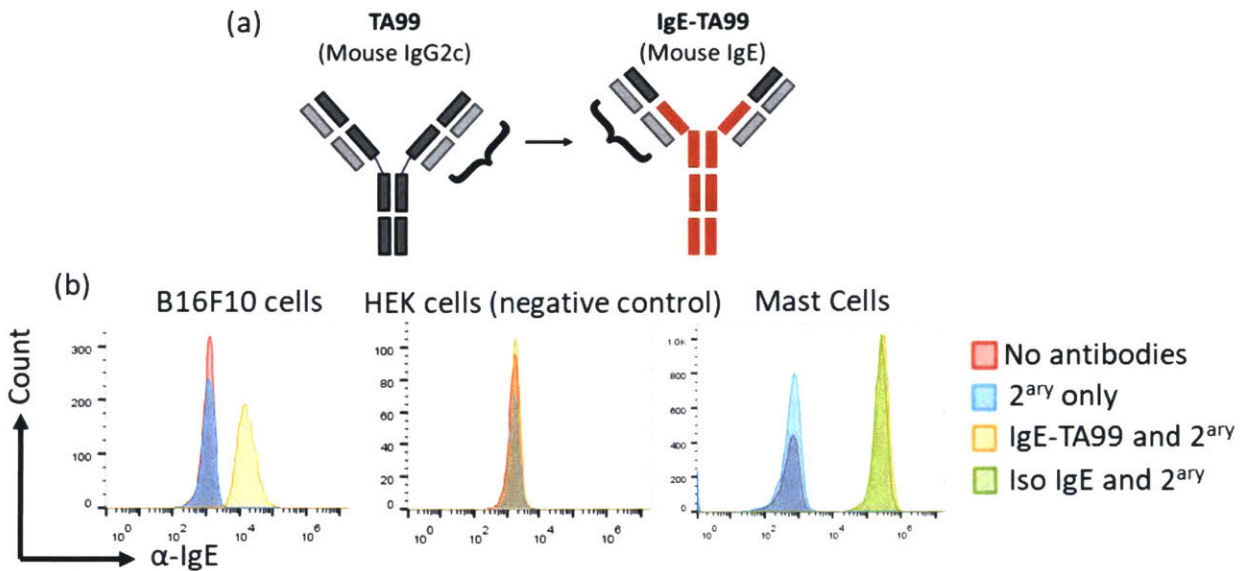


Figure 4: Initial characterization of IgE

(a) Schematic of IgE-TA99 construction from IgG TA99 and (b) characterization of specific binding to mast cells via FcεRI and tumor cells via the TRP-1 antigen using flow cytometry. Iso, isotype control IgE.

Since mast cell degranulation is a key IgE effector mechanism active in allergic responses, the ability of IgE-TA99 to induce degranulation of mast cells in response to B16F10 cells was tested. Allergic degranulation normally occurs when a mast cell coated with some allergen-specific IgE through FcεRI receptors encounters a multivalent allergen, which cross-links the FcεRI receptors and triggers release of mast cell granules. In the situation of a tumor cell, the antigen on the tumor cell surface would have to act as the multivalent allergen. Studies using different lengths of rigid DNA as antigen spacers have shown optimal degranulation cross-linking distance between epitopes on a multivalent allergen to be about 5 nm⁶⁵. Although tumor antigen is unlikely to be dense enough to be 5 nm apart, the heterogeneous distance distribution of antigen on tumor cells could lend itself to local antigen spacing sufficient for mast cell degranulation.

Using a degranulation assay that quantified mast cell granules released in response to antigen (B16F10 cells) as well as unreleased granules remaining in the mast cells, we quantified percent granulation as the ratio of released granules to total (released and unreleased) granules. Using a variety of concentrations of IgE, we found an optimal concentration range for IgE to induce degranulation in response to B16F10 cells to be about 1 nM (Figure 5 (a)). IgE-TA99 induced optimal mast cell degranulation at a concentration predicted to have low TRP-1 antigen saturation on B16F10 cells but high saturation of FcεRI on mast cells. This suggests that too much IgE accumulation around B16F10 cells would not be ideal in vivo in order to activate optimal mast cell degranulation response (Figure 5 (b)).

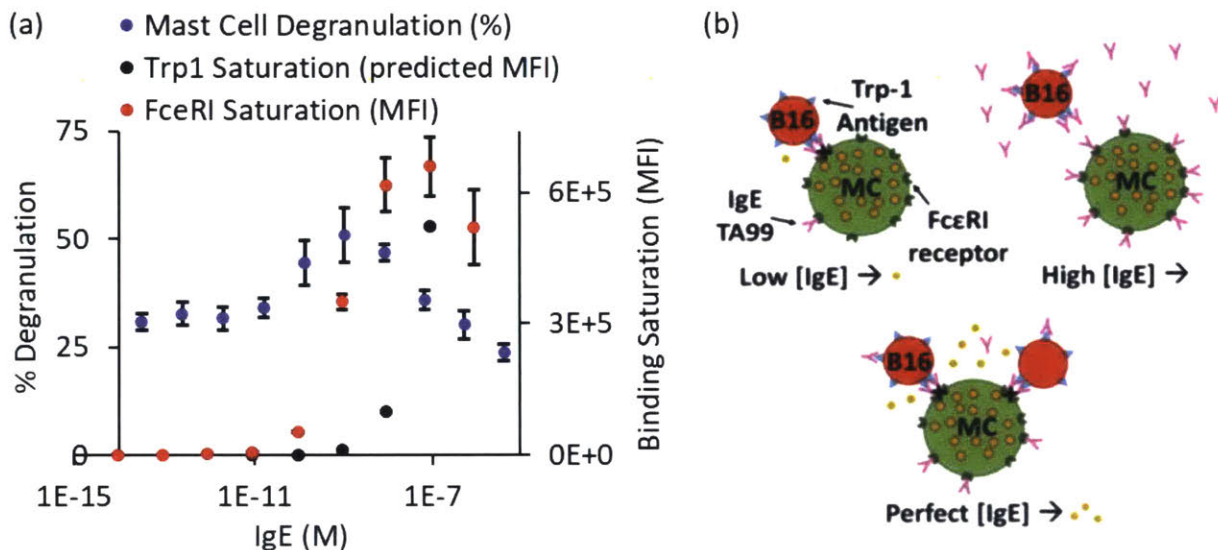


Figure 5: Mast cell degranulation and implications for optimal IgE concentration

(a) Engineered IgE-TA99 induced degranulation of the mouse mast cell line C1.MC/C57.1 in response to B16F10 cells after IgE incubation at a variety of concentrations. The predicted equilibrium binding curve of B16F10 cells based on known TA99 Kd in the 100s of nM as well as the measured equilibrium binding curve of IgE to mast cells are superimposed on the degranulation plot to demonstrate the (b) difference in mast cell and B16F10 saturation at the concentration of IgE optimal for degranulation.

IgE targeting tumor antigens confers weak tumor control in cytokine and antibody combination therapies

Two different versions of IgE targeting tumor antigens were used for initial assessment of therapeutic efficacy in two different subcutaneous, syngeneic mouse tumor models. The IgE-TA99 characterized in vitro was used to target B16F10 tumors. Another version of IgE called 2.5F-FcE was made by fusing a peptide called 2.5F to the second through fourth mouse IgE heavy chain domains. 2.5F is a peptide engineered to target integrins overexpressed on mouse and human tumors that was fused to the second and third heavy chain domains of mouse IgG2c to drive therapeutic efficacy as a tumor-targeting agent in tumor models including the mouse MC38 colon adenocarcinoma cell line⁶⁶. IgE-TA99 and 2.5F-FcE were used in combination and comparison with their respective IgG2c counterparts of the same specificity, TA99 and 2.5F-Fc. In hopes to

enhance T cell proliferation after antibody treatment, the cytokine IL2 was added to each treatment in an extended half-life version of L2 fused to mouse serum albumin (MSA-IL2) ⁶⁷.

IgE-TA99 and 2.5F-FcE conferred no survival improvement alone against subcutaneous B16F10 and MC38 tumors, respectively, in C57BL/6 mice (Figure 6 (a)-(b)). IgE-TA99 improved survival in combination with MSA-IL2 compared to PBS-treated mice, although it did not result in any tumor cures (Figure 6 (a)). Combination of both IgE-TA99 and MSA-IL2 with the IgG2c version of TA99 did not further enhance the survival benefit from the double combination of MSA-IL2 and TA99 (Figure 6 (a)). Although the survival curve of the combination of 2.5F-FcE and MSA-IL2 results in three cures, there was not a statistically significant improvement in survival compared to MSA-IL2 monotherapy (Figure 6 (b)). Area curves were plotted and reflect the same trend for these tumor studies (Figure 14).

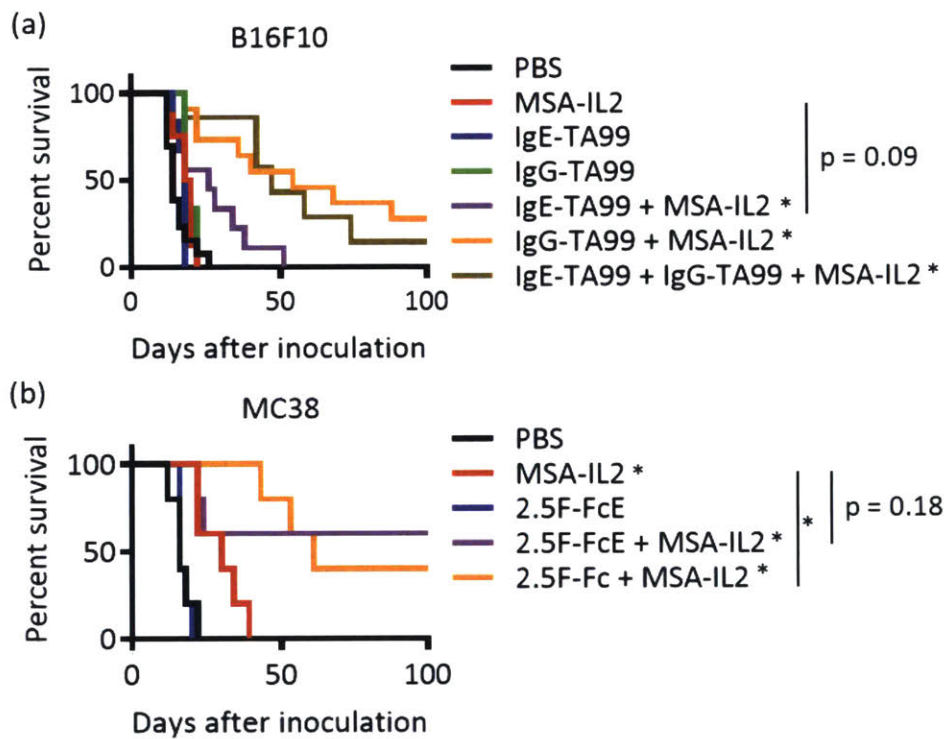


Figure 6: IgE antibodies provide weak or no therapeutic efficacy in B16F10 and MC38 tumor models (a) B16F10 tumor-bearing mice were treated every 6 days starting on day 6 for a total of 5 treatments. (b) MC38 tumor-bearing mice were treated every 6 days starting on day 6 for a total of 4 treatments. * indicates $p < 0.05$ for the given treatment compared to PBS, except where line indicates two different treatments being compared.

Limited IgE on tumor cells and short pharmacokinetic half-life of IgE-TA99 indicate intraperitoneal injection may not effectively reach the tumor

Since all treatments in the prior study were administered through intraperitoneal (IP) injection, the documented shorter pharmacokinetic half-life of IgE antibodies compared to IgG could prevent sufficient IgE from reaching the tumor. To compare the abilities of IgE-TA99 and the IgG

version of TA99 to reach subcutaneous tumors, B16F10 tumors were excised 24 hours after treatment. To detect presence of the antibody component of each treatment, IgE-TA99 and TA99 were fluorescently labeled with AF647 prior to injection. Tumor cells were identified by co-expression of GFP, allowing for assessment of the presence of antibody on tumor cells.

IP injection of fluorescently labeled IgE-TA99 in combination with (IP injected) MSA-IL2 did not increase tumor cell AF647 median fluorescence intensity (MFI) compared to baseline fluorescent intensity of tumor cells due to MSA-IL2 alone (Figure 7 (a)). Although not statistically significant, there appeared to be an increase in AF647 intensity on tumor cells 24 hours after IT treatment with IgE-TA99 or TA99 compared with the baseline tumor cell fluorescence intensity in the AF647 channel from mice treated only with MSA-IL2 (no AF647 introduced to system) (Figure 7 (a)). The tumor cell AF647 MFI was highest and statistically significantly different than MSA-IL2 alone after IP injection of fluorescently labeled TA99 injected in combination with unlabeled MSA-IL2 (IP) (Figure 7 (a)).

Although IT injection of either TA99 or IgE-TA99 would be expected to instantaneously have the highest tumor concentration at time of injection, after 24 hours these antibodies would have drained into blood and surrounding tissue, significantly diluting the local concentration in the tumor. On the other hand, IP injected antibody would have higher tumor concentration 24 hours after injection than immediately after, since time is needed to distribute to tissues and around 10% of injected TA99 has been documented to be retained in tumor 1 week after injection⁶⁸. An additional factor explaining why the IP injected TA99 group's tumor cells have the highest AF647 intensity could be that 100ug of each antibody was injected IP whereas only 3.4ug was injected IT. This IT concentration was chosen because this quantity of antibody would result in approximately 10^{-7} M concentration in the tumor if the antibody became distributed perfectly in the volume of an average day 6 tumor. 10^{-7} M is the concentration predicted by the Kd of TA99 for TRP-1 to achieve nearly complete surface saturation of B16F10 cells. Thus, although the IT injected antibodies did not result in tumor cells with the highest MFI 24 hours after injection, their instantaneous local concentration would be expected to be higher than IP injected therapies.

The failure of IgE-TA99 after IP injection to reach the tumor compared with TA99 may at least in part be due to the short pharmacokinetic half-life of IgE. After 100ug fluorescently labeled IgE-TA99 was injected retro-orbitally, serum IgE was quantified by repeated small-volume blood sampling over time. Instead of ELISA, the fluorescence of serum was directly measured by spectrophotographic methods and compared with a standard curve of serum spiked with known concentrations of fluorescently labeled IgE-TA99. Results from this study show that the beta half-life of IgE clearance from the serum is about 6 hours (Figure 7 (b)). The fast clearance of IgE-TA99 compared with the approximately 1-week half-life of TA99 may explain why limited IgE-TA99 is found at the tumor after IP injection and motivated subsequent tumor efficacy studies with IT injections of IgE-TA99.

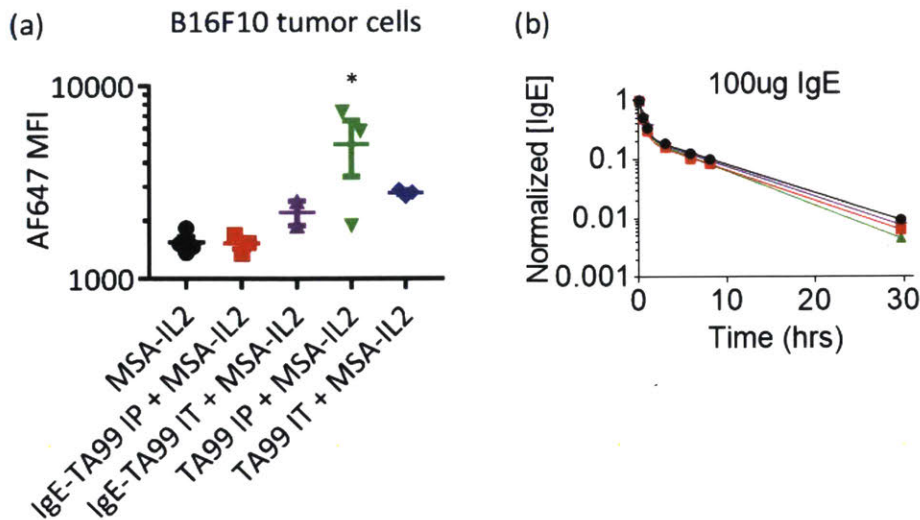


Figure 7: Tumor distribution and pharmacokinetics of IgE-TA99

(a) Median fluorescence intensity (MFI) of AF647 in tumor cells (identified by presence of B16F10 cells expressing GFP) is shown 24 hours after injection of the given treatments. 30ug MSA-IL2 was injected IP in all groups. 100ug of AF647-labeled antibody of either IgE (IgE-TA99) or IgG (TA99) was injected IP and 3.4ug of labeled antibody was injected IT. (b) 100ug of fluorophore labeled IgE was injected intravenously (retro-orbital route) into 4 mice and serum fluorescence was quantified over time to generate a PK clearance curve. * indicates $p < 0.05$ for the given treatment compared to MSA-IL2.

IT injection of IgE targeting tumor antigens performed worse or similarly to IP treatment in improving survival

IgE antibodies tend to have higher tissue residency time than IgG⁶⁹, so injecting these antibodies directly into the tumor was hypothesized to be more efficacious and circumvent the poor biodistribution of the antibody. Comparison of survival curves shows that IT injection of IgE-TA99 at two different dose levels (Low and Hi) did not improve survival in combination with MSA-IL2 over treatment with MSA-IL2 alone (Figure 8 (a)). The two dose levels of IgE-TA99 were chosen to optimize mast cell degranulation (Low, 0.034ug, estimated to be 1nM concentration (Figure 5) distributed in a small tumor) and to be 100 times higher than the optimal degranulation concentration (Hi, 3.4ug). This result was surprising because of the small improvement in survival of IgE-TA99 with MSA-IL2 over MSA-IL2 alone when IgE-TA99 was injected IP, and indicated that IgE effector cells outside the tumor may be most important for efficacy. The same lack of improvement in survival was observed for 2.5F-FcE intratumoral injections. 2.5F-FcE IT in combination with MSA-IL2 did not improve the therapeutic efficacy of MSA-IL2 monotherapy (Figure 8 (b)), although this result mirrors the lack of statistically significant survival improvement from IP-injected 2.5F-FcE and MSA-IL2. Tumor area curves were plotted for each treatment and confirm the results seen in the survival curves from both tumor models (Figure 15).

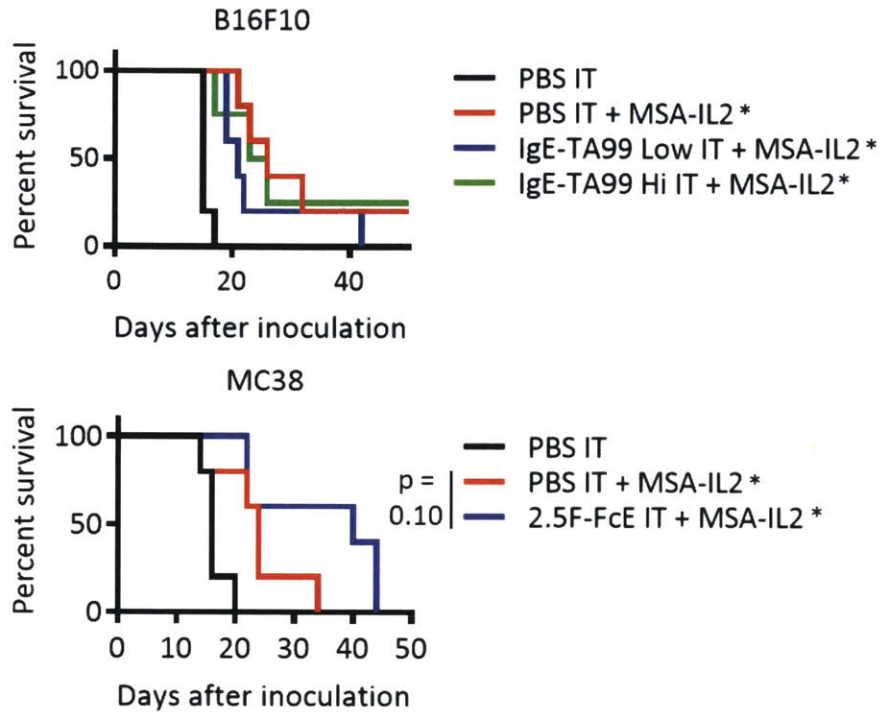


Figure 8: Survival curves for Intratumoral injections of IgE

Ensuring IgE reaches the tumor by performing intratumoral (IT) injections, IgE-TA99 and Trident IgE Fc did not show therapeutic efficacy against B16F10 and MC38 tumors, respectively, in C57Bl/6 mice. (a) Two different doses of IgE-TA99 (3.4ug for IgE Hi and 0.034ug for IgE Low) were injected IT into day 7 subcutaneous B16F10 tumors every 3 days in 20uL of PBS for 10 total injections. (b) 40ug 2.5F-FcE was injected IT into day 6 MC38 tumors every 3 days in 20uL of PBS for 8 total injections. For groups not receiving IgE, 20uL of PBS was injected IT on the same schedule as IgE. 30ug MSA-IL2 was injected IP every 6 days starting on day 6 for 5 total injections (B16F10) or starting on day 6 for 4 total injections (MC38). * indicates $p < 0.05$ for the given treatment compared to PBS, except where line indicates two different treatments being compared.

B cells were main cellular perturbations in tumor, spleen, and blood after IgE treatment

Since IT injections did not improve therapeutic efficacy compared with IP injections of IgE, we examined whether any different fluctuations in immune cell populations could be found in tumor, blood, or spleen in response to IT compared with IP treatment, and IgE compared to IgG treatment.

24 hours after treatment, tumors were excised and digestion in collagenase / DNase to release cell populations that may not as easily disaggregated from tissue. Stereotypical allergic effector cells like mast cells and basophils were found in the tumor only as very low proportions of live, CD3- cells, and no treatment combination with MSA-IL2 had a statistically significant effect on the cell population from monotherapy with MSA-IL2 (Figure 9 (a)). Despite the lack of statistical significance, there did appear to be increased proportions of mast cells and basophils in the tumor when either IgG or IgE antibody was added to MSA-IL2 monotherapy. These trends toward

increased proportions of effector cells, although still very low numbers, could help explain why there was some therapeutic efficacy from the addition of IgE-TA99 or 2.5F-FcE to MSA-IL2 monotherapy in IP-treated B16F10 or MC38 tumors, respectively. Other less likely IgE effectors like B cells, macrophages, dendritic cells, and eosinophils were found in higher proportions in the tumor, although none seemed perturbed by IgE-TA99 combination with MSA-IL2 over monotherapy MSA-IL2 (Figure 9 (b)). The only statistically significant altered cell population from MSA-IL2 monotherapy was lower eosinophil proportions from the combination of IgG TA99 either IP or IT (Figure 9 (b)).

The only statistically significant cellular fluctuation when antibody treatment was added to MSA-IL2 monotherapy in the spleen or blood was found for B cells. B cells in the blood appear slightly lower from IT administration of IgE-TA99 (Figure 9 (c)), and from IT administration of TA99 in the spleen (Figure 9 (d)).

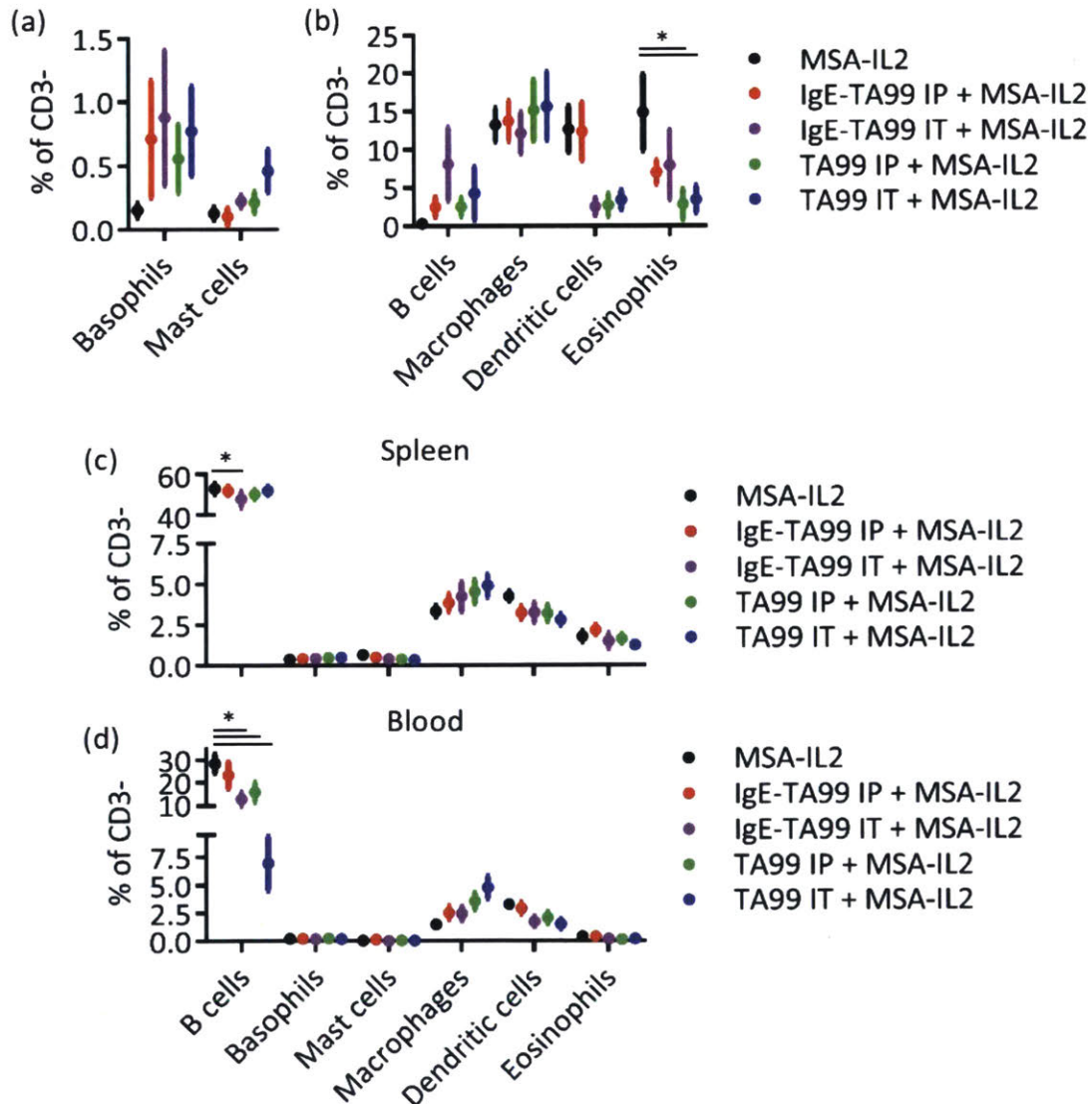


Figure 9: Cell populations found in the tumor 24 hours after treatment

24 hours after injection of given treatment, cell populations found in disaggregated, digested tumors are shown. (a) Basophils and mast cells were plotted with a separate y axis from (b) other cell populations examined because of wanting to zoom in on the lower numbers in the tumors. (c-d) Cell populations in the spleen and blood were plotted as a % of CD3⁺ cells with a split y axis to emphasize both the larger and smaller fluctuations in cell numbers. 30ug MSA-IL2 was injected IP in all groups. 100ug of AF647-labeled antibody of either IgE (IgE-TA99) or IgG (TA99) was injected IP and 3.4ug of the respective labeled antibody was injected IT. * indicates $p < 0.05$ for the given treatment compared to MSA-IL2.

Improving mast cell or dendritic cell responses to IgE did not increase therapeutic efficacy

To examine whether an increase in IgE effector cells would improve therapeutic efficacy, tumor studies were completed with a therapy comprised of C57BL/6 bone marrow derived mast cells. After culturing *ex vivo*, these mast cells were either coated or uncoated with IgE-TA99 or 2.5F-FcE prior to injection into B16F10 or MC38 tumors, respectively. Neither IgE-coated nor IgE-uncoated mast cells had any effect on tumor survival (Figure 10) or area curves (Figure 16) in either tumor model, indicating that mast cells alone were not enough to instigate a productive anti-tumor immune response. No MSA-IL2 combinations were explored in this study, so we cannot comment on whether a combination therapy would rescue the failure of injected mast cells in this treatment regime.

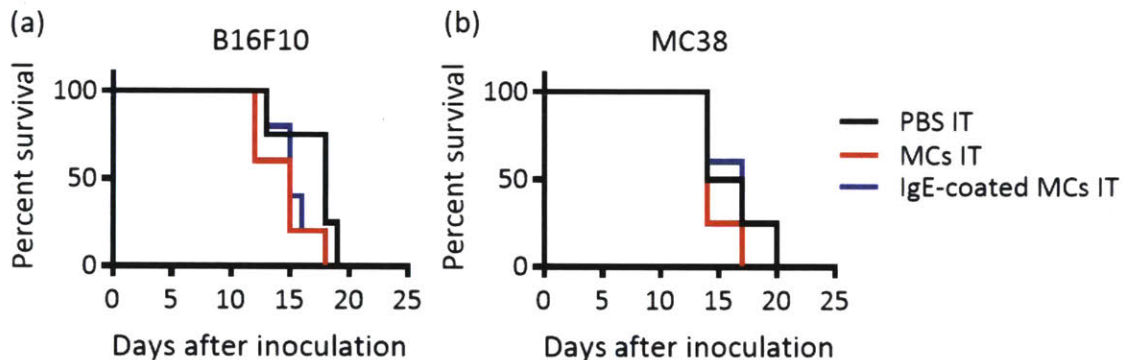


Figure 10: Survival curves from mast cells injected IT

Bone marrow derived mast cells were injected IT every three days either after coating *ex vivo* with IgE or uncoated. IgE-TA99 was used in the B16F10 model (a), and 2.5F-FcE was used in the MC38 model (b). No treatment had statistically significant change in survival compared with PBS.

Because of the importance of dendritic cells for IgE-mediated anti-tumor efficacy and lack of FcεRI expression on mouse dendritic cells⁷⁰, the potential contributions of dendritic cells to the IgE-mediated anti-tumor response were explored using a CD11c human FcεRIα transgenic mouse model. We did not see improvement in B16F10 tumor survival (Figure 11) or growth (Figure 17) over PBS from any of the treatment groups, although there appeared to be a mild but not statistically significant growth delay due just to MSA-IL2.

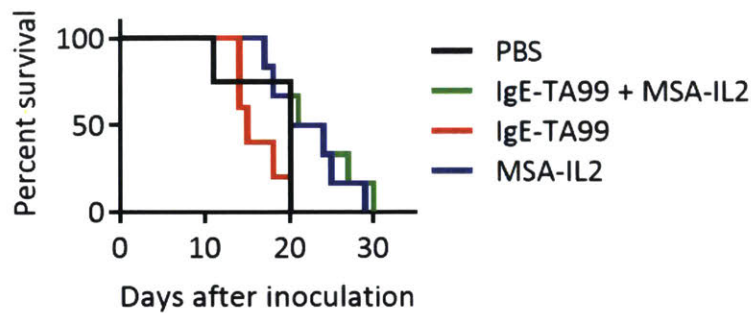


Figure 11: Survival curve for treatment of CD11c hFcεR1a transgenic mice

After inoculation of 10^6 B16F10 tumor cells day 0, 50ug IP injections of IgE-TA99 occurred every 3 days (starting day 3) alone or in combination with MSA-IL2 (30ug IP starting day 6, every 6 days) in this mouse model for a total of 10 IgE-TA99 injections and 5 MSA-IL2 injections. No treatment had statistically significant change in survival compared with PBS.

Biodistribution showed that therapeutic IgE-TA99 honed to basophils in tumor, spleen, and blood

Efforts to improve mast cell and dendritic cell responses to IgE in mice did not improve tumor survival, so we decided to return to the B16F10 model system where IgE-TA99 added to monotherapy efficacy of MSA-IL2 and examined which cell types were taking up IgE-TA99. For this biodistribution study, we injected MSA-IL2 in combination with fluorophore labeled IgE-TA99 or TA99 either IP or IT in B16F10-GFP tumor-bearing mice. 24 hours after injection, we assessed which cell types in the tumor, spleen, and blood had taken up the therapeutic antibody.

Basophils, but not mast cells appeared to be the main cellular compartment that contained IgE-TA99 in the tumor, spleen, and blood (Figure 12), and this effect was seen only with IP and not IT injected IgE-TA99. This significant basophil but not mast cell uptake of IgE was surprising because in mice, both mast cells and basophils upregulate FcεRI in response to IgE^{71,72}. Regardless of why basophils preferentially took up IgE, this result could indicate that basophils played a role in the therapeutic efficacy of IgE-TA99 combined with MSA-IL2 in the B16F10 tumor model.

Mast cells, macrophages, and dendritic cells were the main cellular compartments that took up TA99 antibody when TA99 was added to MSA-IL2 monotherapy, presumably through Fcγ receptors. Although mast cells are one of the few cell populations that express FcεRI+ in mice, mast cells were the only cell type with a statistically significant increase in MFI to indicate antibody uptake from TA99, and only in the tumor compartment and from IP injection (Figure 12 (a)).

Although the B cell compartment as a proportion of CD3- cells was lowered by addition of IgE to MSA-IL2 monotherapy, B cells were not found to be significantly associated with either IgE or IgG antibody. This could mean that B cells do get exposed to IgE, but quickly recycle it back to the surface through FcεRII, or perhaps that B cells change in numbers in response to signals from a different cell type that is affected by IgE.

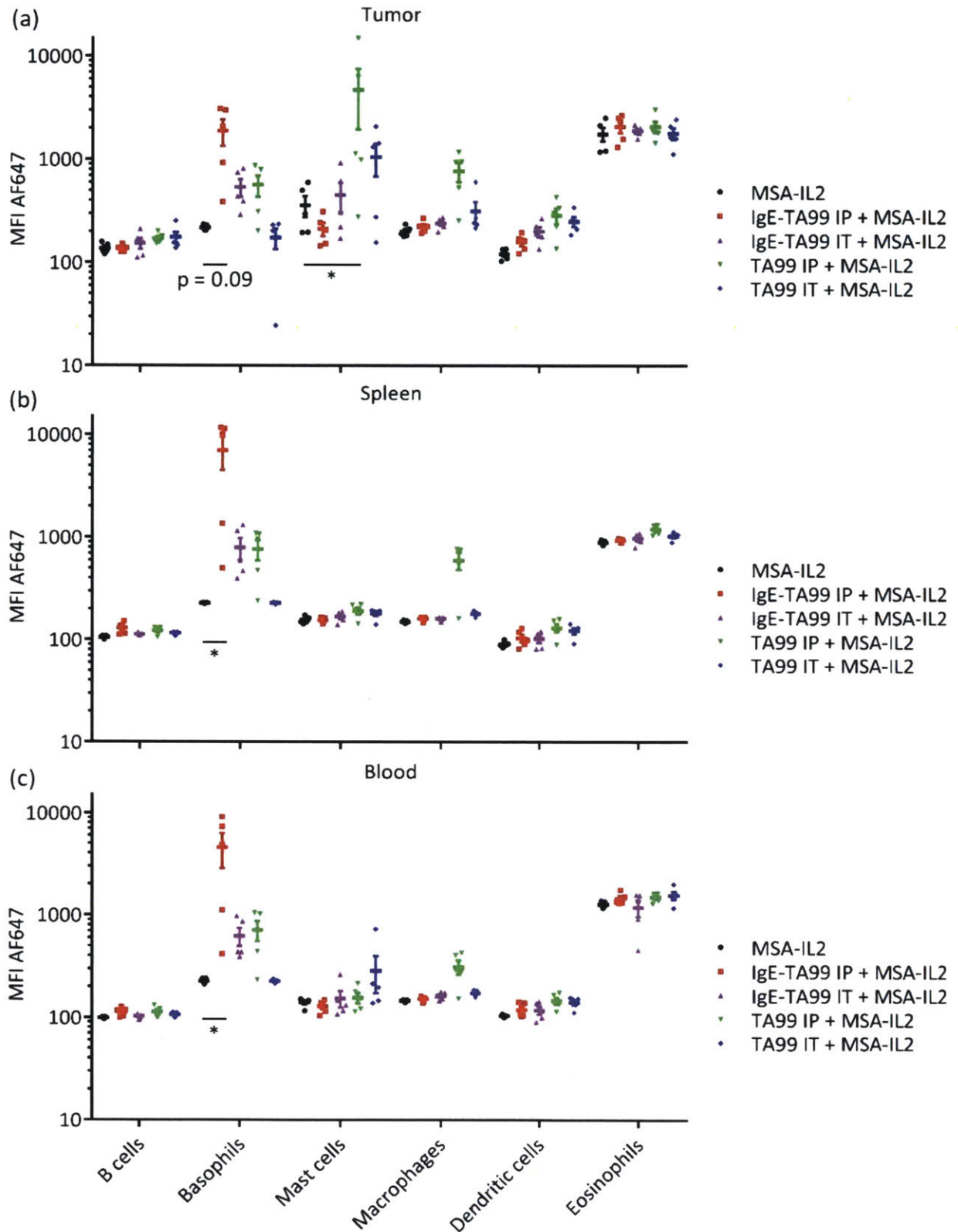


Figure 12: Biodistribution of IgE-TA99 or TA99 24 hours after IP or IT injection

The median fluorescence intensity (MFI) of each cell population in the AF647 channel is shown 24 hours after injection of the given treatments in the tumor (a), spleen (b), and blood (c). 30ug MSA-IL2 was injected IP in all groups. 100ug of AF647-labeled antibody of either IgE (IgE-TA99) or IgG (TA99) was injected IP and 3.4ug of labeled antibody was injected IT. * indicates $p < 0.05$ for the given treatment compared to MSA-IL2.

Supplemental figures

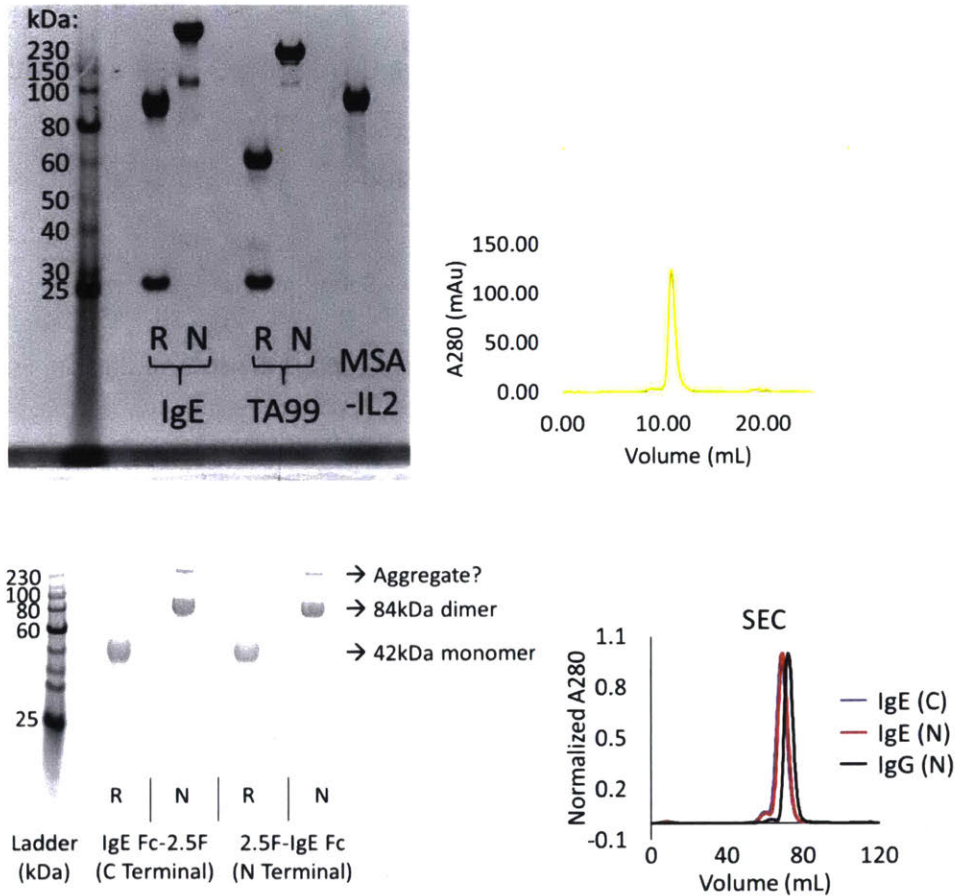


Figure 13: Chromatography of IgE antibodies

PAGE gels of IgE-TA99 (upper left) and 2.5F-FcE (lower left) confirmed expected sizes of these antibodies, including fusions of 2.5F to both the C and N terminal of the IgE Fc. Size exclusion chromatography confirmed relatively monodisperse proteins, although there is a small aggregate before the main IgE peak for both IgE-TA99 (upper right) and 2.5F-FcE versions (lower right), which isn't present for the IgG version of 2.5F-Fc (lower right). In the rest of the paper, 2.5F-FcE refers to 2.5F fused to IgE Fc at the N terminal.

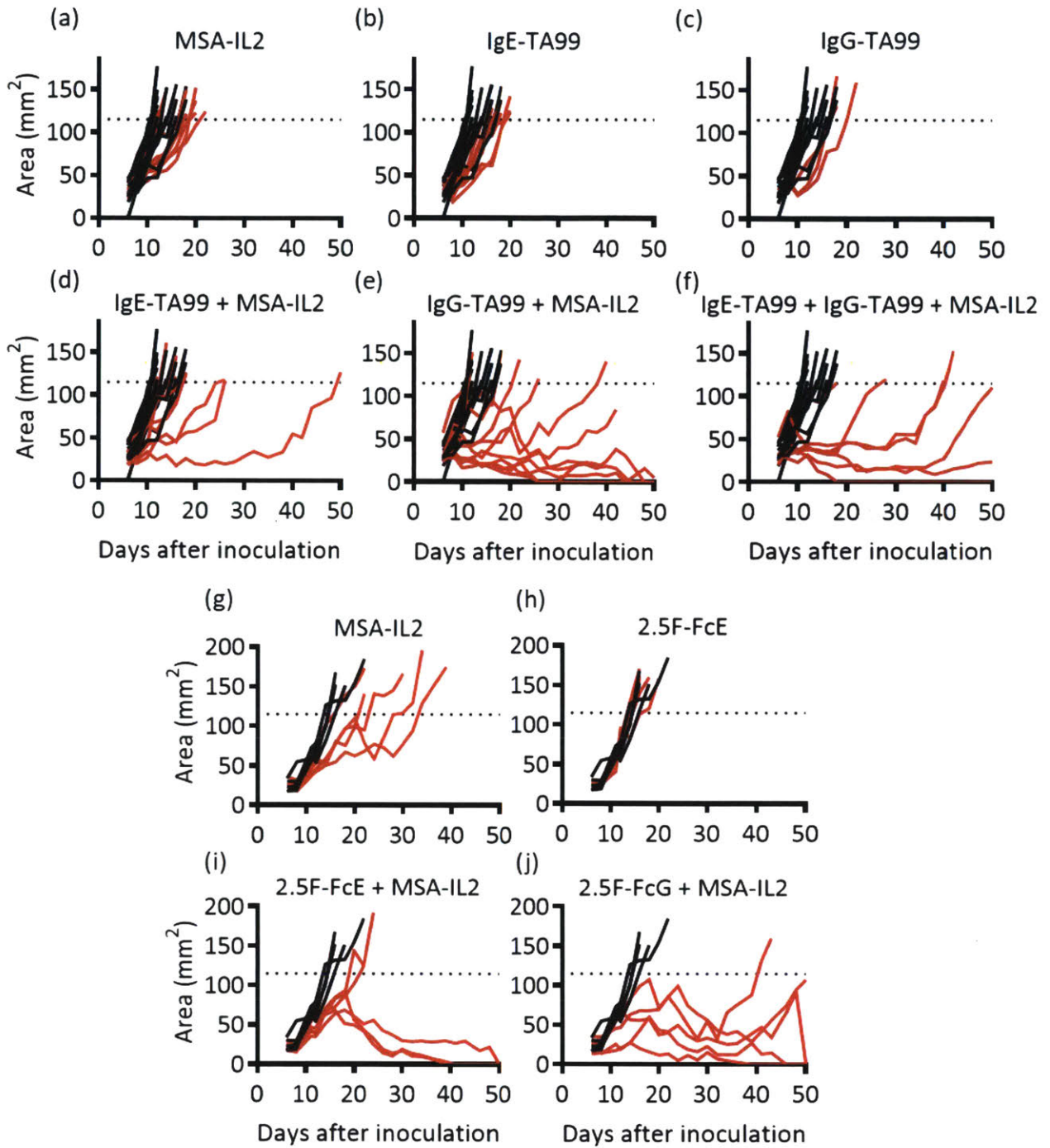


Figure 14: Tumor area curves for the IP IgE tumor studies

Tumor area curves were plotted for all treatment conditions exploring efficacy of intraperitoneal injection of IgE-TA99 and 2.5F-FcE against the B16F10 (a-f) and MC38 (g-j) tumor models, respectively. The red curves are the treatment in the title and the black curves in each plot are the PBS tumor area curves.

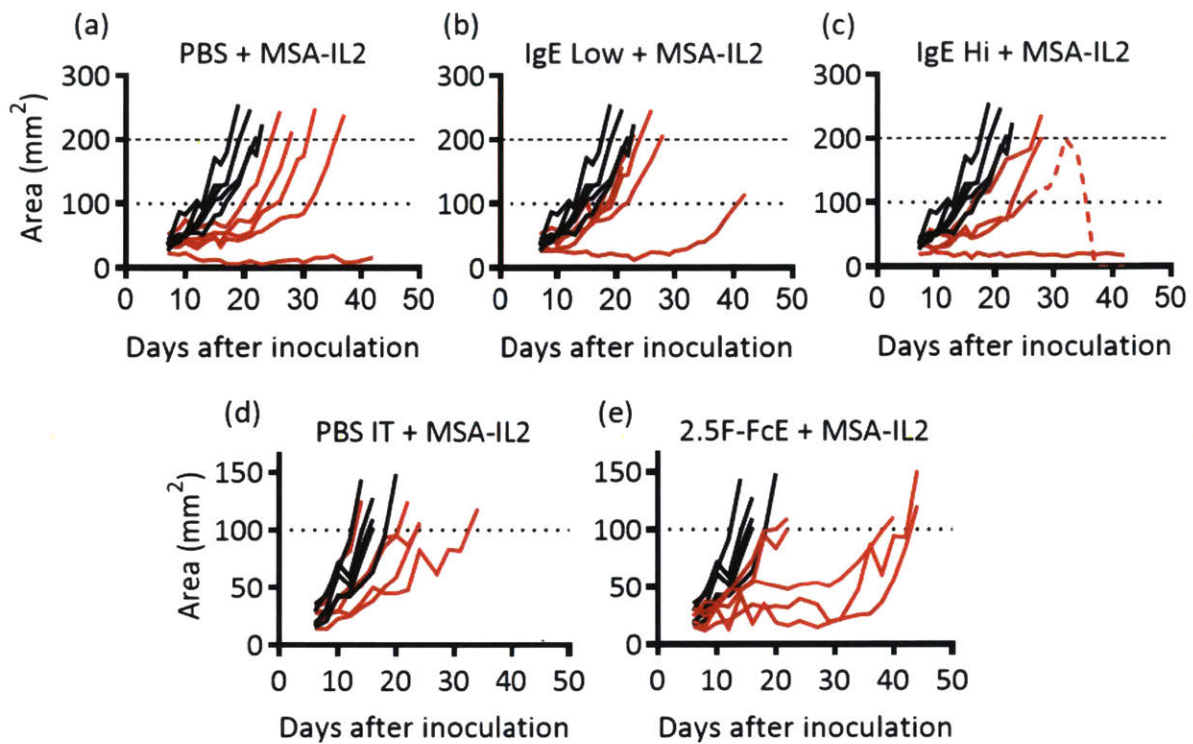


Figure 15: Tumor area curves for the IT IgE tumor studies

Tumor area curves are shown for all treatment conditions exploring efficacy of IT injections of IgE-TA99 and 2.5F-FcE against the B16F10 (a-c) and MC38 (d-e) tumor models, respectively. Although all mice in the survival curves were censored at 100 mm² area (horizontal dashed line), the animal protocol euthanization criteria allows for the longest tumor dimension to reach 20 mm, so areas are shown up to 200 mm² (horizontal dotted line) for mice that maintained good body condition. Note that one mouse (censored in the survival curve once its tumor reached 100 mm² area) in the IgE Hi + MSA-IL2 treatment group actually had its tumor reach approximately 200 mm² area prior to regressing, which was probably due to the high surface spread of the tumor while maintaining low depth. The red curves are the treatment in the title and the black curves in each plot are the PBS tumor area curves.

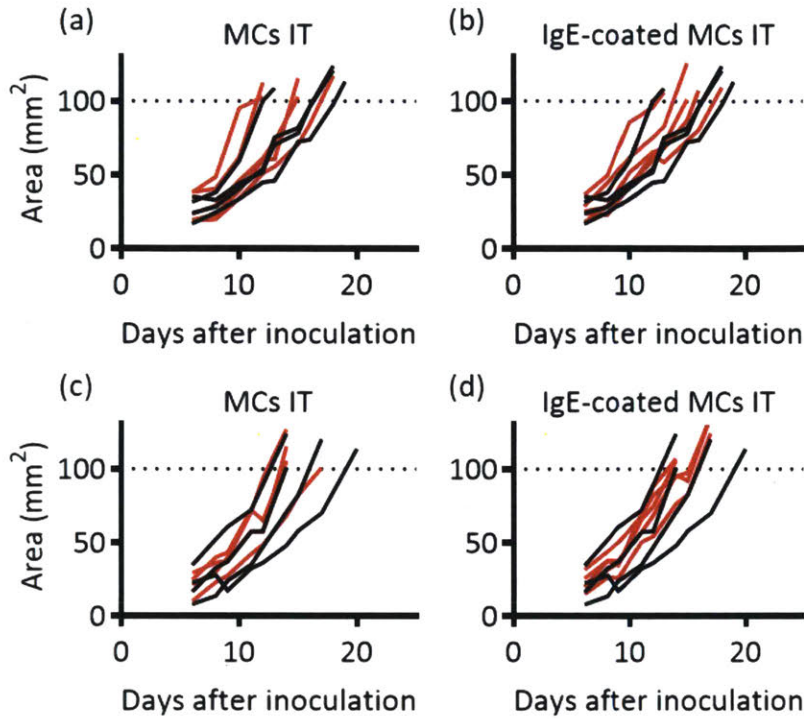


Figure 16: Tumor area curves for the mast cell injection tumor studies

Tumor area curves were plotted for the tumor studies injecting bone marrow derived C57BL/6 mast cells alone or coated with IgE-TA99 into B16F10 tumors (a-b) or coated with 2.5F-FcE (c-d) into MC38 tumors. The red curves are the treatment in the title and the black curves in each plot are the PBS tumor area curves.

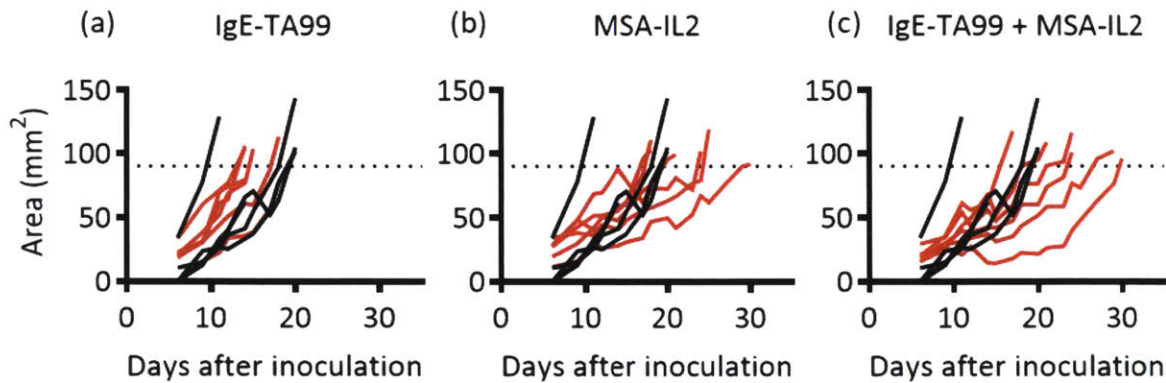


Figure 17: Tumor area curves for the tumor studies in CD11c hFceRIαTG mice

The red curves are the treatment in the title and the black curves in each plot are the PBS tumor area curves. Stricter euthanization criteria of 90mm² was used for these mice since studies were done a different animal facility.

2.3 Discussion

Although the data presented in this work did not indicate strong efficacy for anti-tumor antigen IgE antibodies in syngeneic mouse tumor models, there were some important pharmacokinetic and cellular lessons that could further inform efforts to develop IgE antibodies against cancer.

The short pharmacokinetic half-life of IgE compared with other isotype antibodies like IgG is well-documented to be on the order of a couple days⁷³, although we measured it to be only 6 hours. This pharmacokinetic barrier to biodistribution of exogenously administered IgE could help explain why it could not be found in the tumor after IP injection. In contrast, the potency of IgE-mediated hypersensitivity responses could be explained by the sustained allergen sensitivity period often needed to elicit these responses⁷⁴. Many bursts of IgE released over time could begin to displace already existing IgE-FcεRI complexes on the surfaces of FcεRI+ cells like mast cells and basophils. Then, when allergen challenge occurs, immune cells are preconditioned for response because of the presence of IgE already on their surfaces⁷⁵ since IgE-bound FcεRI is thought to be maintained almost indefinitely on the surfaces of mast cells and basophils^{76,77}. Perhaps if multiple systemic injections of tumor antigen-specific IgE like IgE-TA99 occurred over a period of time prior to tumor inoculation, there would be pre-existing, tissue-resident, tumor-specific IgE that could push mast cells or basophils toward a stronger response. However, the lack of efficacy improvement from intratumoral injections in the current work suggests that exposure in the tissues is not the only challenge for effective IgE-mediated tumor immunity.

This study showed lack of tumor efficacy even when mast cells were coated with IgE, or when dendritic cells with potential for IgE-mediated effects through transgenic human FcεRI expression were introduced. Although some mouse strains are documented to have a stronger mast cell-mediated response than C57BL/6⁷⁸, the lack of efficacy in C57BL/6 mice even when mast cells were IgE coated ex vivo and directly injected into the tumor suggests that even the ideal (albeit transient) mediator release from mast cells is insufficient to control tumors. Prior studies have shown that the human FcεRI receptor can interact with mouse IgE⁷⁹, so we did not attribute lack of efficacy in the CD11c transgenic human FcεRI model to failure to engage the therapeutic mouse antibody IgE-TA99. In fact, prior work indicated that dendritic cells expressing the trimeric form of the high affinity IgE receptor can take up IgE-antigen complexes, and cross-present them to CD8 T cells to enhance anti-tumor immunity⁷⁰. However, this previous work did not inject IgE but rather loaded dendritic cells with IgE-antigen complexes ex vivo in order to avoid any effects from mast cell activation by IgE cross-linking, such as IL4 or Th2 mediator release⁷⁰. Given this work's demonstration of complete lack of mast cell mediated efficacy, and failure to show efficacy when both mast cells and trimeric FcεRI+ dendritic cells were present, mast cells may be suppressing the anti-tumor immune response instead of enhancing it.

Although the focus is often on mast cells in when considering IgE-mediated immunity because of their prominent role in anaphylaxis, this work shows that other cell types like basophils and B cells could be playing important roles. The main cellular changes after anti-tumor IgE in our work were the presence of IgE on basophils in the tumor, spleen, and blood, and decreased levels of B cells in the blood and spleen after IgE treatment. Even though basophils did not increase in density, detecting therapeutic IgE-TA99 on their surface suggests they could be playing some role

in controlling tumors. Indeed, basophils have been shown to contribute to tumor control through recruitment of CD8+ T cells via CCL3/4⁸⁰, suggesting that they have a role to play in anti-tumor immunity. B cells are known to express the low affinity IgE receptor FcεRII⁸¹ and are capable of cell-mediated immunity functions like cytokine production in addition to T cell stimulation and antibody production⁸². Some reports also suggest that B cells can help transfer antigen to dendritic cells through FcεRII-mediated internalization of IgE-antigen complexes⁸³, which is one possible explanation for how IgE could help B cells fight against tumors. The lower B cell numbers in the blood and spleen, coupled with a slight (but not statistically significant) increase in B cells in the tumor, suggested B cells could be leaving exiting the blood stream to migrate to the tissues like the tumor, where they could play a direct or indirect role in coordinating an anti-tumor response. One additional cell type that could play a role in IgE-mediated anti-tumor immunity and not examined in this manuscript is neutrophils. Since mouse neutrophils have been reported to express a trimeric form of the high affinity IgE receptor in an experimental cerebral malaria model⁸⁴, and prior work has shown the importance of neutrophils to efficacy antibody and IL2 cooperation in mouse tumor models⁶⁷, neutrophils could also be a contributing factor to IgE-mediated anti-cancer immunity. Although we did not verify that either basophils or B cells contribute to the mild improvement in survival from IgE-TA99 therapy, they were the main cellular compartments that appeared changed by IgE therapy.

Several strategies could be employed to build upon the mild, but statistically significant efficacy of anti-tumor IgE in B16F10 and trend toward potential efficacy in MC38 mouse tumor models if future work pursues IgE-based cancer immunotherapy. Firstly, different cytokine or agonist combination partners other than IL2 should be considered for synergy with anti-cancer IgE or Th2 type immunity. For example, combination of IgE with eotaxin or IL3/anti-IL3 complexes could help attract more eosinophils or basophils⁸⁰, respectively. Perhaps adjuvants that steer toward an IgE-based response like cholera toxin, pertussis toxin, and carrageenan could further improve efficacy⁸⁵. The choice of mouse strain could have a significant effect on the ability to respond to allergic challenge. C57BL/6 mice tend to be biased toward Th1 immunity compared with Balb/c or C3H mice that are Th2 biased⁷⁴, indicating that anti-tumor IgE may elicit a stronger immune response in strains other than C57BL/6. In fact, even within the Th2-skewed mice, reports suggest that Balb/c and C3H mice can both be sensitized well to make allergen-specific IgE, but actually that hypersensitivity responses were more often elicited and IgE-mediated in C3H mice⁷⁴. Lastly, due to the longevity and importance of tissue-associated IgE and IgE effector cells, different sites of tumor inoculation could potentially change the magnitude of the IgE-mediated tumor response. Careful attention to improving combination therapy partners, mouse strain, and tumor location would be needed for further preclinical development of anti-tumor IgE antibodies.

2.4 Materials and methods

Mice

Female C57BL/6 (Taconic) mice were used at 6-10 weeks of age. Mice were housed in pathogen free environments. Except the study in the CD11c human FcεRIα transgenic mouse model, all

procedures were approved by the MIT Division of Comparative Medicine (DCM) and consistent with federal, state, and local regulations using animal protocol number 0512-040-15 or 0515-043-18 under MIT's Institutional Animal Care and Use Committee.

For the study in the CD11c human FcεR1α transgenic mouse model, CD11c human FcεR1α transgenic C57BL/6 mice were bred and housed under specific-pathogen-free conditions at Boston Children's Hospital (Boston, MA) and female mice were put on study at 6 weeks of age. All procedures were approved by the animal care and use committees of Boston Children's Hospital and consistent with federal, state, and local regulations using Animal Care Resources Children's Hospital (ARCH) protocol number 12-06-2415R.

Cell lines and media

B16F10 cells were maintained in Dulbecco's Modified Eagle's Medium (DMEM) with 10% FBS and Penicillin-Streptomycin and MC38 cells were maintained in DMEM with 10% FBS.

The C1.MC/C57.1(C57) mouse mast cell line was a kind gift from the lab of Professor Stephen J. Galli (Stanford) and cultured as previously described^{86,87}. Briefly, cells were kept in suspension in DMEM with 10% FBS, Penicillin-Streptomycin, and 50uM beta-mercaptoethanol.

Tumor treatment experiments

For experiments with B16F10 and MC38 tumors, mice were inoculated subcutaneously in the right flank with 10⁶ cells. The following agents were administered through intraperitoneal (IP) injection either on day 6 or 7 after tumor inoculation unless otherwise noted: 100 μg TA99 or IgE-TA99 (B16F10 tumors), 500 μg 2.5F-Fc⁶⁶ or 700ug 2.5F-FcE (MC38 tumors), and 30 μg eIL2. Unless otherwise noted, B16F10 tumors were treated with 5 treatments every 6 days and MC38 tumors were treated with 4 treatments every 6 days. Tumor areas were calculated as the product of the two perpendicular tumor diameters and mice were euthanized when tumor area exceeded 100 mm² unless otherwise noted. The few mice that died from reasons other than tumor area (low body condition due to ulceration or weight loss exceeding 20%) are noted in figure legends and are not included in the survival study analysis or plots.

Protein production and purification

All therapeutic proteins were made in house. TA99 (mouse IgG2c heavy chain and kappa light chain) was purified from a stably transfected HEK293 F cell line grown in FreeStyle 293 media (Life Technologies). 2.5F-Fc (mouse IgG2c heavy chain), 2.5F-FcE, IgE-TA99, and eIL2 (a fusion of mouse serum albumin and IL2 (MSA-IL2))⁶⁷ were purified 6-8 days after transfecting gWiz plasmids into HEK293 cells using polyethylenimine in FreeStyle supplemented with OptiPro (Life Technologies). For TA99 and 2.5F-Fc, supernatant from centrifuged HEK293 cells was purified through rProtein A Sepharose Fast Flow resin according to manufacturer's instructions (GE Healthcare). IgE-TA99, 2.5F-FcE, and MSA-IL2 were purified from HEK293 cell supernatant using TALON® Metal Affinity Resin according to manufacturer's instructions (Clontech) and subsequent gel chromatography on a HILOAD 16/600 Superdex 200 PG column on an AKTApurifier 10 fast protein liquid chromatography machine (GE Healthcare) to remove aggregate. All proteins were

tested to be below 0.1 EU/ dose by the QCL-1000 chromogenic LAL assay (Lonza) and run on reducing and non-reducing SDS PAGE 4-12% Bis-Tris gels (Life Technologies) to confirm size.

Degranulation assay

Ability of IgE-TA99 to induce mast cell degranulation in response to B16F10 cells was tested using the C1.MC/C57.1(C57) mouse mast cell line in a protocol adapted from previously described methods⁸⁸⁻⁹⁰ (Figure 18). Mast cells were incubated overnight at 37 degrees C in DMEM with 5 nM IgE. The next day, mast cells were washed to remove IgE from the supernatant and 4×10^4 mast cells and 8×10^4 B16F10 cells were added to each well of a 96 well plate and incubated for 2 hours at 37 degrees C. Plate was spun, then supernatant was separated from cells. Cells were lysed in 0.1% triton X-100. 25uL of lysate or supernatant was added to 100uL of a substrate for β -hexosaminidase, 1.2mM 4-Methylumbelliferyl N-acetyl- β -D-glucosaminide (Sigma) in 50mM sodium acetate buffer pH 4.5. Substrate cleavage occurred over the course of 90 minutes at 37 degrees C. Reaction was quenched with 175uL of glycine carbonate buffer (100mM glycine 80mM sodium carbonate buffer, pH 10) and 50uL of supernatant per well was read on a plate reader by exciting at 365 and reading at 445⁹¹. Percent degranulation was reported by comparing fluorescence of released (supernatant) versus total (supernatant and cells) granule contents.

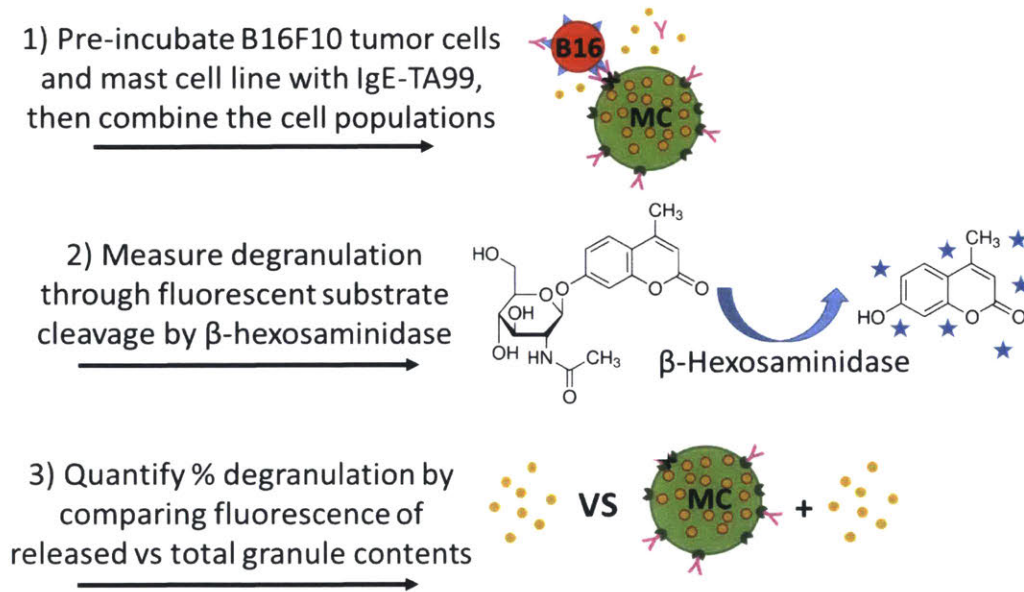


Figure 18: Degranulation assay protocol overview

Pharmacokinetics

To measure the serum half-life of IgE-TA99, IgE-TA99 was labeled with Alexa Fluor (AF) 647 NHS ester (succinimidyl ester) (ThermoFisher A20006). 100ug was injected retro-orbitally at time = 0 hours, then small blood aliquots were collected into heparin-coated capillaries from the edge of the tail at the indicated time points. Blood was spun and 3-5uL serum was pipetted back into a capillary. All capillaries with serum were kept at 4c in the dark until the study was over. A standard

curve with known concentrations of AF647 labeled IgE was made in serum and put in capillaries. Capillaries were read on a Typhoon fluorescence imager (GE Healthcare Life Sciences) and fluorescence intensity compared by image processing using ImageJ.

Biodistribution and flow cytometry

For analysis of IgE biodistribution, mice were inoculated with 10^6 B16F10 cells with stable co-expression of GFP day 0. On day 8, 100ug of AF647-labeled antibody of either IgE (IgE-TA99) or IgG (TA99) was injected IP and 3.4ug of labeled antibody was injected IT. 30ug MSA-IL2 was injected IP in all groups. Mice were sacrificed 24 hours after therapeutic injection and tumors, blood, and spleens were removed. After manual disaggregation, tumors were digested in collagenase/dispase/DNAse before filtering through a 70um filter before plating. Spleens were dissociated through a 70um filter, lysed with ACK buffer, and then single cell suspensions were plated. Blood was lysed with ACK buffer before plating. Samples were stained and run on a LSRFortessa flow cytometer (BD Biosciences) at the Koch Institute Swanson Biotechnology Center Flow Cytometry Core Facility. Zombie Aqua Fixable Viability Dye and TruStain fcX (Biolegend) were used for viability and Fc block prior to antibody staining. Antibodies against CD3 (145-2C11), FcεRI (MAR-1), FcεRII (B3B4), CD200R3 (Ba13), CD117 (2B8 from BD Biosciences), CD19 (6D5), CD11c (N418), CD11b (M1/70), F4/80 (BM8), and Siglec F (E50-2440 from BD Biosciences) were purchased from Biolegend unless otherwise noted. After gating for single, live cells, the following strategies were used to identify cell populations: CD3- CD19+ B cells; CD3- CD200R3+ cKit-basophils; CD3- CD200R3- CD117+ mast cells; GFP+ B16F10 tumor cells; CD3- CD11b high F4/80+ SSC low macrophages; CD3- CD11c+ CD11b mid dendritic cells; CD3- Cd11b mid Siglec F+ eosinophils. Notably, mast cells and basophils were identified without using FcεRI as a marker because we did not see staining above background using the MAR-1 clone of this antibody. This could be due to surface FcεRI saturation with IgE, which perhaps blocked the anti-FcεRI antibody.

Therapeutic mast cell tumor study

Mast cells derived from C57Bl/6 mouse bone marrow by culture with IL3 and SCF (Peprotech). Mast cells were injected IT every three days either after coating ex vivo with IgE or uncoated. IgE-TA99 was used in the B16F10 model, and 2.5F-FcE was used in the MC38 model. Because of concerns about toxicity of these mast cells, the injections increased from 10,000, to 50,000, to 100,000 cells in the first, second, and third injections, respectively, then stayed at 100,000 cells for all subsequent injections. After inoculation on day 0 with 10^6 B16F10 or MC38 tumor cells, treatments occurred on days 7, 10, 12, 15, 18, and 21.

Statistics

All statistical analysis was done using GraphPad Prism. Antibody and cellular biodistribution plots were compared using a two-way ANOVA with Dunnett's multiple comparisons test. Tumor survival curves were compared using the Log-rank (Mantel-Cox) test.

2.5 Acknowledgments

We would like to acknowledge and thank Professor Edda Fiebiger of Harvard Medical School, and her lab's generous support and collaboration on studies using the CD11c FcεRI transgenic mice. In particular, we are grateful for the help and advice of Dr. Barbara Platzer, technical assistance from Madeleine Stout and Justin Jacobse.

Thank you to Professor Stephen J. Galli at Stanford University for gifting us the C1.MC/C57.1 mouse mast cell line.

Thank you also to Grayson Rodriguez, an undergrad researcher who assisted with many of these studies.

This material was based upon work supported by the National Science Foundation Graduate Research Fellowship Program under Grant No. 1122374. Any opinions, findings, and conclusions or recommendations expressed in this material are those of the author(s) and do not necessarily reflect the views of the National Science Foundation.

This material was also based upon work supported by the NIH/NIGMS T32 GM008334, Interdepartmental Biotechnology Training Program.

This work was supported in part by the Koch Institute Support (core) Grant P30-CA14051 from the National Cancer Institute. We thank the Koch Institute Swanson Biotechnology Center for technical support, specifically the Flow Cytometry core.

Chapter 3. Decoupling toxicity from efficacy in cancer immunotherapy by modulating the order and timing of combination immunotherapy

Abstract

In combination cancer immunotherapies, consideration should be given to designing treatment schedules that harmonize with the immune system's natural timing. An efficacious temporally programmed combination therapy of extended half-life interleukin 2 (eIL2), tumor targeting antibody, and IFN α was recently reported,³⁰ however tumor-ablative efficacy was associated with significant toxicity. In the current work, altering the order and timing of the three agents is shown to decouple toxicity from efficacy. Delaying the administration of eIL2 to be concurrent with or after IFN α eliminates toxicity without affecting efficacy in multiple syngeneic tumor models and mouse strains. The toxicity resulting from eIL2 administration before IFN α is dependent on multiple systemic inflammatory cytokines including IL6, IL10, IFN γ , and TNF α . Natural killer (NK) cells are the main cellular contributor to toxicity, but are not essential for tumor control in this system. When pre-conditioned with eIL2, splenic NK cells became hyperactivated and upregulate IFN α signaling proteins that cause an excessive, toxic response to subsequent IFN α exposure. This work illustrates an example where accounting for the temporal dynamics of the immune system in combination therapy treatment schedule can favorably decouple efficacy and toxicity.

3.1 Introduction

Improvement in efficacy of cancer immunotherapy is generally expected to require combination therapies. For example, recent combination of Nivolumab and Ipilimumab resulted in a 58% rate of objective response in updated results of the phase 3 Checkmate 067 trial in untreated advanced melanoma.²⁰ These two agents act on adaptive immunity via T cells;⁹² so perhaps non-T-cell-inflamed cancers could be made responsive by enlisting components of the innate immune system.⁹³ However, maintaining acceptable therapeutic index while increasing the number of administered agents is a challenge. For example, the combination arms of the Checkmate 067 trial resulted in grades 3 or 4 adverse events in 59% of patients and 39% of combination-treated patients had a treatment-related adverse event leading to discontinuation of therapy.

The inflammatory cytokines interleukin (IL) 2 and IFN α are promising options for combination therapies because they are FDA approved agents capable of enhancing both innate and adaptive immunity.^{94,95} As a monotherapy, high dose IL2 engenders 10-20% response rates against renal cancer and melanoma⁹⁶ and is capable of enhancing innate mechanisms like antibody-dependent cell-mediated cytotoxicity (ADCC)^{97,98} as well as stimulating T cell activation and proliferation.⁹⁹ Unfortunately, high dose IL2 therapy must be administered under intensive care conditions due to significant toxicities including fevers and severe hypotension from vascular leak syndrome,¹⁰ causing 50% of patients to cease treatment after one of four courses according to

a study of metastatic renal cell carcinoma treatment.¹⁰⁰ Similar to IL2, IFN α also promotes a multi-faceted anti-cancer response^{101,102} including direct anti-proliferative effects on cell growth¹⁰³ and enhanced communication between innate and adaptive immunity.^{104–106} Beyond any direct tumoricidal effects,¹⁰⁷ IFN α is a key cytokine in the stimulator of interferon genes (STING) pathway response and augments maturation of antigen presenting cells (APCs) like dendritic cells (DCs).^{108,109} Given in high dose in an adjuvant setting in surgically resected melanoma, IFN α improved relapse free survival (RFS) and had variable effects on overall survival.^{110–112} Despite improvements in RFS of adjuvant IFN α , toxicity resulted in between 10% and 37% rates of treatment cessation.^{113,114} Although IL2 and IFN α continue to improve survival in some adjuvant and primary cancer indications, motivation for development of either IL2 or IFN α as new monotherapies has slowed due to these unfavorable therapeutic indices.

Combinations of IL2 and IFN α with each other or with different types of clinically approved immunotherapies have been explored but generally do not have the therapeutic window to offer adequate tumor control. A small clinical trial concurrently dosing these two agents 3 times per week against various cancer types showed very limited efficacy.⁹⁴ In a later clinical trial for metastatic melanoma that assessed whether the combination of IFN α and IL2 improved chemotherapy, the cytokines were administered continuously over the course of 4 days and added no survival advantage.⁹⁵ Additionally, occurrence of grades 3 and 4 toxicities tripled including nausea, diarrhea, and drops in white blood cell counts below 3000 per mm³ in the combination cytokine group.⁹⁵ Since efficacy for single agents is often linked to higher dose level and number of doses received, combination therapy treatment schedule follows that precedent. The elements of innate and adaptive immunity believed to be most important for the mechanisms of action of IL2 and IFN α (e.g. CD8 T cell clonal expansion and DC maturation, respectively) can occur at differing times during the steps of the anti-cancer immune response²⁵. This indicates that the therapeutic window might be improved by dosing agents at different times in treatment schedules rationally designed to match the current immune system response. In fact, emerging evidence suggests that a shorter exposure burst to type I or type II IFNs could prevent tumors from acquiring resistance, while chronic treatment might paradoxically foster resistance to checkpoint blockade.¹¹⁵ Critical thinking is needed to re-direct schedule design away from the paradigm of sustained maximum-tolerated dose (MTD) treatment and towards dosing at the proper timescale and duration for therapeutic efficacy of each individual agent.

Recent preclinical studies using an extended half-life version of IL2 (eIL2)⁶⁷ and IFN α in combination with tumor targeting antibodies have successfully used temporally designed treatment schedules to significantly improve therapeutic efficacy.³⁰ Staggering the IFN α to be 2 days after a tumor targeting agent and eIL2 instead of concurrently raised the cure rate from 0% to 60-100% for large, established syngeneic mouse tumor models. Despite the high cure rates from delayed IFN α administration, toxicity remained a significant drawback, with mice losing 10-20% of their body weight. In this work, altering the order of cytokine administration was shown to eliminate toxicity without affecting therapeutic efficacy by tempering the strength of innate inflammation. Although eIL2 was dosed in prior work³⁰ at the same time as the tumor targeting antibody to potentiate ADCC and maintain pharmacological presence during subsequent T cell proliferation days later, the current work was motivated to investigate whether eIL2's most important role is expansion of activated lymphocytes in a therapy engaging adaptive immunity.

When IFN α administration was staggered after a tumor targeting antibody, treating with eIL2 at the same time or after IFN α eliminated weight loss toxicity without compromising therapeutic efficacy in two tumor models. The reduction in toxicity conferred by dosing eIL2 concurrently instead of before IFN α was mediated by lower systemic levels of inflammatory cytokines and reduced NK cell activation state, which were not essential to therapeutic efficacy. This study underscores the potential importance of order and timing in treatment schedule design to decouple efficacy and toxicity in combination immunotherapy.

3.2 Results

The order of eIL2 with respect to IFN α decouples efficacy and toxicity

To investigate ways to lower toxicity of the efficacious combination of tumor targeting antibodies, eIL2, and staggered IFN α , the timing of eIL2 was varied while keeping 1-day separation between antibody and IFN α (Figure 19 (a)). Mouse weights were monitored every day or every 2 days and maximal weight loss was observed 2 and 3 days after IFN α (Figure 30 (a)). Subsequent weight change is reported as percent decrease between first day of treatment (0%) and 2 or 3 days after IFN α treatment unless otherwise noted. In C57BL/6 mice with B16F10 tumors treated with the anti-TRP1 antibody TA99, administering eIL2 concurrent with or after IFN α eliminated the 10-20% weight loss seen when eIL2 was given before IFN α (Figure 19 (b)). This stark difference in toxicity did not lower the therapeutic efficacy from 20-40% survival, even when eIL2 was given as late as 3 days after treatment initiation (Figure 19 (c)). We confirmed that IFN α synergized with the eIL2 and tumor targeting antibody to increase efficacy against B16F10 tumors by eliminating IFN α treatment but delivering the eIL2 concurrently with TA99 or 1, 2 or 3 days after TA99 (Figure 30 (b-d)). Our previous work confirmed the importance of both antibody and eIL2 to therapeutic efficacy³⁰ and that monotherapies of eIL2 or TA99 do not lead to tumor cures,⁶⁷ so we did not repeat these conditions in this work. In this work, the memory response of pooled, surviving mice from B16F10 tumors originally treated with all three agents was examined. Consistent with prior studies³⁰, rechallenged mice had extended survival compared with age-matched, naïve mice, with around 25-50% cure rate (Figure 30 (e)). Importantly, there was not a statistically significant difference in survival in this rechallenge study between mice originally treated with the staggered (toxic) and concurrent (non-toxic) eIL2 and IFN α regimens. Weight loss curves without IFN α show that weight loss did not occur without this agent (Figure 30 (a)). Since weight loss was eliminated by leaving out IFN α or by giving the eIL2 at or after IFN α , we did not quantify weight loss of antibody alone or under conditions with eIL2. Individual tumor area curves for every treatment condition confirm the survival results (Figure 30 (f-m)).

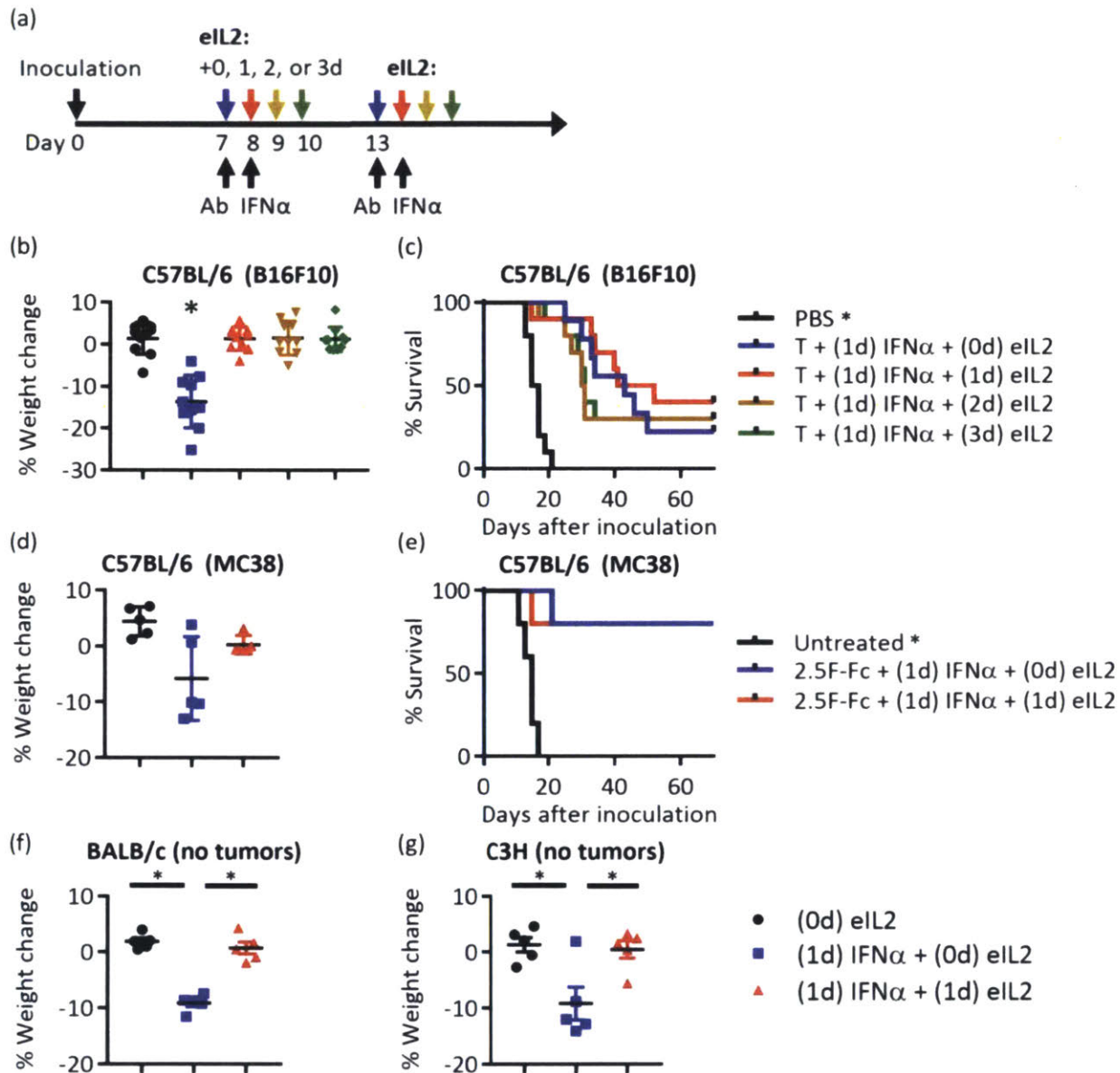


Figure 19: Delaying eIL2 eliminated the weight loss toxicity but did not affect therapeutic efficacy (a) Schematic of experimental design is shown. 2 courses of therapy were given beginning on days 7 and 13, keeping the timing of tumor targeting antibody (Ab) and IFN α 1 day apart. In the four groups of treated mice, eIL2 was administered at the same time as Ab (0d), 1d, 2d, or 3d after Ab. (b,c) Percent weight change and survival curves are shown for 4 different times of eIL2 administration using the TA99 Ab (T) against B16F10 tumors. Reported weight loss is 4 days after TA99. Data are from 2 independent experiments totaling 9-10 mice per group. (d,e) eIL2 is administered with or 1 day after Ab (concurrent with IFN α) using the 2.5F-Fc antibody-like construct against MC38 tumors. Reported weight loss is 3 days after 2.5F-Fc. $p = 0.11$ comparing (0d) eIL2 and (1d) eIL2 weight change. Data are from 1 independent experiment totaling 5 mice per group. (f,g) In non-tumor bearing BALB/c or C3H mice, percent weight change plots are shown for eIL2 given 1 day before or concurrent with IFN α . No Ab was used for this study. Data are from 1 independent experiment totaling 5 mice per group. * indicates $p < 0.05$ and error bars are +/- SEM.

The same toxicity trends occurred in a different tumor model and in two different mouse strains. In the MC38 colon carcinoma model, toxicity was reduced and efficacy was maintained when eIL2 was given concurrently with IFN α , following treatment with an antibody-like construct (2.5F-Fc) that targets integrins overexpressed on many mouse and human tumors⁶⁶ (Figure 19 (d-e)). Weight loss curves over time (Figure 31 (a)) as well as individual tumor area curves (Figure 31 (b-f)) support the summarized weight loss and survival results. This trend of weight loss from staggered eIL2 and IFN α held independent of the presence of tumors and in different mouse strains. Giving eIL2 at the same time as IFN α in non-tumor-bearing BALB/c and C3H mice ameliorated weight loss observed when eIL2 was given 1 day before IFN α (Figure 19 (f-g) and Figure 31 (g-h)), confirming that the observed toxicity is independent of both tumor burden or mouse strain.

Inflammatory serum cytokines are partially responsible for toxicity of staggered eIL2 and IFN α

The sources of differential toxicity between giving eIL2 prior to versus simultaneous with IFN α were investigated through looking for organ-level toxicity and then systemic levels of inflammatory cytokines or chemokines.

Blood clinical chemistry, serum protein and enzyme levels, and organ pathology were assessed at multiple time points after treating mice with the toxic staggered eIL2 and IFN α or giving these agents at the same time. In order to look at time points weeks after treatment began and to avoid conflating tumor-related toxicity with treatment-related toxicity, these studies were completed in non-tumor-bearing C57BL/6 mice. Complete blood count (CBC) analysis revealed an increased proportion of monocytes as a percent of white blood cells in the staggered eIL2 and IFN α -treated group 3 days after the first round of treatment began (Figure 32 (a)), which could reflect systemic over-activation of innate immunity. Although not outside normal ranges, mice from the toxic, staggered treatment had low red blood cell counts and increased mean corpuscular hemoglobin, red cell distribution width, and mean platelet volume (Figure 32 (c-e)). Coupled with a trend toward decreased (not statistically significant) mean cellular hemoglobin concentration (Figure 32 (f)) in both treated groups after the first treatment, the staggered eIL2 and IFN α -treated mice could be suffering from mild anemia, which has been seen in clinical immune-related toxicities.¹¹⁶ The decreased activity of the liver enzyme alkaline phosphatase (Figure 32 (g)) could be indicative of malnourishment, but it was found in both the more and less toxic treatment groups. Decreased blood protein levels and albumin-to-globulin ratio (Figure 32 (h-j)) may be indicative of mild liver or kidney damage, which could be associated mainly with eIL2 treatment. Organ pathologies in the lung, kidney, liver, and spleen seem associated with proximity to eIL2 treatment (Figure 32 (k-n)). Overall, these results do not explain the weight loss differences between the staggered and concurrent eIL2 and IFN α .

Since the toxicity associated with staggered treatment-related weight loss was not manifested in bloodwork or organs examined, inflammatory cytokines and chemokines were assessed using a Luminex multiplex bead-based assay. Mouse serum was collected from B16F10 tumor-bearing

mice at multiple time points before and after treatment comparing administering eIL2 1 day before and concurrently with IFN α . Using each time point (excluding the 0+ hours point present for only one treatment condition), the area under the curve (AUC) was calculated for each individual factor for a given treatment condition. The ratios of the AUCs for the toxic versus non-toxic treatment conditions were then plotted for the various factors (Figure 20 (a)). This AUC analysis revealed increases in multiple agents including leukemia inhibitory factor (LIF), IL6, IL15, and KC in the toxic (staggered eIL2) treatment group (Figure 20 (a)). It was not unexpected that LIF and IL6 both had high AUC ratios, since LIF signals through the same, shared gp130 signaling receptor subunit as IL6 and IL6 plays a well-documented role in autoimmune related toxicities.¹¹⁷ KC, also known as CXCL1, is a neutrophil chemoattractant and activator that shares signaling with many other chemokines.¹¹⁸ Although not statistically significant, other cytokines or chemokines such as IFN γ , IL5, IL10, TNF α , M-CSF, and IL12(p40) also were increased in the toxic group in this AUC ratio analysis (Figure 20 (a)). The partial least squares regression (PLSR) analysis scores plots for the cytokines/chemokines (variables) (Figure 33 (a)) and weight changes (response) (Figure 33 (b)) indicated the separation of the toxic treatment group (group 2) along both components compared to non-toxic, concurrent IFN α and eIL2 (group 3), toxic and non-toxic NK depletions (groups 7 and 8), and leaving out each of the individual cytokines (groups 4-6). The loadings plot confirmed the importance of KC, IL6, and IL10 with the weight loss toxicity because these AUCs were anti-correlated with weight change (Figure 33 (c)). Thus, increases in these cytokines accompany decreases in weight. LIF, IFN γ , TNF α (upper left cluster of points), IL5, and IL12(p40) were all also anti-correlated with the weight change on the loading plot at least along the first component. IL6, IL10, IFN γ , and TNF α are upregulated in clinical **cytokine release syndromes**,¹¹⁷ so their contributions to weight loss in the toxic treatment group are not surprising. The average levels over time of every cytokine and chemokine used for the AUC and PLSR analysis were also plotted for every treatment condition, supporting the conclusions of the prior analysis (Figure 34). Note that IL2 was excluded from the AUC and PLSR analysis because eIL2 was given exogenously in most of the treatment courses, and thus the measured IL2 levels did not reflect toxic response of the mice to treatment. Spikes corresponding to eIL2 administration can be seen in the IL2 time course plot in Figure 34 and are absent in the treatment condition without any eIL2. Based on the AUC analysis, the loadings and scores plots from the PLSR analysis, the individual time course plots, and the feasibility of neutralizing these soluble factors, IL5, IL6, IL10, IFN γ , and TNF α were chosen for follow-up studies.

Antibody neutralization of IL10 and IFN γ in B16F10 tumor-bearing mice mildly but statistically significantly reduced weight loss toxicity (Figure 20 (c)), while TNF α , IL5, and IL6 neutralization did not significantly affect weight loss (Figure 20 (b-c)), although the full time course of the weight losses for these agents suggests that all 5 cytokines may contribute to toxicity (Figure 35 (a-c)). IL5 and IL6 neutralizations were continued during 2 treatment courses in B16F10 tumor-bearing mice. Survival analysis and individual tumor area curves (Figure 35 (d-k)) do not indicate that IL5 or IL6 contributed to efficacy. Consistent with the Luminex multiplex analysis, no individual cytokine seemed predominantly responsible for the weight loss, characteristic of a broader cytokine storm in response to eIL2 administered before IFN α .

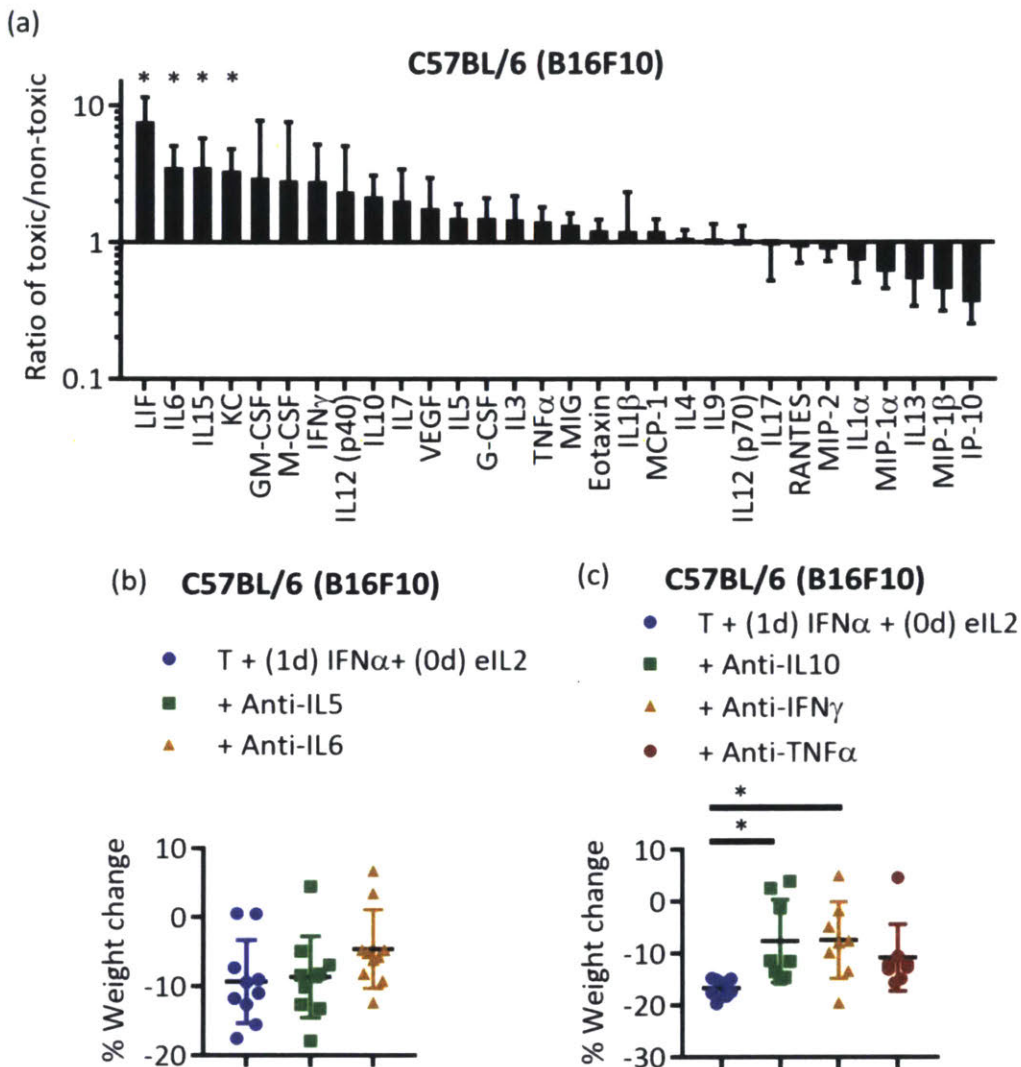


Figure 20: A variety of inflammatory agents were responsible for toxicity of staggered eIL2 before IFN α (a) The ratios of the AUCs over time for individual cytokine levels in the staggered eIL2 and IFN α (toxic) and concurrent eIL2 and IFN α (non-toxic) treatment conditions were plotted. Data are from 1 independent experiment in B16F10 tumor-bearing mice with 3 mice per treatment group. (b,c) Cytokine neutralization studies in B16F10 tumor bearing mice started treatment day 6 (10 mice per group) (b) or day 7 (7-8 mice per group) (c). Percent weight change is shown 3 days after IFN α treatment. Each plot contains data from 1 independent experiment. * indicates $p < 0.05$ and error bars are \pm SEM.

NK cells contribute to toxicity but not efficacy

Once several inflammatory cytokines were identified that contributed to autoimmune-related toxicity, cellular depletions were performed to assess contribution to weight loss toxicity. From an extensive panel of cellular depletions and neutralizations explored to examine weight loss, only depletion using anti-NK1.1 resulted in a statistically significant reduction in weight loss (Figure 36 (a)). Despite the strong correlation of the neutrophil-attracting chemokine KC with weight loss (Figure 33 (c)), depletion of neutrophils through anti-Ly6G did not significantly reduce weight loss.

Depleting NK cells in the toxic treatment schedule of staggered eIL2 and IFN α significantly reduced the weight loss in B16F10-bearing C57BL/6 mice 2 days after IFN α treatment (Figure 21 (a)). At all other time points other than the time point 2 days after IFN α , the mice given staggered eIL2 and IFN α with depletion of NK cells have comparable weight change to untreated mice (Figure 36 (b)). Despite the documented role of NK cells in tumor control in other model systems,^{119,120} NK cells remarkably did not contribute to the 20-40% survival of tumor-bearing mice either in the toxic, staggered eIL2 and IFN α treatment schedule or the non-toxic, concurrent eIL2 and IFN α schedule (Figure 21 (b) and Figure 36 (e-i)). Although depletion using the anti-NK1.1 antibody would deplete both NK cells and NK T cells, depleting with the anti-Asialo-GM1 antibody specific to NK cells (and not NK T cells)¹²¹ showed that NK cells themselves were responsible for the weight loss (Figure 21 (c), Figure 36 (d)). Although anti-Asialo-GM1 also depletes basophils and heterogeneous Asialo-GM1 expression is found on T cell subsets,¹²² using this antibody in a separate group from anti-NK1.1 showed that NK T cells were not responsible for the decreased weight loss of the NK1.1 depletion. Verification of NK depletion showed that at least 95% of splenic NK cells were depleted (Figure 36 (c)). Previous studies emphasizing a role for NK cells in tumor control were often performed in mice lacking T cells, raising questions of their relevance to immunotherapy with an intact immune system. This particular antibody-plus-cytokine treatment protocol has been shown previously to strongly require CD8+ T cells, macrophages, and CD8+ DCs for efficacy.³⁰

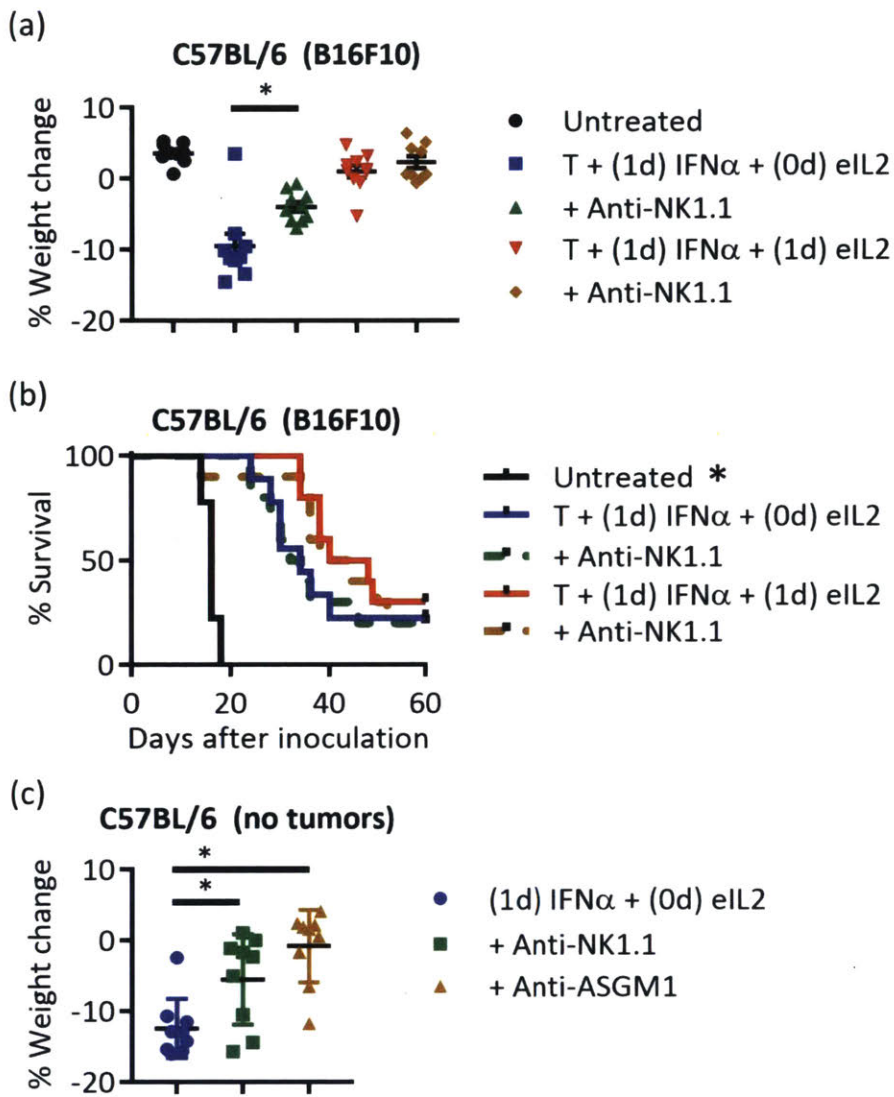


Figure 21: NK cells were important for toxicity but not for therapeutic efficacy

(a,b) Percent weight change and survival plots were compared for the toxic and non-toxic treatment conditions with and without NK cell depletion in the B16F10 tumor model. Data are from 2 independent experiments totaling 9 or 10 mice per group. Treatment in this study began day 6 instead of day 7, so TA99 (T) was dosed days 6 and 12, IFN α was dosed days 7 and 13, and eIL2 was dosed days 6 and 12 or 7 and 13. (c) Non-tumor bearing mice were given anti-NK1.1 or anti-ASGM1 depleting antibodies before treatment with 1-day staggered eIL2 and IFN α . Percent weight changes were quantified 2 days after IFN α . Data are from 1 independent experiment totaling 9 mice per group. * indicates $p < 0.05$ and error bars are \pm SEM.

Staggering eIL2 before IFN α increases NK cell activation and sensitivity to IFN α

To determine how NK cells contributed to toxicity when treated with eIL2 prior to IFN α , splenic NK cells were characterized using flow cytometry 1 day after treatment with eIL2, which was when IFN α was typically administered. Representative flow cytometry plots for each treatment

condition are shown (Figure 37, Figure 38). NK cell activation markers described previously such as CD11c, CD43, CD44, CD69, and B220¹²³ were significantly increased in spleens of B16F10 tumor-bearing mice 1 day after antibody and eIL2 treatment compared with treatment with antibody alone (Figure 22 (a-e)). At a higher activation state, NK cells would be poised to produce more inflammatory cytokines and react more strongly to IFN α . In addition to increasing activation marker expression, eIL2 caused an increase in expression of signaling proteins important to the IFN α response. 1 day after eIL2 administration, splenic NK cells had increased expression of the IFN α receptor IFNAR1 (Figure 22 (f)). Since IFN α signaling is propagated through JAK/STAT pathways,¹²⁴ levels of STAT1 and STAT3 proteins were examined and also shown to be increased on NK cells 1 day after eIL2 administration (Figure 22 (g-h)).

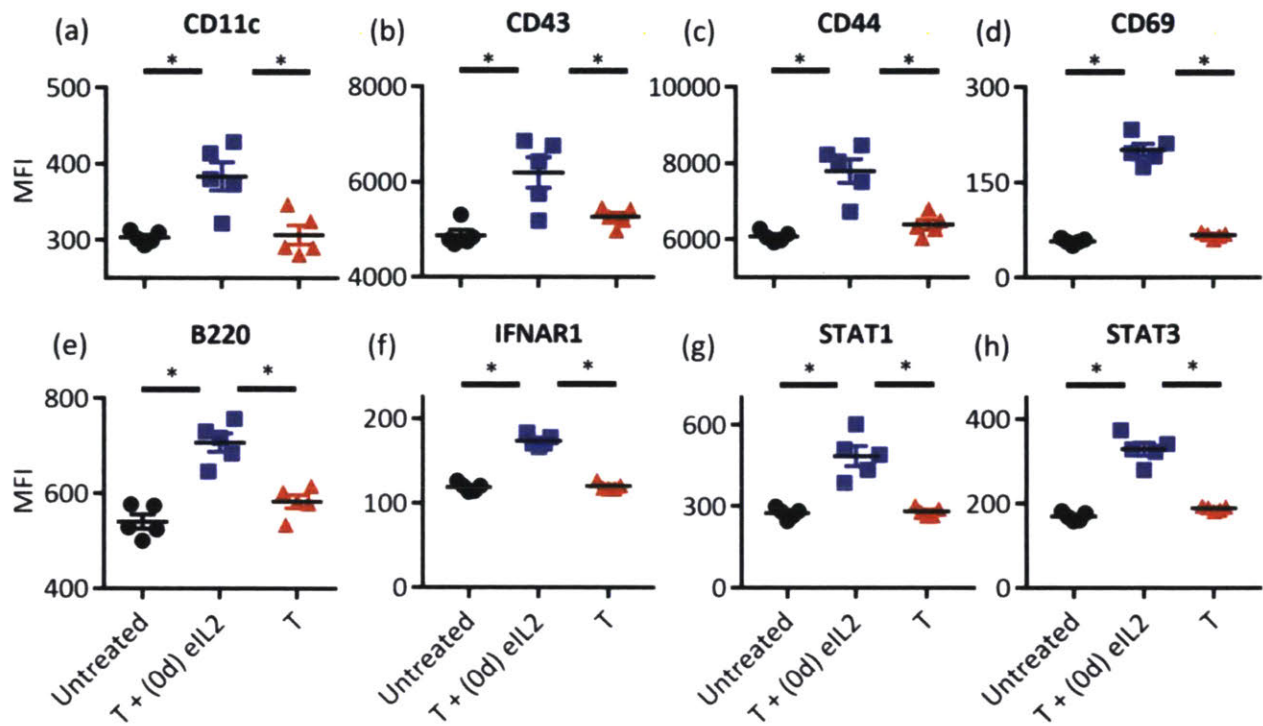


Figure 22: Staggering eIL2 before IFN α increased the NK cell activation prior to exposure to IFN α
 Splenic NK cells were harvested from mice bearing established B16F10 tumors 1 day after the indicated treatment and NK cell activation markers (a-e) and IFN α -responsive signaling proteins (f-h) were quantified by flow cytometry. Median fluorescence intensity (MFI) of all single, live, CD3 negative, NK1.1 positive cells is plotted on the y axis. Data are from 1 independent experiment totaling 5 mice per group, with separate staining panels for NK activation markers (a-e) and IFN signaling proteins (f-h). * indicates $p < 0.05$ and error bars are +/- SEM.

Minimal treatment course and amount of anti-tumor antibody needed for efficacy in combination with eIL2 and IFN α

After realizing the importance of the order of administration of eIL2 and IFN α in the combination therapy with TA99, we became interested in a different type of treatment schedule design. Namely, whether the immune system needed the same type of combination stimulation in multiple courses of treatment or whether immunological processes may be set in motion after the first therapy that need more minimal stimulation on subsequent rounds of therapy. An initial pilot study suggested that eIL2 and IFN α were necessary for each round of treatment, but that TA99 may be superfluous after the first round of treatment (Figure 23). If TA99 were only needed for one round of therapy, it could suggest that a strong burst of innate inflammation were only needed once to generate antigen, and we called this the ‘antibodies as vaccines’ hypothesis.

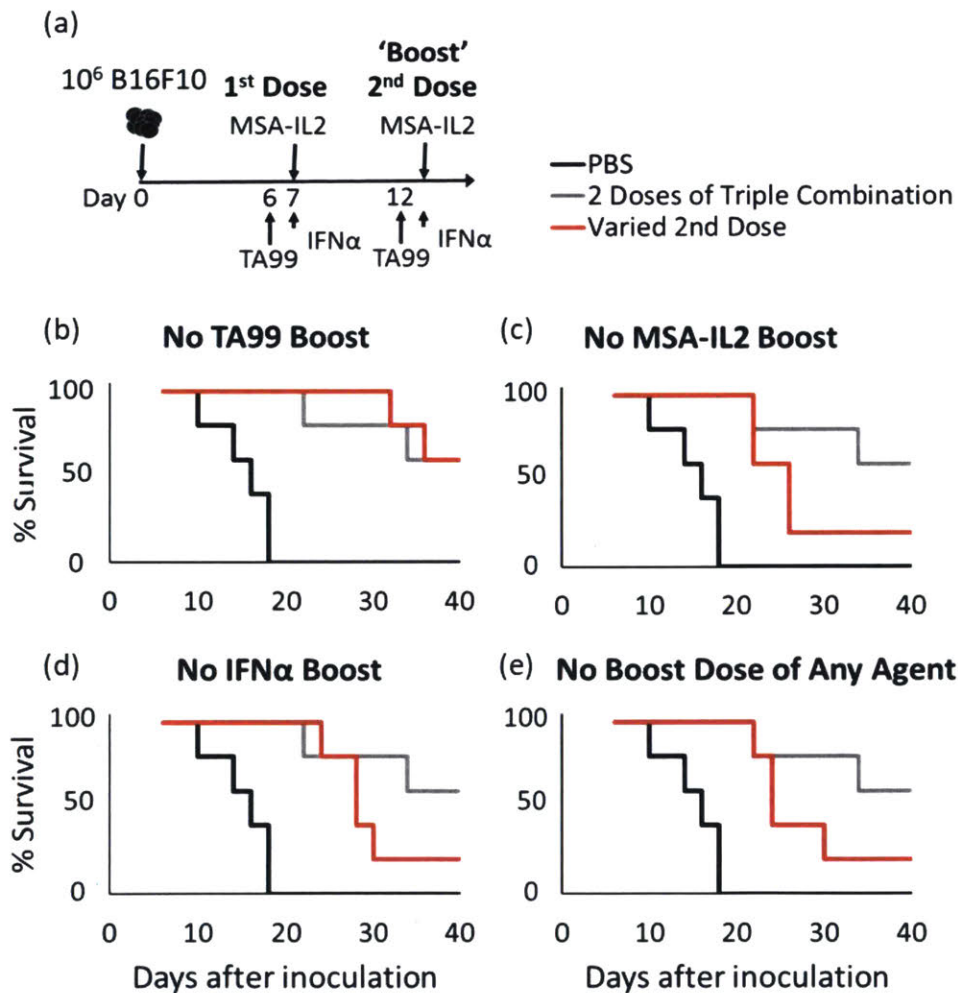


Figure 23: Pilot study leaving off TA99, MSA-IL2, or IFN α in the 2nd dose

(a) Treatment schedule outline showing the dosing of each of the 3 agents after injecting 10⁶ B16F10s on day 0. The 2nd dose was varied by leaving off either (b) TA99, (c) MSA-IL2, (d) IFN α , or (e) all 3 agents for no 2nd dose.

When we followed up on this pilot study trend to further explore the antibodies as vaccines hypothesis, our larger study did not support this theory. We found that survival correlated with frequency of TA99 dosing, with mice dosed with saturating TA99 (3 times per week) having the best survival (Figure 24).

(a)

Group	Day 7	Day 9	Day 11	Day 14	Day 16	Day 18
Untreated						
No TA99		MSA-IL2 IFNa			MSA-IL2 IFNa	
TA99 1 st dose	TA99	MSA-IL2 IFNa			MSA-IL2 IFNa	
TA99 both doses	TA99	MSA-IL2 IFNa		TA99	MSA-IL2 IFNa	
Saturating TA99	TA99	TA99 MSA-IL2 IFNa	TA99	TA99	TA99 MSA-IL2 IFNa	TA99
One dose all agents	TA99	MSA-IL2 IFNa				

(b)

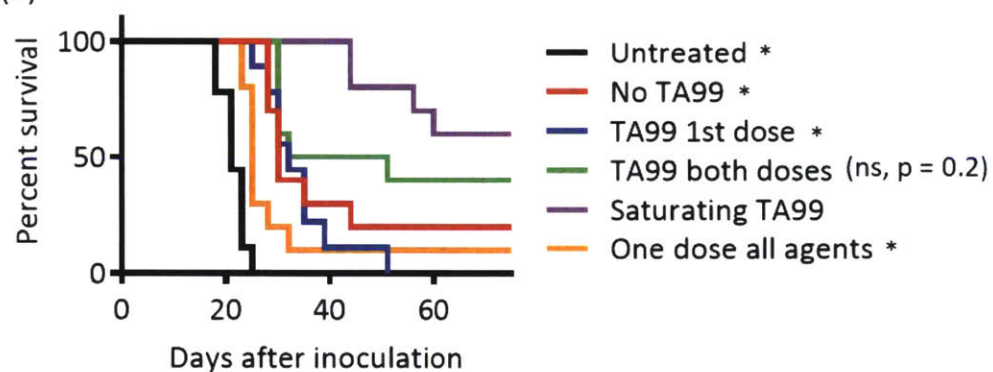


Figure 24: Testing antibodies as vaccines theory with varied TA99 dosing

(a) Treatment schedule outline showing the dosing of each of the 3 agents after injecting 10^6 B16F10s on day 0. Each dose of TA99 was 100ug. IFN α was dosed 10ug and MSA-IL2 30ug. Every treatment was given IP. (b) Survival curves comparing efficacy of each of the treatment groups. * denotes p < 0.05 compared with the Saturating TA99 group.

Extending timing concepts: checkpoint blockade and antigen-independent tumor targeting

The prior work on order and timing in immunotherapy combinations focused on IL2, IFN α , and the antibody TA99. Although IL2 and IFN α are pleiotropic and affect a variety of innate and adaptive cellular processes, we were interested in whether we could expand timing concepts to other combination partners. Since checkpoint blockade antibodies are some of the most influential, recently approved immunotherapy biologics in the clinic, we decided to explore using antibodies against PD-1, CTLA-4 (approved), TIM-3, and TIGIT (clinical stage trials). In addition to incorporating these immunomodulatory antibodies, we also sought to move beyond TA99 (targeting the melanoma antigen TRP-1) to find treatment combinations that were tumor-antigen independent. In place of TA99, we substituted in an antibody like construct called 2.5F-Fc, which targets a wide variety of mouse and human integrins overexpressed in tumors⁶⁶.

Imagining these new agents along the anti-cancer immune cycle, we envision 2.5F-Fc playing a role as an initial stimulator of innate inflammation similar to TA99. Checkpoint blockade antibodies, although precise mechanism of action not known, would likely be most valuable to stimulate T cells during or after antigen priming. We additionally hypothesized that these antibodies may have fewer effects on innate immunity than cytokines, thus imprecisely timed administration prior to T cell expansion may not cause the dysregulation of innate and adaptive communication seen, for example, when the sequencing of IL2 and IFN α were wrong. Since these antibodies do not typically cause dose-limiting toxicity in mouse models and have long half lives, we decided to simplify the number of timed combinations by administering the checkpoint blockade antibodies concurrently with tumor targeting agent 2.5F-Fc. Lastly, since IFN α plays such an important role in stimulating communication between innate and adaptive immunity when given after antigen generation³⁰, we decided to continue to include this cytokine in combinations given staggered 2 days after other agents.

For our first study, we explored 2.5F-Fc in combination with a wide variety of checkpoint blockade antibodies and IFN α in the MC38 tumor model because this mouse model is known to have high integrin expression and was previously characterized thoroughly with 2.5F-Fc. Survival curves were examined after 3 courses of treatment 6 days apart and show that the combination of 2.5F-Fc, staggered IFN α , and anti-CTLA-4 have the strongest effect on improving survival (Figure 25 (a)). TIGIT and PD-1 combinations with 2.5F-Fc also did well, so singlets and doublets of these agents were tested in MC38 survival studies and showed that the efficacy of the doublet of 2.5F-Fc and anti-PD-1 was not improved by anti-TIGIT, and that 2.5F-Fc was necessary for efficacy with these agents since the anti-PD-1 and anti-TIGIT doublet resulted in much lower survival without 2.5F-Fc (Figure 25 (b)). Since anti-TIM-3 also did not improve the efficacy seen from treatment with anti-PD-1 and 2.5F-Fc (Figure 25 (c)), anti-TIM-3 and anti-TIGIT were not further explored in mechanistic studies. Although the combination of anti-CTLA-4 seemed to improve therapeutic efficacy of 2.5F-Fc and anti-PD-1 combinations (Figure 25 (c)), the strongest survival of close to 100% was seen from the triple combination of 2.5F-Fc, staggered IFN α , and anti-CTLA-4.

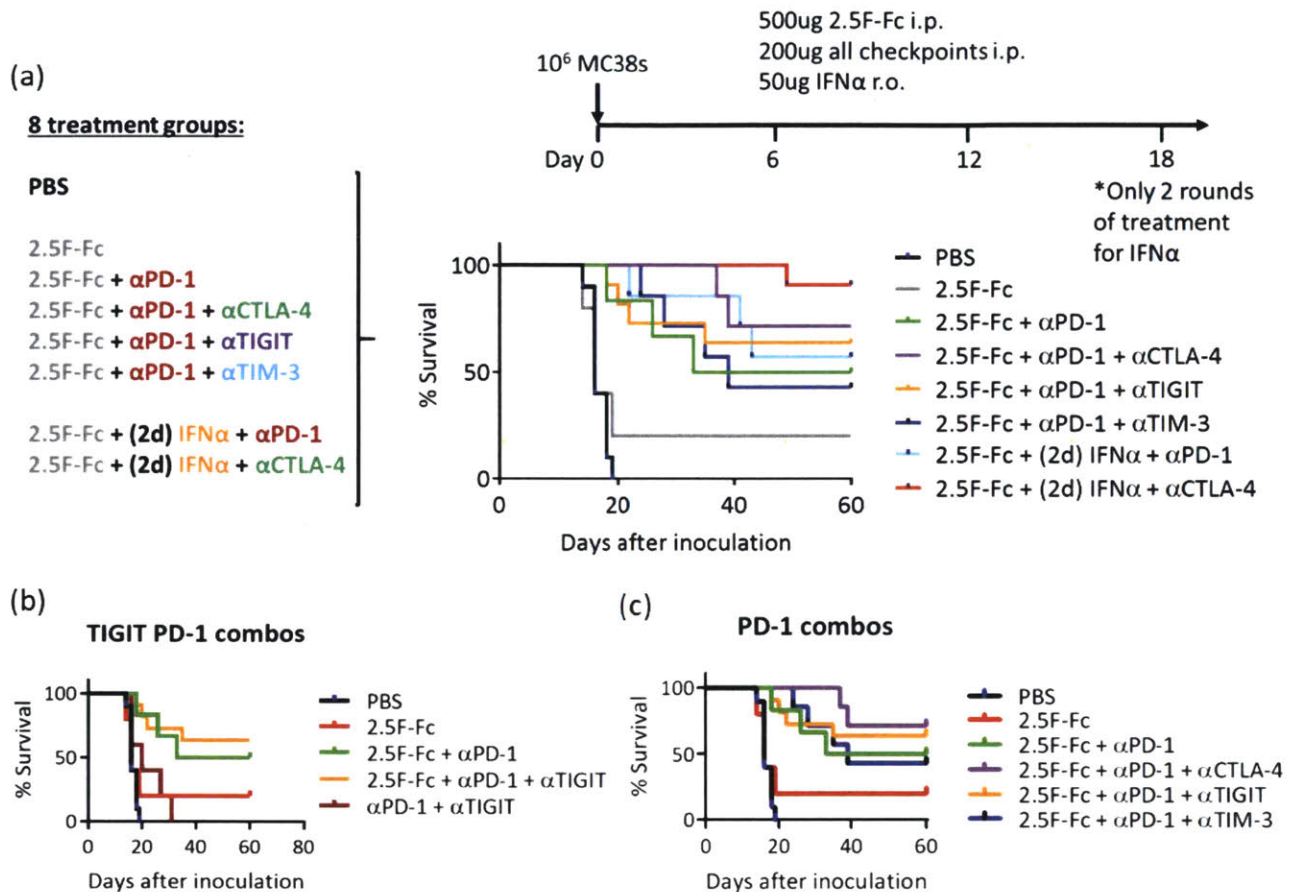


Figure 25: Survival studies with 2.5F-Fc, PD-1, TIGIT, TIM-2, and IFN α combinations

(a) Combinations of various checkpoint blockade antibodies with the tumor antigen-independent, antibody-like construct 2.5F-Fc, without or without IFN α emphasize the importance of anti-CTLA-4 for efficacy in the MC38 tumor model. Treatment conditions and cycles are described in the diagrams. (b-c) The same treatment conditions and tumor model were used to more closely examine PD-1 and TIGIT combinations.

Since the combination of 2.5F-Fc, staggered IFN α , and anti-CTLA-4 performed the best, iterations of these agents in singlets, doublets, and different orders were explored next. Firstly, we found 2.5F-Fc was not necessary for therapeutic efficacy when combined with anti-CTLA-4 and IFN α in either the MC38 or B16F10 tumor models (Figure 26 (a-b)). Additionally, anti-CTLA-4 seemed to be the important factor for efficacy when tested alone compared to the combinations (Figure 26 (c)). Although anti-CTLA-4 combined with staggered versus concurrent IFN α perform equally well in survival improvement comparing the orange and red curves (Figure 26 (c)), subsequent T cell infiltration characterization studies continued using 2d staggered IFN α because they were initiated before IFN α staggering was shown to be unnecessary.

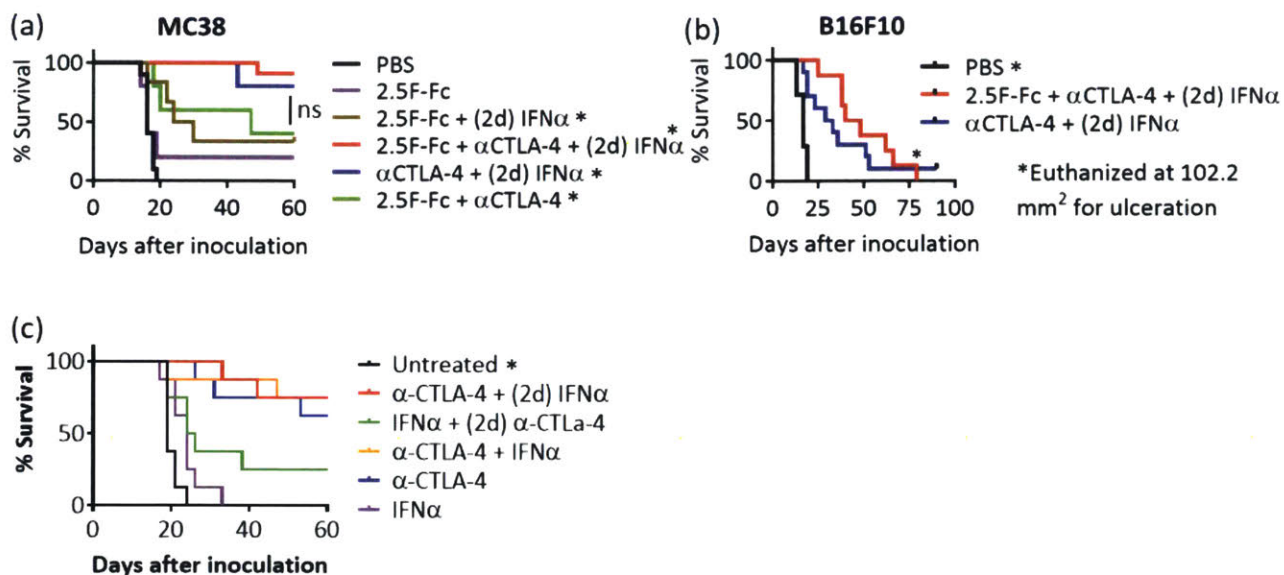


Figure 26: Ant-CTLA-4 alone drove strong therapeutic efficacy

(a) In the MC38 and (b) B16F10 tumor models, improved survival was driven by presence of anti-CTLA-4, independent of 2.5F-Fc. (c) Subsequent studies in the MC38 model showed that staggering IFN α did not matter for therapeutic efficacy. Note that for this study, any days in parentheses refer to days after 6, 12, or 18 along the 6 day treatment course. For example, the green group actually dosed IFN α days 6, 12, and 18 and anti-CTLA-4 on days 8, 14, and 20. * denotes statistical significance compared to PBS unless otherwise noted, or if the * is next to PBS or untreated mice then it is different from all other groups.

Because of the remarkably strong efficacy due to the anti-CTLA-4, IFN α , and 2.5F-Fc combination therapy, we sought to characterize the tumor infiltrating lymphocytes with and without anti-CTLA-4 at various time points after treatment. Anecdotally, we found that tumors often became puffy around days 2-5 after treatment initiation and then subsequently completely shrunk by day 6, so we were curious what sorts of changes occurred during that time range in the T cell compartment. Keeping the same sequencing in the treatment schedule of 2.5F-Fc and anti-CTLA-4, then IFN α staggered 2 days after, we examined mice at time points of 2, 4, and 6 days after initiating treatment with 2.5F-Fc and anti-CTLA-4 (day 0). Although the day 2 time point occurred when mice normally received IFN α , mice for the day 2 time point were euthanized prior to receiving IFN α therapy.

The first striking result from this study was that there was high density of CD8 T cells in the tumors between 4 and 6 days after treatment initiation (Figure 27 (a)). Remarkably, the high CD8 T cell density only occurred when anti-CTLA-4 was present in a triple combination, but was not seen in untreated mice or when the doublet of 2.5F-Fc and IFN α were given. To confirm the trend of a decrease of CD8 T cell density in the tumor over time, until between days 4 and 6 after anti-CTLA-4 treatment if that treatment were given, we repeated the days 4 and 6 time points in independent studies (Figure 27 (b-d)). Indeed, the same trends were seen in the tumor even without 2.5F-Fc, which confirms the survival curves showing that 2.5F-Fc wasn't necessary for efficacy. At the day 4 time point, the CD8 T cell density in the tumor is comparable to that of untreated mice, but by day 6, the density is in the 100s of cells per mg tumor. We next were curious whether this increase in density was due to infiltration of new CD8 T cells or due to

replication of intratumoral T cells present prior to treatment. To ask this question, we examined day 6 CD8 T cell density in the tumor when FTY720 was added to the combination of anti-CTLA-4 and staggered IFN α . FTY720, which is a sphingosine-1 phosphate (S1P) analog, agonizes and internalizes sphingosine-1 phosphate receptor 1 on T cells, which prevents them from sensing gradients of S1P necessary for T cell egress from the lymph nodes¹²⁵. Thus, in FTY720-treated mice, T cells cannot effectively traffic into tumors and the low density of CD8 T cells when FTY720 was added to therapy indicated that these T cells infiltrate into the tumor after therapy as opposed to pre-existing in the tumor and replicating in place (Figure 27 (d)). Treg quantification from the same FTY720 study in the mice not given FTY720 showed the drop in Treg frequency in the tumor typical of depleting anti-CTLA-4 antibodies like 9d9, dropping from around 40% Treg of CD4 T cells in untreated mice down to around 10% in mice given anti-CTLA-4.

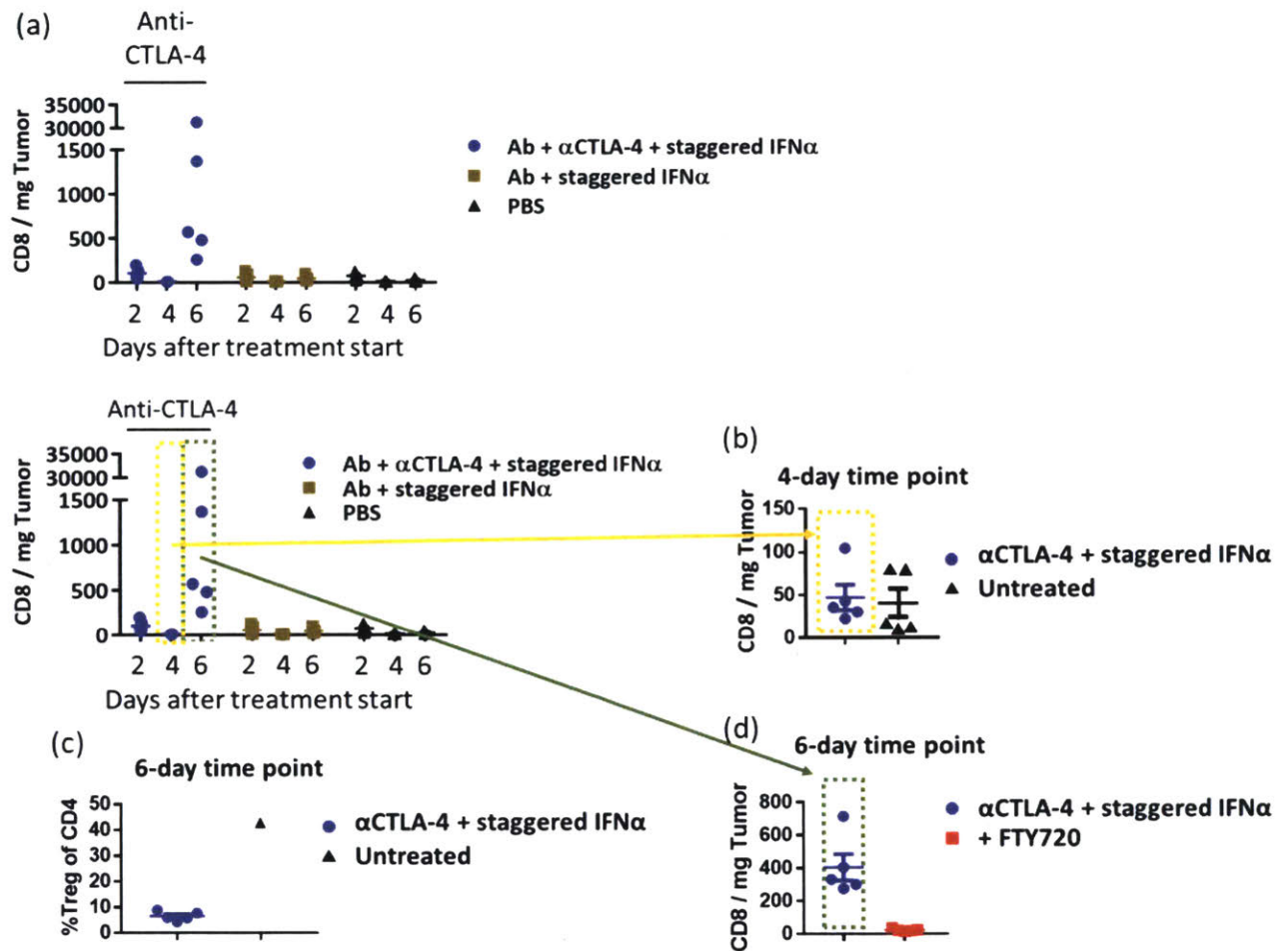


Figure 27: Timing of tumor infiltrating lymphocytes in CTLA-4 combinations

Mice with MC38 tumors were treated day 6 with the indicated treatment (IFN α was dosed day 8), then tumors were examined for lymphocyte infiltration on days 9, 11 ('4-day time point'), and 13 ('6-day time point'), which were 2, 4, and 6 days after the start of treatment. (a), (b), and (c-d) represent data from 3 independent studies. (c-d) FTY720 was dosed in addition to anti-CTLA-4 and IFN α (in some groups) at start of treatment and for the 6 days after treatment until the '6-day time point' relative to treatment

start. For all studies, tumors were excised, disaggregated manually and digested. Ab denotes 2.5F-Fc in this study.

Lastly, for the same treatment regime and time course study, we investigated when different subsets of T cells in various organs expressed CTLA-4. CTLA-4 is thought to be upregulated during antigen priming on CD8 T cells but constitutively expressed at higher levels on Tregs. Although CTLA-4 expression was very low using MFI as a proxy, the day 4 time point seemed to have a mild increased CTLA-4 expression in Tregs and CD8 T cells in the tumor draining lymph nodes and the spleen compared to days 2 or 6 (Figure 28). This increase occurred regardless of whether anti-CTLA-4 was added to the combination of 2.5F-Fc and IFN α , indicating that the day 4 increase in CTLA-4 expression is independent of efficacy. It is possible the day 4 increase in CTLA-4 expression is due primarily to T cell priming and activation, since IFN α was given 2 days prior.

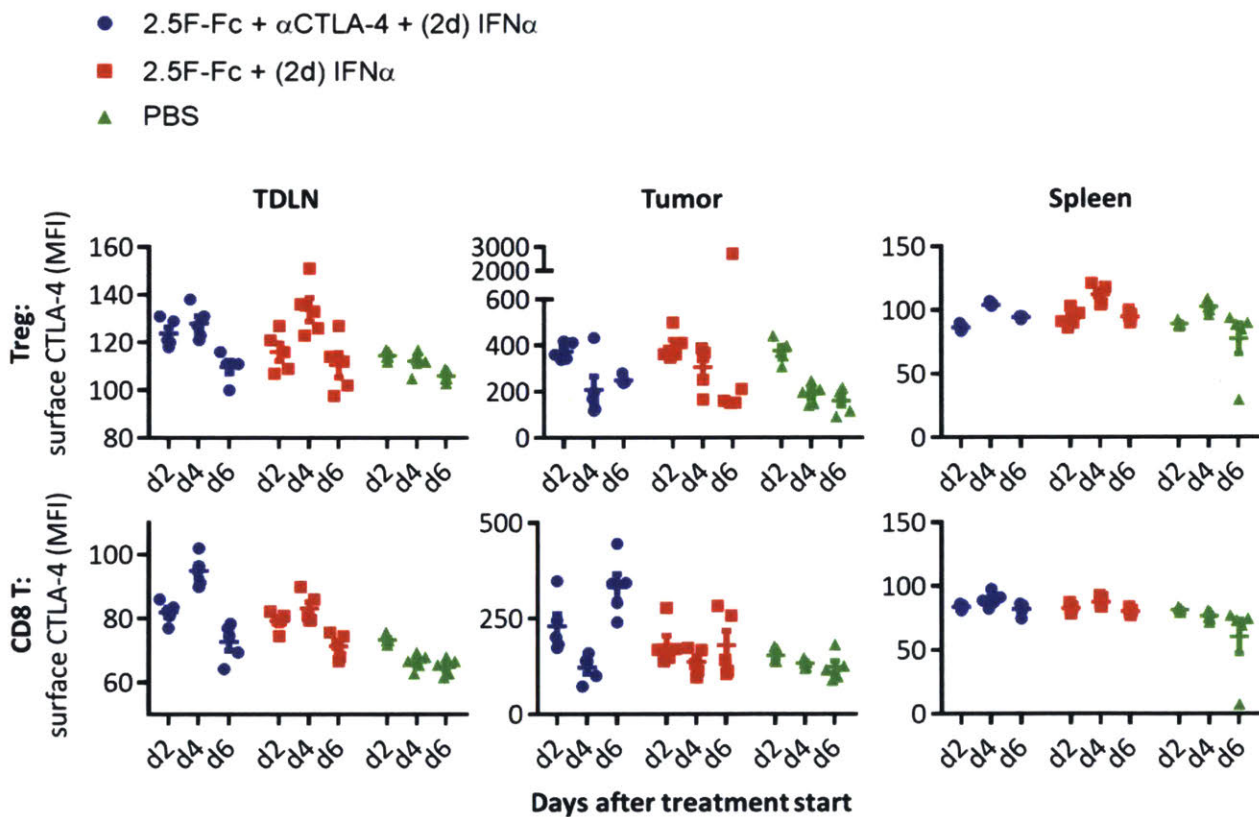


Figure 28: Temporal fluctuations in surface CTLA-4 expression

Surface CTLA-4 expression was characterized on regulatory T cells (Treg) and CD8 T cells in the tumor draining lymph nodes (TDLN), tumor, and spleen on 2, 4, and 6 days after treatment initiation. Treatment of 2.5F-Fc and anti-CTLA-4 occurred day 0 (which was 7 days after tumor inoculation) and IFN α day 2. For all studies, tumors were excised, disaggregated manually and digested.

Since the surface CTLA-4 MFI data indicated CTLA-4 upregulation during priming after IFN α treatment, and only treatment groups also with anti-CTLA-4 had strong T cell tumor infiltration and therapeutic efficacy, these results made us question whether anti-CTLA-4's main role was in enhancing priming of CD8 T cells or in depleting Tregs (which we also saw, although incompletely, looking at Treg density and Treg proportion of CD4 T cells in the tumor). Constitutive expression of CTLA-4 on Tregs in the tumor is thought to allow for CTLA-4-mediated Treg depletion, but it

was not clear whether depletion of Tregs is enough to allow for the strong infiltration of CD8 T cells that we saw in these studies. No tools currently exist in the native mouse immune system to deplete Tregs through CTLA-4 without affecting priming of CD8 T cells.

Because of the strong efficacy of anti-CTLA-4, and potentially decreased toxicity of staggering IL2 at or after IFN α , we initiated a tumor study in the genetic KP model. The KP model is a poorly immunogenic, conditional, genetic non-small cell lung cancer model with activation of K-ras through the G12D mutation as well as complete knockout of p53 tumor suppressor¹²⁶. This tumor model has never had significant cure rates, and is especially challenging because significant toxicity has developed in the past in response to 2.5F-Fc in combination with MSA-IL2. Our hope is that the reduced toxicity through optimal treatment schedules and lower dosing could allow for cures in this model. In order to use this tumor model with a vaccine and also provide antigen in this poorly immunogenic model, we added the CEA antigen into tumors.

We treated these KP-CEA tumor-bearing mice (mice had only KP background, not also CEA background) a total of 3 times starting week 8 after viral tumor induction, then did intracellular cytokine staining (ICS) at week 11 to look for CD8 T cell responses to the vaccine (Figure 29 (a)). Although we also did a couple rounds of CT scanning to try to identify the tumors, tumor ID was very challenging and an initial look at the data suggested no differences between treated and untreated mice. Additionally, CT scanning required leaving the mice under isoflurane for over 10 minutes, and the mice were very weak from treatment toxicity, so we did not continue with CT because the gained information was minimal compared with the risk of mice weakening from isoflurane.

The survival curves show no therapeutic efficacy for this 5-component treatment since the curves overlapped for untreated and treated mice (Figure 29 (b)). Unfortunately, only 6 mice were included in the survival curve in the treated group because 8 of the original 14 mice in the treated group actually died from treatment related toxicity during the 3rd round of treatment (Tx3). While it's possible the 8 mice who died from treatment-related toxicity would have had a stronger therapeutic response, we can only hypothesize about that. After overnight 200ug/mL MSA-CEA stimulation of blood samples, ICS showed antigen specific CD8 T cells of about 1.5-2% expressing IFN γ , with no noticeable TNF α expression above background (Figure 29 (c)). Although this IFN γ expression alone was not remarkably high for a vaccine regimen that can have numbers closer to 5-10%, we also used the ICS data to try to draw correlations with toxicity by using weight loss 4 and 9 days after Tx2 as a proxy (blood for ICS was taken 7 days after Tx2). The correlation of weight change with %CD8 T cells out of all live blood cells was negative, with R² values between 0.3-0.5, indicating that mice with more CD8 T cells in their blood tended to lose more weight (Figure 29 (d)). The correlation of weight change with % IFN γ positive CD8 T cells was positive, but the R² values were all less than 0.1, indicating a very weak to no correlation and it also really does not make biological sense why % IFN γ + CD8 T cells in the blood would increase for mice gaining weight (Figure 29 (e)).

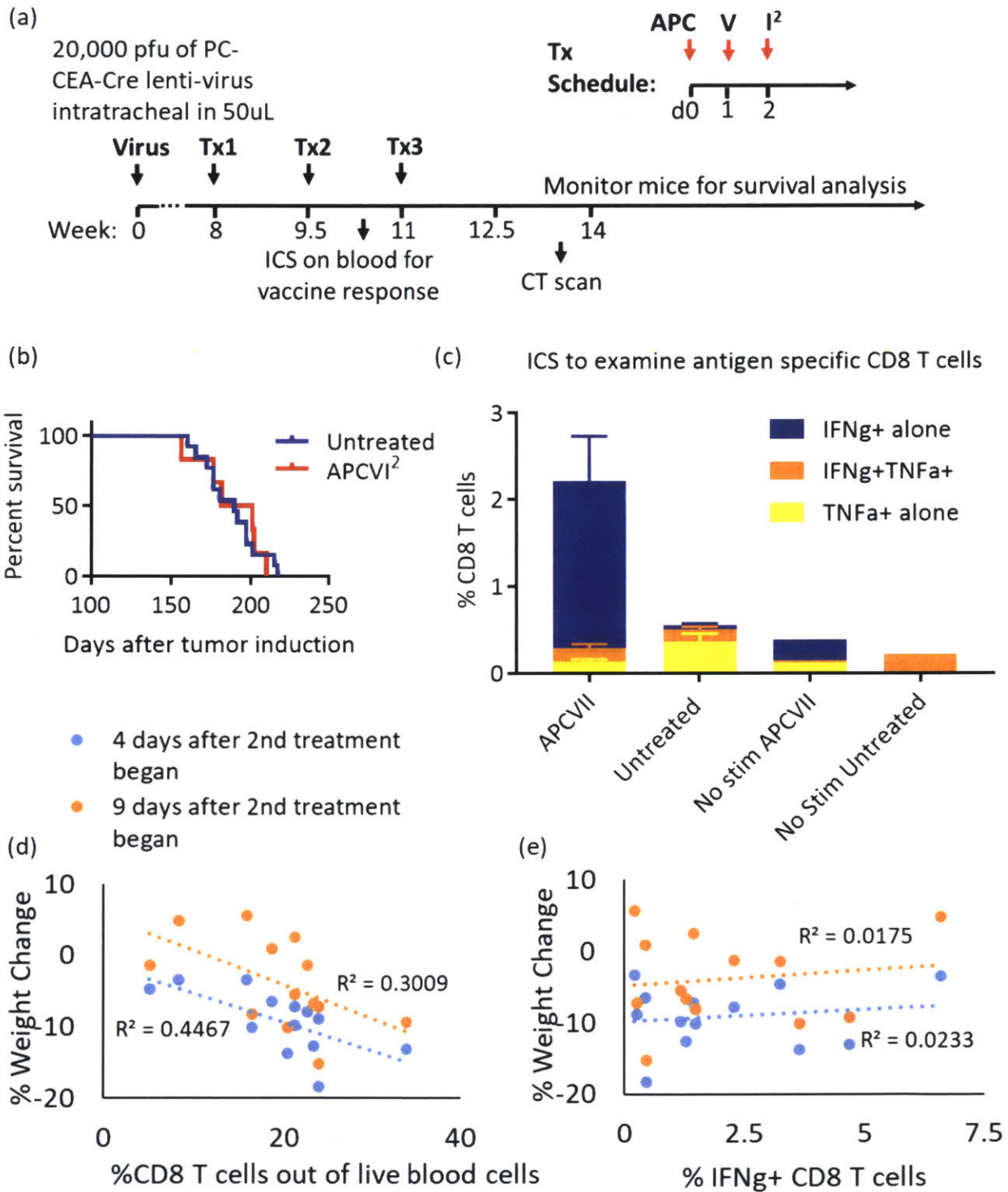


Figure 29: Using anti-CTLA-4 in 5-agent combination therapy in the KP genetic lung tumor model
 (a) Experimental outline showing induction of tumors at week 0, then 3 total treatments starting week 8. A, 2.5F-Fc 500ug IP; P, anti-PD-1 200ug IP; C, anti-CTLA-4 200ug IP; V, 20ug CEA epitope equivalent MSA-CEA + 25ug CDNs, SC half on each tail base side; I², MSA-IL2 30ug IP + IFN α 50ug RO. (b) Survival curve for 6/14 original treated mice that did not succumb to treatment related toxicity, and 13/13 untreated mice.

Mice were checked every day, and were euthanized when body condition became low due to labored breathing or gasping, to the point of hunching or impairing movement. (c) Intracellular cytokine staining showing antigen specific CD8 T cells in the blood 1 week after Tx2. (d-e) Correlation plots of % weight change with blood CD8 T cell numbers and characteristics from the ICS to understand potential sources of toxicity and weight loss.

Since the 5-part combination therapy APCVI² did not show therapeutic efficacy in this KP-CEA lung tumor model, we did not move forward to test this combination therapy in a truly antigen independent KP tumor model without CEA.

3.3 Discussion

Combination cancer immunotherapies hold promise for improving clinical response rates, but strategies to mitigate the associated auto-immune toxicities are needed. Our work used the cytokines IFN α and IL2 in syngeneic mouse tumor models to demonstrate that therapeutic efficacy and toxicity may sometimes be decoupled by alterations in the treatment schedule. Although translation of the exact murine time scales into the clinic would be challenging, several lessons can be learned from this work.

The common clinical practice in combination therapy of using the treatment schedule of each individual agent until toxicity ends treatment should be considered carefully in the context of temporally designed treatment schedules. For example, a short burst of IFN α after a tumor targeting antibody is significantly more efficacious than starting to dose IFN α earlier because it allows DCs to take up antigen before maturation by IFN α .³⁰ Clinically, IFN α is infused daily or even PEGylated to increase exposure time,¹²⁷ but in vitro studies looking at DCs' ability to activate CD4 T cells indicate that shorter bursts of DC activation induce a type 1 T cell helper phenotype much more effectively than longer chronic exposure.¹²⁸ In a clinical trial of advanced metastatic melanoma, testing chemotherapy and IFN α with or without the addition of IL2 resulted in no clinical improvement from IL2.⁴¹ Although the results presented in the current work suggest that the order of IFN α before IL2 in the clinical trial would minimize toxicity of these two agents in combination, the lengthy, high-dose of IFN α and failure to stagger IFN α after the chemotherapy could be responsible for the lack of therapeutic synergy of these cytokines. Emerging evidence suggesting that the STING pathway is critical to the success of therapies like checkpoint blockade¹²⁹ and radiation¹³⁰ underscores the importance of lessons about IFN α timing. Although local administration of STING agonists can circumvent toxicity,¹³¹ carefully choosing the timing of combination therapy partners to avoid pre-activation of NK cells is critical, given the toxic strength of their IFN α response when pre-activated by IL2. Agents intended to support T cell expansion and function, such as IL2, may be safest and most efficacious after IFN α administration, whereas delivery of antigen-generating agents like tumor targeting antibodies, chemotherapy, or radiation will be important before IFN α and DC maturation.

Generating a milder burst of initial innate activation using tumor targeting antibodies without initial IL2 may avoid early systemic toxicity, while being sufficient to release tumor debris to be presented to the adaptive immune system. This manuscript demonstrates that cytokines like IL10 and IFN γ contribute to the early systemic toxicity of staggered eIL2 and IFN α therapy. Additional

cytokine depletions of IL5 and IL6, while not statistically significant compared to their control group in Figure 20 (b), may still have some contribution toward weight loss. Although cytokines like IL2¹³² and IFNs¹³³ activate NK cells and these cells can exhibit potent anti-tumor activity,¹³⁴ other innate cell types are capable of initiating more mild inflammation in response to tumor targeting antibodies. Macrophages are capable of antibody mediated attack of tumor cells and subsequent antibody-enhanced DC uptake of tumor antigens can initiate a productive adaptive response.¹³⁵ Antibodies can also engage with eosinophils to generate respiratory burst in response to tumor cells as well as utilize neutrophils or the complement system to attack cancer.⁶⁷ Indeed, the same tumor targeting antibody used in this work, TA99, induced respiratory burst in B16F10 tumors within the first few days after treatment as quantified by a luminol assay in previous work⁶⁷. With initial antibody-driven innate inflammation, IL2 could be given as late as 3 days after tumor targeting antibody in this work and maintain the same efficacy. The toxicities of IL2 are well documented,¹³⁶ so delaying IL2 to avoid excessive, toxic antagonism of innate inflammation from a different combination therapy agent like tumor targeting antibodies, radiation, or chemotherapy would be ideal. In addition to contributing to toxicity, prematurely dosing IL2 prior to T cell priming could preferentially activate Tregs because of constitutive CD25 expression^{137,138} and may also induce anergy in helper T cells.¹³⁹ Although IL2 has traditionally been characterized as an important NK cell stimulator,¹³² IL2's most important role in cancer immunotherapy may be in driving adaptive instead of innate inflammation. Clinical analysis of IL2 immunotherapy responses to melanoma and renal cancer have shown durable responses indicative of adaptive immunity¹⁴⁰ and IL2 is commonly used to enhance T cell proliferation and survival in adoptive cell therapies.^{7,141} NK cells and IL2 may be superfluous to the initial innate melee caused by a tumor-targeting antibody as long as adaptive immunity can be expanded at a later time by IL2 treatment.

This work illustrates that an MTD-focused chronic treatment paradigm should be reconsidered to balance toxicity and efficacy. Although IL2 has traditionally been characterized as an important NK cell stimulator,¹³² IL2's most important role in cancer immunotherapy might instead be to drive adaptive immunity later in the treatment cycle after mild innate inflammation is initiated by other agents. Re-design of treatment schedules with careful attention to order and timing may decouple efficacy and toxicity, opening the therapeutic window of previously discarded cytokine-based therapeutic combinations like IL2 and IFN α .

3.4 Materials and methods

Mice

Female C57BL/6 (Taconic), C3H (Taconic), and Balb/c mice (Jackson) were used at 6-10 weeks of age. Mice were housed in pathogen free environments. All procedures were approved by the MIT Division of Comparative Medicine (DCM) and consistent with federal, state, and local regulations using animal protocol number 0515-043-18 under MIT's Institutional Animal Care and Use Committee.

Cell lines and media

B16F10 cells were maintained in Dulbecco's Modified Eagle's Medium (DMEM) with 10% FBS and Penicillin-Streptomycin and MC38 cells were maintained in DMEM with 10% FBS.

Tumor treatment experiments

For experiments with B16F10 and MC38 tumors, mice were inoculated subcutaneously in the right flank with 10^6 cells. The following agents were administered through intraperitoneal (IP) injection at the following days after tumor inoculation unless otherwise noted: 100 μg TA99 (B16F10 tumors, days 7 and 13), 500 μg 2.5F-Fc⁶⁶ (MC38 tumors, days 7 and 13), 30 μg eIL2 (days 7 and 13 or 8 and 14), and 10 μg IFN α (days 8 and 14). Tumor areas were calculated as the product of the two perpendicular tumor diameters and mice were euthanized when tumor area exceeded 100 mm². The few mice that died from reasons other than tumor area (low body condition due to ulceration or weight loss exceeding 20%) are noted in figure legends and are not included in the survival study analysis or plots.

For tumor rechallenge studies, age-matched naïve mice and cured mice pooled from B16F10 tumor studies treated with TA99, eIL2, and IFN α were rechallenged with 10^5 B16F10 cells on the left flank at least 100 days after cessation of the original treatment. Rechallenged mice were not included in this study if they had any type of depletion during original treatment.

As opposed to more invasive assessments of toxicity, weight loss is our primary metric for toxicity in tumor studies. It can be regularly quantified over time without weakening a mouse to take serum or sacrificing the mouse to look in the organs. Weight loss is generally acceptable as a metric of mouse body condition and has been used to monitor immunotherapy toxicity in mice¹⁴² and cynomolgus macaques.¹⁴³

Depletion and neutralization studies

All depleting or neutralizing antibody injections were purchased from Bio X Cell and injected IP unless otherwise noted. Anti-IL5 (TRFK5) was given at 1mg per dose 1 day before each round of treatment began. Anti-IL6 (MP5-20F3) was given at 400 μg per dose every 2 days starting 1 day before treatment began. Anti-IL10 (JES5-2A5) was given at 500 μg per dose every 3 days starting 1 day before treatment began. Antibodies to neutralize IFN γ (XMG1.2) or TNF α (XT3.11) were given at 600 μg per dose every 2 days starting 1 day before treatment began. Anti-NK1.1 (PK136) was given at 400 μg per dose every 4 days starting 2 days before treatment began for a total of 4 doses during survival studies. Anti-Asialo-GM1 (Poly21460, Biolegend) was given at 50 μg per dose every 4 days starting 2 days before treatment began. Schedules and dosing for depletions or neutralization were chosen to be at least as frequent and as high of doses as previous work.^{30,32,144,145} Although we recognize that verifying NK cell depletion is problematic when done with the same clone, other strong antibody clones used to stain for NK1.1 do not exist and so prior work has demonstrated depletion by staining with the same clone.³²

For the supplemental depletion and neutralization study, depletions not already described were done by giving anti-NK1.1, anti-Ly6G (1A8), anti-CD8 α (2.43), anti-CD4 (GK1.5), or anti-CD19

(1D3) at 600 µg per dose every 3 days starting 2 days before treatment began. Anti-CSF1R (AFS98) antibody was given at 600 µg per dose every 2 days starting 2 days before treatment began.

Protein production and purification

All therapeutic proteins were made in house. TA99 (mouse IgG2c heavy chain and kappa light chain) was purified from a stably transfected HEK293 F cell line grown in FreeStyle 293 media (Life Technologies). 2.5F-Fc (mouse IgG2c heavy chain) and eIL2 (a fusion of mouse serum albumin and IL2 (MSA-IL2))⁶⁷ were purified 6-8 days after transfecting gWiz plasmids into HEK293 cells using polyethylenimine in FreeStyle supplemented with OptiPro (Life Technologies). For TA99 and 2.5F-Fc, supernatant from centrifuged HEK293 cells was purified through rProtein A Sepharose Fast Flow resin according to manufacturer's instructions (GE Healthcare). MSA-IL2 was purified from HEK293 cell supernatant using TALON[®] Metal Affinity Resin according to manufacturer's instructions (Clontech) and subsequent gel chromatography on a HILOAD 16/600 Superdex 200 PG column on an AKTApurifier 10 fast protein liquid chromatography machine (GE Healthcare). IFN α was produced in Rosetta-gami 2 (DE3) competent E. coli (EMD Millipore) as previously described.³⁰ All proteins were tested to be below 0.1 EU/ dose by the QCL-1000 chromogenic LAL assay (Lonza) and run on reducing and non-reducing SDS PAGE 4-12% Bis-Tris gels (Life Technologies) to confirm size. Fc-IL2 fusion protein used as eIL2 for the supplemental depletion and neutralization study was made by transfecting HEK293 cells and purified in two steps using TALON resin and anti-FLAG M2 Affinity Gel (Sigma-Aldrich) as previously described.
67

Flow cytometry

For analysis of NK cell activation, mouse spleens were collected with no treatment or 1 day after treatment with TA99 and eIL2 or TA99 alone. After dissociation through a 70µm filter and ACK lysis, single cell suspensions were stained and run on a LSRFortessa flow cytometer (BD Biosciences) at the Koch Institute Swanson Biotechnology Center Flow Cytometry Core Facility. eBioscience™ Fixable Viability Dye eFluor™ 780 (Thermo Fisher Scientific) and TruStain fcX (Biolegend) were used for viability and Fc block prior to antibody staining. Antibodies against CD3 (145-2C11), NK1.1 (PK136), B220 (RA3-6B2), CD11c (N418), CD43 (1B11), CD44 (IM7), CD69 (H1.2F3), and IFNAR-1 (MAR1-5A3) were purchased from Biolegend. Antibodies against STAT1 (Clone 1/Stat1) and STAT3 (232209) were purchased from BD Biosciences and Thermo Fisher Scientific, respectively. For intracellular staining of STAT proteins, the cells were first fixed and permeabilized using the BD Biosciences Cytotfix/Cytoperm kit according to manufacturer instructions. For the gating strategy, NK cells were gated first for single cells and viability, then on CD3 low and NK1.1 high, before plotting the resulting NK cell population median fluorescence intensity.

Systemic cytokine and chemokine levels

Blood was collected from three B16F10 tumor-bearing mice per treatment group into BD Microtainer Clot Activator/ SST Gel tubes at time points 3, 24, 27, 51, and 75 hours after injection of TA99. The second and third time points are before and 3 hours after injection of IFN α . eIL2

was injected either concurrently with TA99 or concurrently with IFN α . Serum was collected after blood centrifugation, diluted 1:2 with PBS, and flash frozen. Luminex multiplex assays were completed by Eve Technologies using the Mouse Cytokine Array / Chemokine Array 31-Plex panel. IL2 was excluded from the analysis because IL2 was injected systemically so it would not be indicative of a toxic response.

All data were analyzed using Microsoft Excel or Matlab (Mathworks). To analyze the data from the multiplex assay, AUCs of concentration versus time were calculated for each cytokine/chemokine across the different treatment conditions for all time points. The ratios of these AUCs for each cytokine/chemokine were plotted for TA99 and 1-day staggered IFN α comparing eIL2 given with TA99 versus given with IFN α .

PLSR analysis with 3 components and 7-fold cross validation was also done to assess which chemokine and cytokine AUCs best explained the weight loss for each mouse. The AUCs using only the time points 3 hours after IFN α up to 2 days after IFN α were used for best explanation of the weight loss, quantified as change from treatment start to 2 days after IFN α . AUCs and weight losses were z-scored prior to the PLSR. The first two components explained 52% and 19% of the variation in weight change, so plots shown were composed of loadings and scores for just the first two components.

Organ and blood toxicity

Mice were euthanized at indicated time points after first treatment with TA99 and whole blood samples or serum from non-tumor-bearing C57BL/6 mice were submitted at to the diagnostics facility at the MIT DCM. This facility performed automated CBC analysis and sent frozen serum samples to be screened on a Chem 11 panel by IDEXX Laboratories. Organs were also taken at the same time points for histology by the Histology Core Facility at the Koch Institute's Swanson Biotechnology Center. Kidneys, spleen, and liver were fixed in 10% neutral buffered formalin before being transferred to 70% ethanol for preservation prior to sectioning and H&E staining. During necropsy, lungs were first inflated with 10% neutral buffered formalin through intratracheal injection prior to excision, fixation, sectioning, and staining. Each organ was assessed for level of inflammatory infiltrates by pathologist Dr. Roderick Bronson at the Histology Core.

Statistical analysis

All statistical analysis was done using Graphpad Prism statistical software. Kaplan Meyer tumor survival curves were compared using a Log-rank (Mantel-Cox) test. Comparison between the toxic and each other treatment group in weight loss plots was done using one-way ANOVA with Dunnett's multiple comparisons test. Flow cytometry plots compared all groups with each other through one-way ANOVA with Tukey's multiple comparisons test. AUC ratios were assessed for significance using a two-way ANOVA with Bonferroni's multiple comparisons test. Organ toxicity study results were examined using one t test per time point for each metric, then correcting for multiple comparisons using the Holm-Sidak method with an alpha of 0.05. All * indicates $p < 0.05$ for the statistical test and all error bars are +/- SEM.

ICS on KP mice

100uL of blood was drawn and after 2 rounds of ACK red blood cell lysis, the blood was split into two identical wells (one stimulated, one unstimulated). After overnight incubation with 200ug/mL of MSA-CEA in RPMI, Brefeldin A was added to a concentration of 5ug/mL for the final 4.5 hours of incubation prior to flow staining.

3.5 Supplemental figures

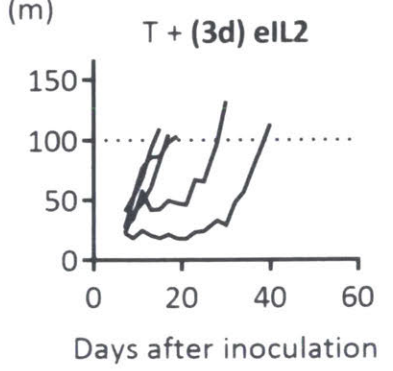
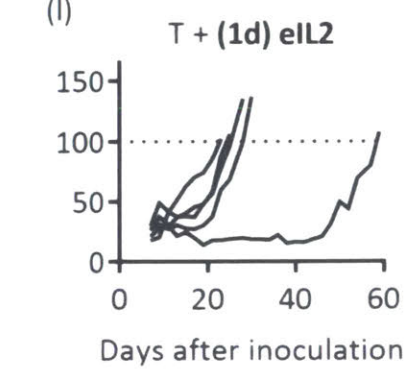
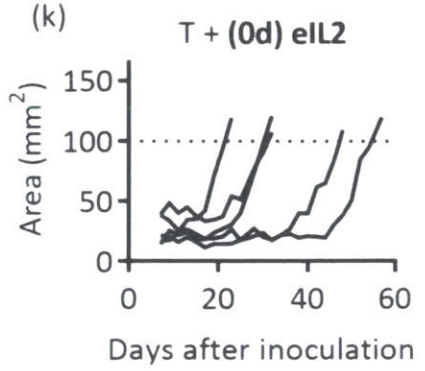
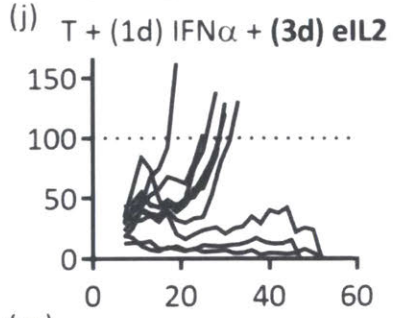
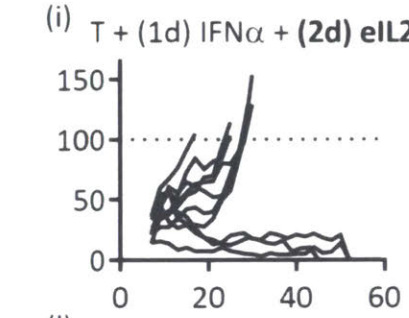
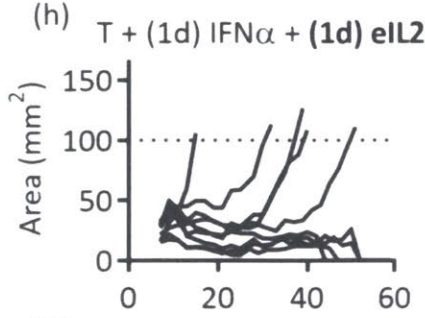
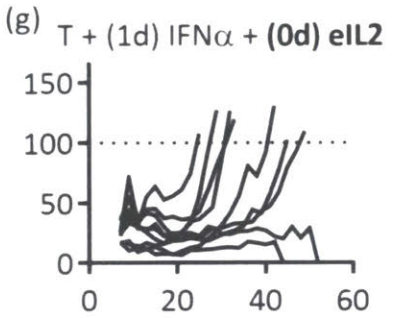
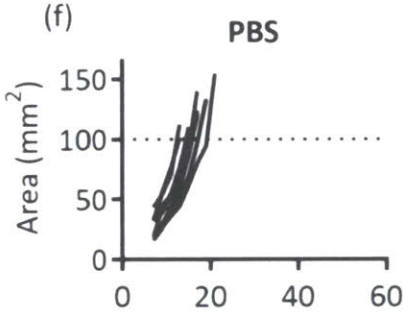
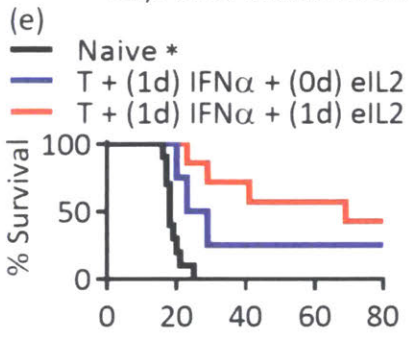
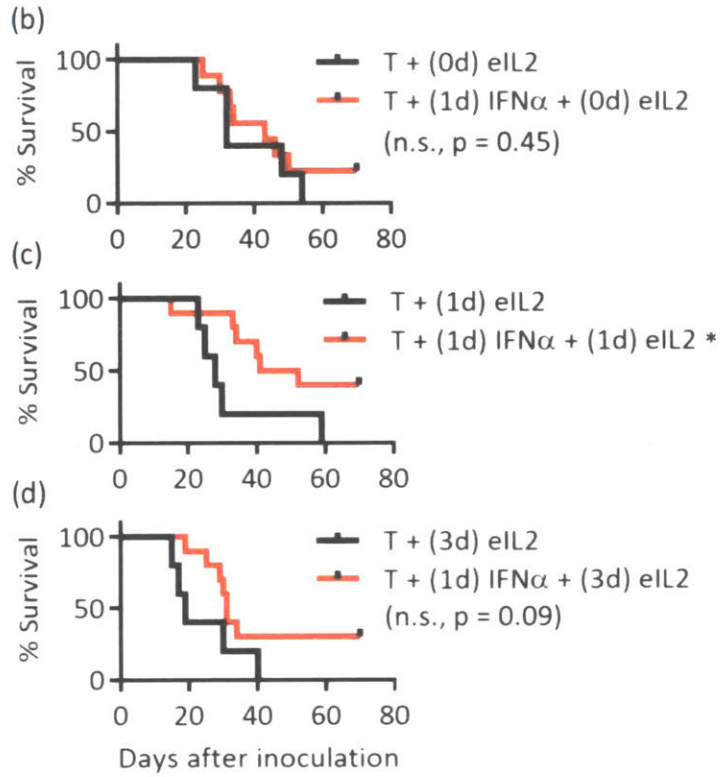
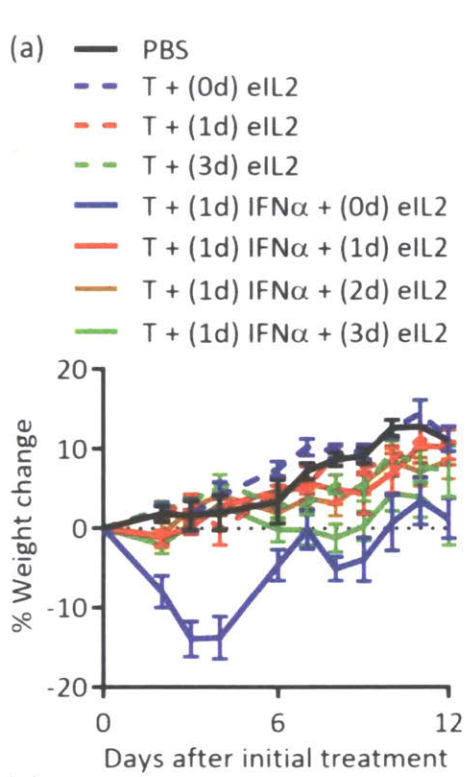


Figure 30: Tumor and full weight loss curves for eIL2 before and after IFN α

(a) Full weight loss time course curves are shown over the course of two treatment cycles with and without IFN α for the B16F10 tumor study in Figure 19. The days count from 0 after first TA99 administration. (b-d) Survival from the Figure 19 B16F10 tumor study was compared with and without IFN α . (e) Pooled, surviving mice from B16F10 tumor studies using TA99, eIL2, and IFN α were rechallenged with B16F10 tumors and survival is compared with age-matched, naïve mice. (f-m) Individual area curves are shown for the two treatment cycles with and without IFN α for the B16F10 tumor study in Figure 19. Mice euthanized for poor body condition due to ulceration (1 mouse) or weight loss exceeding 20% (1 mouse) were excluded from the area and survival analysis. PBS-treated mice and all groups with IFN α are from 2 independent experiments totaling 9-10 mice per group each. Treatment groups without IFN α are from 1 experiment totaling 5 mice per group. * indicates $p < 0.05$ and error bars are +/- SEM.

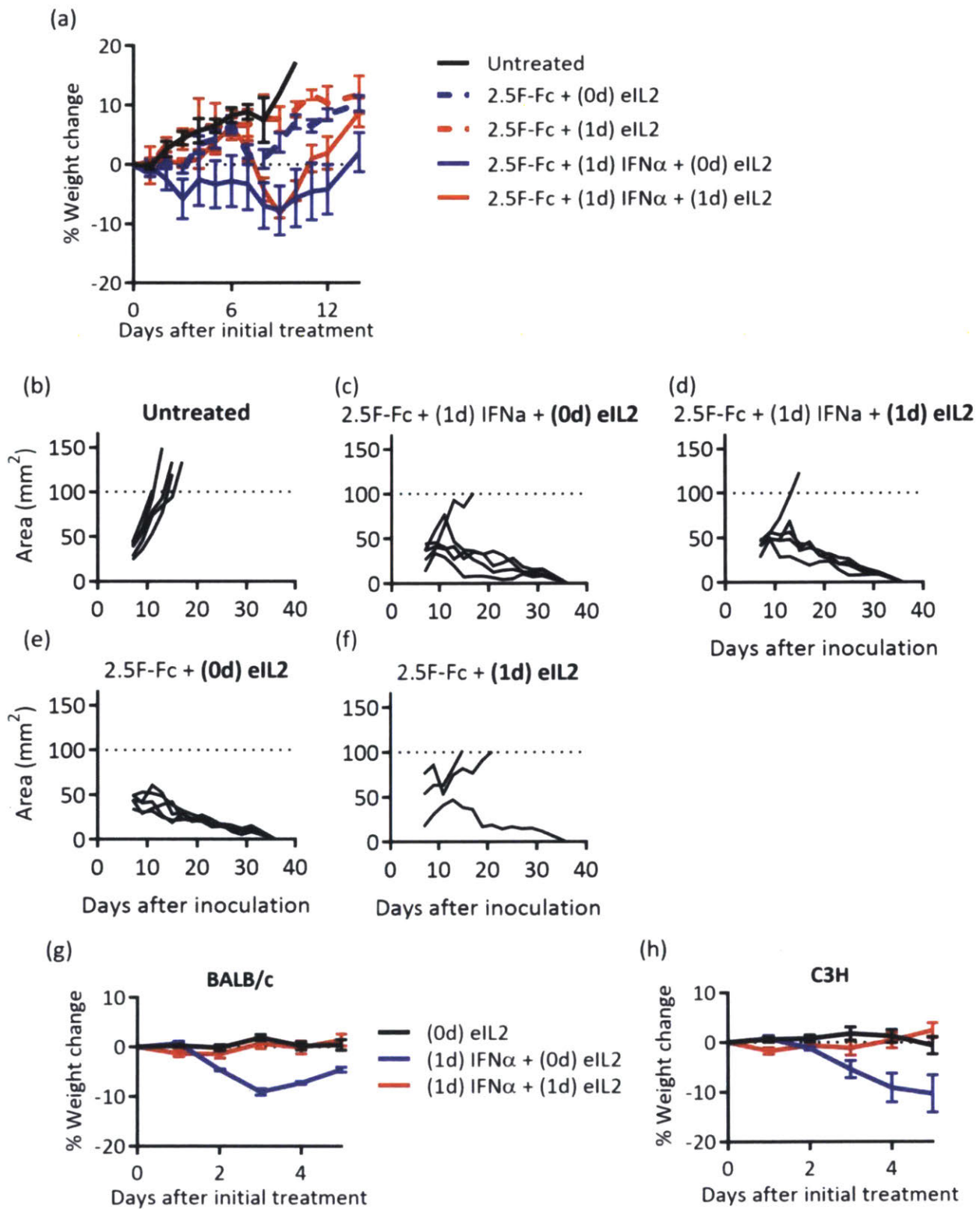


Figure 31: Weight loss time courses and tumor curves for 2.5F-Fc studies and BALB/c, C3H mice
 (a) Full weight loss time course and (b-f) tumor area curves for each treatment condition are shown for the MC38 tumor study in Figure 19. In (a), the days count from 0 after first 2.5F-Fc administration. Data

are from 1 independent experiment with 5 mice per group except the 2.5F-Fc + (1d) eIL2 group, which has 3 mice. (g-h) The full weight loss time course is also shown for the non-tumor-bearing BALB/c and C3H mice in Figure 19. The days count from 0 after the (0d) eIL2 administrations. Data are from 1 independent experiment with 5 mice per group. Error bars are +/- SEM.

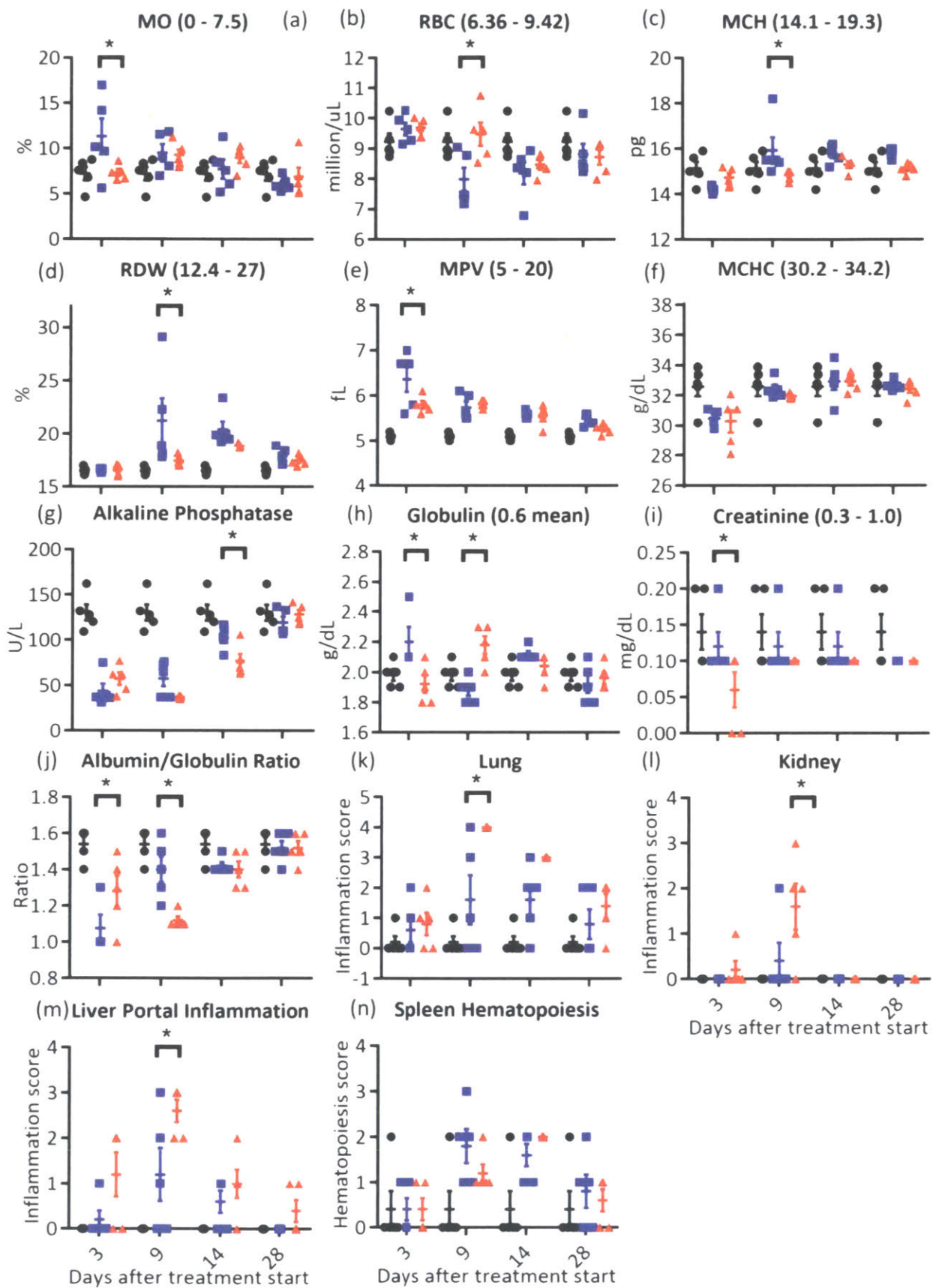


Figure 32: Bloodwork and organ toxicity

(a-f) CBC results are included for the 5 metrics that had a statistically significant difference between TA99 plus staggered eIL2 and IFN α (blue) compared to TA99 plus concurrent (red) for at least one time point (black dots are PBS-treated mice) MO = monocytes as a percent of white blood cells, RBC = red blood cell, MCH = mean corpuscular hemoglobin, RDW = red cell distribution width, MPV = mean platelet volume, MCHC = mean corpuscular hemoglobin concentration. (g-j) Serum protein and enzyme levels were plotted. (k-n) Lung, kidney, liver, and spleen histology inflammatory infiltrate numbers were plotted. Inflammation score was assessed by a pathologist blinded to treatment condition. The days count from 0 after first TA99 administration. Data are from 1 independent experiment totaling 5 mice per treatment group at each time point in non-tumor-bearing mice. * indicates $p < 0.05$ and error bars are \pm SEM.

- 21, 22, 23: TA99 + (1d) IFN α + eIL2
- 31, 32, 33: TA99 + (1d) IFN α + (1d) eIL2
- 41, 42, 43: TA99 + (1d) IFN α
- 51, 52, 53: TA99 + eIL2
- 61, 62, 63: TA99 + (1d) eIL2
- 71, 72, 73: Anti-NK1.1 + TA99 + (1d) IFN α + eIL2
- 81, 82, 83: Anti-NK1.1 + TA99 + (1d) IFN α + (1d) eIL2

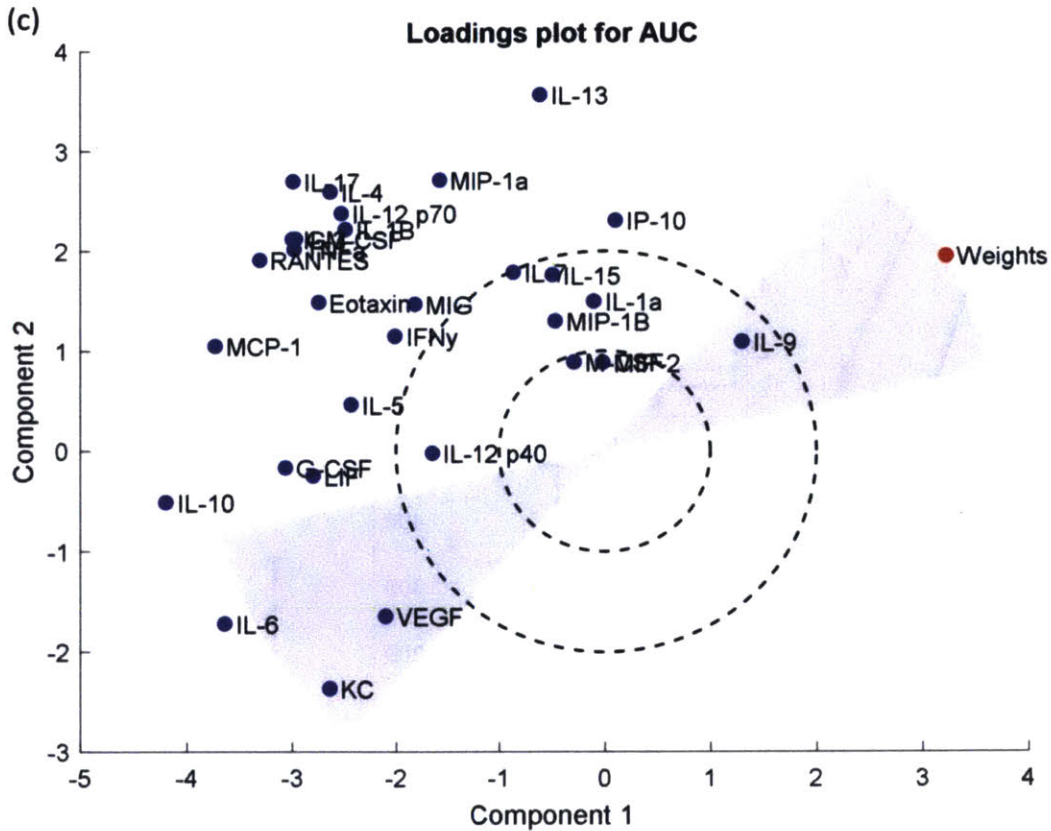
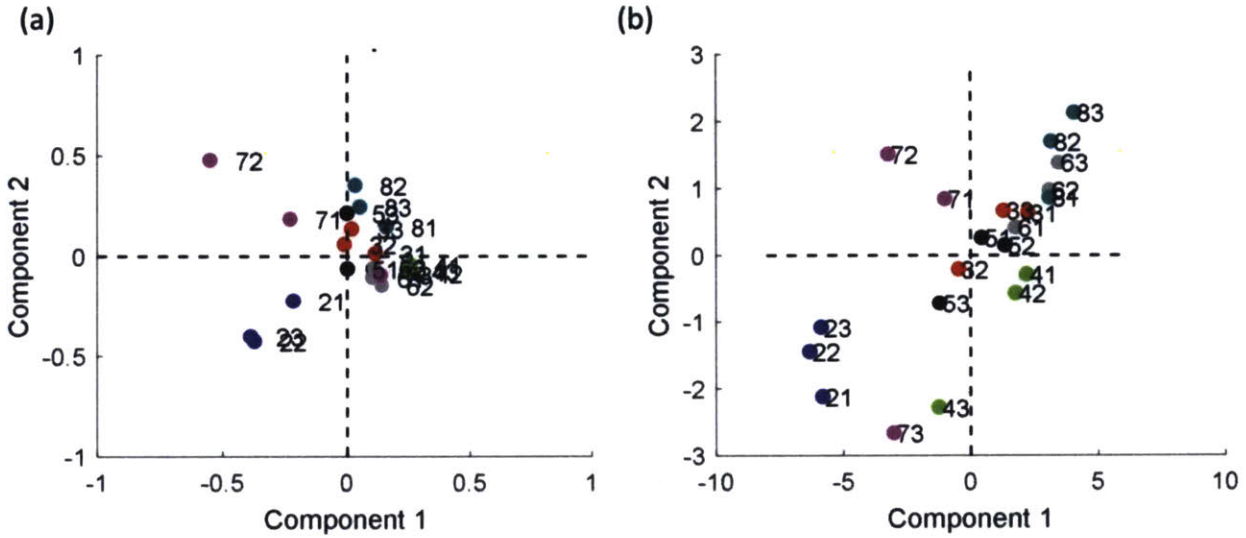
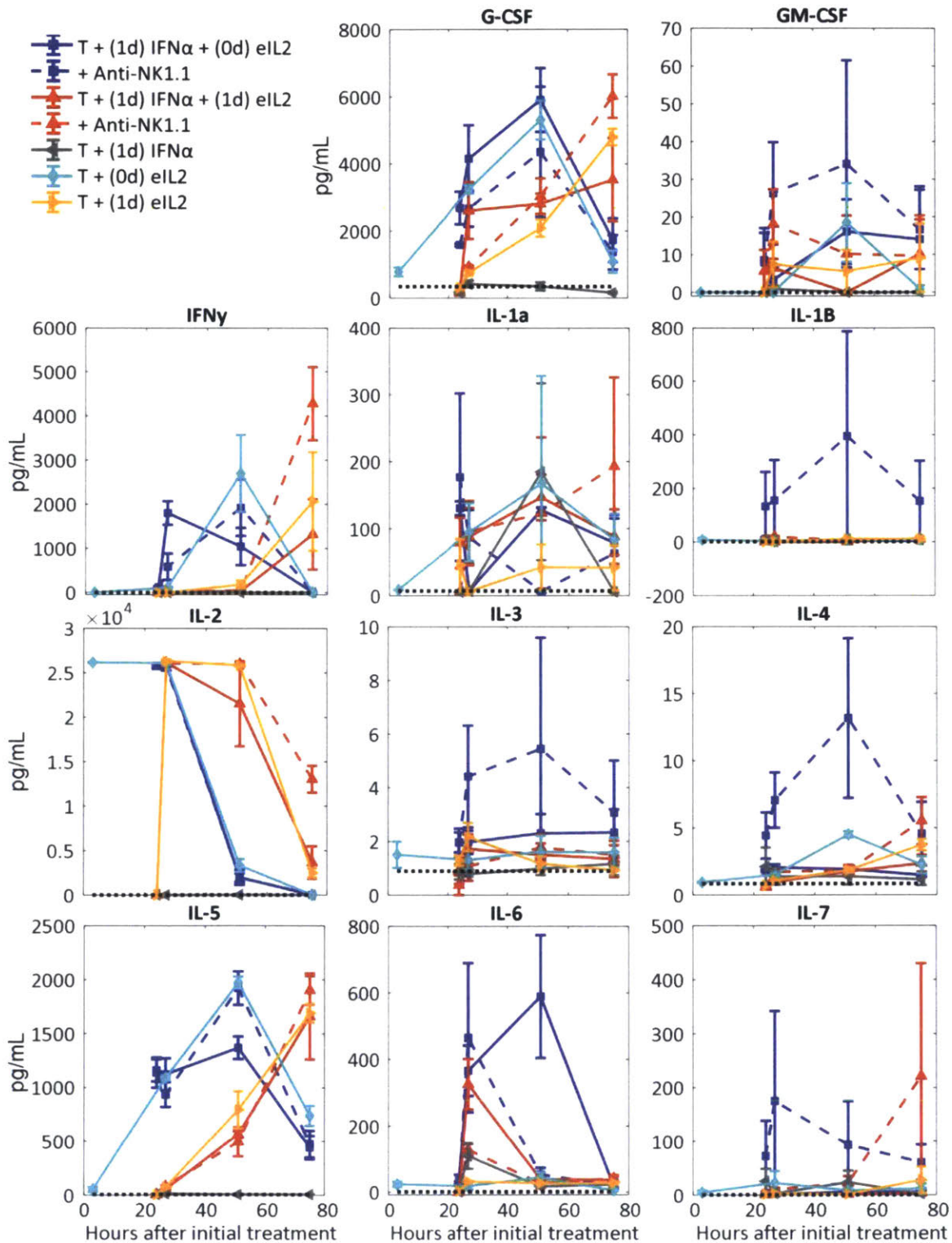
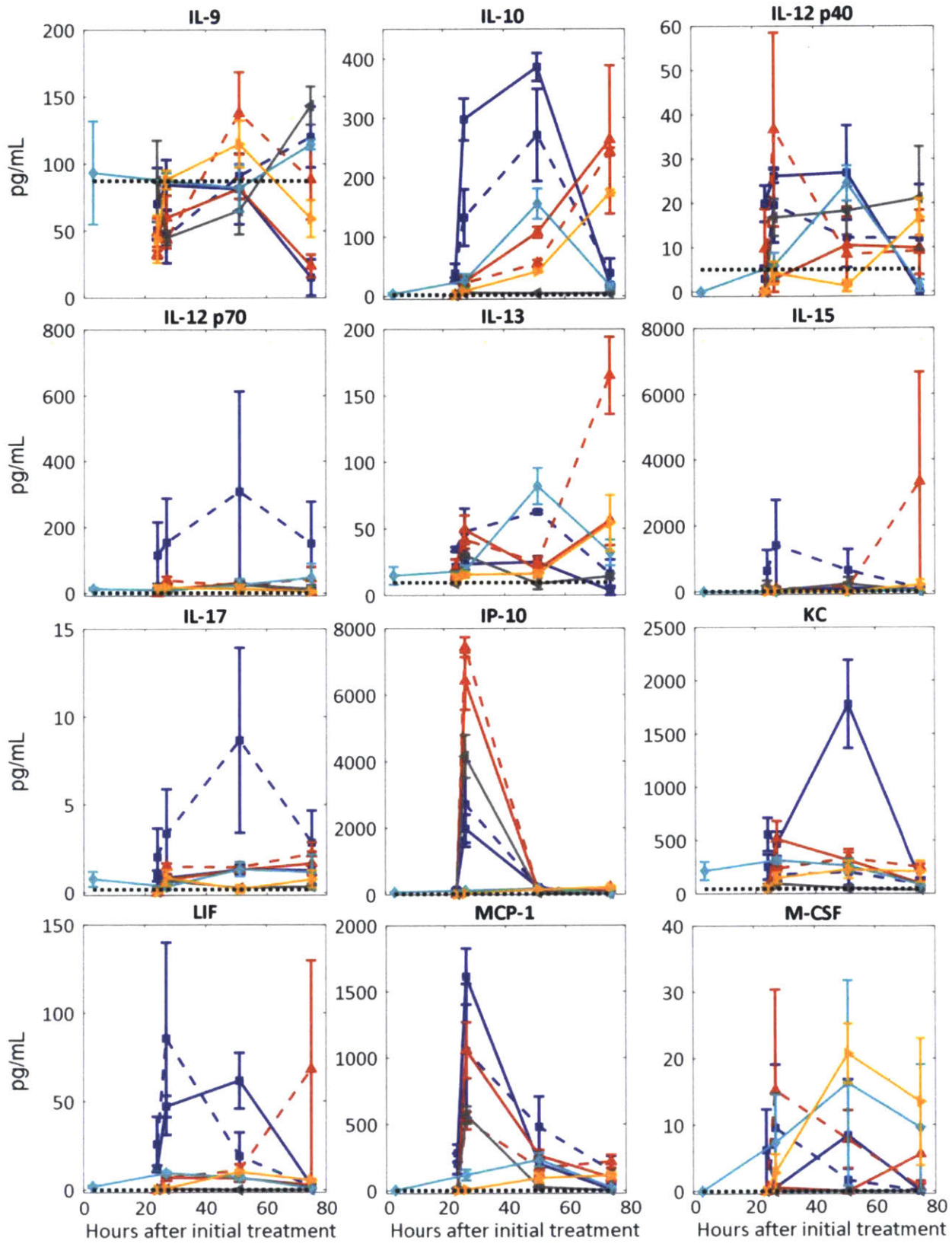


Figure 33: PLSR analysis on luminex time course data

PLSR (a) variable and (b) response (percent weight change) scores for each individual mouse as well as (c) loadings were plotted. These plots were generated by using z-scored weights and z-scored AUCs (using 3 hrs after IFN to 51 hours IFN time points). Data are from the same experiment as Figure 20 (a) in B16F10 tumor-bearing mice.





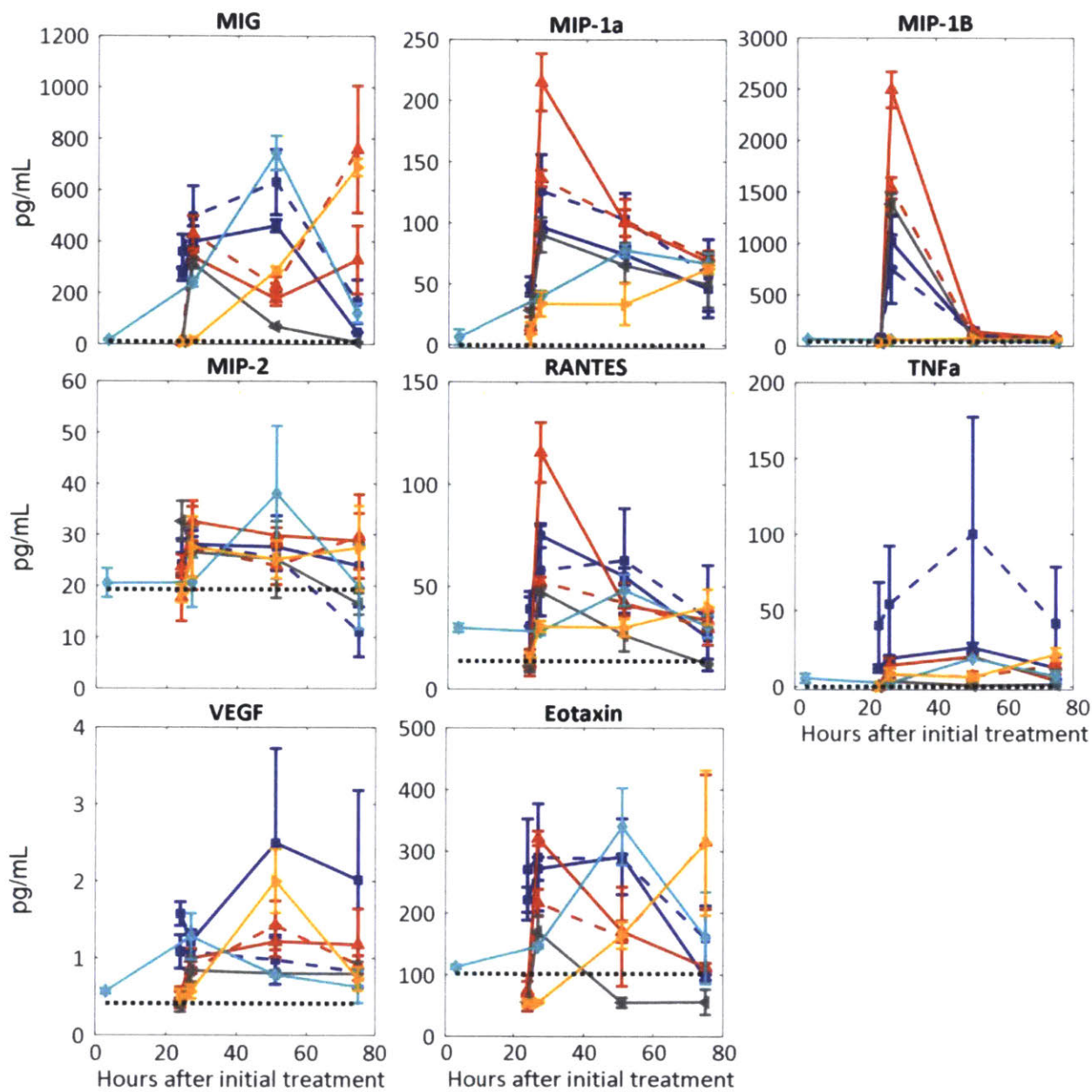


Figure 34: Full time course of each cytokine or chemokine in luminex assay for every treatment condition. Time course curves are shown for the AUC analysis in Figure 20 (a) for every cytokine and chemokine and for every treatment condition included in the PLSR analysis. The dotted line shown is the average level of 3 untreated mice at the beginning of the study. The hours count from 0 after first TA99 administration (initial treatment day). Data are from the same experiment as Figure 20 (a) in B16F10 tumor-bearing mice. Error bars are +/- SEM.

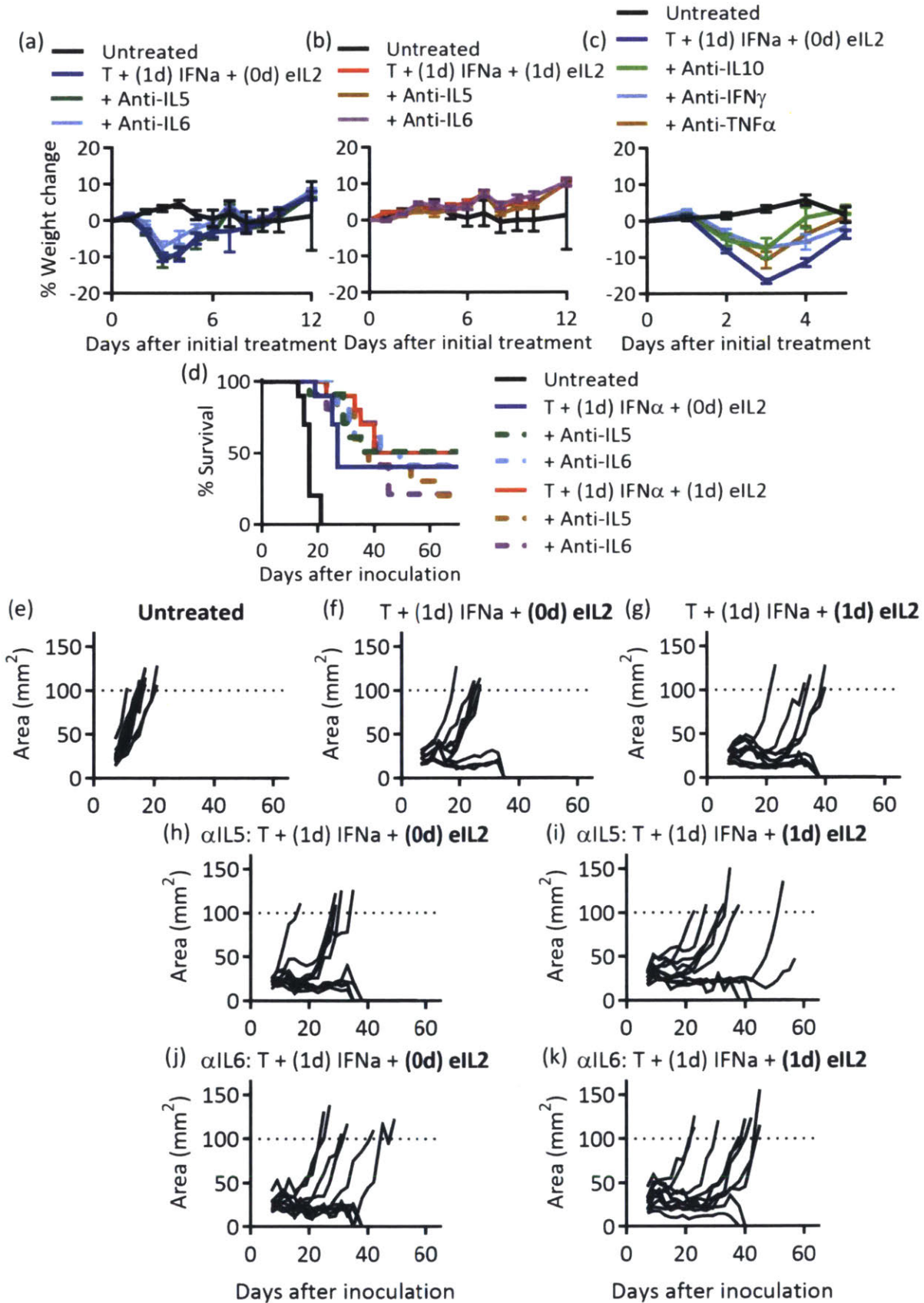


Figure 35: Weight loss time course and tumor area curves for neutralization and depletion

Full weight loss time course curves are shown for the (a-b) IL5, IL6, (c) IL10, IFN γ , and TNF α neutralization studies in B16F10 tumor-bearing mice in Figure 20. The days count from 0 after first TA99 administration. (d) Survival and (e-k) tumor area curves for each treatment condition are shown from the B16F10 tumor study corresponding to long-term depletion of IL5 and IL6 in Figure 20. Note that one mouse in the treatment group α IL5: T + (1d) IFN α + (1d) eIL2 was euthanized on day 63 for tumor burden but its tumor dimensions were not written down. Data are from 1 independent experiment totaling 10 mice per group (IL5 and IL6) or a separate independent experiment totaling 7-8 mice per group (IL10, IFN γ , and TNF α). * indicates $p < 0.05$ and error bars are +/- SEM.

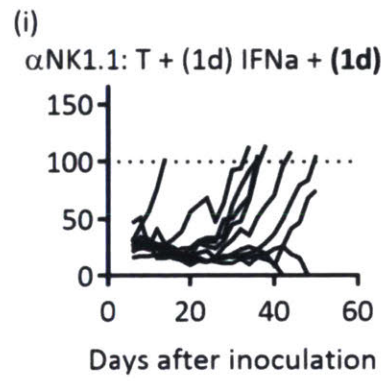
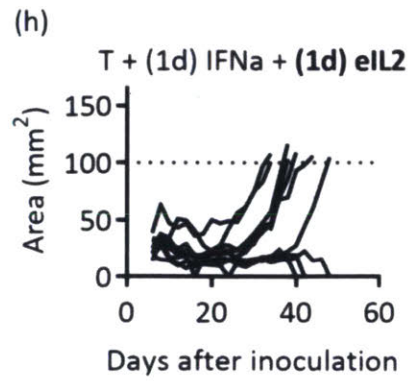
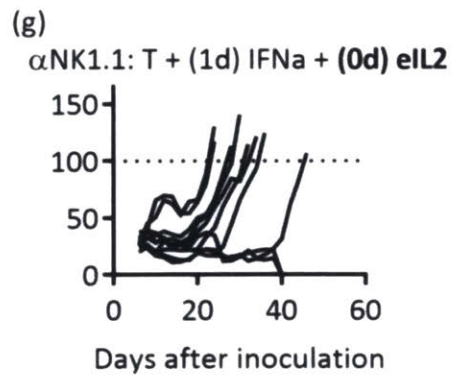
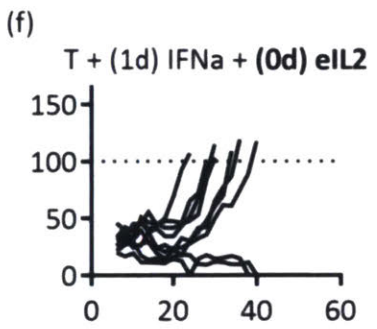
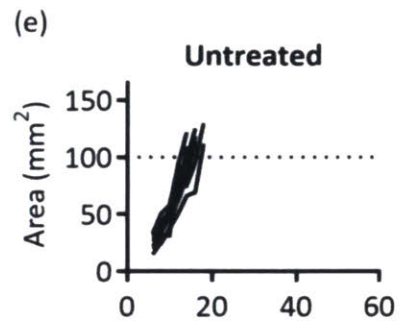
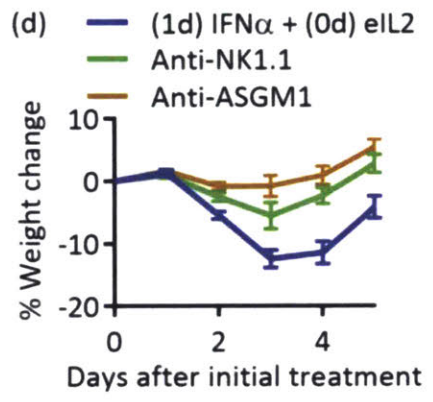
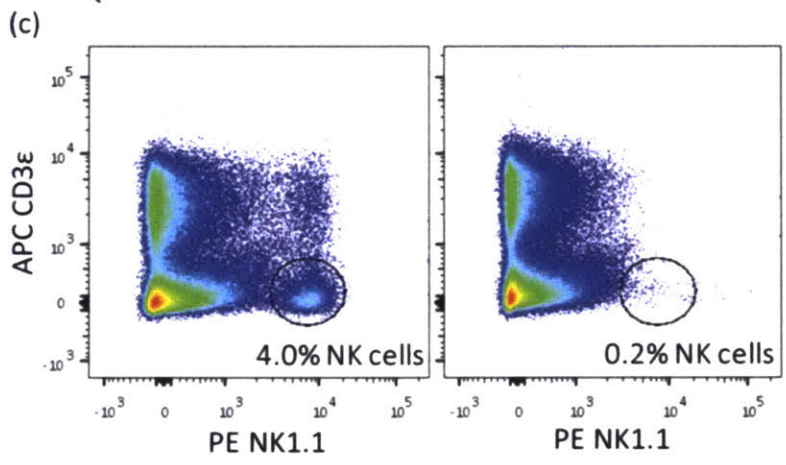
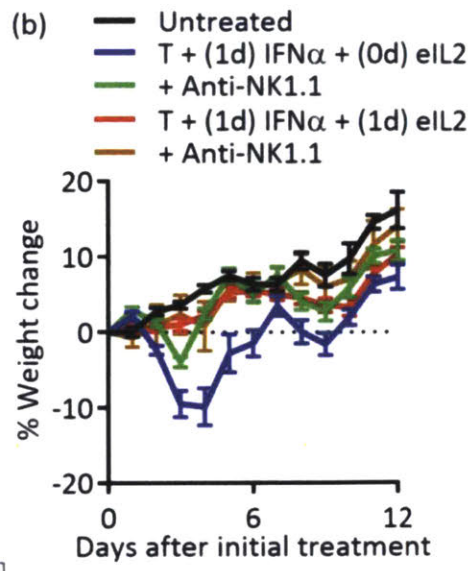
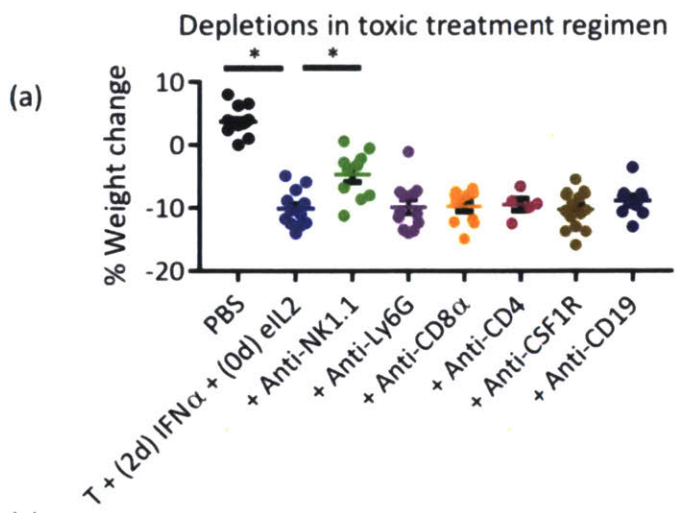


Figure 36: Cellular depletion weight loss, example flow staining, and NK depletion full weight loss and tumor areas

(a) Cellular depletions were completed to investigate which were responsible for the weight loss toxicity. All groups except PBS in this study were treated 6 days after B16F10 tumor inoculation by retro-orbital injection with TA99 and 25ug Fc-IL2 (a different version of eIL2), then 8 days after inoculation with 50ug IFN α . Percent weight changes were reported 4 days after treatment began. A one-way ANOVA with Dunnett's multiple comparisons test was used to compare each treatment group to the "No depletion" group. (b) The full weight loss time course curve is shown for the NK depletion studies in B16F10 tumor-bearing mice in Figure 21. The days count from 0 after first TA99 administration. (c) Depletion of NK cells was verified by examining splenic NK cells on flow cytometry. Left is no depletion and right is 4 days after injection of NK1.1 depleting antibody. (d) The full weight loss time course curve is shown for the study comparing the ASGM1 and NK1.1 depleting antibodies in Figure 21. The days count from 0 after first TA99 administration. (e-i) Tumor area curves for each treatment condition are shown. Note that one mouse in the last treatment group was euthanized on day 52 for tumor burden but its tumor dimensions were not written down. Data are from 2 independent experiments totaling 9 or 10 mice per group. * indicates $p < 0.05$ and error bars are +/- SEM.

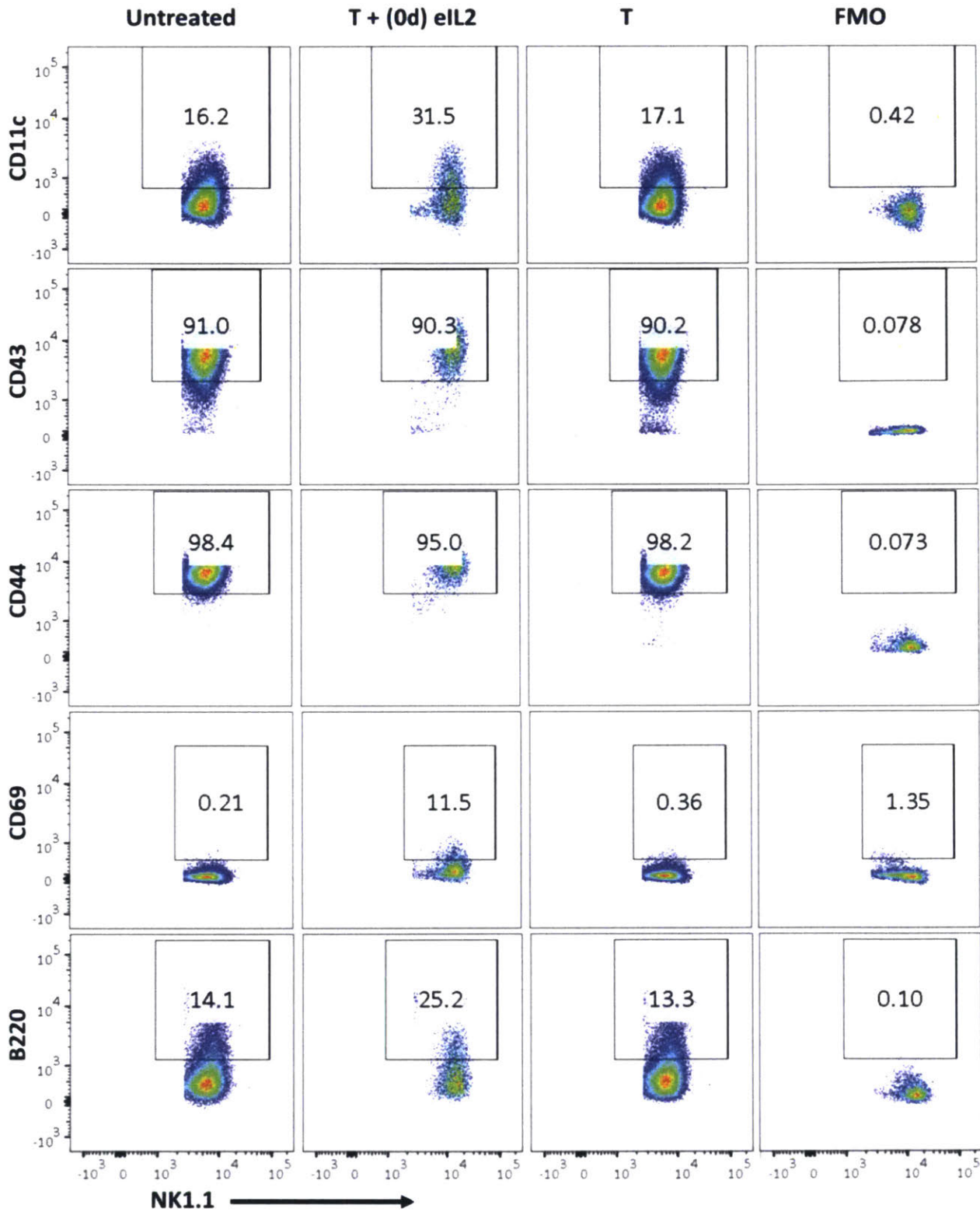


Figure 37: NK activation representative flow plots

Representative plots from each treatment condition for the NK activation markers in Figure 22 (a-e) are shown. Data are from 1 independent experiment, with representative plot from 1 mouse per treatment group. Fluorescence minus one (FMO) is a plot of pooled sample stained with the full flow panel except

replacing the marker in each row with an isotype control antibody of the same color. Samples are gated on single, live, CD3 negative, NK1.1 positive cells.

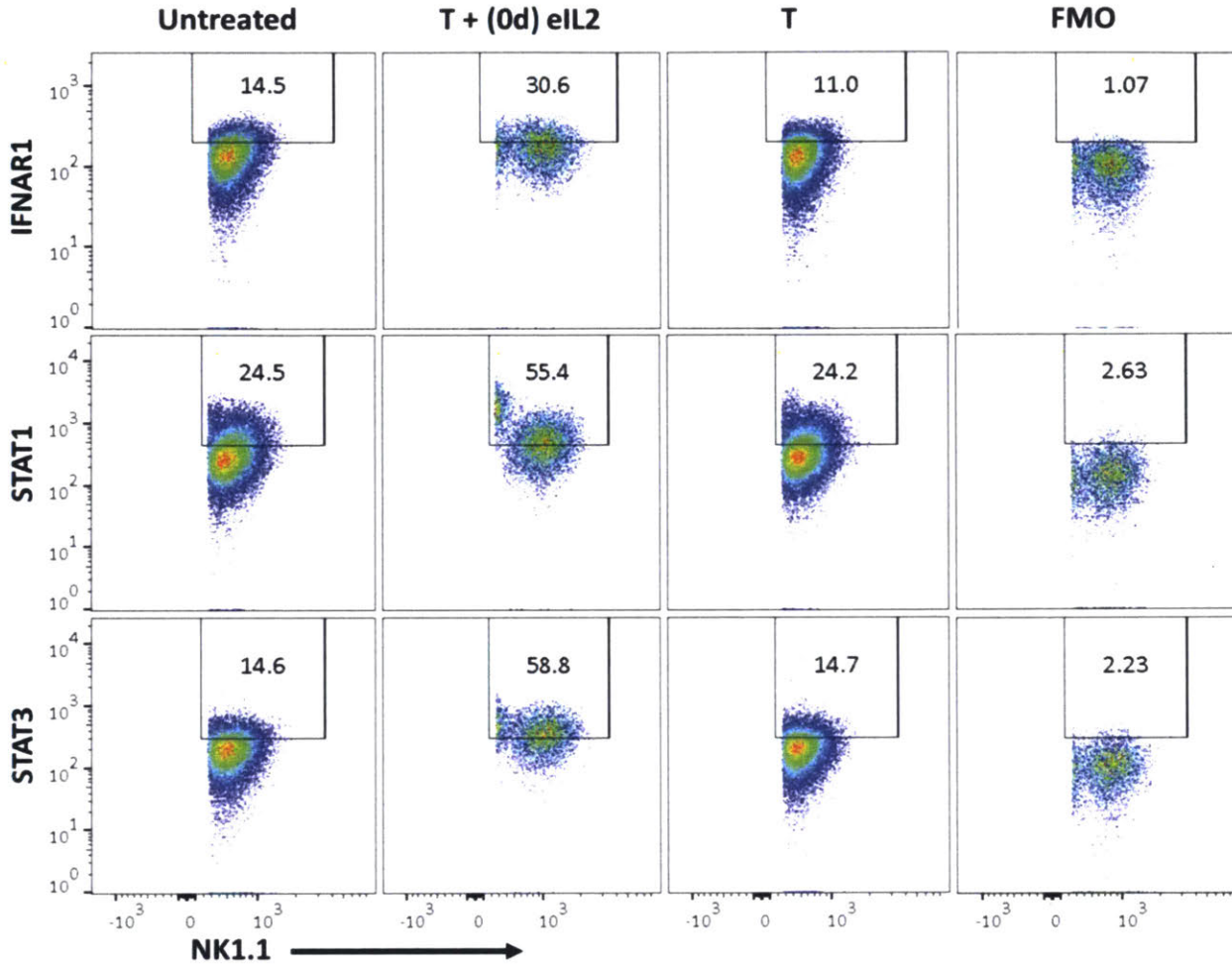


Figure 38: NK IFN α signaling protein representative flow plots

Representative plots from each treatment condition for the IFN α signaling proteins in Figure 22 (f-h) are shown. Data are from 1 independent experiment, with representative plot from 1 mouse per treatment group. Fluorescence minus one (FMO) is a plot of pooled sample stained with the full flow panel except replacing the marker in each row with an isotype control antibody of the same color. Samples are gated on single, live, CD3 negative, NK1.1 positive cells.

3.6 Acknowledgments

We would like to acknowledge and thank MIT and Koch Institute Professor Darrell Irvine, and his lab's generous support and collaboration on the KP mice studies. In particular, we are grateful for Dr. Kavya Rakhra for teaching techniques and sharing the workload on the KP mouse tumor studies and we also appreciate the support from Wuhbet Abraham on these studies.

Thank you also to Grayson Rodriguez, an undergrad researcher who assisted with many of these studies.

This work was supported in part by the Koch Institute Support (core) Grant P30-CA14051 from the National Cancer Institute. We thank the Koch Institute Swanson Biotechnology Center for technical support, specifically the Flow Cytometry, Histology, and the Animal Imaging and Preclinical Testing cores.

This material was also based upon work supported by the NIH/NIGMS T32 GM008334, Interdepartmental Biotechnology Training Program.

This chapter references material with permission from: Rothschilds et al, OncoImmunology 2019⁴⁰.

Chapter 4. Engineering CTLA-4 binders to understand and improve upon mechanisms of anti-CTLA-4 cancer immunotherapy

Abstract

Anti-CTLA-4 antibodies have been in clinical use in cancer immunotherapy for eight years, and have been shown to improve tumor infiltration of CD8 T cells as well as reduce numbers of regulatory T cells (Tregs). Mechanistic studies have shown Treg depletion to be important for efficacy of anti-CTLA-4 antibodies in mouse models, but debate continues about the importance of enhancing CD8 T cell priming by blocking CTLA-4-B7 interactions. To our knowledge, no mouse CTLA-4 antibodies have been made to be noncompetitive with B7 to test whether Treg depletion without blocking B7 is enough for efficacy. In this work, we used yeast surface display to engineer novel mouse CTLA-4 binders nc19 and nc20 that were noncompetitive with B7. Unfortunately, these binders did not bind surface-expressed CTLA-4. Epitope mapping suggested that nc19 and nc20 bound soluble CTLA-4 at residues situated close to the cell surface, which could sterically hinder binding to cell surface CTLA-4. Because nc19 and nc20 were the dominant clone in yeast sorts at an early stage, next generation Illumina sequencing was done to identify rare sequences of B7-noncompetitive CTLA-4 binders for further development. 11 unique CDRH3 motifs were identified from this analysis, and if any of these shows surface CTLA-4 binding noncompetitive with B7, this novel CTLA-4 binder can be affinity matured and used as a tool to answer the questions of CTLA-4 mechanism motivating this project.

4.1 Introduction

The anti-CTLA-4 antibody Ipilimumab was approved by the FDA in 2011 and is at the leading edge of the new wave of cancer immunotherapies. Ipilimumab, the Bristol-Myers Squibb anti-CTLA-4 antibody, elicited overall survival of around 20% against unresectable metastatic melanoma ¹⁷, and has since been shown to improve survival as adjuvant treatment of resected cutaneous melanoma and in combination with anti-PD-1 in indications such as advanced renal-cell carcinoma ¹⁴⁶. Another clinical anti-CTLA-4 candidate, Tremelimumab, has not yet received clinical approval but is being developed by MedImmune (AstraZeneca). Unlike the activating human IgG1 isotype of Ipilimumab capable of effector functions like antibody-dependent cell-mediated cytotoxicity (ADCC), Tremelimumab is human IgG2 ¹⁴⁷. Tremelimumab failed to improve efficacy over standard of care in a phase III clinical trial against metastatic melanoma ¹⁴⁸, and some have suggested that the IgG2 isotype could account for these differences in efficacy when compared with Ipilimumab ¹⁴⁹.

The debate over anti-CTLA-4 isotype is founded on two different possible mechanisms for anti-CTLA-4 antibodies in cancer immunotherapy. Early studies on CTLA-4 showed that it is rapidly upregulated to the site of the T cell receptor on surface of T cells after activation, where it binds to B7 molecules with higher affinity than CD28 ¹⁵⁰⁻¹⁵². Additional studies also showed that CTLA-4 is constitutively expressed on the surface of regulatory T cells (Tregs) ^{153,154}. Thus, anti-CTLA-4 antibodies could have utility by blocking the CTLA-4-B7 interaction and enhancing T cell priming

and activation or by cellular depletion of Tregs, which are suppressive to the anti-cancer immune response.

Preclinical studies exploring the mechanism of anti-CTLA-4 antibodies provide evidence for efficacy from both possible roles of anti-CTLA-4 antibodies. In 2009, CTLA-4 blockade was shown to be necessary on both T effectors (CD4 and CD8) and Tregs for efficacy in a B16 melanoma model in combination with GVax¹⁵⁵. In this study, lymphocyte chimeras restricted expression of mouse CTLA-4 to individual compartments, and the antibody used was specific to mouse CTLA-4. In 2013, three pivotal studies emphasized the importance of anti-CTLA-4 to have a depleting isotype like IgG2a or 2c in preclinical tumor models^{45,156,157}, implying that depletion of CTLA-4+ Tregs was critical for therapeutic efficacy. Additional studies adding to the complexity of the CTLA-4 Treg mechanism suggested that Tregs were also less suppressive when CTLA-4 was blocked¹⁵⁸, and that CTLA-4 on Tregs can strip B7 off the surface of antigen presenting cells and reduce their priming capability through a process called trans-endocytosis¹⁵⁹.

Several recently published studies in 2018 further ignited the debate over whether the primary role of anti-CTLA-4 is to block CTLA-4-B7 interactions on CD8 T cells or to deplete Tregs. One publication developed and used an alpaca heavy chain only antibody fragment that was B7-competitive, and showed that this protein was only efficacious when fused to an activating Fc region¹⁶⁰. Based on binding studies and in vitro analysis in addition to in vivo studies, claims were made that Ipilimumab did not effectively block CTLA-4-B7 interactions and that new B7-competitive antibodies were needed¹⁶¹. Direct comparison of anti-CTLA-4 antibodies with human IgG1 versus human IgG2 isotypes in a mouse model with humanized Fc γ receptor expression showed that both isotypes exhibited equal depletion of Tregs and similar efficacy in B16F10, MCA205, and MC38 tumor models¹⁶². Importantly, in this study, both the IgG1 and IgG2 performed identically during in vivo studies to the human IgG1_{SDALIE} that has stronger binding to the activating CD16a Fc γ receptor, which implied that efficacy may not relay on the extent of Treg depletion. Despite these papers emphasizing the importance of Treg depletion, clinical histology data published last year suggested that intratumoral Tregs were not depleted by either Ipilimumab nor Tremelimumab¹⁶³, although this lack of observed depletion may have been due to inspection at the wrong time point. An additional paper associated with the company Agenus showed in a non-tumor model of systemic inflammation induced by the bacterial superantigen (SEB peptide) that antigen-specific CD8 T cells were activated and expanded with anti-CTLA-4 utilizing activating Fc γ receptor interactions, but that this was independent of Treg depletion¹⁶⁴. That work suggested that the dependence of efficacy on activating CTLA-4 isotype could be due to Fc γ receptor interactions independent of Tregs. Clearly, questions of the role of anti-CTLA-4 in cancer immunotherapy are still front and center in the immunotherapy landscape, with potential to affect choice of future antibody isotypes and optimal binding characteristics.

Although there is general acceptance of the importance of Treg depletion, recent studies have not been conclusive regarding whether blocking B7-CTLA-4 interactions adds to the therapeutic efficacy. The goals of our efforts in engineering new CTLA-4 antibodies were both for mechanistic understanding of CTLA-4 blockade in cancer immunotherapy and to potentially improve upon current therapeutics. For the biological insight of CTLA-4-mediated Treg depletion without enhanced CD8 T cell priming, we needed to engineer CTLA-4 binders that would not interfere with CTLA-4 binding to B7. Thus, our first requirement was that our CTLA-4 binders were

noncompetitive with B7. Since we planned to test our new antibodies in the mouse immune system, binding to mouse CTLA-4 was of highest importance. However, to improve translational relevance of our binders in the case of improved therapeutic efficacy, we decided to search for binders that were cross-reactive with human CTLA-4. Because of the high sequence homology of CTLA-4 with CD28, we also needed to ensure we did not also bind CD28. Lastly, we wanted ideally to have binders with Kd in the 10s of nM range. A high-affinity, mouse CTLA-4 scFv binder noncompetitive with B7 could enable production of different versions of anti-CTLA-4 (Figure 39). Bispecific antibodies with both B7-competitive and B7-noncompetitive variable regions could potentially allow for disruption of CTLA-4-B7 complexes, improve internalization of CTLA-4, or change CTLA-4 surface recycling. Finding CTLA-4 binders meeting these characteristics could allow us to address looming questions regarding CTLA-4 mechanism, but additionally explore improvements in therapeutic efficacy.







	B7 Non-comp	B7 comp	Bi-specific
mIgG2c (active)			
mIgG2c LALA-PG (inactive)			

Figure 39: 6 different antibodies to make using B7-competitive and noncompetitive CTLA-4 binders

4.2 Results

Yeast surface display strategy to find B7-noncompetitive CTLA-4 binders nc19 and nc20

Since each of our proteins of interest for yeast surface display sorts (CTLA-4, B7.1, and CD28) are found as dimers on the cell surface, we expressed each of these as Fc fusions. Allowing these dimers to maintain their native conformations was very important, so we introduced 3 cysteine to serine mutations to modify the Fc hinge region and allow for less structural constraint imposed by the Fc region on the angle of the dimers. Mouse Fc from 2.5F-Fc was used, which enabled use of 2.5F-Fc in negative sorts against Fc binders. We decided to use only B7.1 as the competitor in our sorts for the following reasons: there were too many sort requirements to separately find B7.1 and B7.2 noncompetitive binders; the main epitope on CTLA-4 important for B7.1 and B7.2 binding is the same indicating a B7.1 noncompetitive CTLA-4 binder might also be noncompetitive with B7.2; and lastly, because B7.1 has higher affinity and slower dissociation from CTLA-4 and CD28 than B7.2¹⁶⁵, suggesting B7.1 may play important roles in priming and making it more likely B7.1 will stay bound to CTLA-4 for effective sorting for noncompetitive binders.

Prior to yeast surface display, we validated binding characteristics of our antigens using ELISAs to ensure they maintained expected properties after in-house expression and purification as Fc

fusions. Importantly, we showed that mB7.1-Fc expressed in-house and a form purchased from Biologend behaved identically as competition for mCTLA-4-Fc binding to 9d9, a B7-competitive anti-CTLA-4 antibody previously made and characterized (Figure 40 (a)). We made the decision to use 1uM mB7.1-Fc in initial yeast sorts for CTLA-4 binders because it appeared to significantly impede binding of 9d9, the B7-competitive anti-CTLA-4 mouse antibody. These ELISAs also confirmed that mouse and human CTLA-4-Fc are cross-reactive with mouse B7.1-Fc, and that mouse CD28-Fc has lower affinity for B7.1-Fc as expected (Figure 40 (b)).

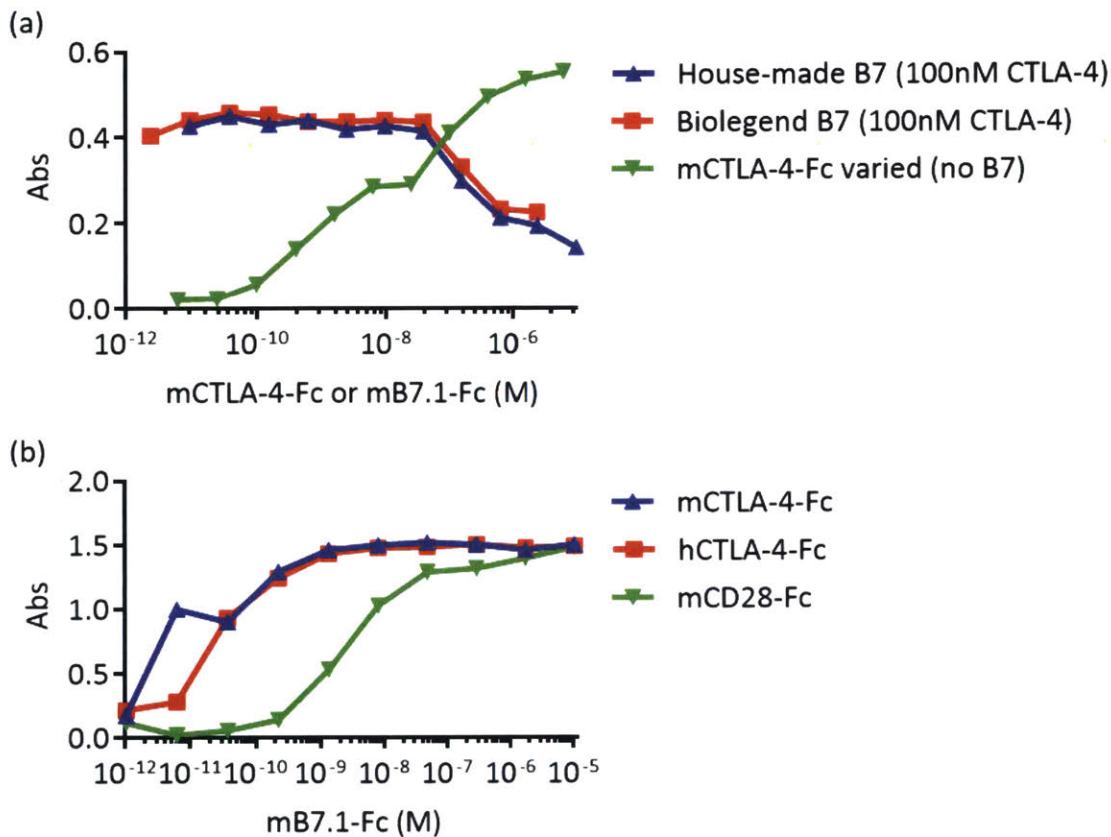


Figure 40: ELISAs validated CTLA-4-, CD28-, and B7.1- Fc fusion proteins

(a) Plate was coated with anti-CTLA-4 9d9 clone expressed into supernatant by EPFL and purified in-house (used for all prior mouse studies). Biotinylated mouse (m) CTLA-4-Fc was detected via HRP linked SA. Dilutions were made of biotinylated mCTLA-4-Fc (with no B7 added) or of mB7.1-Fc (keeping the concentration of biotinylated mCTLA-4-Fc constant, '100nM CTLA-4'). House-made mB7.1-Fc (used for subsequent yeast sorts) was validated by comparing with Biologend mB7.1-Fc. (b) Plates were coated with Fc fusions of mouse CTLA-4 (mCTLA-4-Fc), human CTLA-4 (hCTLA-4-Fc), or mouse CD28 (mCD28-Fc) then incubated with varying dilutions of His-tagged mB7.1-Fc detected via HRP linked anti-His antibody. Unless noted, all proteins were made in-house instead of purchasing.

The format of yeast surface display using our in-house proteins as antigens or competitors was described in a schematic adapted from a prior publication ¹⁶⁶.

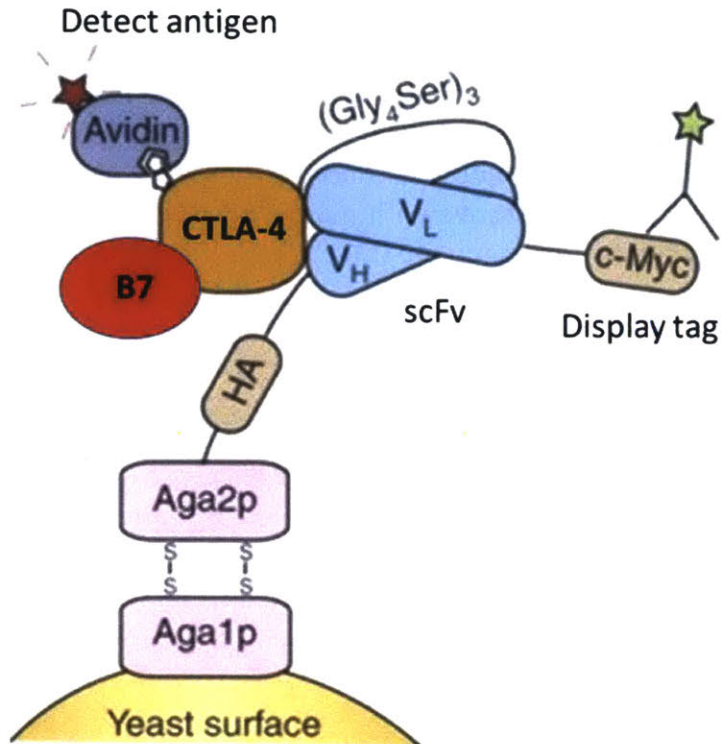


Figure 41: Schematic for yeast surface display for B7-noncompetitive CTLA-4 binders

This diagram was adapted a 2006 publication by Ginger Chao ¹⁶⁶. Biotinylated CTLA-4-Fc fusion was detected by a fluorophore linked streptavidin secondary. Yeast displaying full length scFv were labeled with a chicken antibody against the c-Myc tag, then detected through a fluorophore linked goat anti-chicken antibody. B7.1-Fc was used in many sorts to bias binding of CTLA-4 by scFvs away from the B7 binding site on CTLA-4.

The requirements for engineering CTLA-4 binders were B7-noncompetitive binding to mouse CTLA-4, no binding to homologous proteins like CD28, and cross-reactivity to human CTLA-4. Keeping these important requirements in mind, we employed the following sort strategy on a recently developed yeast scFv 'clean H3' library ¹⁶⁷. Firstly, we selected for mouse CTLA-4 binders, then weeded out B7-competitive binders and CD28 binders, then looked for human cross-reactivity and improving affinity by lowering concentration of CTLA-4 used in sorts (Figure 42). Most yeast incubation steps occurred for at least 2-3 hours, during which time we maintained constant, high concentration of B7.1 in applicable sorts to circumvent B7 dissociation that would allow scFvs to bind CTLA-4 at the B7 binding site. At the completion of those sorts, we identified two main (but very similar) CTLA-4 binding scFv clones in yeast that we called nc19 and nc20.

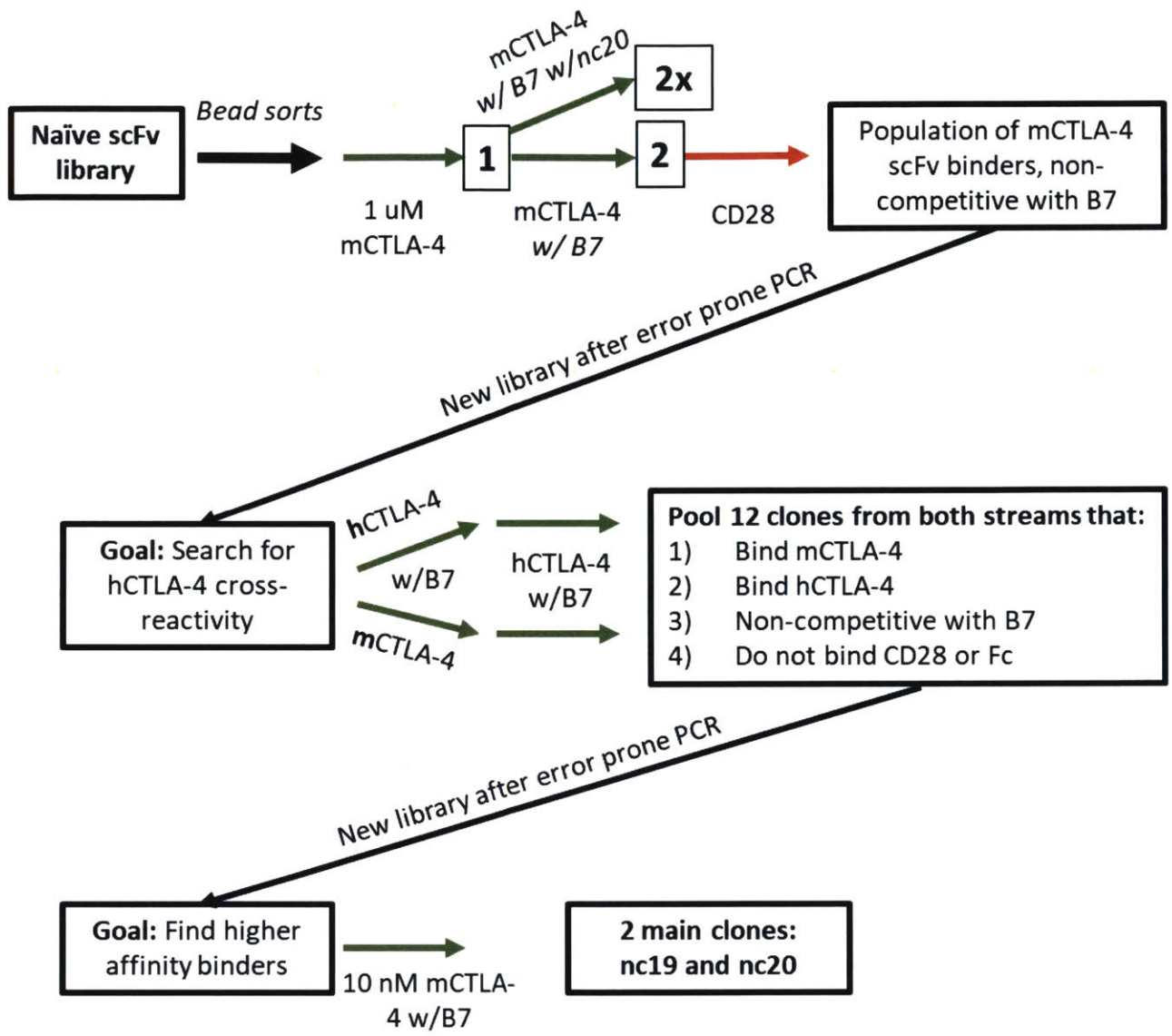


Figure 42: Sort strategy for engineering novel CTLA-4 binders from the clean H3 scFv library. All proteins in sorts were Fc (mouse) fusions. 'm' denotes mouse and 'h' denotes human. All concentrations of mCTLA-4-Fc, hCTLA-4-Fc, and mCD28-Fc were 100 nM for sorts unless otherwise noted. B7 is mouse B7.1-Fc used at ≥ 1 μ M. Except the first black arrow, all sorts were done with flow cytometry (FACS sorts). Green arrows denote a positive sort against the antigen listed and red arrows denote a negative sort. Prominent generations '1' and '2' referenced later are surrounded by boxes. The bead sorts that occurred on the naïve library prior to flow sorts were: Negative using uncoated SA beads followed by positive using beads coated with mCTLA-4-Fc; negative twice in a row with beads coated with 2.5F-Fc followed by positive using beads coated with mCTLA-4-Fc.

The 2 clones nc19 and nc20 that emerged from yeast sorts and 2 rounds of affinity maturation had complementary determining regions (CDRs) very different from other B7-competitive antibodies in the clinic and used for mouse studies, with, most notably, the DGLP motif in the CDR H3 (Figure 43). Since the clean H3 yeast library used for sorts resulting in nc19 and nc20 was

created with most of its diversity in the H3 region, differences in the other CDR regions were likely selected for from affinity maturation. The light chain framework was VK3-20 (with a couple mutations, like the V to I mutation in nc19 CDR1), although the CDR3 in nc20 is actually from VK 1-39. The heavy chain CDRs for both nc19 and nc20 belong to VH3-23.

Name	B7 comp?	CDRL1	CDRL2	CDRL3
Ipilimumab	yes	RASQSVGSSYLAW	GAFSRATGIPD	QQYGSSPWTF
Tremelimumab	yes	RASQSINSYLDW	AASSLQSGVPS	QQYYSTPFTF
9d9 (murine)	yes	RSSQSIVHSNGNTYLEW	KVSNRFSGVDP	FQGSHVPYTF
nc19	no	RASQSISSSYLAW	GASSRATGIPD	QQYGSSPSTF
nc20	no	RASQSVSSSYLAW	GASSRATGIPD	QQSYSTPLTF

Name	B7 comp?	CDRH1	CDRH2	CDRH3
Ipilimumab	yes	GFTFSSYTMHW	VTFISYDGNNK	ARTGWLGPFDYW
Tremelimumab	yes	GFTFSSYGMHW	VAVIWDYDGSNK	ARDPRGATLYYYYYGMDVW
9d9 (murine)	yes	GYTFTDYMMNW	IGVINPYNGDTS	ARYYGSWFAYW
nc19	no	GFTFSSYAMSW	VSAISGSGGST	ARHDGLPFDYR
nc20	no	GFTFSSYAMSW	VSAISGSGGST	ARHDGLPFDYR

Figure 43: CDR regions are listed for nc19, nc20 and a variety of CTLA-4 antibodies

nc19 and nc20, the two new clones from the yeast library, were listed in the bottom two rows. Three other antibodies competitive with B7 including Ipilimumab and Tremelimumab (clinical anti-CTLA-4 antibodies that bind human CTLA-4) and 9d9 (anti-CTLA-4 specific to mouse CTLA-4 and commonly used in mouse studies) were listed.

Characterization of nc19 and nc20 as scFvs in yeast binding assays

Yeast binding assays showed nc19 and nc20 scFvs to fit the CTLA-4 binding characteristics in our original set of criteria. Nc19 and nc20 had Kds of around 10nM apparent affinity for mouse CTLA-4, although the affinity for human CTLA-4 was about 20-fold lower ((a-b)). These scFvs also had immeasurable affinity for CD28-Fc, indicating that they were not cross-reactive with CD28 and were not Fc binders. Additionally, these scFvs were B7-noncompetitive, as evidenced by the lack of drop in MFI moving to concentrations of mB7.1-Fc above 1uM, shown in contrast with different scFv that was B7-competitive and had a clear knockdown of MFI as the B7 concentration increased ((c-d)).

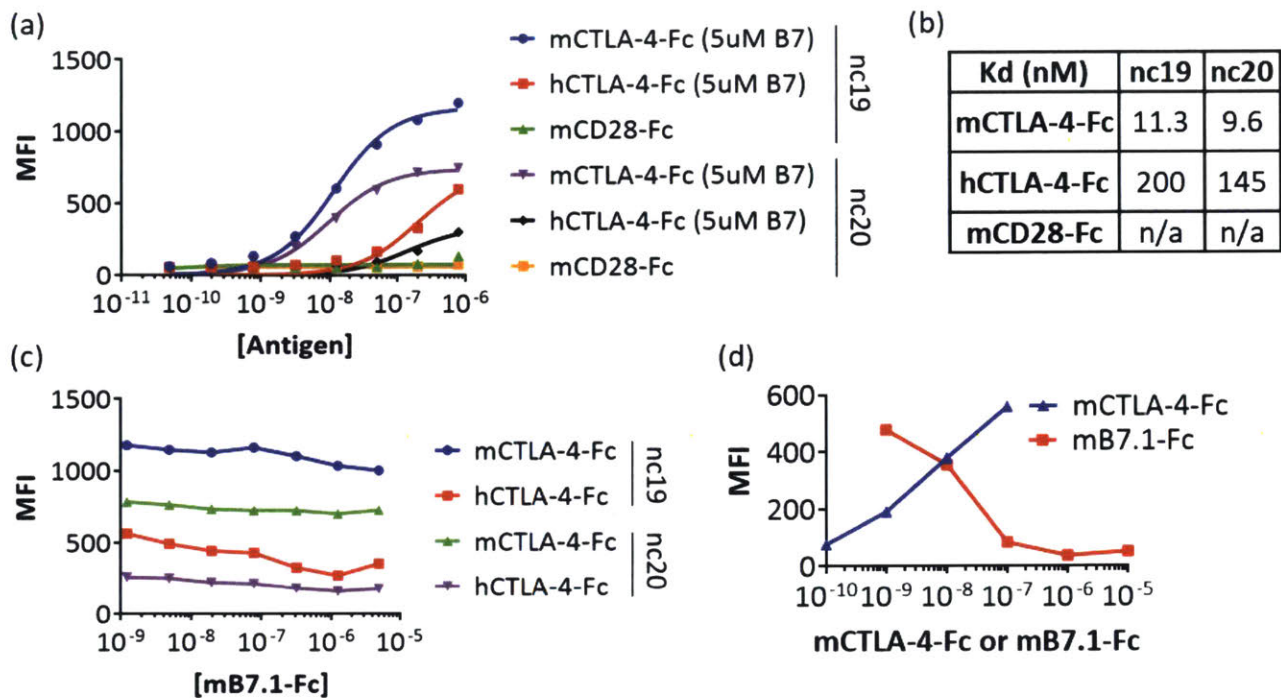


Figure 44: Yeast binding assays characterizing nc19 and nc20 as scFvs

(a) Yeast binding assays show two clones nc19 and nc20 are B7-noncompetitive and have (b) apparent affinity constants of around 10 nM for mCTLA-4. (c) Titration with mB7.1-Fc, holding the concentration of m- or h-CTLA-4 constant at 200 nM. (d) For reference, yeast surface titrations of B7 for a different scFv clone that is B7-competitive show that B7 reduced the MFI from 100 nM mCTLA-4 binding to the scFv starting around 10nM B7 (red curve), compared to the 100 nM concentration point along the curve with titration of mCTLA4-Fc with no B7.

Nc19 and nc20 did not bind cell surface CTLA-4

Given favorable results in the yeast binding assays, we moved forward with cloning nc19 and nc20 sequences from scFvs into full-length mouse antibodies in IgG2c that could be used in mouse studies. Up to this point, we had only performed yeast binding assays with nc19 and nc20 to soluble antigens. Since we wanted to use nc19 and nc20 as antibodies to cell surface CTLA-4 in mouse models, it was important to characterize their binding on the cell surface. Since prior studies showed CTLA-4 on activated mouse T cells had low MFI even on Tregs, where it is constitutively expressed, we decided to transiently express CTLA-4 on the surface of HEK cells for in vitro assays testing nc19 and nc20 as antibodies. To do this, we cloned all 4 domains of CTLA-4 (signal peptide, extracellular region, membrane domain, and cytoplasmic tail) into a plasmid called pIRESacGFP. This plasmid was used because it allowed us to identify HEK cells with surface CTLA-4 by co-expression of GFP. The GFP in this plasmid is expressed bicistronically with CTLA-4, which allowed for intracellular GFP expression and avoided fusing GFP to CTLA-4 because it could change the shape of CTLA-4 on the cell surface. We used two different versions of this plasmid including full length CTLA-4 (which has all 4 domains full length) and CTLA-4 DEL36, which has the last 36 amino acid residues curtailed. The DEL36 version of surface CTLA-4 was thought to stop

or reduce CTLA-4 internalization, which would be a useful contrast to full length CTLA-4 which is thought to be internalized very quickly ¹⁵⁹.

Using this system of HEK cell transfection with pIRES CTLA-4 acGFP or pIRES CTLA-4 DEL36 acGFP to get transient CTLA-4 surface expression in GFP-expressing cells, we did not observe binding of nc19 or nc20 to surface CTLA-4 (Figure 45). We were confident CTLA-4 expressed onto the cell surface because both B7.1-Fc and 9d9, the B7-competitive mouse CTLA-4 antibody, were detectable on the surface of HEK cells co-expressing GFP as a proxy for CTLA-4. Since this assay was done by staining for antibody binding with an anti-mouse secondary antibody, we wanted to ensure that lack of secondary staining for nc19 and nc20 was not due to these antibodies driving internalization when complexed with CTLA-4. Although the DEL36 version of CTLA-4 should have avoided this problem because it should have low or no internalization, we wanted to use orthogonal methods to verify lack of nc19 and nc20 binding to surface CTLA-4.

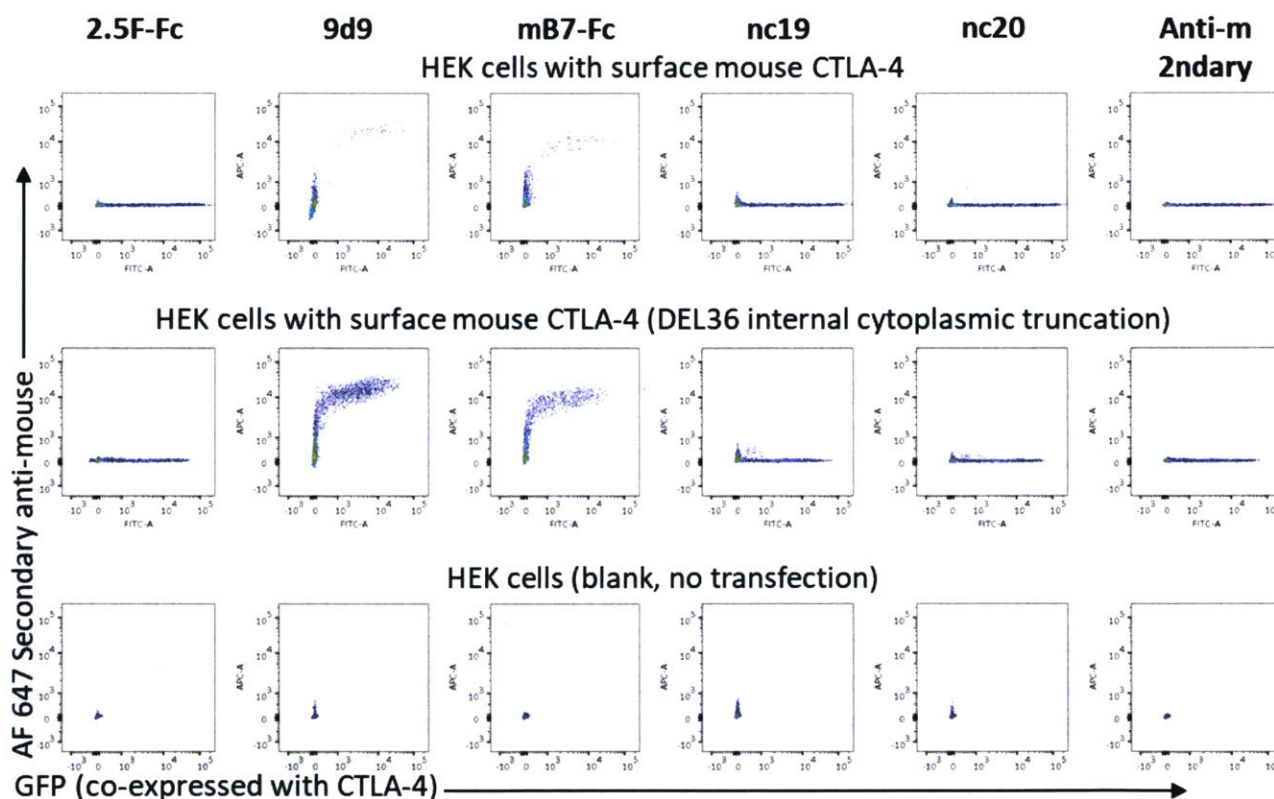


Figure 45: CTLA-4 surface binding to nc19 and nc20 was not detected with a secondary antibody
 Binding of nc19 and nc20 expressed as mouse IgG2c antibodies was quantified using an anti-mouse secondary antibody on the surface of HEK cells transiently transfected with the pIRES acGFP plasmid, which couples expression of surface CTLA-4 to internal GFP expression.

To ensure that lack of nc19 and nc20 detection was due to internalization eliminating surface detection with a secondary antibody, we repeated this assay with both 9d9 and nc20 directly labeled with fluorophores. Unfortunately, we saw robust binding of 9d9 to CTLA-4-expressing HEK cells that was knocked down when B7 was present, but no nc20 antibody fluorescence in CTLA-4-expressing HEK cells regardless of the presence of B7 (Figure 46).

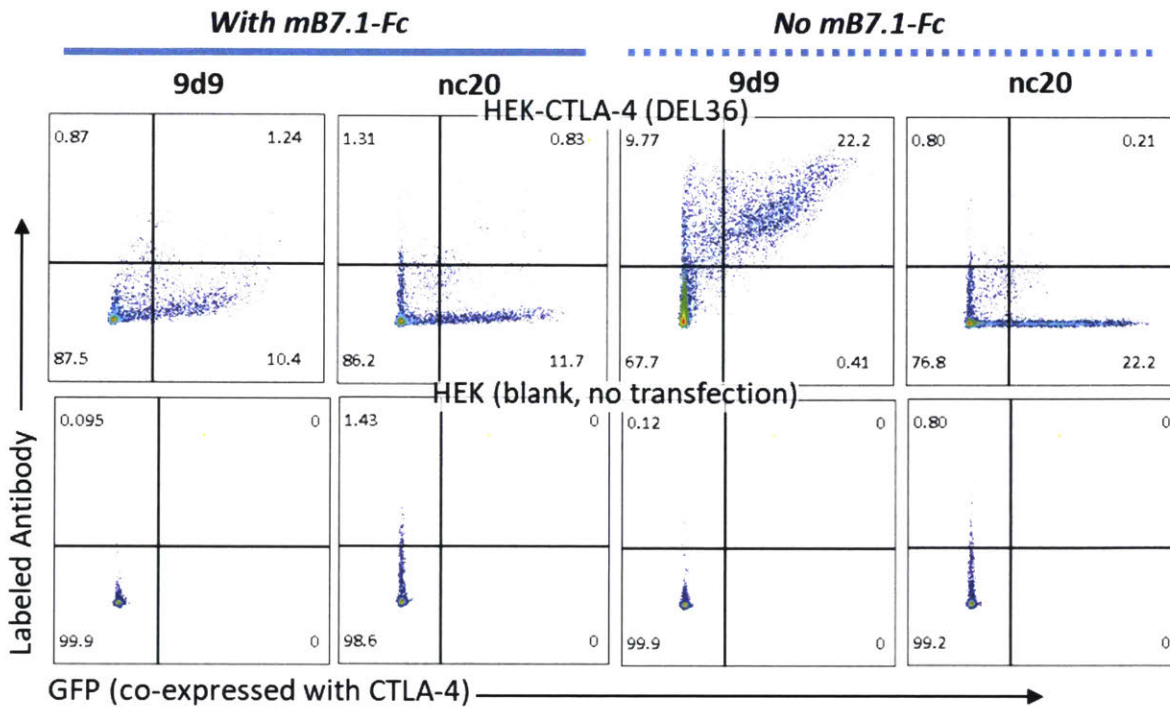


Figure 46: Detecting binding of fluorophore labeled 9d9 or nc20 to surface CTLA-4

When fluorophore labeled antibodies 9d9 or nc20 were incubated with HEK cells expressing surface CTLA-4, no fluorophore was detected, indicating the cells neither have antibody on the surface nor internalized. Since nc19 and nc20 are very similar and likely to bind the same CTLA-4 epitope, only nc20 was labeled and tested for internalization.

Binding of nc19 and nc20 to the same soluble antigens used for yeast sorts was next tested to investigate whether the full-length antibodies were dysfunctional compared to the yeast surface assays when nc19 and nc20 were scFvs. These ELISAs showed that nc19 and nc20 as antibodies still had expected binding to mCTLA-4-Fc, noncompetitively with B7, and that they did not bind mCD28-Fc (Figure 47). We also tested whether scFv-Fc versions of nc19 and nc20 would bind surface CTLA-4 in case the more compact size of scFv-Fcs would allow access to surface CTLA-4 epitopes unreachable by bulky antibodies, but surface CTLA-4 binding was still not detected (data not shown).

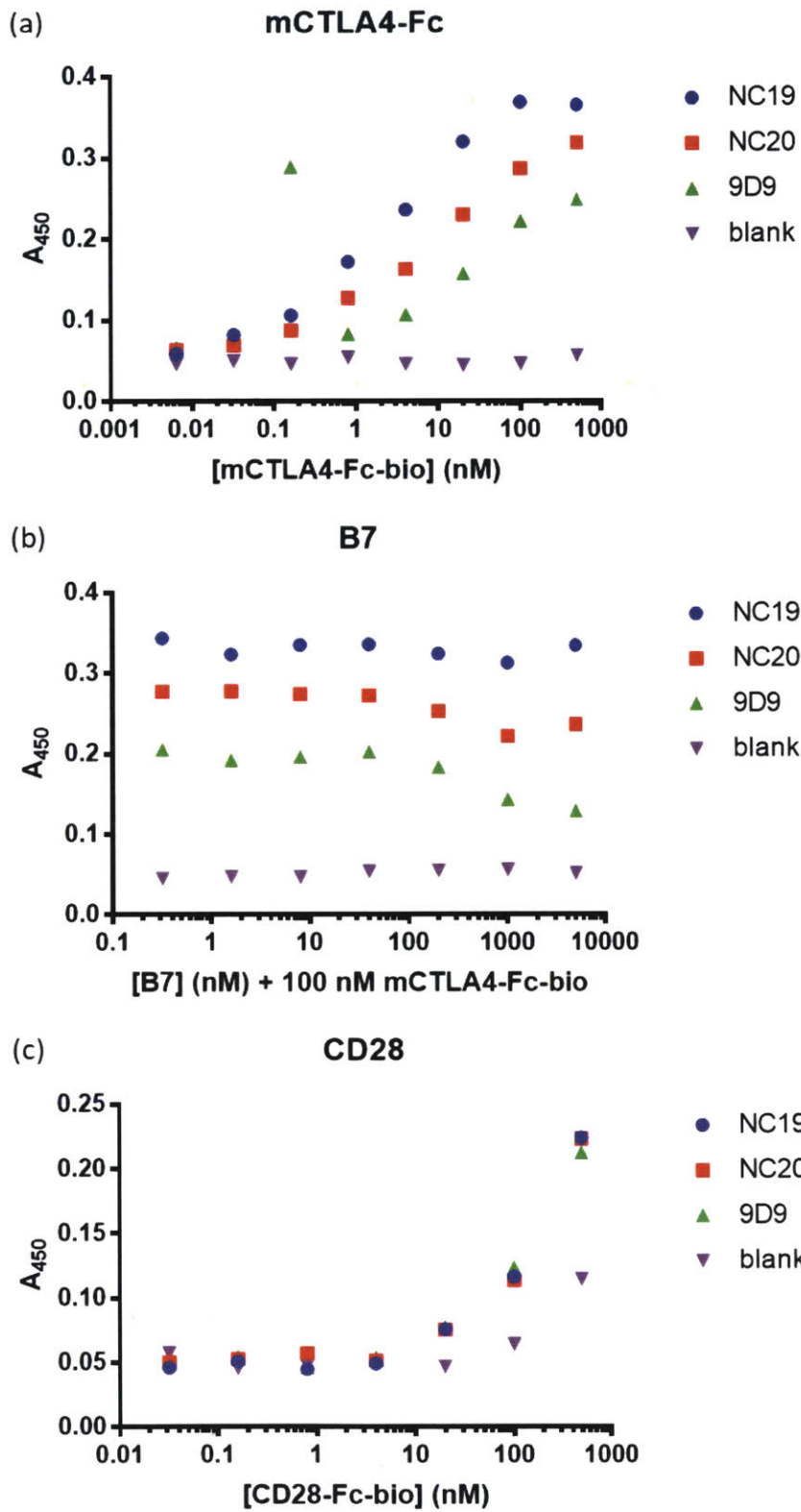


Figure 47: nc19 and nc20 as full-length antibodies still bound the soluble antigens used in yeast sorts

ELISAs confirmed that nc19 and nc20 in antibody format still bound soluble mCTLA-4-Fc noncompetitively with mB7.1-Fc, and did not bind mCD28-Fc. Plates were coated with nc19, nc20, or 9d9. Binding of either biotinylated mCTLA-4-Fc or biotinylated mCD28-Fc was detected through SA-HRP.

Epitope mapping to characterize why nc19 and nc20 did not bind surface CTLA-4

Since nc19 and nc20 still bound soluble CTLA-4-Fc but did not bind surface CTLA-4, we considered several hypotheses to explain this phenomenon. Clearly, there was an epitope on CTLA-4-Fc that was not present or not accessible to surface CTLA-4. Firstly, it was possible that soluble CTLA-4-Fc dimerized differently than surface CTLA-4, resulted in an epitope exposed on soluble CTLA-4-Fc that was hidden by dimerization on surface CTLA-4. Secondly, it was also possible that nc19 and nc20 bound residues on CTLA-4-Fc that were too close to the cell surface in surface CTLA-4. Thus, steric hindrance would prevent an antibody like nc19 or nc20 from binding CTLA-4 when it is on the cell surface but allow binding to soluble CTLA-4. To generate evidence to support either of these theories, we decided to do alanine scan epitope mapping of mCTLA-4 to find the residues important for nc19 and nc20 binding. We chose to mutate 23 amino acid residues in mCTLA-4 based on criteria including location outside of the B7 binding site and whether they were outward facing residues (Figure 48).

(a)

Mouse E A I Q V T Q P S V V L A S S H G V A S F P C E Y S P S H N T D E V R V T V L R Q T N D Q M T E V C A
 Human K A M H V A Q P A V V L A S S R G I A S F V C E Y A S P K A T E V R V T V L R Q A D S Q V T E V C A

Mouse T T F T E K N T V G F L D Y P F C S G T F N E S R V N L T I Q G L R A V D T G L Y L C K V E L M Y P P
 Human A T Y M M G N E L T F L D D S I C T G T S S C N Q V N L T I Q G L R A H D T G L Y I C K V E L M Y P P

Mouse P Y F V G M G N G T Q I Y V I D P E P C P D S D
 Human P Y Y L G I G N G T Q I Y V I D P E P C P D S -

* Tested mCTLA-4 with residue mutated to Alanine

Difference in sequence between mCTLA-4 and hCTLA-4

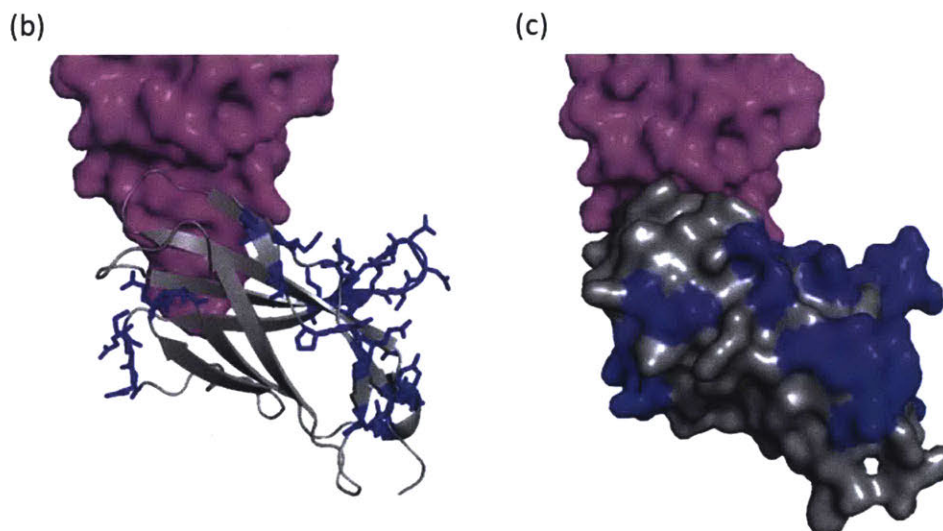


Figure 48: Choosing residues for CTLA-4 epitope mapping for nc19 and nc20

(a) Alignment of mouse and human CTLA-4 extracellular regions showing which residues we decided to mutate. (b-c) Ribbon and volume structures of mouse CTLA-4 (PDB ID: 1DQT, gray) bound to human B7 (magenta). Since the mouse CTLA-4 complex with B7 is not solved structurally, the mouse CTLA-4 structure was aligned with human CTLA-4 in a human CTLA-4-B7 complex. Thus, this structure represents mouse CTLA-4 aligned with the location of human B7.1. The binding site of mouse and human CTLA-4 to B7 is the same conserved MYPPPY motif, suggesting that the location of the binding interface for human B7/CTLA-4 would be the same for mouse and that this representation would be accurate. Residues colored in blue were included in the alanine scan.

To perform the alanine scan, we had to mutate residues on soluble CTLA-4-Fc since surface CTLA-4 did not bind nc19 and nc20. To assess binding, we used nc19 and nc20 in their scFv formats on the yeast surface and did yeast binding assays with the 23 mutant mCTLA-4-Fc constructs. We used two different concentrations of mCTLA-4-Fc at the K_d (10nM) and 10-fold above the K_d (100nM) for the non-mutated mCTLA-4-Fc wild type (WT) and for each of the 23 mutants. After doing triplicates of the yeast binding assays with nc19 and nc20 scFv clones, we normalized each MFI from flow cytometry to the MFI of binding for the 100nM WT mCTLA-4-Fc within either nc19

or nc20 and plotted the resulting normalized MFIs (Figure 49 (a)). Thus, within the 10 and 100nM values plotted for nc19 for example (teal and blue dots), the WT blue (100nM) point was at a value of 1 because its MFI was divided by itself, and the 10nM WT value was close to 0.55 because it is normalized to the ~91% binding saturation expected from 100nM. Thus, within the whole plot, any of the 100nM points over 1 indicate higher binding, and lower than 1 indicate lower. Any of the 10nM points below the WT 10nM value (roughly indicated by the dotted line) also indicated lower binding. If the CTLA-4 mutants have a lower or higher K_d than WT, the ratio of 10nM to 100nM would be expected to vary, which explains why the distance apart of 10nM and 100nM values within a particular mutant was not always the same as for the WT.

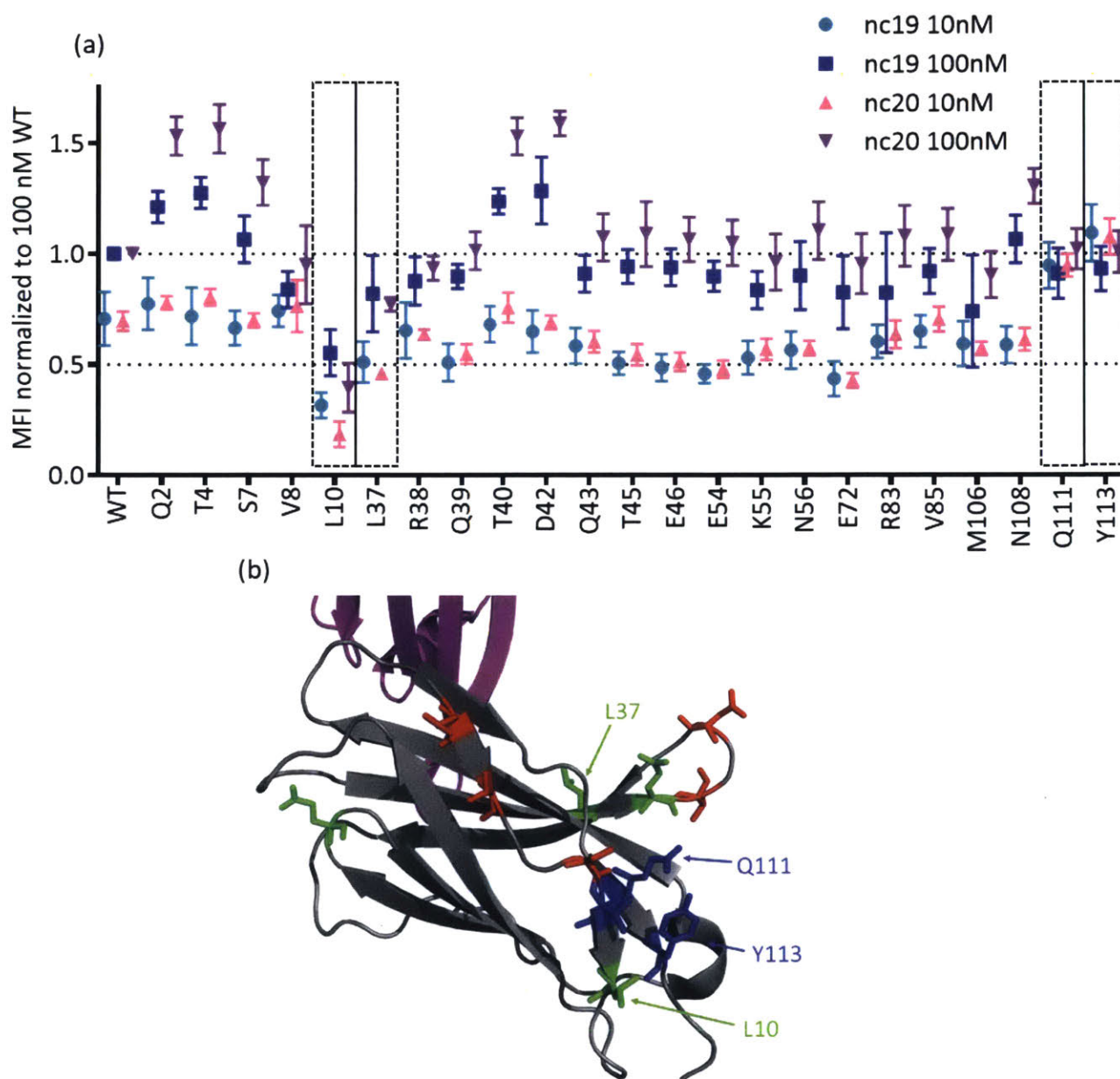


Figure 49: mCTLA-4-Fc epitope mapping results for nc19 and nc20 scFv yeast binding assay
 (a) WT or mutant mCTLA-4-Fc was incubated for at least 2 hours with yeast expressing scFvs nc19 or nc20. The mCTLA-4-Fc constructs were used at two different concentrations of 10nM or 100nM and

detected on the yeast surface through an anti-mouse secondary antibody. The MFI of scFv displayers (c-Myc+ yeast population) was plotted normalized to the 100nM WT mCTLA-4-Fc MFI from either nc19 or nc20. (b) Ribbon structure of mCTLA-4 (grey) aligned to human B7 (magenta), highlighting some of the residues that were shown to either reduce or improve binding in the alanine scan.

The results that the mutation of L10A lowered binding while Q111A and Y113A improved binding suggested that nc19 and nc20 bind CTLA-4 near the cell surface since these 3 residues were near each other structurally and all located near the surface side of CTLA-4 (Figure 49 (b)). Although leucine itself is not a large amino acid, perhaps its side chain sticks out enough to enable binding of nc19 and nc20 that was ablated when mutated the smaller alanine side chain. The residues glutamine and tyrosine at positions 111 and 113 both have large side chains, and perhaps mutating these side chains to alanine improved binding of nc19 and nc20 because it allowed them better access to the epitope area near L10. Regardless, the location near the cell surface side of CTLA-4 for these 3 residues that affected nc19 and nc20 binding supported the hypothesis that the cell surface sterically hindered nc19 and nc20 from binding their epitope on CTLA-4.

New set of sorts to bias library away from nc19 and nc20 uncovers new clones, but all B7-competitive

Looking back in sanger sequencing data from many different generations of yeast sorts, it became clear that the DGLP motif in nc19 and nc20's CDR H3 region emerged very early as a dominant clone as soon as B7 was used to bias library (starting in the generation labeled '2', Figure 42). Since nc19 and nc20 are dominant, but undesirable clones, we decided to try to bias the library away from anything binding CTLA-4 at the same epitope as nc19 or nc20. Thus, the sort from generations '1' to '2' was repeated also in the presence of nc20 to create generation '2x' (Figure 42). Although CTLA-4 may be sterically crowded when both B7 and nc20 are already bound, which could make it hard for yeast scFvs to find epitopic real estate on CTLA-4, we did identify 6 new clones after the set of sorts leading to '2x' with very different CDR H3 region than had been seen before (Figure 50 (a)). These 6 scFvs were cloned and expressed in a human IgG1 backbone and were shown to bind HEK surface CTLA-4 using the same pIRES acGFP transfection system (Figure 50 (b)). Interestingly, the anti-CTLA-4 flow cytometry labeling antibody clone UC10 was blocked from binding CTLA-4 by 9d9 (B7-competitive) but not blocked by any of the new clones, suggesting that the new clones may bind a different site on surface CTLA-4 than 9d9 (Figure 50 (c)).

(a)

1	CARSRYNYFDYW
2	CARYRYNYFDYW
3	CARYDKNYFDYW
4	CARYSKNYFDYW
5	CARYKINYFDYW
6	CARYGISSVFDYW

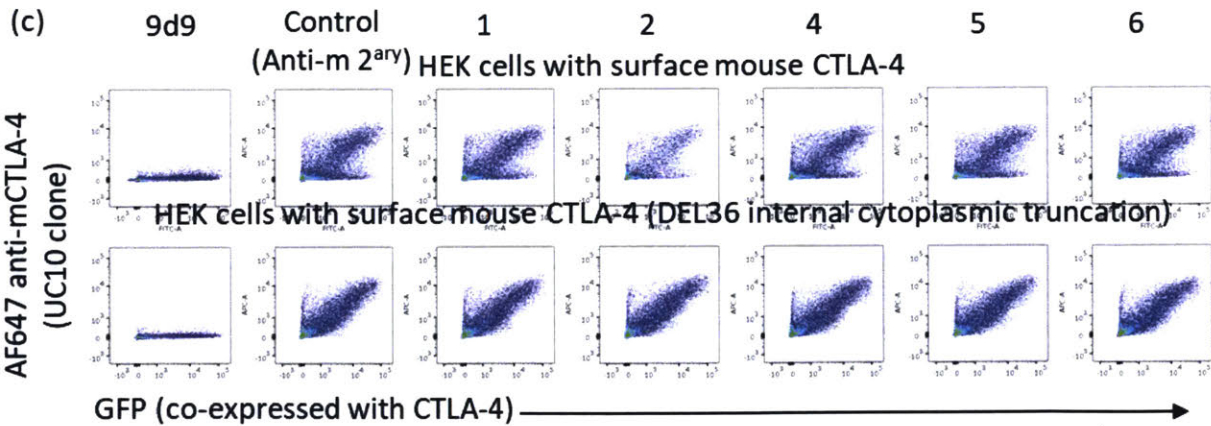
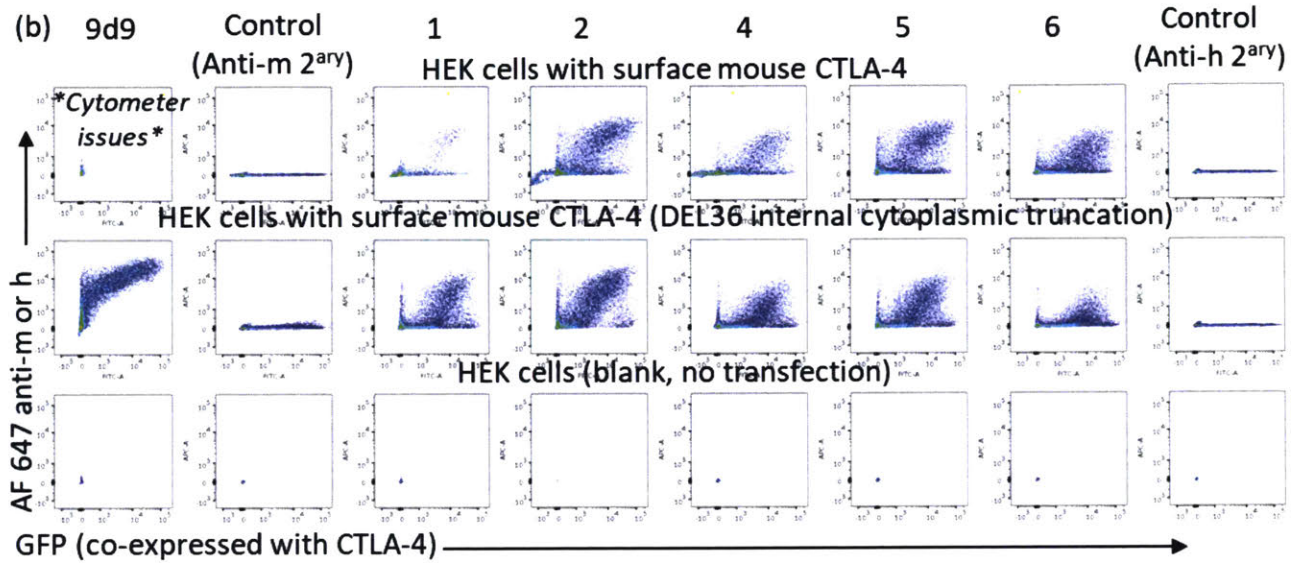


Figure 50: 6 new clones were expressed as antibodies and tested from 2x generation of yeast sorts

(a) List of 6 new clones that were expressed as human IgG1. (b) These clones are shown to bind surface mouse CTLA-4 by staining cells with anti-human secondary antibody (anti-mouse was used for the mouse 9d9 antibody). (c) After labeling cells with either 9d9 or the new clones, cells were then labeled with the anti-mouse CTLA-4 antibody UC10 clone. Since the anti-mouse CTLA-4 antibody cell surface staining was seen for the new clones but not 9d9, it is possible the new clones actually bind a different epitope than 9d9.

Unfortunately, and despite the fact that these clones emerged after sorting in the presence of B7, these clones all appeared to be B7-competitive (Figure 51). Using an anti-human secondary antibody to detect staining, presence of any of the 6 new clones was only detected when the concentration of B7 drops below 200nM to 40nM, indicating that the clones could not access surface CTLA-4 when bound to B7. This meant that the 6 new clones would not be good candidates to move forward with for further development of B7-noncompetitive CTLA-4 binders.

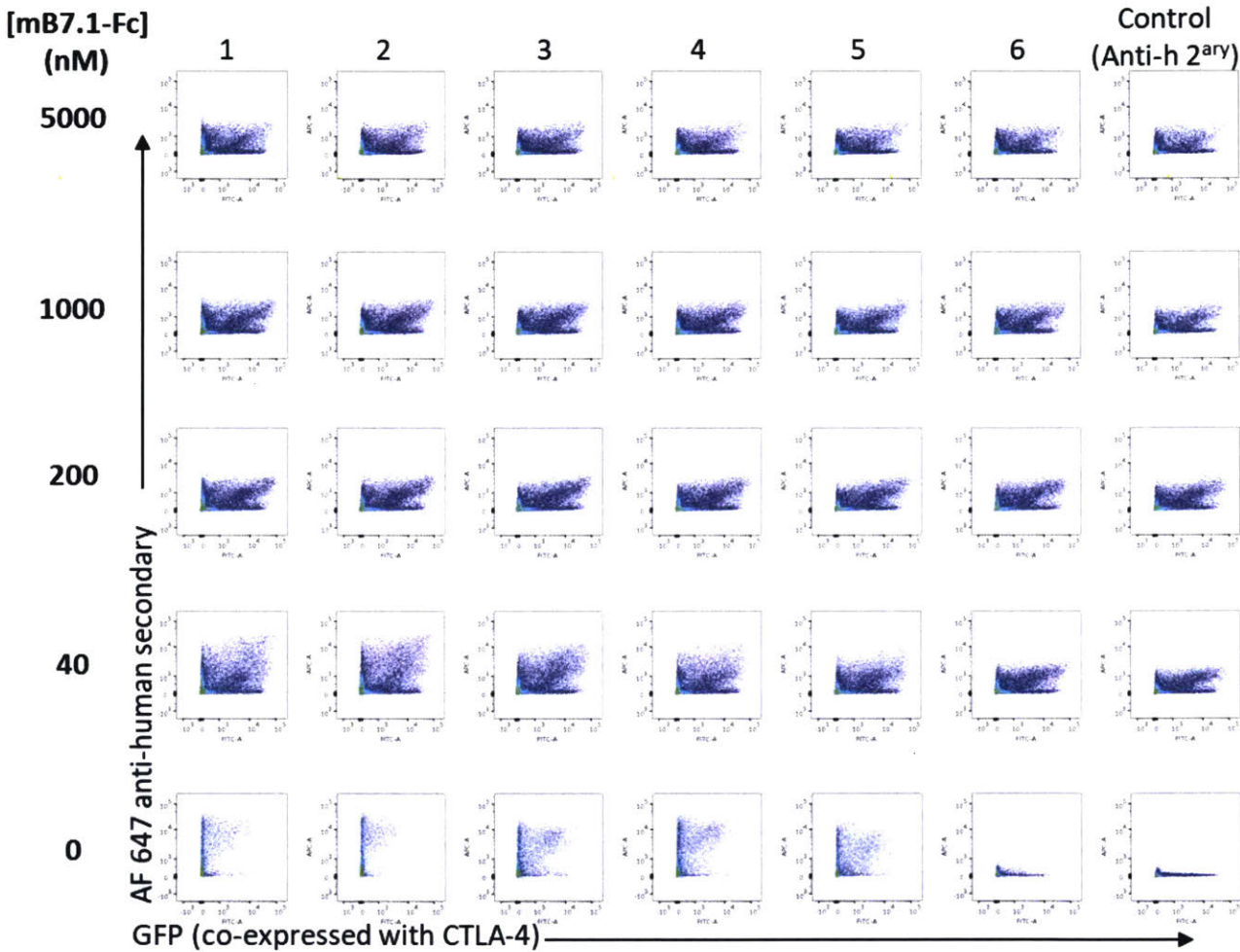


Figure 51: CTLA-4 binding with B7 competition of 6 new clones from 2x generation
 CTLA-4 expressing HEK cells were incubated with the 6 new clones and dilutions of mB7.1Fc prior to labeling with anti-human secondary antibody.

Although some other clones were identified other than nc19 and nc20 at various sort generations, all of them emerged to be B7-competitive. For example, clones emerged with motifs similar to YGITSVFDYW or SLGVGHYFDYR but were B7-competitive, although only tested on the yeast surface as scFvs and never actually tested for surface CTLA-4 finding. Clones with the SRANYFDYW, YKYNFYFDYW, and YGISSVFDYW motifs did emerge at other points in the sorts, but those were all identical or in the same family as the 6 clones tested from the 2x generation (Figure 51 (a)).

Next gen sequencing

Since the above, newly-found binders did bind surface CTLA-4, but they are all B7-competitive, the more comprehensive approach of next generation sequencing (NGS) was used to computationally identify rare clones enriched after the sort with B7 competition. In order to find clones outside of the nc19 and nc20 binding site that were also B7-noncompetitive, parse out enrichment of B7-noncompetitive binders from all CTLA-4 binders, we prepared illumina libraries from

Since the yeast libraries used for NGS were before any affinity maturation, there is minimal variation in the light chain and first two CDRs of the heavy chain composed of three original light chain frameworks and 5 original heavy chain frameworks¹⁶⁷. Paired end Illumina sequencing was done with 144 nucleotides on the 'Forward' read (starting in the post H3 region reading toward the light chain direction) and 15 nucleotides for the 'Reverse' read (starting in the region prior to the light chain reading light chain in the direction of the heavy chain). These read lengths were enough to identify which light chain framework and which heavy chain framework was associated with a given CDR H3, which would be useful for synthesizing genes to express any H3s of interest after analysis.

Aside from the heavy and light chain framework identification, the bulk of the data analysis was on the CDR H3 regions. To get to the CDR H3 sequences, the reads were first filtered based on the Illumina quality scores for having a probability less than 0.05 for 1 or more mis-identified nucleotides near the CDR H3 region. This filtering step reduced the library size from the original 2-8 million reads per library down to about 20-30% of its original size. Next, each read was translated and filtered based on presence of the amino acids before and after the H3 region, 'DTAVYYCAR' (before) and 'GQGT' (after), which eliminated only a small fraction of remaining H3s. Finally, lists of unique H3s were created with an associated frequency and count, and only unique H3s within each library with counts greater than or equal to 3 were kept for further analysis. There were 1266, 365, and 376 unique CDRH3 regions resulting from libraries 1, 2x, and 2 respectively, and there were 158 sequences shared by all 3 libraries (Figure 52).

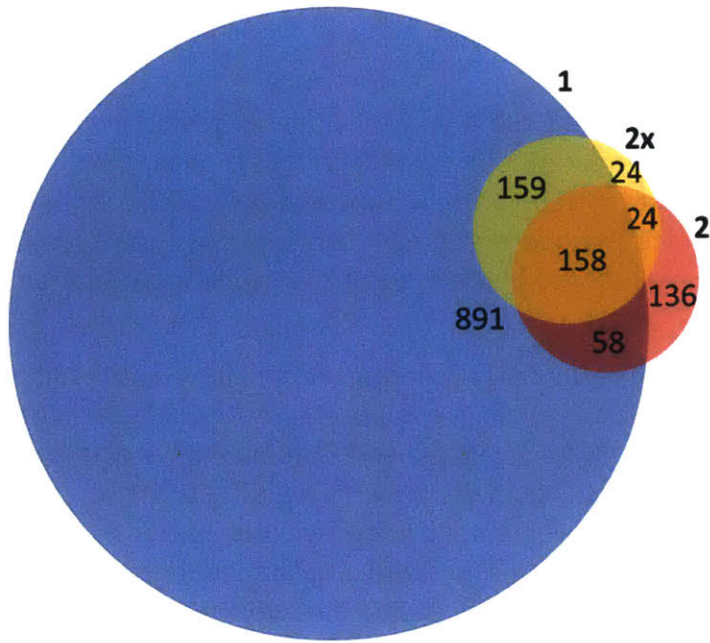


Figure 52: Venn diagram of Illumina results

This Venn diagram showed the overlap in unique H3 sequences between the three different libraries submitted for Illumina sequencing.

With these unique H3s of greater or equal to 3 counts, we next sought to assess whether they were enriched in the libraries that were sorted against CTLA-4 in the presence of B7 (2 and 2x) in order to parse out B7-noncompetitive binders. To do this, we calculated the frequencies of each H3 within its library (1, 2, or 2x). Next, the enrichment over library 1 (prior to B7 sorts) was calculated by dividing each H3 frequency in 2 or 2x by its corresponding frequency in 1. Thus, an enrichment score was associated with each H3 in 2 and each H3 in 2x. An enrichment score more than 1 indicated that a particular H3 occurred at a higher frequency in the daughter library (2 or 2x) compared with the parental library (1), and was used as an indication of potentially being B7-noncompetitive. For all H3s occurring in 2 or 2x but not identified in sequences for 1, we decided to calculate the enrichment score of that H3 by using a frequency in library 1 equal to the lowest frequency found. This assumption was made because, theoretically, all of the sequences in 2 and 2x should have come from 1, indicating that under sampling prevented discovery of that H3 in 1. Thus, assigning the frequency of an H3 not found in 1 to be the lowest frequency of an H3 found in 1 was the conservative assumption we used in order to avoid throwing out those sequences from 2 or 2x.

Within the 182 unique H3s shared by both 2 and 2x, enrichment scores were plotted of the score in 2x over 1 versus 2 over 1 (Figure 53 (a)). Both library 2x and 2 were sorted against mCTLA4 with B7 from library 1, but library 2x had additional selective pressure imposed by the presence of nc20. Ideally, this would bias 2x away from scFvs that bound the nc20 epitope of CTLA-4. If that occurred, then the enrichment for that H3 in library 2x should be greater than enrichment of the same H3 in 2. H3s above the $y = x$ line would indicate potential enrichment of B7-noncompetitive binders to CTLA-4 outside the nc20 epitope. Thus, we zoomed in onto the plot in the 0-20 range on both axes to look a little more closely at the points above the $y = x$ line (Figure 53 (b)).

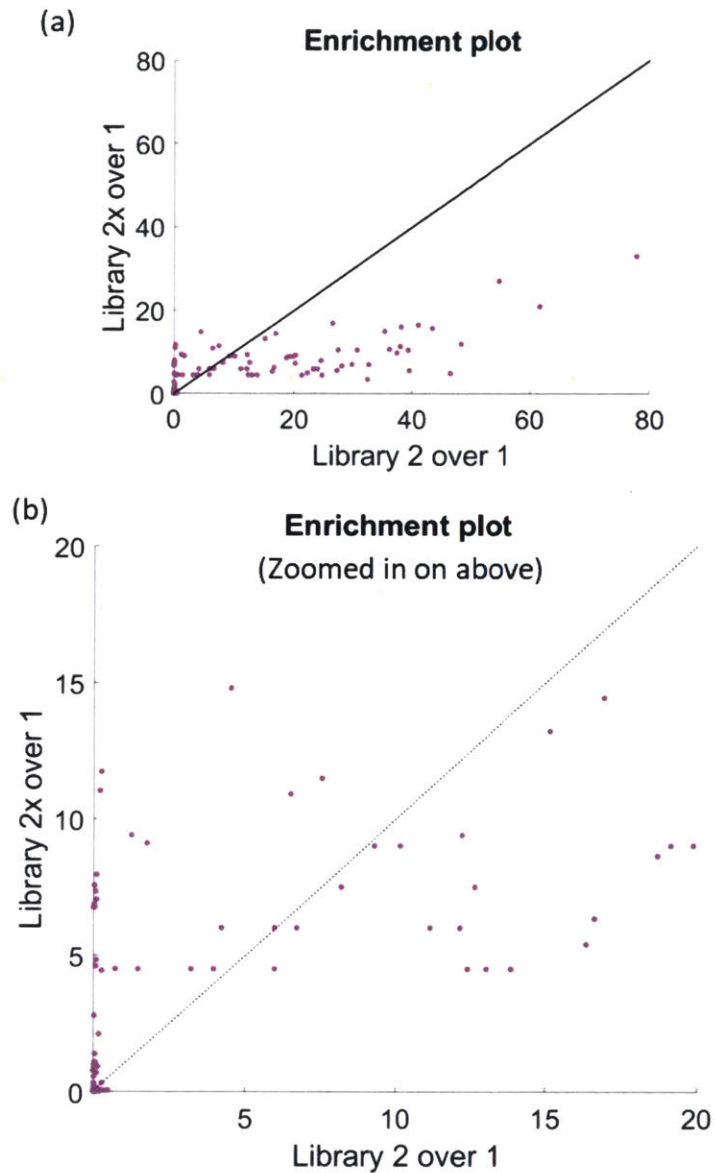


Figure 53: Enrichment plot showing scatter of H3 enrichment in 2x and 2 over the parent library 1

For the 182 H3s plotted that are found in both 2x and 2, their enrichment scores comparing 2x to 1 is on the y axis and enrichment comparing 2 to 1 is on the x axis. Each point corresponds to one H3. The $y = x$ line was plotted to make it clear which had higher enrichment in 2x, vs in 2. (a), all H3s. (b), zoomed in on region of both axes less than 20, to emphasize the individual H3s that have higher enrichment in 2x than 2.

To assess which of the H3s above $y = x$ were important, we deduced that only H3s that have scores above 1 for both 2x and 2 would be expected to be biased towards being B7-noncompetitive. We then chose to conservatively examine H3s with 2x enrichment of more than 2-fold. Resulting from the more stringent analysis imposing that 2:1 enrichment score also had to be greater than 1, only a limited list of H3s emerged that unfortunately reflected motifs very similar to nc19 and nc20, and also B7-competitive clones based on prior testing of scFvs (Figure

54 (a)). When the requirement that the H3 had enrichment score more than 1 in library 2 was eliminated, and focus was put only on 2x enrichment score more than 2, we found 3 new H3 sequences of interest that were dissimilar to nc19/20 and prior B7-competitive motifs (Figure 54 (b)).

(a)	Scores:		(b)	Scores:	
	2:1	2x:1		2:1	2x:1
'YDGLPFDCW'	4.2	6.0	'FSGDSKGSYFDYW'	0.0	6.8
'YDGQPFDFYL'	7.5	11.5	'FYGDAYSYFDYW'	0.1	2.8
'YDGQPFDFYW'	6.5	10.9	'GAYAGGTFDYW'	0.1	4.8
'YDGRPFDFYR'	3.2	4.5	'HKYNYFDYW'	0.2	11.0
'YGISDIFDYW'	4.5	14.8	'SRYNYFDYW'	0.1	6.9
'YGISSVFDCW'	1.5	4.5	'YDENYFDYW'	0.2	2.1
'YGISSVFDYG'	4.0	4.5	'YDGLPFDCW'	4.2	6.0
'YGITSVFDYR'	5.9	6.0	'YDGQPFDFYL'	7.5	11.5
'YGLSDIFDYW'	1.3	9.4	'YDGQPFDFYW'	6.5	10.9
'YRYNYFDYW'	1.8	9.1	'YDGRPFDFYR'	3.2	4.5
			'YGISDIFDYW'	4.5	14.8
			'YGISSVFDCW'	1.5	4.5
			'YGISSVFDYG'	4.0	4.5
			'YGISTVFDYW'	0.1	8.0
			'YGITSVFDYR'	5.9	6.0
			'YGLSAIFDYW'	0.3	4.4
			'YGLSDIFDYW'	1.3	9.4
			'YHNYFDYW'	0.7	4.5
			'YKYNYFD*W'	0.1	7.6
			'YKYNYFDY*'	0.1	7.1
			'YKYNYFDYG'	0.3	11.7
			'YKYNYFDYR'	0.1	6.8
			'YKYNYFDYW'	0.1	7.4
			'YRYNYFDYW'	1.8	9.1
			'YSKNYFDYW'	0.1	4.6

Figure 54: Selected H3s were extracted from the enrichment 2x versus 2 plot analysis

Grey box signified the same motif as nc19 or nc20, and the purple boxes signified motifs that had been shown to be B7-competitive. The red sequences were concluded to be of interest after this analysis. (a) H3s were listed corresponding to having higher enrichment score in 2x than 2 (above the $y = x$ line), score higher than 2 in in library 2x (y axis score), and score higher than 1 in library 2 (x axis score). (b) H3s were listed corresponding to higher enrichment score in 2x than 2 (above the $y = x$ line) and score higher than 2 in in library 2x (y axis score), regardless of the value of their score for library 2 enrichment (x axis score). This was done to capture the points on the y axis of the enrichment plots.

After finding a few H3s of interest in 2x from only enrichment analysis, we decided to further stratify the data by clustering H3s based on biological similarity. Library 2x would hypothetically be the most relevant because it could reveal binders outside the nc19/nc20 CTLA-4 binding site.

However, we acknowledged that sorting for binders to CTLA-4 when it is already bound to both B7-Fc and nc20 could limit results because the bulkiness of the Fc on B7 and full antibody nc20 could sterically hinder scFvs from binding CTLA-4 in other locations. Thus, we separately clustered and examined the 376 and 365 unique H3 sequences in both 2 and 2x, respectively.

In order to decide how many clusters were the best fit for the data, we plotted either within- or between- cluster dissimilarity against increasing total numbers of clusters. If there were an infinite amount of clusters, one would imagine that the cluster dissimilarity would go down to zero because there might only be one item in that cluster. Conversely, with only 1 or 2 clusters, there are many dissimilar items, so that metric would be very high. One important region of these plots for choosing a relevant number of clusters is the elbow, which is a region where the rate of similarity gained from increasing number of clusters begins to decrease. In other words, this is the region where there starts to be diminishing returns from increasing numbers of clusters. Among the 4 metrics of cluster dissimilarity (Figure 55 (a)), heavy consideration was placed on the ratio metric, because this metric reflects not only the intraclustal similarity but also the nuance of how dissimilar clusters get to other clusters when the number is increased. So, we focused on cluster numbers in the elbow region of this ratio metric, which appeared to be less than 20 for every library (Figure 55 (b, d, f)). Focusing on the elbow region of the ratio metric, but using all 4 different metrics to assess either within or between cluster pairwise distance, we assessed that 9, 11, and 6 clusters would be the most relevant numbers for libraries 1, 2, and 2x (Figure 55 (c, e, g)).

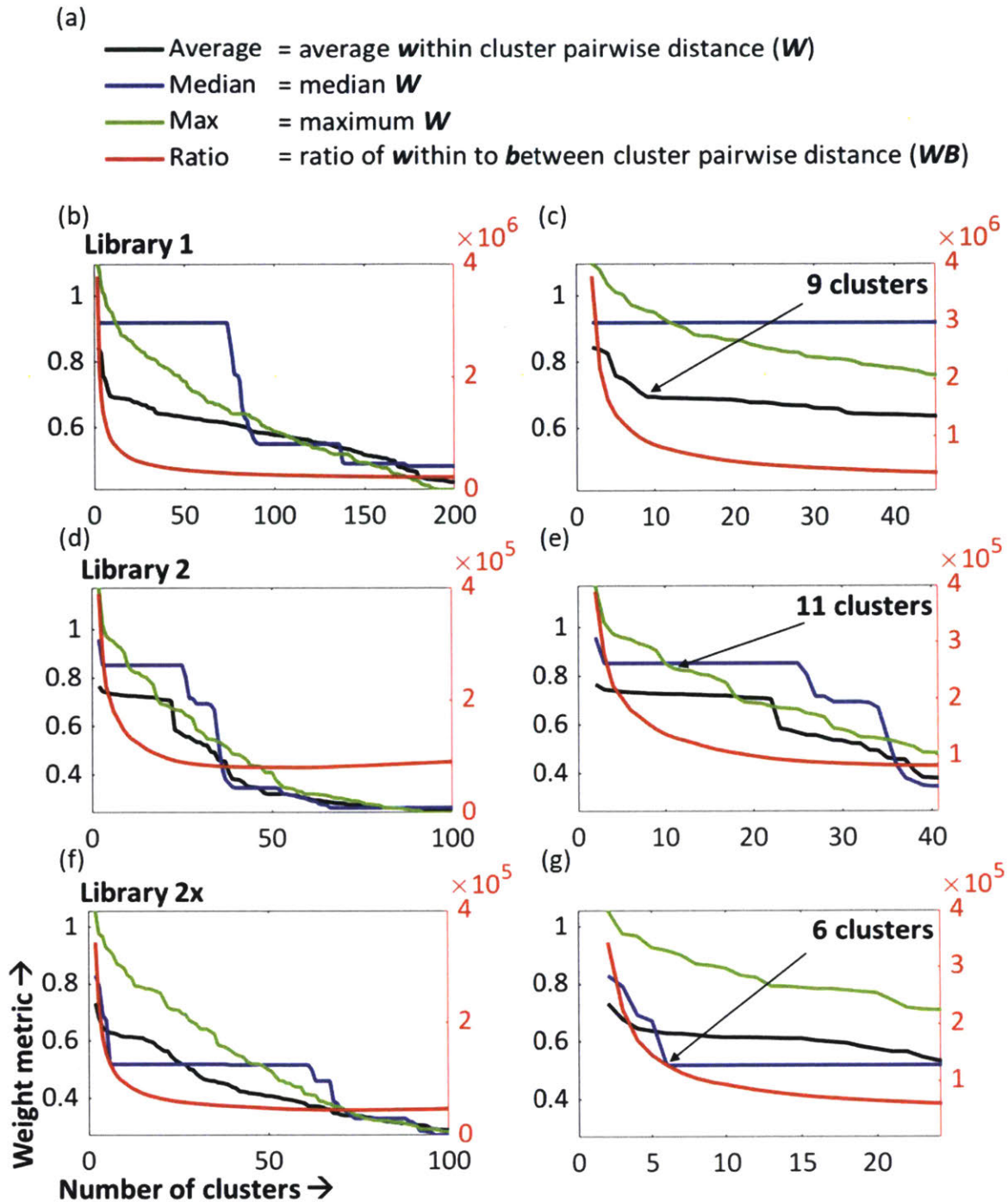


Figure 55: Cluster validation analysis on unique H3s in each library

(a) Description of the different types of weight metric used to decide optimal cluster number. Cluster distance metrics **W** and **B** were based on biological distance between amino acids in the clusters. (b, d, f) The weight metric was plotted as a function of discrete numbers of clusters for libraries 1, 2, and 2x, respectively. (c, e, g) Regions of the weight plots for 1, 2, and 2x respectively were zoomed from the corresponding full plot on the left side. The number of clusters chosen for that library is listed in bold with an arrow highlighting the portion of the plot that informed the decision on cluster number.

Moving forward with the 11 and 6 validated cluster numbers for libraries 2 and 2x, respectively, we plotted dendrograms to describe the similarity found within each cluster of the unique H3s (Figure 56). Based on the horizontal distance from leaves (H3 sequence) on the left side to their cluster parental node, similarity within a cluster was assessed. For example, within library 2, cluster 8's parental node was located around 0.35, indicating this cluster may be more cohesive than clusters 1 and 5, with parental nodes around 0.2. Cluster 8 in 2 contained the motif for nc19 and nc20, which was strongly enriched in library 2. Although cluster 7 in library 2 had parental node relatively far from the leaves at 0.2, the two main subnodes within cluster 7 were a large group of B7-competitive motifs defined by GITS, GISS, etc, and a small node of very de-enriched sequences compared with library 1.

Similarly for the 2x dendrogram, cluster 6 appeared to be very cohesive because it's parental node lies around 0.4. Examining some of the individual sequences in cluster 6 of 2x, this made sense because they were almost exclusively the nc19 and nc20 motifs. However, cluster 1 within 2x appears very diverse and has a parent far from the leaves at 0.1. The YNYKYRY motif was very prominent in cluster 1 of 2x, which unfortunately is B7-competitive. There were a wide smattering of other motifs, however, that were examined further after stratification based on enrichment score.

Libraries 2 (a) and 2x (b) were plotted as dendrograms, and the cluster number associated with each of the 11 clusters in library 2 and 6 clusters in library 2x were labeled based on color.

The enrichment scores were re-plotted, but this time including all H3s within 2 or all H3s within 2x, and grouped based on cluster (Figure 57). Within these plots, it was easier to pick out notable motifs that defined the high end of a particular cluster's enrichment, like the EDLAYHLDFDYW motif that appears highly enriched in both 2 and 2x in clusters 3 and 2, respectively. The wide diversity of cluster 1 in library 2x was also exemplified in this plot, with a large spread of enrichments. Cluster 4 of library 2 also showed fairly consistently low enrichment, which made sense because it had motifs like the GVGHY motif that was shown to be B7-competitive.

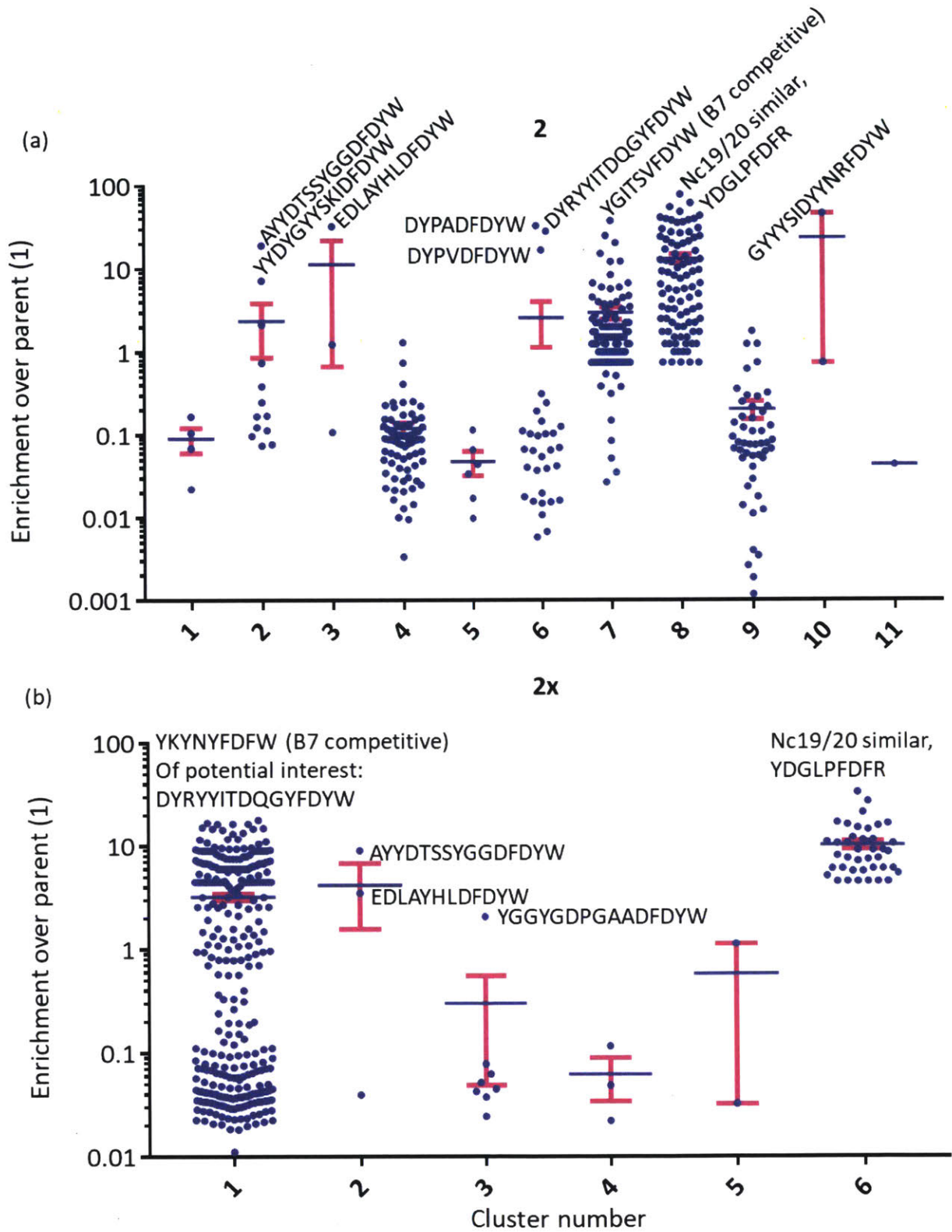


Figure 57: Scattered enrichment in each H3 grouped by cluster
 Enrichment scores for the unique H3s in libraries 2 (a) and 2x (b) were grouped according to cluster and scatter plotted. H3s of interest based on particularly high enrichment were labeled individually.

Although looking at enrichment within the clusters was important, another factor relevant for deciding whether to pursue a particular H3 was amount of reads that occurred. Thus, volcano plots were made that emphasized which H3s of high read count also had high enrichment (Figure 58). Sequences of interest from this analysis were also annotated.

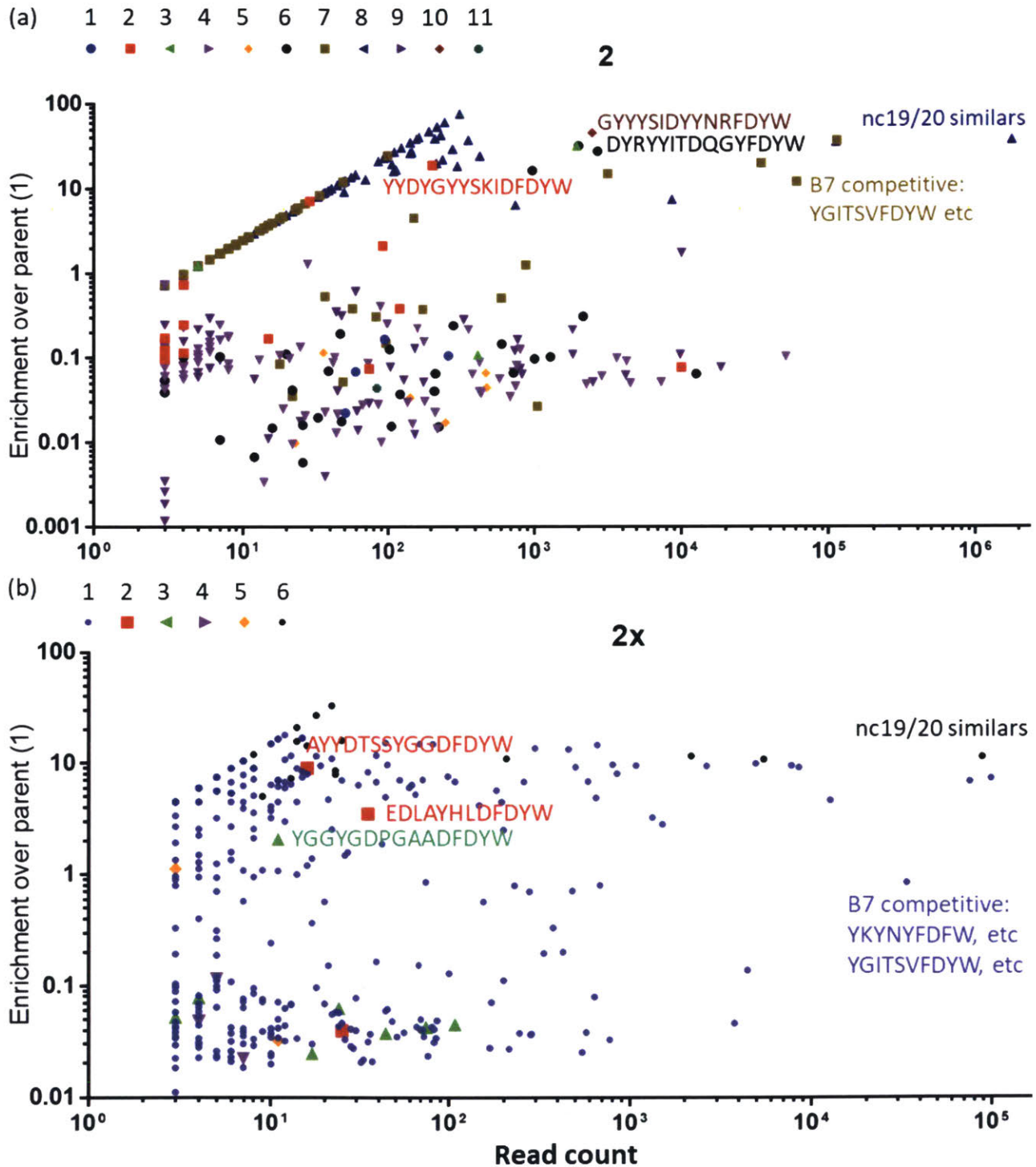


Figure 58: H3 enrichment scores plotted against read count

Enrichment scores for the unique H3s in libraries 2 (a) and 2x (b) were plotted against the read count of that particular score. Clusters were identified within each library with color coding. H3s of interest based on particularly high enrichment and read count were labeled individually.

Summarizing the next generation Illumina sequencing results, we created a table of relevant H3s from various analysis, along with their enrichments over parental library 1 (Figure 59). In order to expedite expression of these H3s, we also noted the particular heavy and light chain frameworks associated with each sequence. There were 22 total H3s of interest because of high enrichment, coupled with high read count or unique sequence. Since expression of 22 antibodies would likely be lengthy, these H3s were grouped based on similarity and color coded within the table (white background denotes lack of grouping). If only one H3 sequence were chosen for expression from each grouping, and all unique H3s were expressed, there would be only 11 different antibodies to synthesize and express. Within a color-coded grouping, an H3 could be chosen based on lack of challenging residues (like avoiding cysteines), higher enrichment or count within a library (for example, choosing the first of the 2 orange H3s), or accurate reflection of the grouping (like choosing GDYGGGTFDYW, which reflects many trends within the group and also has high enrichment and counts). The next step for this project would be to express these 11 antibodies and test whether they bind to surface mCTLA-4, bind noncompetitively with B7, and do not bind CD28. Any antibodies meeting those characteristics, regardless of affinity, should be used as a scaffold for affinity maturation and further explored in this project.

Source	H3	HC	LC	2x count	2x:1 enr	2x #	2 count	2:1 Enr	2 #	In 1?
2x vs 2	FSGDSKGSY	VH3-15	VK1-39	587	6.78	1	22	0.042	6	yes
2x vs 2	FYGDAYGSY	VH3-23	VK1-39	1522	2.8	1	215	0.065	6	yes
2x vs 2	GAYAGGT	VH3-15	VK3-20	652	4.84	1	103	0.013	6	yes
Clusters	SNYAGGS	VH3-15	VK1-39	805	9.62	1				yes
Clusters	GQYAGGT	VH3-15	VK3-20	1338	3.22	1				yes
Clusters	GDYGGGT	VH3-15	VK3-20	300	13.55	1				yes
Clusters	GEYAGGS	VH3-15	VK3-20	200	2.49	1				yes
Clusters	FGYGGGA	VH3-15	VK1-39	502	9.14	1				yes
Clusters	DGYGGGG	VH3-15	VK1-39	44	15.29	1				yes
Clusters	DGYAGGG	VH3-15	VK1-39	662	14.51	1				yes
Clusters	YDIPSAT	VH4-39	VL1-40	69	14.84	1				yes
Clusters	YDIPYAS	VH4-39	VL1-40	6	9.03	1				yes
Clusters	GGLTEI	VH1-69	VK3-20	22	2.55	1				yes
Clusters	GGLTNI	VH1-69	VK3-20	10	3.23	1				yes
Clusters	DYPAD	VH3-23	VK1-39 & 3-20				2024	32.72	6	yes
Clusters	DYPVD	VH3-23	VL1-40				984	16.63	6	yes
Clusters	DYRYITDQGY	VH3-23	VK3-20	108	6.77	1	2724	28.13	6	yes
Clusters	GYYSIDYYNR	VH1-69	VL1-40	44	4.97	1	2503	46.53	10	yes
Clusters	EDLAYHLD	VH3-23	VK3-20	35	3.51	2	1967	32.5	3	yes
Clusters	AYYDTSSYGGD	VH3-23	VK1-39	16	9.03	2	206	19.15	2	yes
Clusters	YYDYGYSKID	VH3-23	VK3-20				29	7.19	2	no
Clusters	YGGYGDPGAAD	VH4-39	VL1-40	11	2.07	3				yes

Figure 59: Summary table of H3s to pursue after next generation Illumina sequencing

List and characteristics of 22 CDR H3s (CAR_FDYW) of interest from different analysis of the Illumina next generation sequencing data. The color indicates grouping based on motif similarity, limiting the number of unique motifs to 11. Uncolored H3s did not appear to share motifs with any other H3. Their source refers to which particular type of analysis indicated an interest in that H3. The HC and LC columns refer to the framework region(s) associated with that H3. The 2x or 2 count, enr, and # columns refer to

the count, enrichment score, and associated cluster number of that particular H3 within either library. Gray boxes indicate that the H3 was not present in that library. The final column noted whether that H3 was found in the sequencing data for the parental library 1 or not.

4.3 Discussion

Searching for novel CTLA-4 binders continues to be a worthwhile pursuit to shed light on the anti-CTLA-4 mechanism of action and improve upon current therapeutic efficacy. Bispecific anti-CTLA-4 antibodies binding CTLA-4 both competitively and noncompetitively with B7 have potential promote improved disengagement of CTLA-4 with B7 and could change CTLA-4 internalization or recycling. Although the binders we isolated, nc19 and nc20, looked promising in yeast against soluble antigen, they ultimately did not bind to CTLA-4 on the cell surface. ELISAs to soluble CTLA-4 antigen showed they were still functional in antibody format, but the epitope mapping suggested that these binders could bind soluble CTLA-4 at a location sterically hindered by the cell surface. Despite the challenges we faced during this process, there were key learnings that inform future strategy to find CTLA-4 binders.

Firstly, during future engineering to find CTLA-4 binders, strategies could be employed to ensure that the resulting binders still bind surface CTLA-4 by changing conditions on the antigen used for selections. In order to do this, yeast selections could employ CTLA-4-Fc antigen with a couple different linker lengths between the CTLA-4 and Fc in the hopes that these different versions of antigen would have slightly different dimerization, and may not all expose some consistent epitope not present when CTLA-4 dimerizes on the surface. Additionally, to bias binders away from residues of CTLA-4 that are accessible in Fc fusion format but not on surface CTLA-4 due to steric hindrance, CTLA-4-Fc fusions could be made with a portion of the extracellular region on the C terminal side (the side closest to the cell surface and membrane region) curtailed. Although it's possible soluble CTLA-4 could fold slightly differently without some of those C terminal residues, it would stop those residues from being part of a binding epitope. With any of these strategies to switch around the CTLA-4 antigen, alternating sorts should be used to hedge against any one version of altered antigen exposing residues that are not on surface CTLA-4.

In addition to potential improvements to the antigen used, binding to surface CTLA-4 should be tested as early as possible during the engineering process. This can be challenging when a large diversity of clones exist, but as soon as any dominant clone can be recognized, it should be expressed solubly and tested in binding studies to surface CTLA-4. A technique that could be used to increase the throughput for testing emergent yeast CTLA-4-binding clones is a scFv-Fc yeast surface display and secretion system developed in 2015 by the Wittrup Lab with an accompanying scFv scaffold library 'G' of 10^9 members of CDR L3 and H3 diversity already made¹⁶⁸. In this system, galactose induces yeast to express scFv-Fcs, but an amber stop codon terminates the scFv-Fc unless o-methyl-tyrosine is present to allow an orthogonal tRNA synthetase to read through the stop codon to also express Aga2p for display. Thus, galactose-induced yeast display scFv-Fc when o-methyl-tyrosine is in the media and instead secrete scFv-Fc without o-methyl-tyrosine.

Finally, the extracellular portion of CTLA-4 has limited epitopic real estate outside of the B7 binding site. Additional regions of CTLA-4 are obscured by dimerization, and some regions lie too close to the cell surface to be easily accessible. Due to binding constraints and potential issues with steric hindrance, alternative smaller binding scaffolds may be more optimal to develop. For example, a library was published by the Wittrup Lab in 2016 using as its scaffold a reduced charge (RC) version of a highly stable DNA-binding protein from bacteria called Sso7d¹⁶⁹. The RCSso7d library scaffold is only 7 kDa, compared with 27 kDa scFvs, and its smaller size and smaller binding surface may enable it to fit into more sterically crowded epitopes on CTLA-4 near the cell surface, dimer interface, or B7 binding site.

Although the strategies in this chapter did not successfully lead to antibodies that bind to surface CTLA-4, the project's future directions are promising. The list of yeast clones identified from the next generation sequencing data may yield a binder to surface CTLA-4 noncompetitively with B7 that can be affinity-matured into a valuable tool. Alternatively, new binders can be engineered by thinking more carefully about antigen and alternating the antigen, testing surface CTLA-4 binding as early as possible in the process, and using alternative scaffolds that could circumvent steric hindrance issues.

4.4 Materials and methods

Sequences

All DNA sequences used will be made available through the Wittrup Lab dropbox plasmid database.

Next gen sequencing files are addressed in a separate methods section below.

Protein expression and purification

Extracellular regions of mouse CD28, mouse B7.1, mouse CTLA-4, and human CTLA-4 were fused to a mouse IgG2c Fc region separated by a GGS linker region. 3 cysteines in the Fc hinge region were mutated to serine to avoid constraining the homodimerization of the fused protein. These proteins, and subsequent antibodies made from various scFv clones of interest were purified on protein A resin.

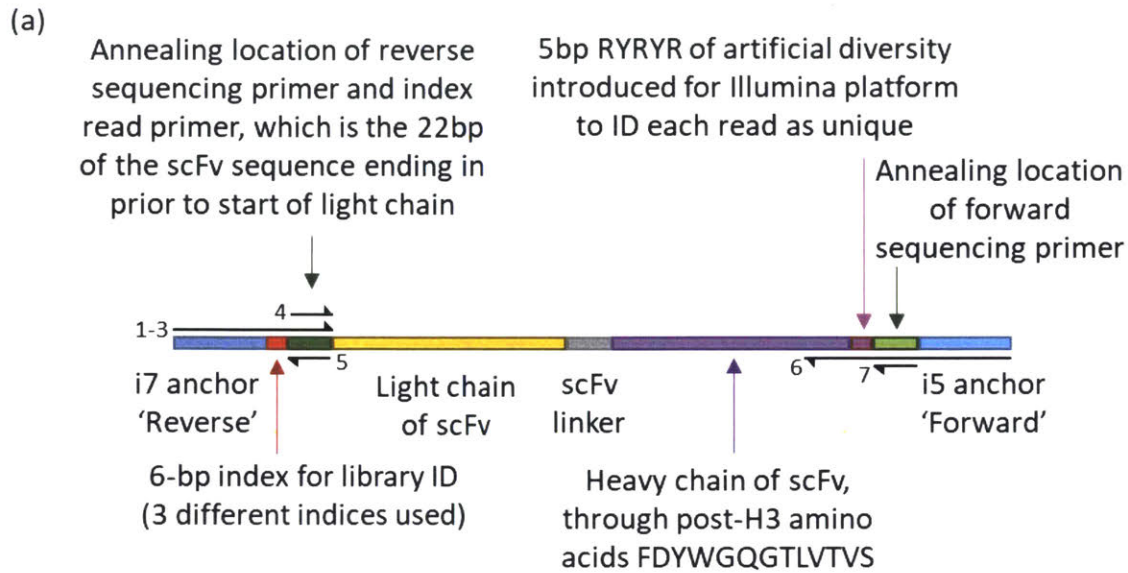
Yeast surface display

Yeast surface display was done according to previously described methods^{166,170,171} using a recently developed scFv library with 5 human heavy chain and 3 human light chain framework regions, characterized by H3 diversity designed to reduce nonspecificity by eliminating tryptophan and reducing the frequency of arginine and valine ('clean H3' library)¹⁶⁷.

Next generation sequencing Illumina library preparation

After overnight growth, yeast populations of interest (generations 1, 2, and 2x (Figure 42)) were diluted to absorbance of 1 and then grown several hours until absorbance of 2 or 3. At least 10 times the expected diversity from each yeast population were pelleted and 1 zymoprep was performed per 10^7 yeast, using 6uL of zymolyase instead of the recommended 3uL and incubating at 37c for 1.5 hours. After neutralization with solution 3, tubes were spun at 14000g for 5 mins and supernatants transferred to Epoch mini prep kit DNA binding columns and the Epoch miniprep protocol was followed for the rest of the steps. Because the DNA binding capacity of the Epoch columns is high relative to the expected amount of yeast plasmid, supernatant was pooled onto 1 or 2 Epoch columns from each generation of yeast.

The resulting pctcon2 plasmids from the yeast minipreps were amplified with primers of unique characteristics to make the Illumina library. PCR for submitting the Illumina libraries was run for only 16 cycles instead of all the way to saturation in order to limit PCR amplification biases from influencing the proportions in the resulting sequencing data. The PCRs were very sensitive to the amount of plasmid template added from the yeast miniprep, so many small scale test PCRs with 10uL were done testing out conditions by adding 1uL template, then dilutions of 4x down from there, and the resulting PCRs examined for brightness on a gel after 20 cycles in order to choose how much PCR volume would be needed for optimal library amplification. We found that about 0.25uL of template worked well per 10uL of PCR volume using 2x HiFi polymerase from Clontech. The PCRs of the full yeast plasmid prep (large volume considering PCR reaction of 0.25uL plasmid per 10uL PCR volume) were not run on a gel, and were instead just PCR purified using a standard Qiagen PCR purification kit prior to submitting to the Koch Core facility for sequencing on a miSeq 10 million read tile using the kit for up to 150nt reads. The resulting libraries submitted to the core had the i5 (forward) and i7 (reverse) anchor sites at either end, index sites, sites for sequencing primers, and some artificial diversity on the forward site right where the sequencing read started, shown in a diagram (Figure 60 (a)). Sequencing primers for NGS are also listed, corresponding to their numbering on the diagram (Figure 60 (b)).



(b)

#	Name	Sequence (all 5' to 3')
1	PCR R1	CAAGCAGAAGACGGCATAACGAGATAGGTTCCGGAGGCGGAGGGTTCGGCTAGC
2	PCR R2x	CAAGCAGAAGACGGCATAACGAGATGTTCCAAGGAGGCGGAGGGTTCGGCTAGC
3	PCR R2	CAAGCAGAAGACGGCATAACGAGATTCCAAGGAGGCGGAGGGTTCGGCTAGC
4	Seq R	CGGAGGCGGAGGGTTCGGCTAGC
5	IX F	GCTAGCCGACCCTCCGCCTCCG
6	PCR F	AATGATACGGCGACCACCGAGATCTACACACTCTTTCCCTACACGACGCTCTT CCGATCTRYRYRGGAGACAGTGACCAGGGTACCTTGGCCCCAGT
7	Seq F	ACACTCTTTCCCTACACGACGCTCTTCCGATCT

Figure 60: Illumina library design

(a) A schematic showed the Illumina library that was amplified from pctcon2 scFv template from the yeast mini preps. Note that the right side was labeled 'Forward' (and associated with the i5 because that is where the most important diversity, the H3 region, is). The left side was labeled 'Reverse' (b) The primers used to amplify the NGS library were listed and color-coded to correspond to their regions in the diagram. Note that primers 1-3 were identical except for a different set of the 6 index base pairs, which were used to identify each of the 3 libraries 1, 2x, and 2.

Matlab, excel, graphpad files from Illumina sequencing data analysis and framework identification

All files for this analysis are found in the Wittrup Lab Dropbox, Database folder, in a folder called “Next gen sequencing analysis files from Adrienne Rothschilds”.

Lists of the frameworks associated with each unique H3 and the lists of H3s with enrichment scores and associated clusters are found in the excel files: “**frameworks associated with each unique AA**” and “**20190402 enr 2 and 2x with clusters**”, in addition to analysis graphpad file “**4-2-19 prism enrichment plots vs count for 2x and 2**”. To run these scripts on matlab, you’ll need to install the bioinformatics toolbox if it’s not already installed. Many functions are ones I wrote and are included in the data and matlab files folder. Note that **N** means that there is one of these files for each of the libraries, N = 1, 2, and 2x.

H3 identification, analysis, enrichment, and clustering:

filtering_fN.mlx: script files for each of the libraries that load and go through and filter the raw fastq read files based on nucleotide quality that the user can input. Note that only the forward reads (object variables titled f1, f2, f2x) are used for filtering, because these are the ones containing the 144nt with H3 and heavy chain framework. The reverse reads (r1, r2, r2x) contain 15 nucleotides from the light chain that are only used to ID the light chain framework. Unfortunately, some commands in this script crash for running more than a million at a time, so the number of millions of reads present (based on first importing the bioread objects in the first section of the file) must be entered as a variable, rounded up to the nearest number of millions, as the script comments. The output from this script is stored in a matlab file called **fNFilt.mat**, which contains:

- **filtSeqN**: (column 1) sequences filtered based on quality and then truncated to keep only the first ~85 relevant nucleotides from the forward read to subsequently translate the CDR H3 region; (column 2) the ascii code for quality scores associated with every nucleotide from the read (not just the first ~85 ones used to decide whether to quality filter).
- **indexKeepN**: This stores the indices of the filtered sequences from the original bioread file. There are separate cell arrays in **indexKeepN** that correspond to each loop that occurs in the **filtering_fN.mlx** script, but if these separate cell arrays were concatenated, the indexes would work (ie, the 2nd cell array corresponds to correct indices from the 1,000,001st to 2,000,000th item that may have been filtered from the original fastqread files). This is probably really confusing, so feel free to reach out to the thesis author Adrienne if you have questions.
- **percentKeepN**: Same number of items as there are cell arrays in **indexKeepN**, but these items correspond to the percents of reads that were kept in each loop through a million reads after filtering

getAAs.mlx: this script takes the **filtSeqN** variables and first finds their reverse complement, storing them in **RCfiles.mat**, which contains:

- RCN: 3 different cell arrays with 1 column corresponding to each sequence from filtSeqN column 1, but reverse complement. This is done because the RC form is then the right orientation to translate into H3.

Next, the getAAs script aligns and translates each RC into amino acids based on using the constant region before the H3, 'GACACGGCCGTGTACTGTGCGAGG'. 3 different matlab files are saved at this point called '**transFilesN.mat**':

- alignN: structure with score and start matrices with description of the alignment score and the start index for each read sequence's alignment with the pre-H3 nucleotide region
- transN: the amino acid translation for each sequence, should be in frame with the H3
- truncN: the nucleotide sequence from the RC, but truncated in the way it was done to spit out the translated AA sequence

Next, the getAAs script filters and trims the AAs in transN (for the 3 different libraries) based on starting with DTAVYYCAR and ending with GQGT using filtTrimAAFun2. The output is stored in **AAFilesFiltTrim.mat**, which contains:

- AAN: cell array with list of filtered, and trimmed amino acid CDR H3 regions. At this point, library 1 has ~1.74 million, library 2 has ~2.34 million, and library 2x has ~385,000
- ixAAN: the index list corresponding to each filtered, trimmed amino acid's location in the transN (and also in the RCN, and filtSeqN) variable

Finally, the unique amino acids in each library are quantified using a matlab function called tabulate, and the outputs are saved as '**TableN.txt**' that have 3 columns. First contains the unique amino acid H3 sequence; 2nd contains the number of counts of that H3 in the larger list; 3rd contains the frequency of that H3 as a %. Keep in mind that H3s that have a stop codon (presumably due to Illumina sequencing errors) were kept, so don't be alarmed if you see stop codons in the list of H3s periodically.

aa_analysis.mlx: First loads the tables and removes the quote marks that appear for some reason as characters before and after each H3. Next, filters the unique amino acid H3 sequences based on having a count greater than 2 using the function filtCounts to generate filtAA1, filtAA2, and filtAA3. Then, enrichFun is used to calculate enrichment scores associated with each unique amino acid, generating '**enrMatrices.mat**', which contains enrichment matrices en_p, which is enrichment of library n over library p. For example, e1_1 is actually just a control because it should all have enrichment ratios of 1 because it's compared with itself. Each file in en_p contains 5 columns. The first 3 columns are unique H3 in library n, counts in library n, and frequency in library n (should be same as stats for that H3 in the TableN.txt file). The next 2 columns are the enrichment ratio of that H3 in library n over p (enrichment > 1 means it has a higher frequency in n than in p) and whether that particular H3 in 'n' actually occurs in 'p' (1 if yes, 0 if no). Because everything in 2x and 2 should theoretically be contained in library 1, it is assumed that the frequency of an H3 that wasn't detected in library 1 is equal to the minimum frequency of any H3 present in 1. This decision was made because we wanted to avoid eliminating any H3s from 2x and 2 in order to capture the most diversity possible.

Next in the aa_analysis script, the en_p matrices were then used (based on the 5th column of 0s and 1st to create lists of overlapping H3s in each library. Then, the first enrichment plot was made of H3s that were in 2x and 2, plotting their enrichment scores (over library 1) in a scatter plot.

The matlab functions seqpdist, seqlinkage, and cluster were used to calculate biological distances between H3s for a particular library, and then validate the numbers of clusters based on a similarity metric. Although the validating was mainly done on line 100, the clustering (using optimal number from the validation) for export to graphpad was done starting on line 142, where names of each H3 were put into the seqlinkage function so that resulting leaves from the clustering are associated with which H3 it is.

Lastly, the function clustToSeqFun was used to create the lists of H3s with their associated information (enrichment, cluster number, etc) into excel (**20190402 enr 2 and 2x with clusters**) and then graphpad (**4-2-19 prism enrichment plots vs count for 2x and 2**).

Framework identification:

In the script file **'frameworkID_find_full_seq'**: After initial filtering based on quality of nt sequence, each remaining sequence (defined by indices stored in indexKeepn variable in fnFilt.mat variables for n = 1,2,2x for the 3 libraries) was extracted (using the handwritten function fullFiltSeq) in full including forward and reverse and stored in the matlab file fullFiltN_F_R.mat with a variable where the first column is the forward sequencing read (which ironically is the RC of the listed frameworks) and the 2nd column is the reverse sequence read (the short one, which corresponds to the light chain framework).

Next, after uploading short regions of the frameworks (and making the reverse complement of the heavy chain frameworks), a heavy chain and light chain framework was assigned to each sequence in the function frameFun and the frameworks corresponding to each sequence are stored in **frn.mat** (for each n=1,2,2x library).

- Note that shorter framework regions than the full ones listed in R Kelly's clean h3 paper were used here for this alignment in order to try to save computational time doing the alignment because both the forward and reverse sequencing reads will only have about 100nt and 15 nt corresponding to the heavy and light chain frameworks, respectively.
- frameFun took 30 mins to 2 hours per library, because it is computationally intensive. frameFun loops through every sequence in an outer loop. Then, for each sequence, it runs a heavy chain (and separate light chain) inner loop returning the score associated with the alignment of that sequence with each heavy chain (5 from ryan's library, but this function is agnostic to the number of possible frameworks) and then light chain in another loop. Next, the function finds the max alignment score for each heavy (and light, respectively) chain framework alignment, and assignments the corresponding framework and max alignment score for heavy chain (columns 1:2) and light chain (columns 3:4) frameworks. I validated this function for sequence 10 by manually finding which frameworks align for heavy and light and comparing them to the function, and the function seems to be working correctly.

- The cell arrays with the framework IDs corresponding to each sequence are found in frn.mat for each of the 3 libraries.

In the **FrameworkUniqueAA** script: A framework is assigned to the list of filtered and trimmed amino acids using the indices stored in the variable ixAA in the AAFilesFiltTrim.mat file (this doesn't use a function, it's just a few lines of code creating new variables from parts of each frn variable corresponding to the filtered, trimmed AAs). Next, the function 'assignFrameFun' is used to tally the counts associated with each of the 5 HC and 3 LC frameworks for a particular unique H3. This is done because most of the H3s occur for many counts in each library. This step was not filtered for counts greater than 2, as the unique H3s used for analysis were, so this framework h3 list is actually longer than the unique H3 list used for analysis. Finally, an excel file is created with columns of counts of light and heavy frameworks corresponding to each unique amino acid sequence, "**frameworks associated with each unique AA**".

4.5 Acknowledgments

This work was supported in part by the Koch Institute Support (core) Grant P30-CA14051 from the National Cancer Institute. We thank the Koch Institute Swanson Biotechnology Center for technical support, specifically the Flow Cytometry, Genomics: High Throughput Screening, and Genomics cores.

Thank you also to Grayson Rodriguez, an undergrad researcher who assisted with many of these studies.

Chapter 5. Perspective and future directions

This dissertation addresses very different challenges within the field of cancer immunotherapy, but all three chapters involve questioning accepted treatment paradigms to engineer improved efficacy or understanding.

Firstly, the IgE project critically examined the ubiquitous IgG class of current tumor targeting antibodies, and quantitatively investigated whether and how allergic immunity could be activated against cancer. We thoroughly characterized the advantages in potency but pharmacokinetic and cellular biodistribution pitfalls of using this different therapeutic modality. Although the IgE project's conclusions from studies in the mouse immune system did not support moving forward with IgE tumor targeting antibodies, the information gained about spatial distribution of IgE and allergic effector cells in mouse cancer models may help instruct the current research on allergo-oncology and could even be useful for understanding allergy.

The last project, engineering novel CTLA-4 binders to better understand and improve upon anti-CTLA-4 antibodies, started with the premise that we first need to understand how anti-CTLA-4 antibodies work before we can rationally incorporate them into treatment schedule design or improve their functionality. We do not currently have the right tools to parse out the importance of enhancing CD8 T cell priming versus depleting Tregs during anti-CTLA-4 therapy. In fact, several papers in 2018 had conflicting conclusions about the mechanism of the same clinical anti-CTLA-4 antibodies¹⁶¹⁻¹⁶³. The nc19 and nc20 B7-noncompetitive CTLA-4 binders described in this dissertation ultimately will not help answer these questions because of their lack of cell surface CTLA-4 binding, but new strategies were proposed that portend optimism for the future success of this project and ability to address some questions enshrouding anti-CTLA-4 antibodies.

The findings of the second project on timing in immuno-oncology and strategies for improving the tradeoffs between toxicity and efficacy have the potential for the greatest impact on the field of immuno-oncology. Unlike the other two dissertation projects, this project provided a strong proof of concept as an example for the paradigm shift proposed. Namely, that the order (or sequence) of combination immunotherapies is critical for their success. Aligning combination immunotherapies with the natural rhythms of the immune system is a paradigm shift that can and should be applied to many combination immunotherapies in preclinical and clinical development, so the final perspectives of this dissertation will address challenges and strategies for implementing these ideas that were recently published⁴⁹.

Effort invested in examination of combination dose scheduling can return qualitatively significant returns with respect to improved efficacy and decreased toxicity, all without necessitating approval of new agents. Putting the "when" into the cancer immunotherapy paradigm will require synthesizing existing knowledge of the progression of the anti-cancer immune response with timing principles established in preclinical and clinical examples, and validating new putative biomarkers to help classify stages of the immune response against tumors. Although the studies described herein begin to establish frameworks for when to administer therapeutic agents along the anti-cancer immune cycle, many open questions remain. Combinations of agents do not always act the same together as their individual components, so how can rational decisions be made about these agents instead of using a guess and test approach? Many individual

immunotherapy agents have pleiotropic roles and the potential to enhance multiple steps of the immune response. Can biomarkers be developed to indicate not only the stage of the anti-cancer immune response, but which agent or agents would enhance that stage? How can researchers and clinicians work together to establish a set of guidelines drawing parallels between the timescales of preclinical and human immune responses for efficient clinical translation of rationally designed treatment schedules?

The time has never been more appropriate to bring these new timing concepts to the clinic. Immuno-oncology garnered international attention in 2018 with the Nobel Prize in Physiology or Medicine, but skyrocketing drug costs and dose-limiting toxicities in regimens indicate that there is significant room for improvement. Immunotherapies such as combination nivolumab and ipilimumab are estimated to cost up to \$300,000 per patient ¹⁷² and cancer care in the US is estimated to cost \$174 billion in 2020 ¹⁷³. In recent immuno-oncology trials such as the CheckMate 067 trial, 39% of patients discontinued treatment due to adverse events ²⁰. Thus, next-gen immunotherapies incorporating timing have the potential to address these economic and toxicity roadblocks through careful duration and sequencing choices that may enable equal or better outcomes from fewer total doses. It will thus be exciting to see some of these testing strategies come into action.

References

1. Couzin-Frankel, J. Breakthrough of the year 2013. Cancer immunotherapy. *Science* **342**, 1432–1433 (2013).
2. Tang, J. Timeline of Anti-Pd-1/L1 Antibody Approvals by the FDA, Cancer Research Institute/ The Anna-Maria Kellan Clinical Accelerator (<http://www.cancerresearch.org/scientists/clinical-accelerator/landscape-of-immuno-oncology-drug-development>). (2018).
3. Tang, J., Pearce, L., O'Donnell-Tormey, J. & Hubbard-Lucey, V. M. Trends in the global immuno-oncology landscape. *Nat. Rev. Drug Discov.* **17**, 783–784 (2018).
4. Coley, W. B. II. Contribution to the Knowledge of Sarcoma. *Ann. Surg.* **14**, 199–220 (1891).
5. Old, L. J., Clarke, D. A. & Benacerraf, B. Effect of Bacillus Calmette-Guérin Infection on Transplanted Tumours in the Mouse. *Nature* **184**, 291 (1959).
6. Lotze, M. T. *et al.* In vivo administration of purified human interleukin 2. II. Half life, immunologic effects, and expansion of peripheral lymphoid cells in vivo with recombinant IL 2. *J. Immunol. Baltim. Md* 1950 **135**, 2865–2875 (1985).
7. Rosenberg, S. A. IL-2: The First Effective Immunotherapy for Human Cancer. *J. Immunol.* **192**, 5451–5458 (2014).
8. Kirkwood, J. M. *et al.* A randomized study of low and high doses of leukocyte alpha-interferon in metastatic renal cell carcinoma: the American Cancer Society collaborative trial. *Cancer Res.* **45**, 863–871 (1985).
9. Golomb, H. M. *et al.* Alpha-2 interferon therapy of hairy-cell leukemia: a multicenter study of 64 patients. *J. Clin. Oncol. Off. J. Am. Soc. Clin. Oncol.* **4**, 900–905 (1986).
10. Dutcher, J. P. *et al.* High dose interleukin-2 (Aldesleukin) - expert consensus on best management practices-2014. *J. Immunother. Cancer* **2**, 26 (2014).
11. Shankaran, V. *et al.* IFN γ and lymphocytes prevent primary tumour development and shape tumour immunogenicity. *Nature* **410**, 1107–1111 (2001).
12. Kaplan, D. H. *et al.* Demonstration of an interferon gamma-dependent tumor surveillance system in immunocompetent mice. *Proc. Natl. Acad. Sci. U. S. A.* **95**, 7556–7561 (1998).
13. Leach, D. R., Krummel, M. F. & Allison, J. P. Enhancement of antitumor immunity by CTLA-4 blockade. *Science* **271**, 1734–1736 (1996).
14. Iwai, Y., Terawaki, S. & Honjo, T. PD-1 blockade inhibits hematogenous spread of poorly immunogenic tumor cells by enhanced recruitment of effector T cells. *Int. Immunol.* **17**, 133–144 (2005).
15. Iwai, Y. *et al.* Involvement of PD-L1 on tumor cells in the escape from host immune system and tumor immunotherapy by PD-L1 blockade. *Proc. Natl. Acad. Sci. U. S. A.* **99**, 12293–12297 (2002).
16. Hirano, F. *et al.* Blockade of B7-H1 and PD-1 by monoclonal antibodies potentiates cancer therapeutic immunity. *Cancer Res.* **65**, 1089–1096 (2005).
17. Hodi, F. S. *et al.* Improved survival with ipilimumab in patients with metastatic melanoma. *N. Engl. J. Med.* **363**, 711–723 (2010).
18. Topalian, S. L. *et al.* Safety, activity, and immune correlates of anti-PD-1 antibody in cancer. *N. Engl. J. Med.* **366**, 2443–2454 (2012).

19. Hamid, O. *et al.* Safety and tumor responses with lambrolizumab (anti-PD-1) in melanoma. *N. Engl. J. Med.* **369**, 134–144 (2013).
20. Wolchok, J. D. *et al.* Overall Survival with Combined Nivolumab and Ipilimumab in Advanced Melanoma. *N. Engl. J. Med.* **377**, 1345–1356 (2017).
21. Ishihara, J. *et al.* Matrix-binding checkpoint immunotherapies enhance antitumor efficacy and reduce adverse events. *Sci. Transl. Med.* **9**, eaan0401 (2017).
22. Park, C. G. *et al.* Extended release of perioperative immunotherapy prevents tumor recurrence and eliminates metastases. *Sci. Transl. Med.* **10**, eaar1916 (2018).
23. Rekers, N. H. *et al.* The immunocytokine L19-IL2: An interplay between radiotherapy and long-lasting systemic anti-tumour immune responses. *Oncoimmunology* **7**, e1414119 (2018).
24. Sagiv-Barfi, I. *et al.* Eradication of spontaneous malignancy by local immunotherapy. *Sci. Transl. Med.* **10**, eaan4488 (2018).
25. Chen, D. S. & Mellman, I. Oncology meets immunology: the cancer-immunity cycle. *Immunity* **39**, 1–10 (2013).
26. Dunn, G. P., Old, L. J. & Schreiber, R. D. The Immunobiology of Cancer Immunosurveillance and Immunoediting. *Immunity* **21**, 137–148 (2004).
27. Mittal, D., Gubin, M. M., Schreiber, R. D. & Smyth, M. J. New insights into cancer immunoediting and its three component phases — elimination, equilibrium and escape. *Curr. Opin. Immunol.* **27**, 16–25 (2014).
28. Druzd, D. *et al.* Lymphocyte Circadian Clocks Control Lymph Node Trafficking and Adaptive Immune Responses. *Immunity* **46**, 120–132 (2017).
29. Ward-Kavanagh, L., Lin, W. W., Šedý, J. S. & Ware, C. F. The TNF Receptor Superfamily in Costimulating and Coinhibitory Responses. *Immunity* **44**, 1005–1019 (2016).
30. Tzeng, A. *et al.* Temporally Programmed CD8 α (+) DC Activation Enhances Combination Cancer Immunotherapy. *Cell Rep.* **17**, 2503–2511 (2016).
31. Spranger, S., Dai, D., Horton, B. & Gajewski, T. F. Tumor-Residing Batf3 Dendritic Cells Are Required for Effector T Cell Trafficking and Adoptive T Cell Therapy. *Cancer Cell* **31**, 711–723.e4 (2017).
32. Moynihan, K. D. *et al.* Eradication of large established tumors in mice by combination immunotherapy that engages innate and adaptive immune responses. *Nat. Med.* **22**, 1402–1410 (2016).
33. Hodi, F. S. *et al.* Nivolumab plus ipilimumab or nivolumab alone versus ipilimumab alone in advanced melanoma (CheckMate 067): 4-year outcomes of a multicentre, randomised, phase 3 trial. *Lancet Oncol.* **19**, 1480–1492 (2018).
34. McKee, S. J., Doff, B. L., Soon, M. S. F. & Mattarollo, S. R. Therapeutic Efficacy of 4-1BB Costimulation Is Abrogated by PD-1 Blockade in a Model of Spontaneous B-cell Lymphoma. *Cancer Immunol. Res.* **5**, 191–197 (2017).
35. Schadendorf, D. *et al.* Efficacy and Safety Outcomes in Patients With Advanced Melanoma Who Discontinued Treatment With Nivolumab and Ipilimumab Because of Adverse Events: A Pooled Analysis of Randomized Phase II and III Trials. *J. Clin. Oncol. Off. J. Am. Soc. Clin. Oncol.* **35**, 3807–3814 (2017).

36. Kohrt, H. E. *et al.* Stimulation of natural killer cells with a CD137-specific antibody enhances trastuzumab efficacy in xenotransplant models of breast cancer. *J. Clin. Invest.* **122**, 1066–1075 (2012).
37. Kohrt, H. E. *et al.* Targeting CD137 enhances the efficacy of cetuximab. *J. Clin. Invest.* **124**, 2668–2682 (2014).
38. Messenheimer, D. J. *et al.* Timing of PD-1 Blockade Is Critical to Effective Combination Immunotherapy with Anti-OX40. *Clin. Cancer Res. Off. J. Am. Assoc. Cancer Res.* **23**, 6165–6177 (2017).
39. Shrimali, R. K. *et al.* Concurrent PD-1 Blockade Negates the Effects of OX40 Agonist Antibody in Combination Immunotherapy through Inducing T-cell Apoptosis. *Cancer Immunol. Res.* (2017). doi:10.1158/2326-6066.CIR-17-0292
40. Rothschilds, A. *et al.* Order of administration of combination cytokine therapies can decouple toxicity from efficacy in syngeneic mouse tumor models. *Oncolimmunology* **8**, e1558678 (2019).
41. Keilholz, U. *et al.* Dacarbazine, cisplatin, and interferon-alfa-2b with or without interleukin-2 in metastatic melanoma: a randomized phase III trial (18951) of the European Organisation for Research and Treatment of Cancer Melanoma Group. *J. Clin. Oncol. Off. J. Am. Soc. Clin. Oncol.* **23**, 6747–6755 (2005).
42. Young, K. H. *et al.* TGF β inhibition prior to hypofractionated radiation enhances efficacy in preclinical models. *Cancer Immunol. Res.* **2**, 1011–1022 (2014).
43. Young, K. H. *et al.* Optimizing Timing of Immunotherapy Improves Control of Tumors by Hypofractionated Radiation Therapy. *PLOS ONE* **11**, e0157164 (2016).
44. Goudin, N. *et al.* Depletion of Regulatory T Cells Induces High Numbers of Dendritic Cells and Unmasks a Subset of Anti-Tumour CD8+CD11c+ PD-1^{lo} Effector T Cells. *PLOS ONE* **11**, e0157822 (2016).
45. Simpson, T. R. *et al.* Fc-dependent depletion of tumor-infiltrating regulatory T cells co-defines the efficacy of anti-CTLA-4 therapy against melanoma. *J. Exp. Med.* **210**, 1695–1710 (2013).
46. Weber, J. S. *et al.* Sequential administration of nivolumab and ipilimumab with a planned switch in patients with advanced melanoma (CheckMate 064): an open-label, randomised, phase 2 trial. *Lancet Oncol.* **17**, 943–955 (2016).
47. Amin, A. *et al.* Phase II study of vemurafenib followed by ipilimumab in patients with previously untreated BRAF-mutated metastatic melanoma. *J. Immunother. Cancer* **4**, 44 (2016).
48. Ascierto, P. A. *et al.* SECOMBIT (sequential combo immuno and target therapy study): A three arms prospective, randomized phase II study to evaluate the best sequential approach with combo immunotherapy [ipilimumab (I) /nivolumab (N)] and combo target therapy [encorafenib (E)/binimetinib (B)] in patients with metastatic melanoma and BRAF mutation. *J. Clin. Oncol.* **35**, TPS9598–TPS9598 (2017).
49. Rothschilds, A. M. & Wittrup, K. D. What, Why, Where, and When: Bringing Timing to Immuno-Oncology. *Trends Immunol.* **40**, 12–21 (2019).
50. Bacac, M. *et al.* CD20-TCB with Obinutuzumab Pretreatment as Next-Generation Treatment of Hematologic Malignancies. *Clin. Cancer Res. Off. J. Am. Assoc. Cancer Res.* (2018). doi:10.1158/1078-0432.CCR-18-0455

51. Kolstad, A. *et al.* Sequential intranodal immunotherapy induces antitumor immunity and correlated regression of disseminated follicular lymphoma. *Blood* **125**, 82–89 (2015).
52. Kozłowska, R., Bożek, A. & Jarząb, J. Association between cancer and allergies. *Allergy Asthma Clin. Immunol. Off. J. Can. Soc. Allergy Clin. Immunol.* **12**, (2016).
53. Dalton, D. K. & Noelle, R. J. The roles of mast cells in anticancer immunity. *Cancer Immunol. Immunother. CII* **61**, 1511–1520 (2012).
54. Theoharides, T. C. & Conti, P. Mast cells: the Jekyll and Hyde of tumor growth. *Trends Immunol.* **25**, 235–241 (2004).
55. Pos, Z. *et al.* Histamine suppresses fibulin-5 and insulin-like growth factor-II receptor expression in melanoma. *Cancer Res.* **68**, 1997–2005 (2008).
56. Cianchi, F., Vinci, M. C. & Masini, E. Histamine in cancer: the dual faces of the coin. *Cancer Biol. Ther.* **7**, 36–37 (2008).
57. Ribatti, D. & Crivellato, E. Mast cells, angiogenesis, and tumour growth. *Biochim. Biophys. Acta* **1822**, 2–8 (2012).
58. Sinnamon, M. J. *et al.* A protective role of mast cells in intestinal tumorigenesis. *Carcinogenesis* **29**, 880–886 (2008).
59. Wedemeyer, J. & Galli, S. J. Decreased susceptibility of mast cell-deficient Kit(W)/Kit(W-v) mice to the development of 1, 2-dimethylhydrazine-induced intestinal tumors. *Lab. Investig. J. Tech. Methods Pathol.* **85**, 388–396 (2005).
60. Dombrowicz, D. *et al.* Allergy-Associated FcR β Is a Molecular Amplifier of IgE- and IgG-Mediated In Vivo Responses. *Immunity* **8**, 517–529 (1998).
61. Gould, H. J. *et al.* Comparison of IgE and IgG antibody-dependent cytotoxicity in vitro and in a SCID mouse xenograft model of ovarian carcinoma. *Eur. J. Immunol.* **29**, 3527–3537 (1999).
62. Karagiannis, S. N. *et al.* Activity of human monocytes in IgE antibody-dependent surveillance and killing of ovarian tumor cells. *Eur. J. Immunol.* **33**, 1030–1040 (2003).
63. Daniels, T. R. *et al.* Targeting HER2/neu with a fully human IgE to harness the allergic reaction against cancer cells. *Cancer Immunol. Immunother. CII* **61**, 991–1003 (2012).
64. Daniels-Wells, T. R. *et al.* A novel IgE antibody targeting the prostate-specific antigen as a potential prostate cancer therapy. *BMC Cancer* **13**, 195 (2013).
65. Paar, J. M., Harris, N. T., Holowka, D. & Baird, B. Bivalent ligands with rigid double-stranded DNA spacers reveal structural constraints on signaling by Fc epsilon RI. *J. Immunol. Baltim. Md 1950* **169**, 856–864 (2002).
66. Kwan, B. H. *et al.* Integrin-targeted cancer immunotherapy elicits protective adaptive immune responses. *J. Exp. Med.* **214**, 1679–1690 (2017).
67. Zhu, E. F. *et al.* Synergistic Innate and Adaptive Immune Response to Combination Immunotherapy with Anti-Tumor Antigen Antibodies and Extended Serum Half-Life IL-2. *Cancer Cell* **27**, 489–501 (2015).
68. Welt, S. *et al.* Monoclonal antibody to an intracellular antigen images human melanoma transplants in nu/nu mice. *Proc. Natl. Acad. Sci. U. S. A.* **84**, 4200–4204 (1987).
69. Josephs, D. H., Spicer, J. F., Karagiannis, P., Gould, H. J. & Karagiannis, S. N. IgE immunotherapy. *mAbs* **6**, 54–72 (2014).
70. Platzer, B. *et al.* IgE/Fc ϵ RI-Mediated Antigen Cross-Presentation by Dendritic Cells Enhances Anti-Tumor Immune Responses. *Cell Rep.* **10**, 1487–1495 (2015).

71. Lantz, C. S. *et al.* IgE regulates mouse basophil Fc epsilon RI expression in vivo. *J. Immunol.* **158**, 2517–2521 (1997).
72. Yamaguchi, M. *et al.* IgE Enhances Mouse Mast Cell FcεRI Expression In Vitro and In Vivo: Evidence for a Novel Amplification Mechanism in IgE-dependent Reactions. *J. Exp. Med.* **185**, 663–672 (1997).
73. Lawrence, M. G. *et al.* Half-life of IgE in serum and skin: Consequences for anti-IgE therapy in patients with allergic disease. *J. Allergy Clin. Immunol.* **139**, 422–428.e4 (2017).
74. Van Gramberg, J. L., de Veer, M. J., O’Hehir, R. E., Meeusen, E. N. T. & Bischof, R. J. Use of Animal Models to Investigate Major Allergens Associated with Food Allergy. *Journal of Allergy* (2013). doi:10.1155/2013/635695
75. Galli, S. J. & Tsai, M. IgE and mast cells in allergic disease. *Nat. Med.* **18**, 693–704 (2012).
76. MacGlashan, D. IgE receptor and signal transduction in mast cells and basophils. *Curr. Opin. Immunol.* **20**, 717–723 (2008).
77. MacGlashan, D. W. Endocytosis, recycling, and degradation of unoccupied FcεRI in human basophils. *J. Leukoc. Biol.* **82**, 1003–1010 (2007).
78. Noguchi, J., Kuroda, E. & Yamashita, U. Strain difference of murine bone marrow-derived mast cell functions. *J. Leukoc. Biol.* **78**, 605–611 (2005).
79. Kinet, J. P. The high-affinity IgE receptor (Fc epsilon RI): from physiology to pathology. *Annu. Rev. Immunol.* **17**, 931–972 (1999).
80. Sektioglu, I. M. *et al.* Basophils Promote Tumor Rejection via Chemotaxis and Infiltration of CD8+ T Cells. *Cancer Res.* **77**, 291–302 (2017).
81. Kehry, M. R. & Yamashita, L. C. Low-affinity IgE receptor (CD23) function on mouse B cells: role in IgE-dependent antigen focusing. *Proc. Natl. Acad. Sci. U. S. A.* **86**, 7556–7560 (1989).
82. Hoffman, W., Lakkis, F. G. & Chalasani, G. B Cells, Antibodies, and More. *Clin. J. Am. Soc. Nephrol.* **11**, 137–154 (2016).
83. Martin, R. K., Brooks, K. B., Henningsson, F., Heyman, B. & Conrad, D. H. Antigen Transfer from Exosomes to Dendritic Cells as an Explanation for the Immune Enhancement Seen by IgE Immune Complexes. *PLOS ONE* **9**, e110609 (2014).
84. Porcherie, A. *et al.* Critical role of the neutrophil-associated high-affinity receptor for IgE in the pathogenesis of experimental cerebral malaria. *J. Exp. Med.* **208**, 2225–2236 (2011).
85. Helm, R. M. Food Allergy Animal Models. *Ann. N. Y. Acad. Sci.* **964**, 139–150 (2002).
86. Young, J. D., Liu, C. C., Butler, G., Cohn, Z. A. & Galli, S. J. Identification, purification, and characterization of a mast cell-associated cytolytic factor related to tumor necrosis factor. *Proc. Natl. Acad. Sci. U. S. A.* **84**, 9175–9179 (1987).
87. Tsai, M. *et al.* The C1.MC/C57.1(C57) mouse mast cell line is of balb/c origin and is tumorigenic in BALB/c MICE. **10**, (1996).
88. Naal, R. M. Z. G., Tabb, J., Holowka, D. & Baird, B. In situ measurement of degranulation as a biosensor based on RBL-2H3 mast cells. *Biosens. Bioelectron.* **20**, 791–796 (2004).
89. Kuehn, H. S., Radinger, M. & Gilfillan, A. M. Measuring Mast Cell Mediator Release. *Curr. Protoc. Immunol. Ed. John E Coligan Al* **CHAPTER**, Unit7.38 (2010).
90. Ali, K. *et al.* Essential role for the p110delta phosphoinositide 3-kinase in the allergic response. *Nature* **431**, 1007–1011 (2004).

91. van Tilbeurgh, H., Loontjens, F. G., De Bruyne, C. K. & Claeysens, M. Fluorogenic and chromogenic glycosides as substrates and ligands of carbohydrases. in *Methods in Enzymology* **160**, 45–59 (Academic Press, 1988).
92. Wei, S. C. *et al.* Distinct Cellular Mechanisms Underlie Anti-CTLA-4 and Anti-PD-1 Checkpoint Blockade. *Cell* **170**, 1120–1133.e17 (2017).
93. Ott, P. A., Hodi, F. S., Kaufman, H. L., Wigginton, J. M. & Wolchok, J. D. Combination immunotherapy: a road map. *J. Immunother. Cancer* **5**, 16 (2017).
94. Budd, G. T. *et al.* Phase I clinical trial of interleukin 2 and alpha-interferon: toxicity and immunologic effects. *Cancer Res.* **49**, 6432–6436 (1989).
95. Rosenberg, S. A. *et al.* Prospective randomized trial of the treatment of patients with metastatic melanoma using chemotherapy with cisplatin, dacarbazine, and tamoxifen alone or in combination with interleukin-2 and interferon alfa-2b. *J. Clin. Oncol. Off. J. Am. Soc. Clin. Oncol.* **17**, 968–975 (1999).
96. Skrombolas, D. & Frelinger, J. G. Challenges and developing solutions for increasing the benefits of IL-2 treatment in tumor therapy. *Expert Rev. Clin. Immunol.* **10**, 207–217 (2014).
97. Flieger, D. *et al.* Enhancement of antibody dependent cellular cytotoxicity (ADCC) by combination of cytokines. *Hybridoma* **18**, 63–68 (1999).
98. Hank, J. A. *et al.* Augmentation of antibody dependent cell mediated cytotoxicity following in vivo therapy with recombinant interleukin 2. *Cancer Res.* **50**, 5234–5239 (1990).
99. Cousens, L. P., Orange, J. S. & Biron, C. A. Endogenous IL-2 contributes to T cell expansion and IFN-gamma production during lymphocytic choriomeningitis virus infection. *J. Immunol. Baltim. Md 1950* **155**, 5690–5699 (1995).
100. Allard, C. B. *et al.* Contemporary trends in high-dose interleukin-2 use for metastatic renal cell carcinoma in the United States. *Urol. Oncol.* **33**, 496.e11–496.e16 (2015).
101. Gresser, I., Bourali, C., Lévy, J. P., Fontaine-Brouty-Boyé, D. & Thomas, M. T. Increased survival in mice inoculated with tumor cells and treated with interferon preparations. *Proc. Natl. Acad. Sci. U. S. A.* **63**, 51–57 (1969).
102. Vilcek, J. Fifty years of interferon research: aiming at a moving target. *Immunity* **25**, 343–348 (2006).
103. Paucker, K., Cantell, K. & Henle, W. Quantitative studies on viral interference in suspended L cells. *Virology* **17**, 324–334 (1962).
104. Diamond, M. S. *et al.* Type I interferon is selectively required by dendritic cells for immune rejection of tumors. *J. Exp. Med.* **208**, 1989–2003 (2011).
105. Fuertes, M. B. *et al.* Host type I IFN signals are required for antitumor CD8⁺ T cell responses through CD8 α ⁺ dendritic cells. *J. Exp. Med.* **208**, 2005–2016 (2011).
106. Yang, X. *et al.* Targeting the Tumor Microenvironment with Interferon- β Bridges Innate and Adaptive Immune Responses. *Cancer Cell* **25**, 37–48 (2014).
107. Fidler, I. J. *et al.* Direct antiproliferative effects of recombinant human interferon-alpha B/D hybrids on human tumor cell lines. *Cancer Res.* **47**, 2020–2027 (1987).
108. Luft, T. *et al.* Type I IFNs enhance the terminal differentiation of dendritic cells. *J. Immunol. Baltim. Md 1950* **161**, 1947–1953 (1998).
109. Santodonato, L. *et al.* Monocyte-derived dendritic cells generated after a short-term culture with IFN-alpha and granulocyte-macrophage colony-stimulating factor stimulate a potent

- Epstein-Barr virus-specific CD8+ T cell response. *J. Immunol. Baltim. Md 1950* **170**, 5195–5202 (2003).
110. Kirkwood, J. M. *et al.* Interferon alfa-2b adjuvant therapy of high-risk resected cutaneous melanoma: the Eastern Cooperative Oncology Group Trial EST 1684. *J. Clin. Oncol. Off. J. Am. Soc. Clin. Oncol.* **14**, 7–17 (1996).
 111. Kirkwood, J. M. *et al.* High- and low-dose interferon alfa-2b in high-risk melanoma: first analysis of intergroup trial E1690/S9111/C9190. *J. Clin. Oncol. Off. J. Am. Soc. Clin. Oncol.* **18**, 2444–2458 (2000).
 112. Kirkwood, J. M. *et al.* High-dose interferon alfa-2b significantly prolongs relapse-free and overall survival compared with the GM2-KLH/QS-21 vaccine in patients with resected stage IIB-III melanoma: results of intergroup trial E1694/S9512/C509801. *J. Clin. Oncol. Off. J. Am. Soc. Clin. Oncol.* **19**, 2370–2380 (2001).
 113. Eggermont, A. M. M. *et al.* Adjuvant therapy with pegylated interferon alfa-2b versus observation alone in resected stage III melanoma: final results of EORTC 18991, a randomised phase III trial. *Lancet Lond. Engl.* **372**, 117–126 (2008).
 114. Tarhini, A. A., Gogas, H. & Kirkwood, J. M. IFN- α in the Treatment of Melanoma. *J. Immunol.* **189**, 3789–3793 (2012).
 115. Benci, J. L. *et al.* Tumor Interferon Signaling Regulates a Multigenic Resistance Program to Immune Checkpoint Blockade. *Cell* **167**, 1540–1554.e12 (2016).
 116. Khan, U., Ali, F., Khurram, M. S., Zaka, A. & Hadid, T. Immunotherapy-associated autoimmune hemolytic anemia. *J. Immunother. Cancer* **5**, (2017).
 117. Grupp, S. A. *et al.* Chimeric Antigen Receptor–Modified T Cells for Acute Lymphoid Leukemia. *N. Engl. J. Med.* **368**, 1509–1518 (2013).
 118. De Filippo, K. *et al.* Mast cell and macrophage chemokines CXCL1/CXCL2 control the early stage of neutrophil recruitment during tissue inflammation. *Blood* **121**, 4930–4937 (2013).
 119. Gao, Y. *et al.* Tumor immunoevasion by the conversion of effector NK cells into type 1 innate lymphoid cells. *Nat. Immunol.* **18**, 1004–1015 (2017).
 120. López-Soto, A., Gonzalez, S., Smyth, M. J. & Galluzzi, L. Control of Metastasis by NK Cells. *Cancer Cell* **32**, 135–154 (2017).
 121. Smyth, M. J., Crowe, N. Y. & Godfrey, D. I. NK cells and NKT cells collaborate in host protection from methylcholanthrene-induced fibrosarcoma. *Int. Immunol.* **13**, 459–463 (2001).
 122. Nishikado, H., Mukai, K., Kawano, Y., Minegishi, Y. & Karasuyama, H. NK cell-depleting anti-asialo GM1 antibody exhibits a lethal off-target effect on basophils in vivo. *J. Immunol. Baltim. Md 1950* **186**, 5766–5771 (2011).
 123. Elpek, K. G., Rubinstein, M. P., Bellemare-Pelletier, A., Goldrath, A. W. & Turley, S. J. Mature natural killer cells with phenotypic and functional alterations accumulate upon sustained stimulation with IL-15/IL-15R α complexes. *Proc. Natl. Acad. Sci. U. S. A.* **107**, 21647–21652 (2010).
 124. Darnell, J. E., Kerr, I. M. & Stark, G. R. Jak-STAT pathways and transcriptional activation in response to IFNs and other extracellular signaling proteins. *Science* **264**, 1415–1421 (1994).
 125. Mandala, S. *et al.* Alteration of lymphocyte trafficking by sphingosine-1-phosphate receptor agonists. *Science* **296**, 346–349 (2002).

126. DuPage, M., Dooley, A. L. & Jacks, T. Conditional mouse lung cancer models using adenoviral or lentiviral delivery of Cre recombinase. *Nat. Protoc.* **4**, 1064–1072 (2009).
127. Patel, J. N. & Walko, C. M. Sylatron: a pegylated interferon for use in melanoma. *Ann. Pharmacother.* **46**, 830–838 (2012).
128. Langenkamp, A., Messi, M., Lanzavecchia, A. & Sallusto, F. Kinetics of dendritic cell activation: impact on priming of TH1, TH2 and nonpolarized T cells. *Nat. Immunol.* **1**, 311–316 (2000).
129. Wang, H. *et al.* cGAS is essential for the antitumor effect of immune checkpoint blockade. *Proc. Natl. Acad. Sci.* **114**, 1637–1642 (2017).
130. Deng, L. *et al.* STING-Dependent Cytosolic DNA Sensing Promotes Radiation-Induced Type I Interferon-Dependent Antitumor Immunity in Immunogenic Tumors. *Immunity* **41**, 843–852 (2014).
131. Corrales, L. *et al.* Direct activation of STING in the tumor microenvironment leads to potent and systemic tumor regression and immunity. *Cell Rep.* **11**, 1018–1030 (2015).
132. Henney, C. S., Kuribayashi, K., Kern, D. E. & Gillis, S. Interleukin-2 augments natural killer cell activity. *Nature* **291**, 335–338 (1981).
133. Swann, J. B. *et al.* Type I IFN Contributes to NK Cell Homeostasis, Activation, and Antitumor Function. *J. Immunol.* **178**, 7540–7549 (2007).
134. Ferrari de Andrade, L. *et al.* Natural killer cells are essential for the ability of BRAF inhibitors to control BRAFV600E-mutant metastatic melanoma. *Cancer Res.* **74**, 7298–7308 (2014).
135. DiLillo, D. J. & Ravetch, J. V. Differential Fc-Receptor Engagement Drives an Anti-tumor Vaccinal Effect. *Cell* **161**, 1035–1045 (2015).
136. Boyman, O. & Sprent, J. The role of interleukin-2 during homeostasis and activation of the immune system. *Nat. Rev. Immunol.* **12**, 180–190 (2012).
137. Busse, D. *et al.* Competing feedback loops shape IL-2 signaling between helper and regulatory T lymphocytes in cellular microenvironments. *Proc. Natl. Acad. Sci.* **107**, 3058–3063 (2010).
138. O’Gorman, W. E. *et al.* The initial phase of an immune response functions to activate regulatory T cells. *J. Immunol. Baltim. Md 1950* **183**, 332–339 (2009).
139. Sckisel, G. D. *et al.* Out-of-sequence Signal 3 paralyzes primary CD4+ T cell dependent immunity. *Immunity* **43**, 240–250 (2015).
140. Yang, J. C. *et al.* Randomized study of high-dose and low-dose interleukin-2 in patients with metastatic renal cancer. *J. Clin. Oncol. Off. J. Am. Soc. Clin. Oncol.* **21**, 3127–3132 (2003).
141. Rosenberg, S. A. Cell transfer immunotherapy for metastatic solid cancer--what clinicians need to know. *Nat. Rev. Clin. Oncol.* **8**, 577–585 (2011).
142. Guo, Y. *et al.* IL-15 Superagonist-Mediated Immunotoxicity: Role of NK Cells and IFN- γ . *J. Immunol. Author Choice* **195**, 2353–2364 (2015).
143. Selby, M. J. *et al.* Preclinical Development of Ipilimumab and Nivolumab Combination Immunotherapy: Mouse Tumor Models, In Vitro Functional Studies, and Cynomolgus Macaque Toxicology. *PLOS ONE* **11**, e0161779 (2016).
144. Clemente-Casares, X. *et al.* Expanding antigen-specific regulatory networks to treat autoimmunity. *Nature* **530**, 434–440 (2016).
145. Liang, Y. *et al.* Innate lymphotoxin receptor mediated signaling promotes HSV-1 associated neuroinflammation and viral replication. *Sci. Rep.* **5**, 10406 (2015).

146. Motzer, R. J. *et al.* Nivolumab plus Ipilimumab versus Sunitinib in Advanced Renal-Cell Carcinoma. *N. Engl. J. Med.* **378**, 1277–1290 (2018).
147. Comin-Anduix, B., Escuin-Ordinas, H. & Ibarrodo, F. J. Tremelimumab: research and clinical development. *OncoTargets Ther.* **9**, 1767–1776 (2016).
148. Ribas, A. *et al.* Phase III randomized clinical trial comparing tremelimumab with standard-of-care chemotherapy in patients with advanced melanoma. *J. Clin. Oncol. Off. J. Am. Soc. Clin. Oncol.* **31**, 616–622 (2013).
149. Blank, C. U. & Enk, A. Therapeutic use of anti-CTLA-4 antibodies. *Int. Immunol.* **27**, 3–10 (2015).
150. Linsley, P. S. *et al.* Intracellular trafficking of CTLA-4 and focal localization towards sites of TCR engagement. *Immunity* **4**, 535–543 (1996).
151. Lindsten, T. *et al.* Characterization of CTLA-4 structure and expression on human T cells. *J. Immunol. Baltim. Md 1950* **151**, 3489–3499 (1993).
152. Linsley, P. S. *et al.* CTLA-4 is a second receptor for the B cell activation antigen B7. *J. Exp. Med.* **174**, 561–569 (1991).
153. Takahashi, T. *et al.* Immunologic self-tolerance maintained by CD25(+)CD4(+) regulatory T cells constitutively expressing cytotoxic T lymphocyte-associated antigen 4. *J. Exp. Med.* **192**, 303–310 (2000).
154. Read, S., Malmström, V. & Powrie, F. Cytotoxic T lymphocyte-associated antigen 4 plays an essential role in the function of CD25(+)CD4(+) regulatory cells that control intestinal inflammation. *J. Exp. Med.* **192**, 295–302 (2000).
155. Peggs, K. S., Quezada, S. A., Chambers, C. A., Korman, A. J. & Allison, J. P. Blockade of CTLA-4 on both effector and regulatory T cell compartments contributes to the antitumor activity of anti-CTLA-4 antibodies. *J. Exp. Med.* **206**, 1717–1725 (2009).
156. Selby, M. J. *et al.* Anti-CTLA-4 antibodies of IgG2a isotype enhance antitumor activity through reduction of intratumoral regulatory T cells. *Cancer Immunol. Res.* **1**, 32–42 (2013).
157. Bulliard, Y. *et al.* Activating Fc γ receptors contribute to the antitumor activities of immunoregulatory receptor-targeting antibodies. *J. Exp. Med.* **210**, 1685–1693 (2013).
158. Matheu, M. P. *et al.* Imaging regulatory T cell dynamics and CTLA4-mediated suppression of T cell priming. *Nat. Commun.* **6**, 6219 (2015).
159. Qureshi, O. S. *et al.* Trans-endocytosis of CD80 and CD86: a molecular basis for the cell extrinsic function of CTLA-4. *Science* **332**, 600–603 (2011).
160. Ingram, J. R. *et al.* Anti-CTLA-4 therapy requires an Fc domain for efficacy. *Proc. Natl. Acad. Sci. U. S. A.* **115**, 3912–3917 (2018).
161. Du, X. *et al.* A reappraisal of CTLA-4 checkpoint blockade in cancer immunotherapy. *Cell Res.* **28**, 416–432 (2018).
162. Arce Vargas, F. *et al.* Fc Effector Function Contributes to the Activity of Human Anti-CTLA-4 Antibodies. *Cancer Cell* **33**, 649-663.e4 (2018).
163. Sharma, A. *et al.* Anti-CTLA-4 immunotherapy does not deplete FOXP3+ regulatory T cells (Tregs) in human cancers. *Clin. Cancer Res.* clincanres.0762.2018 (2018). doi:10.1158/1078-0432.CCR-18-0762
164. Waight, J. D. *et al.* Selective Fc γ R Co-engagement on APCs Modulates the Activity of Therapeutic Antibodies Targeting T Cell Antigens. *Cancer Cell* **33**, 1033-1047.e5 (2018).

165. Linsley, P. S. *et al.* Human B7-1 (CD80) and B7-2 (CD86) bind with similar avidities but distinct kinetics to CD28 and CTLA-4 receptors. *Immunity* **1**, 793–801 (1994).
166. Chao, G. *et al.* Isolating and engineering human antibodies using yeast surface display. *Nat. Protoc.* **1**, 755–768 (2006).
167. Kelly, R. L., Le, D., Zhao, J. & Wittrup, K. D. Reduction of Nonspecificity Motifs in Synthetic Antibody Libraries. *J. Mol. Biol.* **430**, 119–130 (2018).
168. Van Deventer, J. A., Kelly, R. L., Rajan, S., Wittrup, K. D. & Sidhu, S. S. A switchable yeast display/secretion system. *Protein Eng. Des. Sel. PEDS* **28**, 317–325 (2015).
169. Traxlmayr, M. W. *et al.* Strong Enrichment of Aromatic Residues in Binding Sites from a Charge-neutralized Hyperthermostable Sso7d Scaffold Library. *J. Biol. Chem.* **291**, 22496–22508 (2016).
170. Van Deventer, J. A. & Wittrup, K. D. Yeast surface display for antibody isolation: library construction, library screening, and affinity maturation. *Methods Mol. Biol. Clifton NJ* **1131**, 151–181 (2014).
171. Angelini, A. *et al.* Protein Engineering and Selection Using Yeast Surface Display. *Methods Mol. Biol. Clifton NJ* **1319**, 3–36 (2015).
172. Andrews, A. Treating with Checkpoint Inhibitors—Figure \$1 Million per Patient. *Am. Health Drug Benefits* **8**, 9 (2015).
173. Mariotto, A. B., Robin Yabroff, K., Shao, Y., Feuer, E. J. & Brown, M. L. Projections of the Cost of Cancer Care in the United States: 2010–2020. *JNCI J. Natl. Cancer Inst.* **103**, 117–128 (2011).